Design and Manufacture of Surface Topography with Additive Manufacturing: Properties and Applications

by

Ali Khoshkhoo

A dissertation submitted to the Graduate Faculty of
Auburn University
in partial fulfillment of the
requirements for the Degree of
Doctor of Philosophy

Auburn, Alabama
August 4, 2018

Keywords: additive manufacturing, surface finish, distortion, contact angle, surface topography, algae

Approved by

Dr. Andres L. Carrano, Chair, Professor, Industrial and Systems Engineering
Dr. David M. Blersch, Co-chair, Assistant Professor, Biosystems Engineering
Dr. Gregory Harris, Associate Professor, Industrial and Systems Engineering
Dr. Sa'd Hamasha, Assistant Professor, Industrial and Systems Engineering

Abstract

The first study investigates the impact of surface texture parameters of natural surface specimens on the attachment of algae communities. The primary objective of this effort is to show feasibility in the approach of reverse engineering natural surfaces (developing surface features that are biomimetically inspired) to enhance the attachment and species selectivity of benthic algae used in water pollution recovery systems. A secondary objective seeks to elucidate which surface parameters appear to explain the attachment behavior of a selected species. Finally, a method of reverse engineering natural surfaces is proposed in this study that can be implemented in other real-world applications. This work seeks to reveal the surface topography parameters that were significant for algal attachment by manipulating surface topographies using additive manufacturing. In this study, a method for capturing and reversing natural substrata has been developed and proven feasible. Natural rocks and surfaces with attached biofilms were retrieved from streams, scanned with optical profilometry, and the surface characteristics were analyzed. The results show that certain texture parameters (e.g., Smr, Sa, and Sv) show promise in predicting surface colonization by algae. The Pearson distribution was utilized to generate pseudo-randomized surfaces with surface characteristics. A material jetting process was used to additively manufacture the surfaces followed by optical profilometry to validate the resultant topography. The results validated that the set of Sa, Sv, and Smr significantly predict the surface adhesion of benthic algal species.

The second study aims to demonstrate the effects of geometric parameters such as shape, length, height, and pitch size of custom-3-D printed microtextured surfaces on receding and advancing water contact angle. This study reveals that the wetting behavior is highly dependent on the texture design. In addition, the geometrical parameters of the design such as shape, length, height, and pitch size significantly affect the contact angle. Among the geometrical parameters, the shape parameter had the greatest effect on contact angle, and the results indicated that groove design is strongly more hydrophobic than circular protrusion textures.

In the third study, three different issues regarding surface topography that are induced in 3-D printed surfaces are studied. In this study, three objectives were pursued: a) analyzing the surface finish and dimensional accuracy of material jetting processes in different designs and sizes, b) analyzing the effects of build orientation and surface slope on the fidelity of different surface texture designs, and c) analyzing the effects of tile thickness and build orientation on surface distortion and warpage. The results show that protrusion features have fewer dimensional errors than debossed features, especially for sizes smaller than 500 µm. In sizes smaller than 500 µm, the designs of features are indistinguishable and all printed features appear spherical. Slipping of partially cured (solidified) materials deposited right at the edge of features results in rounded shape edges and dimensional errors in fabricated designs.

This work indicated that surface slope creates stair-stepping, which affects different aspects of surface characteristics. The height and volumetric functional parameters are significant among

others and show a better surface finish for the 0° surface slope compared to the 45° surface slope. This study showed that if the build tray is orientable through the printing process, the build tray can be tilted to variable degrees to increase the dimensional accuracy and create sharper edges for some designs such as polygons (not curved features) and features with recess designs. Increased surface slope also brings disadvantages such as a stair-stepping effect, a rough surface, asymmetry, and remains of the traces of moved material along the slope.

Minimizing the dimensional distortion in material jetting processes requires consideration of both the part design and process conditions. The type of distortion generated by a high aspect ratio specimen is dependent on the part thickness of the specimen, while the build orientation becomes a significant process parameter only when in very thin sections. The development of design guidelines should incorporate the knowledge that most geometries will experience distortion along the longest axis and that increasing wall thicknesses will help minimize potential deformations. Also, whenever thin part sections (~1 mm) are fabricated, the YX build orientation appears to decrease the amplitude of the deformation wave, as expressed by the height of the highest peak.

Acknowledgments

I would like to acknowledge everyone who assisted me throughout my doctoral studies over the years. First and foremost, I would like to thank and dedicate all my success to my lovely family (Parivash Korouni, Fazlollah Khoshkhoo, and my sister Elnaz Khoshkhoo). Their love, support, and encouragement were what made my doctoral studies and this dissertation possible. I would like to acknowledge my advisor, Dr. Andres Carrano for his enthusiastic support and guidance which made my doctoral studies a very rewarding experience. Also, my great appreciation is expressed to my co-advisor, Dr. David Blersch for his support and guidance in navigating through the world of ecological engineering. I want to especially thank members of my research group Dr. Kamran Kardel, Gabriel Proano, and Manjinder Kaur for their stimulating discussions and all the fun I had working with them. Many thanks to my dearest friends Mohammadnaser Ansari, Hossein Talebinezhad, Dr. Hamid Ghaednia, and Bahareh Karimi for their kind supports in my experiments and studies. I also would like to appreciate my committee members Dr. Gregory Harris and Dr. Sa'd Hamasha for their feedback, time, and support. Special thanks to Dr. Marghitu for his willingness to serve as the University Reader and his enthusiastic support. Appreciation is expressed to Dr. Michael Bozack of Auburn University's Physics Department for providing XPS analysis and all his help and support. Finally, I would like to thank my dearest friends Dr. Shahab Shervin and Dr. Kaveh Shervin for all their spiritual and mental support.

Table of Contents

List of Tables

List of Figures

Introduction

Additive Manufacturing (AM) includes most processes that create objects from a 3D computer model by adding material layer by layer [1]. The main advantages of AM technologies compared to traditional manufacturing lie in their capability to fabricate complex geometries with internal features as well as to modulate material composition and properties. Additive manufacturing technologies have been used in industries for prototypes, production tools, as well as final products [2]. A comprehensive taxonomy of AM processes is provided in the ASTM F2792 standard, which classifies AM processes in seven categories: binder jetting, directed energy deposition, material extrusion, material jetting, powder bed fusion, sheet lamination, and vat photopolymerization [1]. Of those categories, material jetting is one of more recently developed AM technologies. In this technology, a photopolymer resin is repeatedly projected over the tray surface through a printing head and cured by ultraviolet (UV) radiation to form a solid layer and, ultimately, a three dimensional part (Figure 1). When the layer has cured, the tray drops the equivalent of a layer thickness along the Z-axis. This procedure is repeated until the part is built. The printing head consists of dozens of micro-jetting orifices that are capable of forming layers with a thickness of few micrometers [3], [4].

Additive manufacturing has applications for surface design because of its capability to fabricate complex models and features that are either impossible or difficult to fabricate with other manufacturing technologies.

The main reason to use material jetting technology in this study for different topics and applications is its high surface build fidelity which affects applications such as algae colonization, surface wettability behavior, dimensional accuracy and surface finish.

Since material jetting is a recent development in AM technologies, few studies have investigated its surface quality and mechanical properties. This work intends to analyze: a) the accuracy of material jetting processes in different designs and sizes, b) the effects of surface slope and build orientation on the surface finish as well as the dimensional accuracy of various features, and c) the effect of specimen thickness and build orientation on the type and magnitude of distortion in material jetting processes.

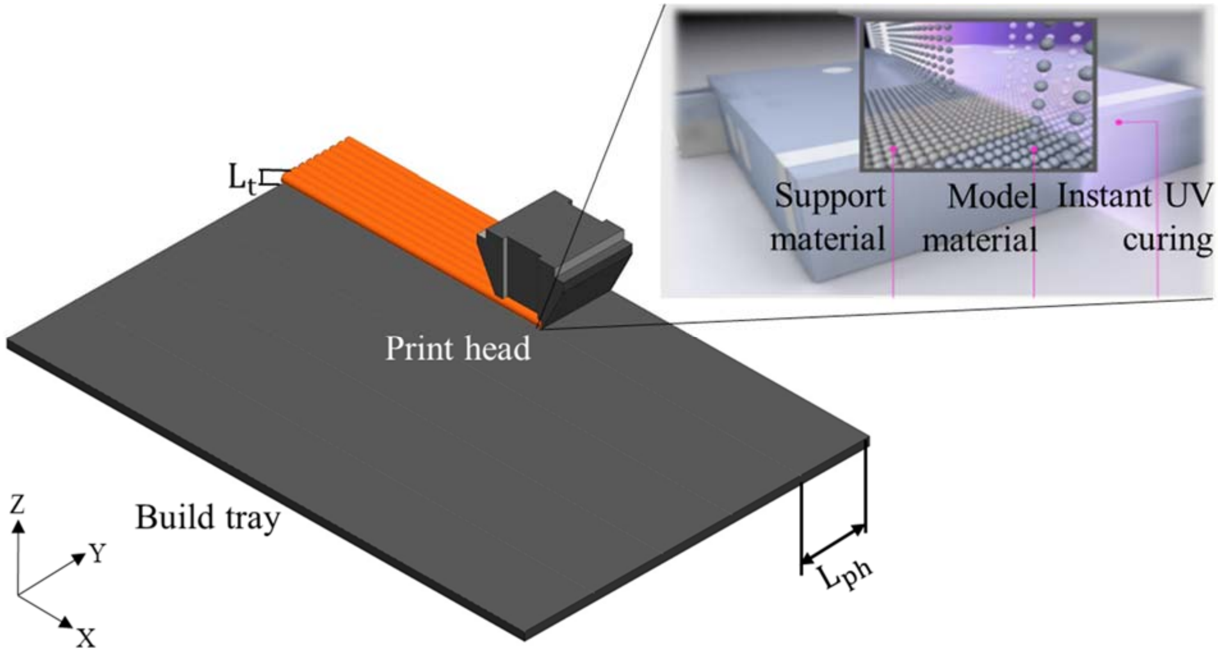

Figure 1 Material jetting processes. The Effective printing width of the head (L_{ph}), layer thickness (L_t) [5]

Many industrial and laboratory applications need polymers to behave as hydrophobic or hydrophilic substrates. The contact angle measurement is a common way to evaluate the hydrophobicity of a substrate. Contact angle measurements are also used to assess liquid purity and the effects of surface treatments in surface science and industrial applications [5] [6]. The balance between hydrophilic and hydrophobic interactions at the solid surface of a substrate is evaluated by the contact angle developed between three phases: liquid, solid, and gas (Figure 2). As shown in Figure 2, θ is the static contact angle between the liquid and solid substrate, γ_{ls} is the surface tension between liquid and solid, γ_{lv} is the surface tension between liquid and gas, and γ_{sv} is the surface tension between solid and gas. Many physical and chemical factors such as type, shape, and size of the particles of material as well as surface roughness and surface geometry influence the contact angle and wetting behavior of a substrate [6]. Additive manufacturing in particular offers the opportunity to design and fabricate customized and complex substratum surfaces to tune the contact angle with a high level of fidelity and repeatability [8]–[10]. To date, no study has investigated the effects of microtextures' geometric parameters such as shape, length, height, and pitch size on contact angle. The pre-described material jetting characterization study helps to design a feasible experiment (i.e., factors and their levels) considering the manufacturing fidelity of the technology. Thus, the aim of this work is to examine the effects of these geometric factors of custom-3-D printed microtextured surfaces on wettability behavior of the surface.

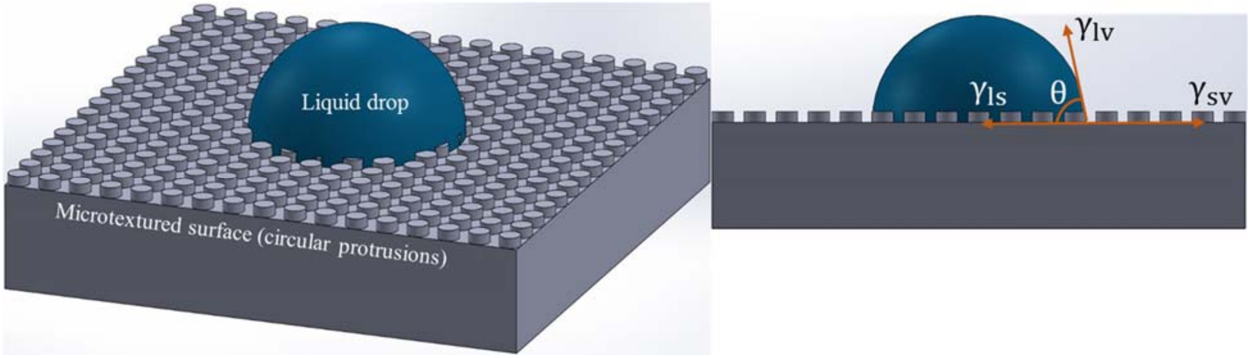

Figure 2 Contact angle developed between three phases: liquid, solid and gas

Algae are a diverse group of photosynthetic organisms that range in size from unicellular genera to multicellular forms which belong to different evolutionary lineage [11]. Due to their fast-growing rates, unique constituent biomolecules, and rapid regeneration capabilities, cultivated algae constitute a promising source of biomass for bio-economic materials and a promising process for water remediation. In particular, benthic algae rely on attachment to solid substrates for colonization and growth. Benthic algae in floway bioreactors are used for wastewater treatment applications, and harvested biomass is used for ecological services to recover aquatic nutrients and capture carbon in wastewaters [12], [13]. In order to control the process via species management in mixed periphytic populations, the physical and chemical features of the substrate can be engineered. For this purpose, natural surfaces can be reverse engineered to investigate the essential surface topographies that help specific benthic algae to settle, attach and thrive, possibly resulting in improvements to the process and economics of the cultivation system. Additive Manufacturing (AM) provides precise fabrication of surface topography, where surface texture parameters can be controlled to affect the characteristics of the overlying fluid velocity boundary layer, nutrient transport delivery, and surface contact angle and energy. Since 3-D printing uses a slicing algorithm to layer a solid model, it offers the ability to fabricate unique geometries that are impossible through traditional methods. Additive manufacturing (3-D printing) is used to enable specific, high fidelity topographical surface features. For this purpose, bare and colonized natural surface specimens were collected from rivers and their surface topography reversed engineered by 3-D printing for the study of attachment dynamics of a benthic algal community.

The primary objective of this effort is to show the feasibility of reverse engineering of natural surfaces to study the attachment and species selectivity of benthic algae used in water pollution recovery systems. A secondary objective seeks to explain the attachment of algae in a typical freshwater benthic community.

Research Questions

This work addresses three separate topics related to additive manufacturing. First, reverse engineering of natural surfaces (rocks) and their specific surface topography is performed in this study. This research provides a methodology to reverse engineer many other natural surfaces in biological and biomedical applications.

Second, the hypotheses in this work are related to the interaction between geometric parameters of 3D-printed, custom-designed surfaces and their wetting behaviors. This research can help improve the understanding of the interactions of physical surface factors on hydrophobicity to tune contact angle and wetting behavior in practical applications.

Third, this work characterizes the surface quality and dimensional accuracy of the material jetting processes of a high-resolution polymeric 3-D printer. The novel methods of surface metrology used in this work can provide a guide for characterizing the surface quality of other additive manufacturing technologies.

To those topics, the research questions addressed in this work are as follows:

- First, how do surface texture parameters of natural rock surfaces impact the attachment of benthic algae species?
- Second, how do the geometric parameters of custom-3-D printed microtextured surfaces affect wettability?
- Third, what are the surface finish and dimensional accuracy of material jetting processes in different designs and sizes? How do the build orientation and surface slope affect the

fidelity of different surface texture designs? How do tile thickness and build orientation affect surface distortion and warpage?

To answer these research questions, three topics have been designed in this study. The first chapter investigates understanding and engineering natural surfaces with additive manufacturing. The second chapter studies effects of 3d printed microtextured surfaces on contact angle. Finally, the third chapter investigates characterizing material jetting processes.

Chapter I

Understanding and Engineering Natural Surfaces with Additive Manufacturing [13], [14]

1. Introduction

Controlling cultivation of periphyton attracted interest for numerous applications in wastewater treatment and biomass production [15]–[19]. Periphyton includes diverse microbial populations with the majority of algae that reproduce attached to a substratum in shallow aquatic environments where water flow and light exist [20]. The advantages of periphyton cultivation for wastewater treatment are ease of operation and biomass recovery. However, the open cultivation systems at the large scale are subject to effects from the indigenous species of the local water source which can influence the quality of the resulting biomass for downstream economic applications [21], [22]. Different approaches are desired for controlling species selection in colonization to use periphytic biomass for ultimate economic applications. Previous efforts have shown that the features of the attaching surface can affect the ecological characteristics of algal biofilm [23]. One of the impacting factors on the colonization, attachment, and growth kinetics of microbial spores is the physical heterogeneity of a substratum. The microbial spores or cells act as seed colonizers for biofilm formation [24]–[26]. Previous experiments have reported that with the same material, algae generally prefer surfaces with physical heterogeneity over smooth surfaces [27]. These and other studies suggest the controlling nature of substratum topography on the development of the colonizing periphytic community in a flow environment to reach higher productivity. Through its influence on the velocity boundary layer, the microtopography of the substratum can determine the periphyton community characteristics by influencing the colonization rate of seed spores and the growth rate of established periphyton [28]. Heterogeneous microtopography includes depressions where the flow velocity is reduced, allowing spores to settle and establish [29], [30].

Physical properties of the substratum can also establish patterns of weak physical and chemical forces that can attract or repel a colonizing spore [28], [31] or can influence the establishment of the attachment polysaccharide polymers that attracts other colonizing spores [30]. Morphological microtopography can also influence microscale hydraulic features, reducing diffusion-limited boundary layers in places around a biofilm and stimulating metabolic activity [30], [32], [33]. Characterizing the algal-attractive surface topography of natural surfaces allows the determination of specific zones for biofilm colonization and growth that can affect overall performance at the larger scale.

The engineering of a surface to determine particular colonization and growth kinetics in a colonizing periphytic biofilm is contingent on the effect of surface textures on the hydrodynamics of the overlying fluid. Recent studies assessing the impacts of surface texture and contact energy on algal cell colonization, as a function of material composition, found that surface tension interaction between the cell size and roughness parameter size was a controlling factor in determining the rate of algal biofilm colonization and growth [34]. The effect of surface roughness characteristics on the velocity boundary layer, affecting diffusive boundary layers at the surface and thus mass transport kinetics at surficial scales, has been clearly demonstrated in a number of studies [34]–[36].

However, few efforts have taken advantage of recent advances in additive manufacturing to elaborate and understand surface topographies for attachment and growth of algal communities. One of the few research attempts used a 3D-printed polymeric-based topographies to show the feasibility of algal biofilm colonization and growth in laboratory and natural environments [10].

However, this study did not address surface topographies and their effect on settlement and growth of algal species.

Bers and Wahl demonstrated how the surface microtopography (<500µm) of different marine species such as *Cancer pagurus*, *Mytilus edulis*, *Ophiura texturata* and *Scyliorhinus canicula* act as antifoul, which is an element of their defense systems. They specified that the antifouling influence of the micro-topographies of these species are not strong and need additional defense support such as surface chemistry and molting to form multiple defense systems [37]. In a similar study, Guenter and De Nys (2007) investigated the role of surface micro-topographies as a significant antifoul in tropical sea stars. The *paxillae* on their aboral surfaces shapes these micro-topographies for each species which act as a defense system in the organisms [38]. In both studies, there is a lack of metrology analysis on surface topographies of the organisms. Dudley and D'Antonio (1991) tracked the effects of natural substrates (i.e., rocks) on settlement of two macro-algae *Cladophora glomerata* (a filamentous chlorophyte) and *Nostoc parmeloides* (a colonial cyanobacterium). They demonstrated that rough surfaces reduce algal mortality from invertebrate grazers and winter storms. The surface metrology of rocks was not considered in this study [39]. Other than rocks, Bers et al. (2006) studied the settlement of barnacle spores by studying the surface properties (i.e., periostracal micro-topographies) of two mytilid mussel (i.e., *Mytilus edulis* and *Perna perna*). They demonstrated the effectiveness of natural surface's roughness properties on the settlement of barnacles. Their results show that replicas of the periostracal surface with micro-topographies and smooth controls were much less prone to attachment than roughened anisotropic surfaces [40].

The topography of natural surfaces has been analyzed with various methods such as fractal analysis in other applications such as friction, wear, lubrication, micro-channels, and cleaning [14], [41]–[53]. Reeves (1985) explained the correlation of the various statistics of surface roughness of rocks and frictional strength. Reeves proposed a successful first-order model to predict friction angle for a broad range of rock surfaces [54]. Brown and Scholz (1985) demonstrated that the mechanical and hydraulic behavior of joints and faults in rocks depends on their surface topography. They have studied the topography of various natural rock surfaces by a fractal model of topography with the wavelengths of 20 µm to 1m [55]. Fischer and Lüttge (2007) demonstrated how weathering converges the surface roughness of rocks. For this purpose, they studied the effects of weathering on numbers of surface texture parameters (i.e. R_q, root mean square height, R_t, the maximum height of surface and F, and surface ratio) [56]. The formulas for R_q, R_t and F are presented in the appendix.

Reverse engineering is the method of extracting data or information from any object for the purpose of re-manufacturing with high fidelity [57]–[60]. Motavalli (1998) reviewed several different reverse engineering approaches. He classified the reverse engineering into three steps, part digitizing (e.g., surface profilometry), features extraction (capturing the surface features), and surface modeling [61]. Once the surface is scanned by a profilometer and the coordinate points are acquired, the significant features (e.g., surface approximation) of the surface are extracted to model the surface. Several methods are proposed in the literature for performing reverse engineering of objects [61]–[64]. Lewis et al. (2011) developed and characterized a method to reverse engineer wood surfaces by using a die casting method to create different surface roughness properties. Some other efforts have used optical profilometry methods to confirm the surface roughness of the fabricated surfaces [65], [66].

Despite the many ways demonstrated in past studies to manipulate surface topography for experimentation, to date, no study has been reported using profilometry to extract the parametric information on those surfaces where benthic algae favor attachment. Also, there are no previous research efforts that use 3-D printing to reproduce surface topographies with high fidelity and to characterize the response of benthic algal species selective attachment and colonization dynamics. The primary motivation of this study was to find the specific surface topography of natural surfaces such as rocks that are attractive for living cultures like algae species. The primary objective of this effort is to show feasibility in the approach of reverse engineering natural surfaces (developing surface features that are biomimetically inspired) to enhance the attachment and species selectivity of benthic algae used in water pollution recovery systems. A secondary objective seeks to elucidate which surface parameters appear to explain the attachment behavior of a selected species. Finally, a derivative contribution of this work includes the development of a method of reverse engineering of natural surfaces which can be implemented in any other real-world applications.

2. *Materials and Methods*

An overview of the reverse engineering methodology proposed in this work is depicted in the general workflow shown in Figure 3. In order to summarize this method (the detailed information on each step will be provided in the following), a collection of rock specimens were retrieved from the stream (a). Then, colonized and bare areas were specified for analyses (b). The selected rocks were placed in a furnace to burn all organic matter and leave a bare rock specimen. The selected colonized and bare areas were scanned by a white-light profilometer to obtain the coordinates of the surface (c). Significant features were then analyzed and extracted from the scanned surface (d and e). Field and feature parameters were calculated and compared for extracted areas to discover the surface parameters that statistically distinguish the colonized and bare areas (f). Based on the significant surface parameters obtained, Pseudo-randomized computer models of surfaces were generated with given characterizations of the rock specimens' surfaces (g). The generated computer models were additively manufactured by a material jetting process (h). The fabricated 3D printed surfaces were scanned with a profilometer to validate the accuracy of the manufacturing process (i). The fabricated substrates were placed in a bioreactor to inoculate the surfaces with algae (j), and the biomass growth in the surfaces was identified, measured, and analyzed (k).

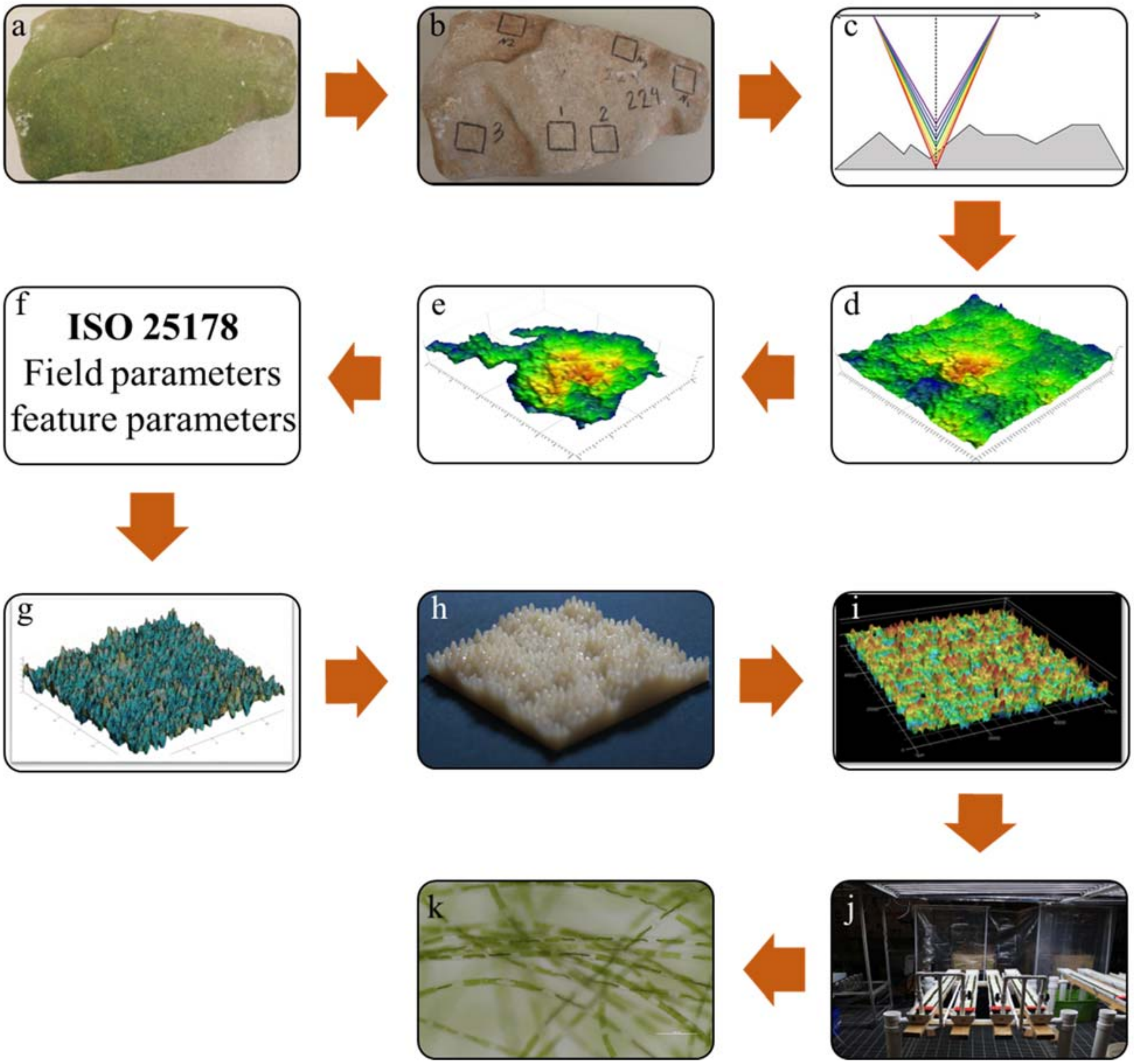

Figure 3 Schematic of the reverse engineering of natural substrata

A collection of natural rock specimens were retrieved from Chewacla Creek, located in Chewacla State Park (Figure 4), Auburn, Alabama (32°32'51.0"N 85°28'53.7"W) on July 7th, 2015 (a).

Figure 4 Collecting rock specimens from the stream [67]

Figure 5 shows the appropriate location of the area were rock specimens were collected. In the particular cross-section of the creek, bankfull width per bankfull depth ratio (Wbkf/dbkf) was measured at about 27 with a slope of 0.005°. Bankfull width and depth are defined as the stream channel width and average depth at bankfull discharge level, respectively [68].

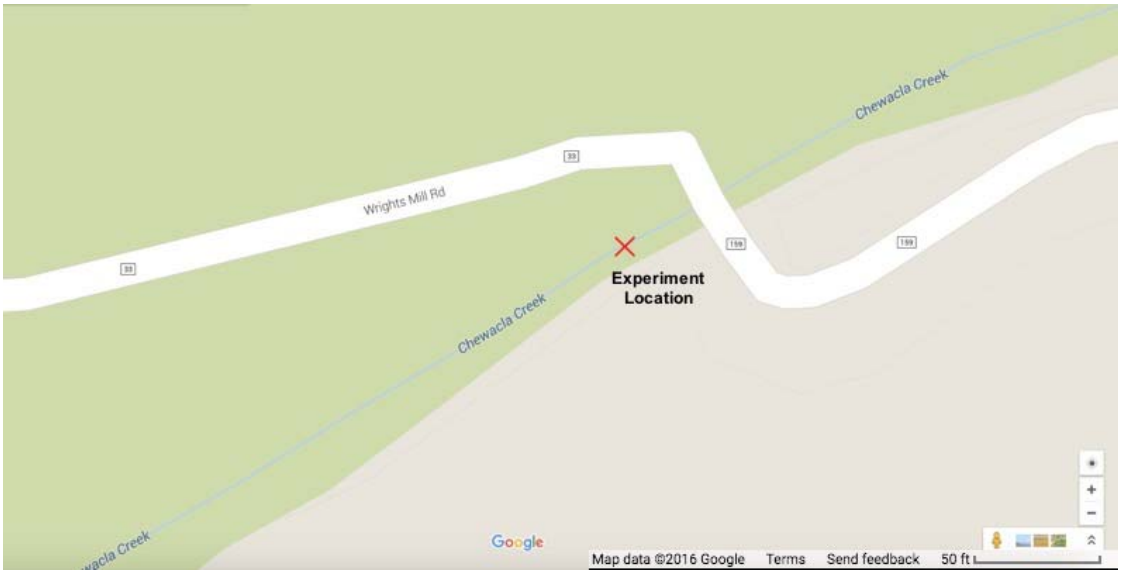

Figure 5 Schematic of rock specimens in Chewacla state park [67]

The rock specimens were collected by considering two criteria: (1) their surfaces should be smooth enough to be scanned with the white-light profilometer, and (2) their surfaces should have a clear contrast between the colonized and bare areas. The rock specimens were collected from the same cross-section of the creek, at which there is a USGS station that records information on water discharge and water level every fifteen minutes [69]. The average gage height was 0.56 ± 0.04 m, while water discharge was 0.52 ± 0.33 m^3/s. The mean water temperature during the collecting the samples was 27.9 ±1.3 ^oC with an average daytime light intensity of 224 $\mu mol/m^2/s$ at the surface of the water. The pH and conductivity of the water were measured with a handheld combination pH/EC probe (HI 98130, Hanna Instruments, Woonsocket, RI), and averaged 7.40 ±0.20 and 0.14 ±0.05 mS/cm, respectively. The local stream velocity was measured with a Model 2100 current flow velocity meter (Swoffer Instruments, Inc., Tukwila, WA) and averaged 0.25 ±0.10 m/s. Both dissolved P and N concentrations were moderately low (PO_4-P: 0.08 ±0.02 mg l-1; NO_3-N: 0.53 ±0.18 mg l-1, n = 5), as measured with a YSI 9500 field photometer (YSI Inc., Yellow Springs, Ohio).

With respect to the collection of natural surfaces (a), eleven rock specimens regardless of considering rock material (i.e., mineral makeup and formation) were retrieved. The reason that the material of the rocks specimens was not considered in this study is that we intended to find the general model (from a variety of rock types, not only one specific type) for surface topography that is attractive for benthic algae to settle, attach, and retrieve. These rock specimens were sought to represent areas that would maximize algal attachment contrast (e.g., bare and colonized) contained on a face flat enough such that most topographical features would be within the profilometer scanning range. Several promising areas contrasting various levels of algal attachment were selected and identified immediately after collection. Several areas of 10 mm × 10 mm were identified and marked with graphite. Following standard dry ashing protocols [70], the rock specimens were placed in crucibles inside a furnace at 575 °F for four hours to burn off all algal matter, bacteria, and any other organic matter (b). Figure 6 shows a sample of one of the rock specimens before and after the furnace treatment. The steps that follow (c and d) involve scanning the selected areas of 10 mm × 10 mm with a structured light profilometer (VR-3000, Keyence, Osaka, Japan) using a 5 µm step size in both X and Y direction and an acquisition rate of 100 Hz. Those areas where missing points accounted for less than 10% of the total raw data were kept. Although several areas were identified in each specimen surface, those presenting the highest visual contrast, as assessed through micrograph inspection, were selected for this preliminary work. One specimen was deemed unsuitable for reliable scanning due to high roughness (out of the range of the profilometer) and thus discarded in the process. For the remaining ten specimens, the raw data was processed with Mountains® (Digital Surf, Besancon, France) surface imaging and metrology software and used for parameter calculation and topography imaging (steps e and f).

Figure 6 Sample of the specimens before and after furnace treatment (showing target scan sections)

In order to characterize the surfaces of the rock specimens (step e and f), a set of field and feature parameters were selected for analysis and calculated. The field and feature parameters comprised a number of different families, such as height, spatial, hybrid and functional parameters. Twenty-six parameters were studied with the intention of narrowing down to a set of parameters that are functionally correlated to algal attachment. The protocol and calculations established by the ISO 25178-2 standard [71] were followed. In order to isolate the relevant surface parameters, the waviness and form components were removed using a Gaussian filter at 0.8 mm cut-off length. The list of 26 considered parameters and their definitions is presented in Table 1. These parameters were selected to characterize the surface of the rock specimens comprehensively.

Table 1 Essential areal surface texture parameters to study the surface topography of natural rocks [71]

Type of parameter	Parameter	Description	Definition
	S_{10z} (μm)	ten-point height of the surface	S_{10z} is the average value of the heights of the five peaks with largest global peak added to the average value of the heights of the five pits with the largest global pit height.
	S_{5v} (μm)	five-point pit height of the surface	S_{5v} is the average value of the heights of the five pits with the largest global pit height.
Height Parameters	S_q (μm)	root mean square height	S_q is the root mean square value of the ordinate values within a defined area.
	S_{sk}	skewness	S_{sk} is the quotient of the mean cube value of the ordinate values and the cube of S_q within a defined area.
	S_{ku}	kurtosis	S_{ku} is the quotient of the mean quartic value of the ordinate values and the fourth power of S_q within a defined area.
	S_p (μm)	maximum peak height	S_p is the largest peak height value within a defined area.
	S_v (μm)	maximum pit depth	S_v is the maximum pit depth value within a defined area.
	S_z (μm)	maximum height of the surface	S_z is the sum of the maximum peak height value and the maximum pit height value within a defined area.
	S_a (μm)	arithmetic mean of the absolute of the ordinate values within a defined area	S_a is arithmetical mean of the absolute of the ordinate values within a defined area.
Functional Parameters	S_{mr} $(\%)$	areal material ratio	S_{mr} (c) is the ratio of the material at a specified height c to the evaluation area.
	S_{mc} (μm)	inverse areal material ratio	S_{mc} (mr) is the height c at which a given material ratio (mr) is satisfied.
	S_{xp} (μm)	peak extreme height	S_{xp} is the difference in height between the p and q material ratio.
Spatial Parameters	S_{al} (mm)	autocorrelation length	S_{al} is a horizontal distance of the fastest decay to a specific value between 0 and 1.
	S_{tr}	texture aspect ratio	S_{tr} is the ratio of the horizontal distance of the fastest decay to a specific value to the horizontal distance of the slowest decay.
	S_{td} °	texture direction of the scale-limited surface	S_{td} is the direction and angle of texture in the surface.
Functional Parameters (Volume)	V_m (mm^3/mm^2)	material volume	V_m is the volume of the material per unit area at a given material ratio calculated from the areal material ratio curve.

	V_v *(mm^3/mm^2)*	void volume	V_v is the volume of the voids per unit area at a given material ratio calculated from the areal material ratio curve.
	V_{mp} *(mm^3/mm^2)*	peak material volume	V_{mp} is the peak material volume of the scale-limited surface.
	V_{mc} *(mm^3/mm^2)*	core material volume	V_{mc} is the difference in material volume between the *p* and *q* material ratio.
	V_{vc} *(mm^3/mm^2)*	core void volume	V_{vc} is the difference in void volume between *p* and *q* material ratio.
	V_{vv} *(mm^3/mm^2)*	dale void volume	V_{vv} is the dale void volume of the scale-limited surface.
Functional Parameters (Stratified surfaces)	S_k *(µm)*	core height	S_k is the distance between the highest and lowest level of the core surface.
	S_{pk} *(µm)*	reduced peak height	S_{pk} is the average height of the protruding peaks above the core surface.
	S_{vk} *(µm)*	reduced dale height	S_{vk} is the average of the protruding dales below the core surface.
	S_{mr1} *(%)*	(peaks) ratio of the area of the material at the intersection line	S_{mr1} (peaks) is the ratio of the area of the material at the intersection line which separates the protruding hills from the core surface to the evaluation area.
	S_{mr2} *(%)*	(dales) ratio of the area of the material at the intersection line	S_{mr2} (dales) is the ratio of the area of the material at the intersection line which separates the protruding dales from the core surface to the evaluation area.

To determine the need for feature segmentation (extracting the desired features from the surface), a preliminary experiment with replicated pseudo-randomized 3D-printed textures (S_a=0.92 mm, S_q=0.83 mm, S_{sk}=-0.13, S_{ku}=2.71, S_v=4.10 mm, S_p=2.77 mm, S_z=6.87 mm, $S_{mr=}$51.52 %) was conducted in floway bioreactor for three weeks to single out the features (hills or dales) of interest for algal communities. It was observed that the algal attachment predominated in dales rather than hills as shown in Figure 7. Therefore, dales were selected for segmentation as the features of interest.

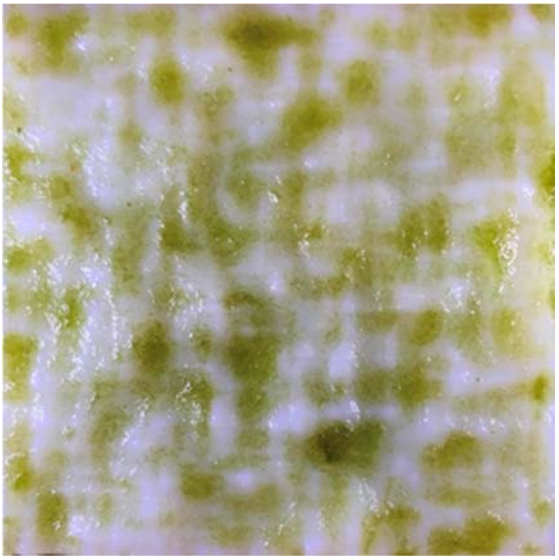

Figure 7 Colonization preference for benthic algae are dales (green areas)

Since the conventional surface texture parameters do not take individual surface features into consideration and because it has been shown that such features play a significant role in algal colonization, a feature characterization approach was undertaken.

This work followed the 5-step feature characterization established in ISO 25178-2 consisting of the following: (I) selection of the type of texture feature, (II) segmentation, (III) determination of significant features, (IV) selection of feature attributes and (V) quantification of feature attribute statistics (steps e and f). Wolf pruning [71] was the approach used for pattern recognition and segmentation of significant and non-significant surface topographies. Since Wolf pruning produces different counts of features at various thresholds, the recommended 10% of S_z (maximum height of the surface) the value was used as the thresholds for features. This pruning of the data retained all data elements above the 10% watershed value, thus deemed significant. An additional area prune was applied if, through software calculation, a dale was found to represent less than 3% of the total area. After that, the remaining features were selected and extracted, and the parameters were calculated on those features. This feature recognition and segmentation as performed in one of the specimens is illustrated in Figure 8.

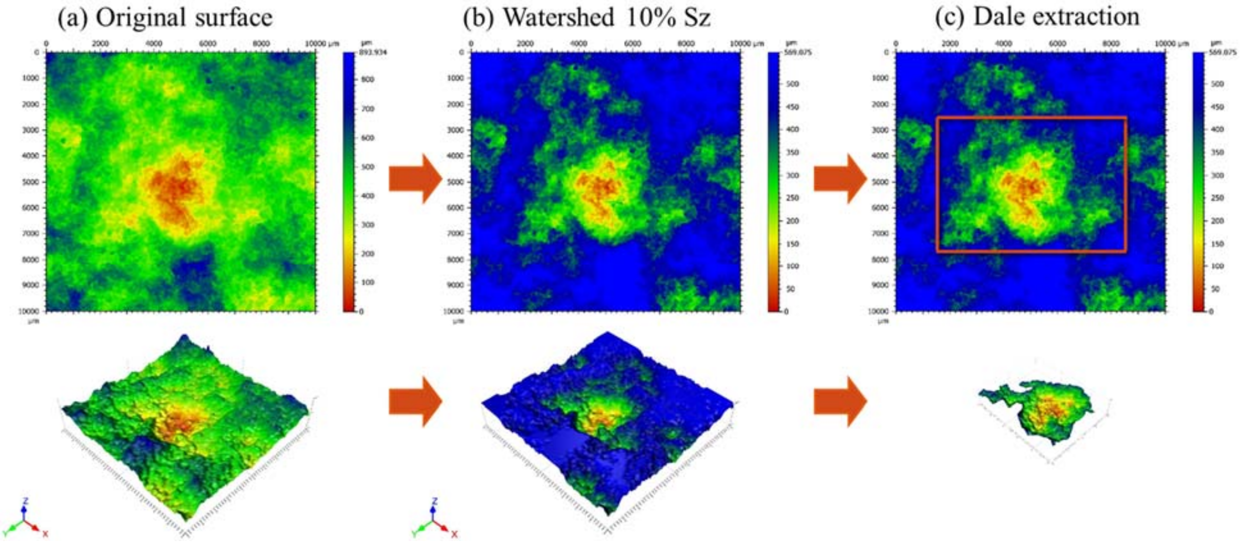
(a) Original surface

(b) Watershed 10% Sz

(c) Dale extraction

Figure 8 Wolf-pruning: (a) original surface, (b) Wolf pruning 10% *Sz*, (c) significant feature (dales) extraction

Statistical paired t-tests on the difference between the means of colonized and non-colonized dales were performed where *A* is the area of the measured surface, *z(x,y)* is the height at the point *(x, y), A (m)* is the area of the cross-sectional area of the surface at mean height m, and A *(N)* is the cross-sectional evaluation area.

Table 2 presents the surface texture and significant features' (dales) parameters, mean of parameters of colonized features and areas, standard deviation of parameters of colonized features and regions (σ colonized), mean of parameters of non-colonized features and regions, the standard deviation of parameters of non-colonized features and regions (σ non-colonized). The p-value column represents the results of t-tests of each parameter for colonized features with 26 samples and non-colonized features with 24 samples features and regions. Among all these parameters, areal material ratio (S_{mr} *(%)*, p-value<0.001, $\alpha = 0.05$), the maximum pit height (S_v, p-value=0.015, $\alpha = 0.05$), and arithmetical mean of the absolute of the ordinate values (S_a, p-value=0.026, $\alpha = 0.05$) were found significant. The S_{mr} (Equation 1) is the areal material ratio (expressed as a percentage) of the cross-sectional area of the surface at a certain height relative to the evaluation cross-sectional area. The S_v is the lowest point found on the surface. The S_a (Equation 2) indicates significant deviations in the texture characteristics. Figure 9 shows the scatter plots of the significant parameters.

$$S_{mr} = \left(\frac{A(m)}{A(N)}\right) \times 100 \tag{1}$$

$$S_a = \frac{1}{A}\iint_A |z(x,y)|dxdy \tag{2}$$

where A is the area of the measured surface, $z(x,y)$ is the height at the point (x, y), $A\ (m)$ is the area of the cross-sectional area of the surface at mean height m, and $A\ (N)$ is the cross-sectional evaluation area.

Table 2 Surface texture and significant features' (dales) parameters of colonized and non-colonized areas

Type of parameter	Parameter	Description	Mean colonized	$\boldsymbol{\sigma}$ colonized	Mean non-colonized	$\boldsymbol{\sigma}$ non-colonized	p-value
	S_{10z} (μm)	ten-point height of the surface	430.9	95.9	441.9	174.8	0.633
	S_{5v} (μm)	five-point pit height of the surface	217.7	50.2	234.9	127.3	0.832
Height Parameters	S_q (μm)	root mean square height	59.2	15.8	50.3	17.0	0.085
	S_{sk}	skewness	-0.2	0.5	-0.3	0.4	0.663
	S_{ku}	kurtosis	2.7	0.3	2.8	0.5	0.581
	S_p (μm)	maximum peak height	207.2	91.3	192.6	75.6	0.542
	S_v (μm)	**maximum pit height**	**203.9**	**49.1**	**163.6**	**55.8**	**0.015**
	S_z (μm)	maximum height of the surface	424.9	114.8	367.4	147.3	0.136
	S_a (μm)	**arithmetical mean of the absolute of the ordinate values**	**46.6**	**12.0**	**38.2**	**10.9**	**0.026**
Functional Parameters	**S_{mr} (%)**	**areal material ratio**	**0.0008**	**0.0007**	**0.0040**	**0.0020**	**0.000**

	S_{mc} (μm)	inverse areal material ratio	87.8	41.3	104.7	55.2	0.224
	S_{xp} (μm)	peak extreme height	133.0	49.1	115.4	46.5	0.222
Spatial Parameters	S_{al} (mm)	autocorrelation length	0.8	0.4	8.7	41.6	0.410
	S_{tr}	texture aspect ratio	0.5	0.2	0.4	0.2	0.150
	S_{td} °	texture direction of the scale-limited surface	87.3	63.1	97.9	66.9	0.112
Functional Parameters (Volume)	V_m (mm^3/mm^2)	material volume	0.01	0.01	0.1	0.2	0.383
	V_v (mm^3/mm^2)	void volume	0.09	0.03	2.2	10.9	0.392
	V_{mp} (mm^3/mm^2)	peak material volume	0.01	0.01	0.04	0.2	0.382
	V_{mc} (mm^3/mm^2)	core material volume	0.06	0.02	1.7	8.3	0.361
	V_{vc} (mm^3/mm^2)	core void volume	0.08	0.03	2.1	10.3	0.424
	V_{vv} (mm^3/mm^2)	dale void volume	0.01	0.00	0.12	0.6	0.383
Functional Parameters (Stratified surfaces)	S_k (μm)	core height	40.9	16.6	44.3	23.8	0.582
	S_{pk} (μm)	reduced peak height	15.2	5.8	14.9	9.9	0.931
	S_{vk} (μm)	reduced dale height	29.5	13.3	29.4	16.1	0.972
	S_{mr1} (%)	(peaks) ratio of the area of the material at the intersection line	8.8	2.1	8.2	1.9	0.102
	S_{mr2} (%)	(dales) ratio of the area of the material at the intersection line	86.5	3.7	86.1	3.2	0.68

As it can be seen in Figure 9, areal material ratio separates the colonized ($0\%<S_{mr}\leq0.0025\%$) and non-colonized ($0.001\%\leq S_{mr}\leq0.009\%$) areas. Therefore, the S_{mr}, S_v, and S_a are chosen for reverse engineering of natural surfaces.

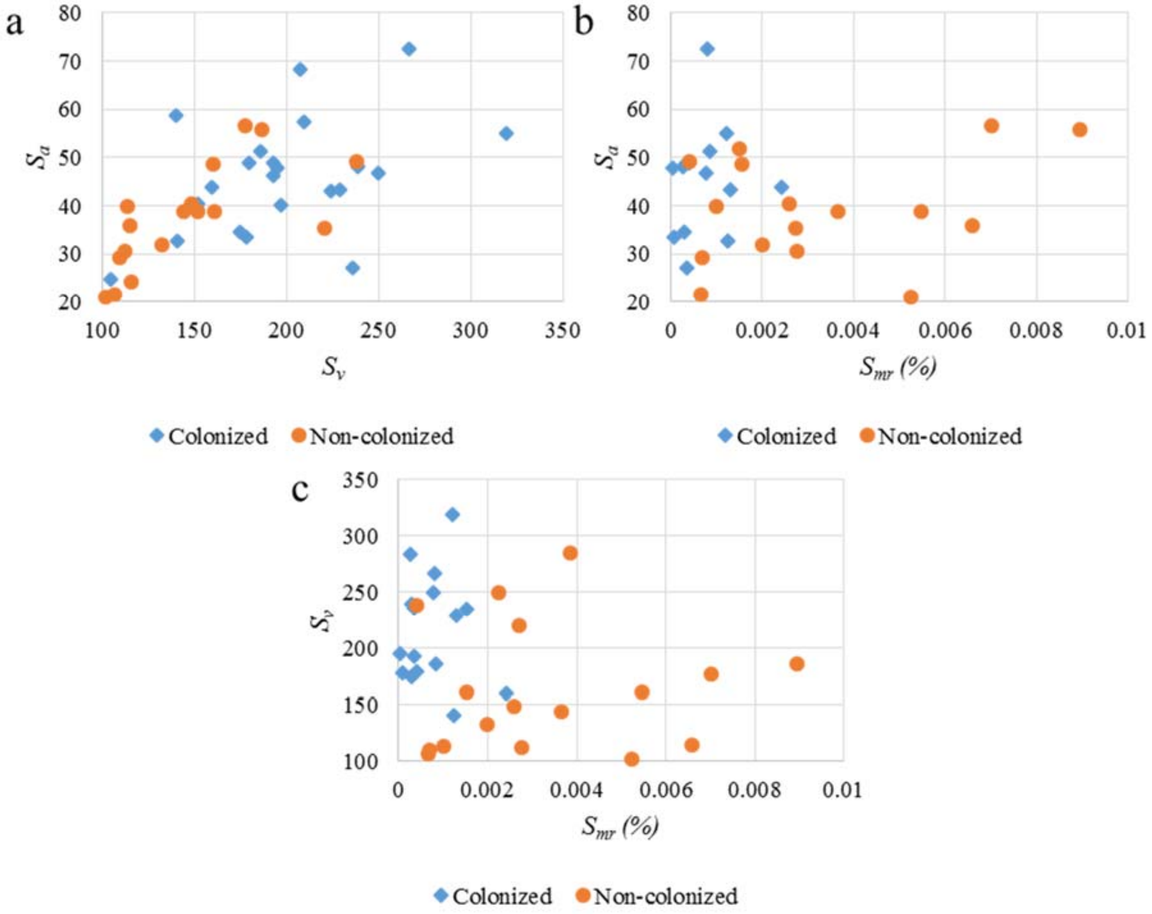

Figure 9 Preliminary results. Scatter plots of significant parameters

Figure 9 shows the scatter plots of the S_{mr}, S_v, and S_a. The results show that a positive correlation exists between S_v, and S_a (Figure 9 (a)), and the S_{mr} parameter clusters the colonized ($0\%<S_{mr}\leq0.0025\%$) and non-colonized ($0.001\%\leq S_{mr}<0.01\%$) areas on the rock specimens (Figure 9 (b) and (c)). This means that benthic algae prefer material ratios in the range of $0\%<S_{mr}\leq0.0025\%$, and that range provides better habitats for algal communities. The low material ratio represents the surface with the majority of holes and sharp peaks.

The modeling and reverse engineering steps (g and h) consisted of generating and fabricating the irregular surfaces with the specified S_{mr}, S_v and S_a values obtained from the bare and colonized areas of the selected rocks. For this purpose, a Pearson continuous probability distribution function is used to generate surfaces (step g) with controlled surface roughness properties [72]–[76]. The Pearson's systems of frequency curves are capable of generating a density function with given properties if its first four moments are known, i.e., the mean, standard deviation, skewness, and kurtosis [74]. The Pearson distribution is used to generate a surface with precise, targeted first four moments values approaching the specific texture parameters from the measured surface [74]. Since the density functions in this study are nondimensionalized (independent of dimensions and scales), they are dependent only on skewness and kurtosis of the surface. The parameter *k* is presented in Equation 3 to identify the type of the Pearson probability density function (pdf) [77]:

$$k = \frac{S_{sk}^2(S_{ku}+3)^2}{4(2S_{ku}-3S_{sk}^2-6)(4S_{ku}-3S_{sk}^2)} \tag{3}$$

where S_{sk} and S_{ku} denote the skewness and kurtosis of surface, respectively. The parameter, *k*, ranges from -∞ to +∞. Based on the value of *k*, the appropriate equation of the density function is selected. The equations and types of the probability density function (pdf) using the Pearson system of frequency curves are presented in Table 3.

Table 3 Equations and types of the probability density function (pdf) using the Pearson system of frequency curves [132], [133]

Type number	Equations with origin at the mean	criterion
I	$\varphi^*(Z^*) = y_0\left(1+\frac{Z^*}{A_1}\right)^{m_1}\left(1-\frac{Z^*}{A_2}\right)^{m_2}$	$-\infty < k < 0$
II	$\varphi^*(Z^*) = y_0\left(1-\frac{Z^{*2}}{a^2}\right)^{m}$	$k = 0, S_{sk} = 0, S_{ku} < 3$
III	$\varphi^*(Z^*) = \frac{1}{\sqrt{2\pi}}e^{\left(-\frac{z^{*2}}{2}\right)}$	$k = 0, S_{sk} = 0, S_{ku} = 3$
IV	$\varphi^*(Z^*) = y_0\left(1+\left(\frac{Z^*}{a}-\frac{v}{r}\right)^2\right)^{-m} e^{-vtan^{-1}\left(\frac{Z^*}{a}-\frac{v}{r}\right)}$	$0 < k < 1$

VI	$\varphi^*(Z^*) = y_0\left(1+\frac{Z^*}{A_1}\right)^{-q_1}\left(1+\frac{Z^*}{A_2}\right)^{q_2}$	$1 < k < \infty$
VII	$\varphi^*(Z^*) = y_0\left(1+\frac{Z^{*2}}{a^2}\right)^{-m}$	$k = 0, S_{sk} = 0, S_{ku} > 3$
The parameters, $y_0, A_1, A_2, m_1, m_2, a, r, v, m, q_1, q_2$ that are used in these equations depend on the skewness and kurtosis [77].		

Based on the data obtained from the rock surfaces by a profilometer, the skewness and kurtosis values for colonized and bare areas are approximately -0.3 and 3.0 (close to the values in a normally distributed surface), respectively. Thus, the skewness and kurtosis values for the reverse-engineered surfaces were then kept as -0.3 and 3.0, respectively. With the assumed skewness and kurtosis values, the criterion k, which designates the density function types, is calculated (-0.256, where corresponds to the Pearson Type I). The S_v value for the generated surface can be targeted by multiplying the constant, h with the pseudo random numbers generated by the Pearson function. The constant h is a constant to multiply to the z coordinates of surface data to control maximum height of the surface. The S_a values can be obtained by changing the standard deviation of the pseudo random numbers. In order to further control the S_{mr} values, micro-patterned depressions (circular holes) are superimposed to the simulated surfaces. These patterns help approach specific S_{mr} values for the generated surfaces by reducing the percentage of contacts after cutting the surface at the mean value of the Z coordinates of the surface data.

With respect to fabricating a pseudo-random surface with specific parameters, the following steps were performed in Matlab®:

a) Calculate the parameter k, Equation 3, to determine the type of Pearson distribution.

b) Specify S_a: generate pseudo-random numbers with specific values for the first four moments (i.e., mean, variance, skewness, and kurtosis of the Z coordinates of the surface data) of the Pearson distribution. A surface with a specific S_a value can be reached with different combinations of the four moments.

c) Mesh the points generated in step (b) in *X* and *Y* direction to create a surface.

d) Allocate the generated numbers to each point in *X* and *Y* direction.

e) Specify the S_v: multiply the random numbers by a variable, *h*, to magnify them in the *Z* direction. Multiply the variable *h* changes the height of the asperities (features) that directly affect the S_v.

f) Convert a surface model to a closed triangulated solid model (manufacture-able solid volume).

g) Specify the S_{mr}: create circular depression (hole) patterns on the surface to change the material ratio of the surface (Figure 10). The frequency and size of the depression patterns reduce the material ratio of the surface.

h) Generate the *.STL* format file from surface data.

i) Fabricate the part.

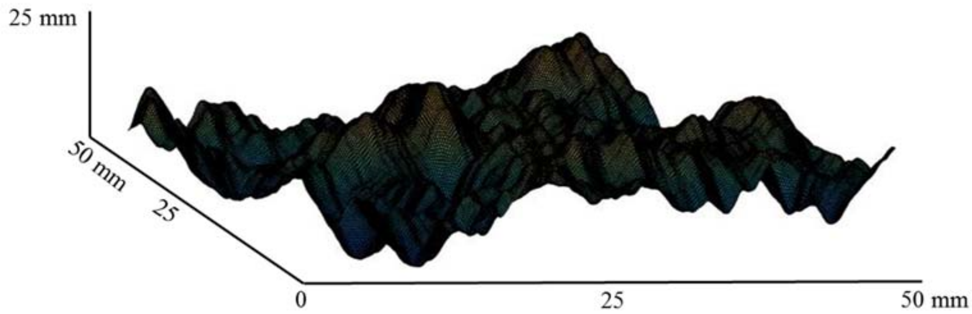

without micro-pattern

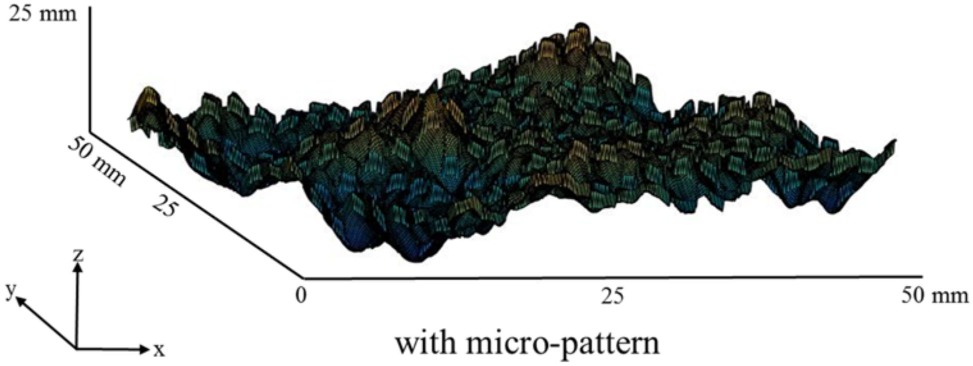

with micro-pattern

Figure 10 Specify the S_{mr}: create circular depressions (hole) patterns on the surface to change the material ratio of the surface. Both have similar surface topography. The surface topography without (top) circular depressions and the topography with (bottom) circular depressions.

In order to validate the proposed reverse engineering method, two levels for S_{mr}, S_v, and S_a parameters were chosen. The levels were chosen to experience two extreme sets of parameters. Low values of surface parameters (i.e., S_{mr}, S_v, S_a) for level 1 and high values for level 2 have been considered. The detailed information of the levels is presented in Table 4. Figure 11 shows the profilometry images of these two levels.

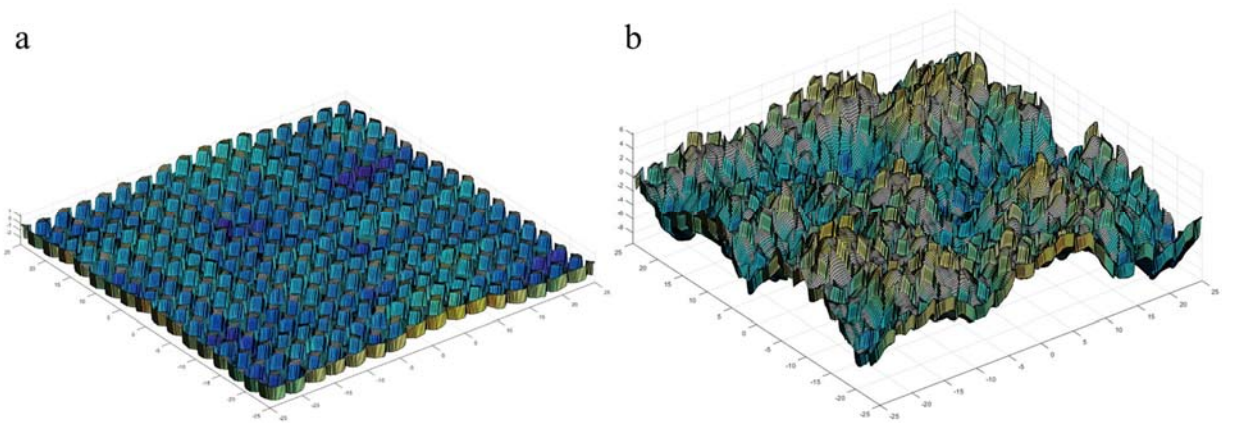

Figure 11 Profilometry images of fabricated specimens for level 1 (a) and level 2 (b)

Table 4 Experimental design factors and levels

Factors	Level 1	Level 2
S_{mr} (%)	S_{mr1}= 52%	S_{mr1}= 30%
S_v (mm)	S_{v1}= 6.6 mm	S_{v2}= 8.4 mm
S_a (mm)	S_{a1}= 0.7 mm	S_{a2}= 2.1 mm

Three runs of the algae inoculation process were performed in this experiment. In each run, 24 fabricated tiles in the bioreactor were inoculated for seven days (168 hours). For each run, as shown in Figure 12, twelve replicates were modeled for each treatment level for a total of twenty-four (2 (levels) × 12 (replicates in each run)) acrylic polymer reversed engineered surfaces (50 mm × 50 mm × 7 mm). In total seventy-two tiles were fabricated for the three runs (3 (runs) × 2 (levels) × 12 (replicates in each run)).

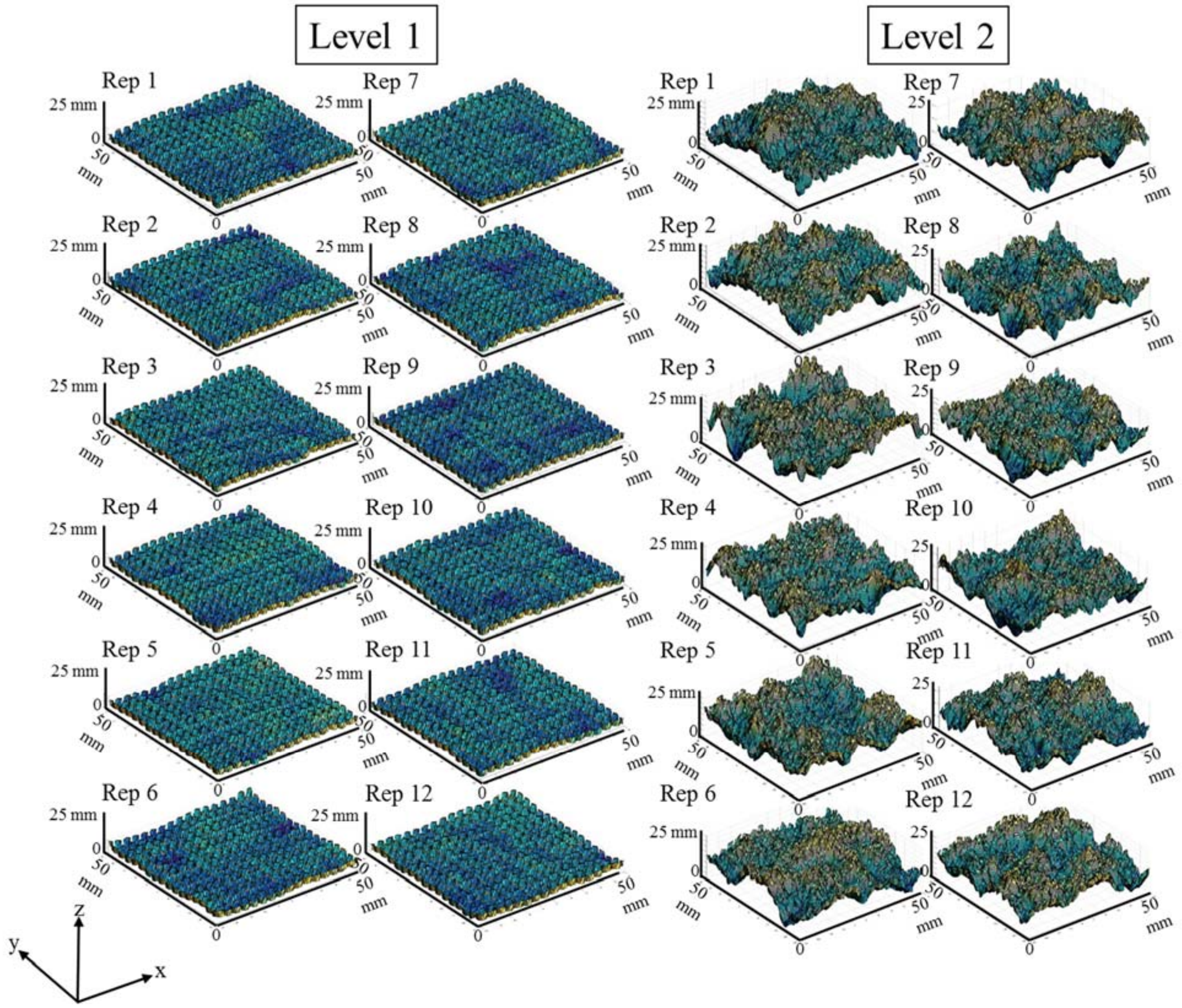

Figure 12 Computer models of the twelve replicate for each treatment level in the first cultivation run

The reversed engineered surfaces were modeled by the Pearson distribution in Matlab® and fabricated (Figure 13) with an Objet30 3D (Stratasys Ltd., Eden Prairie, MN) printer (step h) with a 28 µm layer thickness.

Figure 13 Computer model (a), reverse engineered surface (b) and scanned image (c)

The accuracy of the build was verified with optical methods using a structured profilometer (VR-3000, Keyence, Osaka, Japan) with 20 nm resolution in the vertical direction. Figure 13 shows the areal map and the 3D profile of the surface topography of the reverse engineered surface. Once the model was fabricated with the material jetting process, nine samples were scanned with the optical profilometer to measure the accuracy of the process. Eight surface parameters were examined to test the fidelity of the method, (i.e., S_{mr}, S_p, S_{ku}, S_{sk}, S_z, S_q, S_a, and S_v). Figure 14 and Table 5 present the error percentage (the deviation of the actual measured value from the targeted value of computer model) of the eight parameters that are calculated for the computer model and measured from scanned data. The description and definition of each parameter presented in Table 5. The results show that the S_{mr} has the lowest average error percentage and the S_a, and S_v has the largest errors percentage compared to the others.

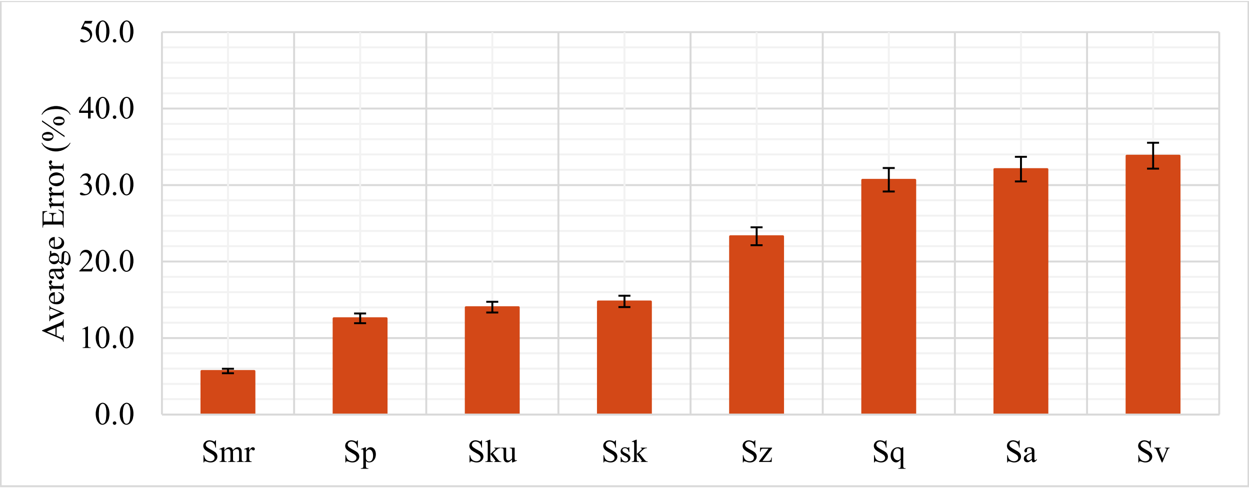

Figure 14 Average error of targeted surface texture parameters of a computer model from scanned surfaces

Table 5 Summary of measured and calculated data for computer model and scanned surfaces

Parameter	Scanned data	Computer model target	Average Error (%)
S_{mr} (%)	43.9	42.5	5.7
S_p (μm)	4362.1	5165.9	12.6
S_{ku}	3.4	3.0	14.0
S_{sk}	0.6	0.5	14.8
S_z (μm)	7635.9	10198.4	23.3
S_q (μm)	904.5	1312.4	30.7
S_a (μm)	706.8	1044.5	32.1
S_v (μm)	3273.8	5032.5	33.8

The summary of the eight parameters for the computer models of level 1 and level 2 are presented in Table 6. Details of parameters for both levels are provided in Appendix II.

Table 6 Summary of computer models data

Parameter	Level 1			Level 2		
	Min	Max	Mean	Min	Max	Mean
S_{mr} (%)	32.07	28.21	30.04	53.75	50.54	51.73
S_p (μm)	2.43	2.83	2.58	7.10	10.06	8.29
S_{ku}	2.76	2.85	2.80	2.57	3.20	2.82
S_{sk}	0.93	1.05	0.99	-0.31	0.06	-0.14
S_z (μm)	8.90	9.91	9.22	13.90	18.78	16.64
S_q (μm)	0.89	0.93	0.91	2.23	2.96	2.63
S_a (μm)	0.71	0.74	0.72	1.81	2.41	2.11
S_v (μm)	6.35	7.16	6.64	6.81	10.34	8.35

One interpretation of the results can be obtained by comparing the resolution of the computer model and the additive machine. The resolution of computer models was set at 100 μm in X and Y direction based on the actual manufacturing resolution of the 3D printer machine. In addition, based on the obtained results it is hypothesized that the accuracy of the printer machine depends on features aspects such as size, geometry, etc. This hypothesis is supported by the minimum feature size analysis of material jetting processes (Chapter III, section 2). Figure 15 indicates that the protrusion features are fabricated with higher fidelity, presenting smaller error than recess features, especially in small sizes (< [700 µm-length and 350 µm-height]). This can explain the higher error percentage for the parameter S_p than for S_v. This shows that the accuracy of the machine is higher while printing the hills (average error 12.5%) than while printing the dales (average error 33.8%), specifically when the height and depth of features are less than 350 μm (orange section in Figure 15).

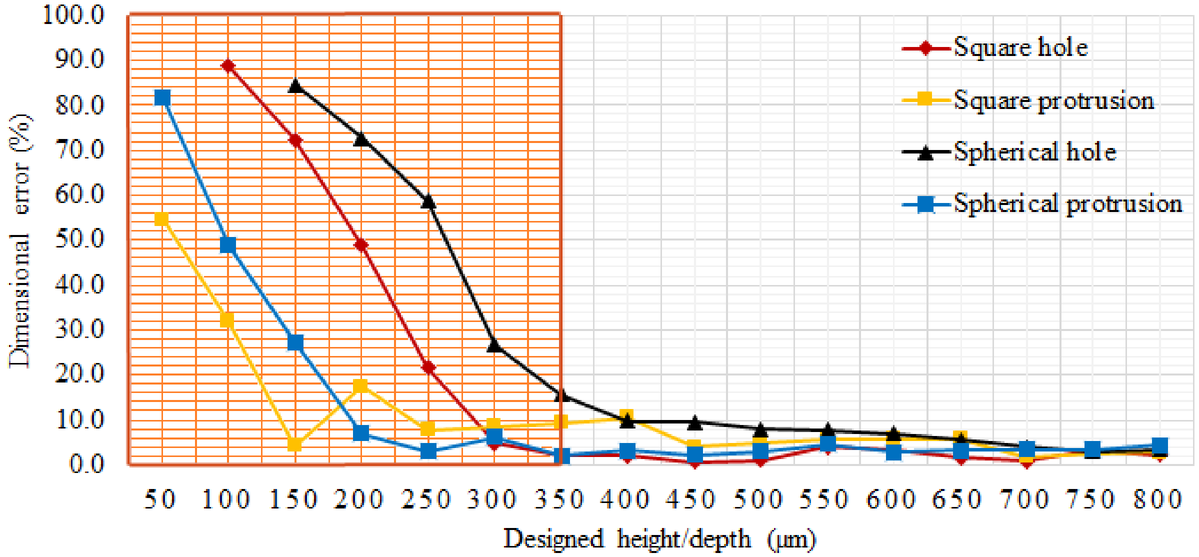

Figure 15 Dimensional fabrication error by type of asperity

The S_{mr} is more robust (average error < 6%) compared to other parameters because it is more dependent on lower frequency signals (waviness) than the higher frequency roughness of the surface (Figure 16). With current capabilities, it should be easier to reproduce the waviness profile than features in the roughness scale.

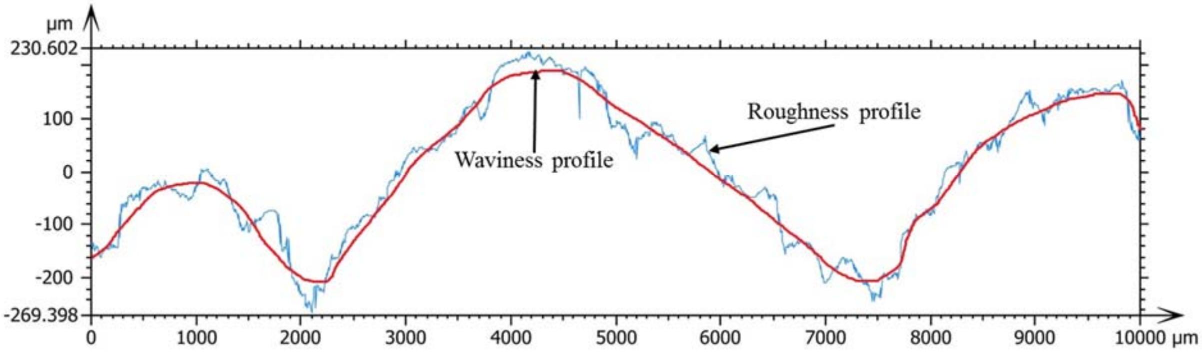

Figure 16 Waviness profile and roughness profile of a scanned rock

3. *Validation Experiment (Steps j and k: Algal Inoculation)*

In order to examine the proposed reverse engineering method, a 4-lane bioreactor was used to cultivate attached benthic algae for the purpose of harvesting biomass. The floway system typically consists of sloping floway surfaces with attachment substratum screens to which a community of attached filamentous algae is cultivated. In practice, the growth rate of algal biomass in the floway bioreactor is dependent on several factors, including algal species mix, light, temperature, pH, nutrient concentration, flow velocities, and substratum characteristics [78]–[80].

For the growth experiments (steps j and k), a 4-lane floway bioreactor system was designed and constructed. The four lanes of the bioreactor system were made using Genova half round gutters (made of PVC plastic) supported by a framework constructed using PVC pipes and wood at a slope of 2.4%. Each of the four lanes of the bioreactor system had dimensions of 152.4 cm × 7.6 cm. The entire lane was used as the growing area. Figure 17 and Figure 18 present the bioreactor system and a schematic representation of the 4-lane bioreactor system respectively. The surface of each Genova half round gutter was covered with a polypropylene screen mat with a 3 mm mesh gap (XV1672, Industrial Netting, Minneapolis, MN).

Figure 17 Four-lane bioreactor system

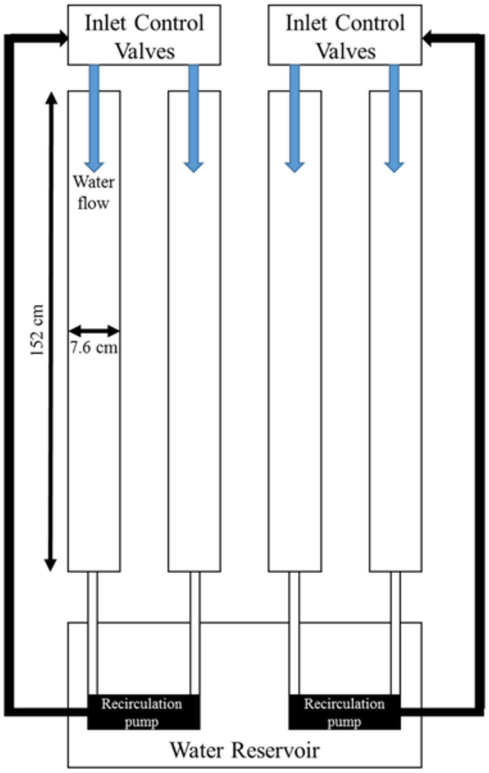

Figure 18 Top view schematic representation of the four-lane bioreactor system

Adjustable PVC valves were used to regulate the flow rates in each of the lanes. Collimators were also fixed at inlets of each flow lane to straighten the flow streamlines. The collimators were constructed using cut 1/2-inch diameter, 32 straws glued together (Figure 19) using 100% silicone all-purpose adhesive sealant (DAP, UNSPSC 31201606, USA).

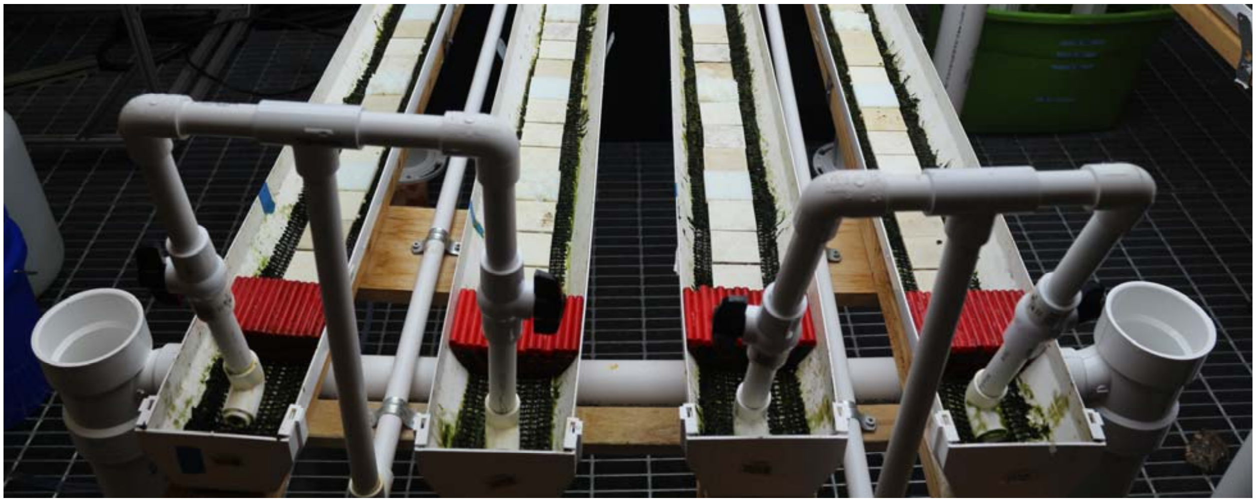

Figure 19 Adjustable valves and collimators included to regulate water flow

Six fluorescent light fixtures (Sun System Sun Blaze T5 High Output), located directly above the 4-lane bioreactor system, provided lighting for the bioreactor system. Each of the fixtures had dimensions of 119.4 cm (length) x 57.2 cm (width) x 6.4 cm (height). Each fixture used 8 bulbs (Spectralux 901618, China), each with a wattage of 54W. The bioreactor system was operated under a continuous light regimen (24 hours of daily light). The height and location of light fixtures were adjusted until moderate light intensity levels were achieved at the cultivation surface. Figure 20 shows the light illumination maps across the bioreactor system after light fixtures were calibrated. Photosynthetic photon flux density on the algal growth substratum averaged 219 ± 28 (range 157 – 268) µmol m^{-2} s^{-1} over the 4-flow lanes of floway bioreactor system. Light intensity measurements were taken using a quantum flux meter and probe (LI-250 Light Meter and LI-190 Quantum Sensor, LI-COR Biosciences, Lincoln, Nebraska, USA).

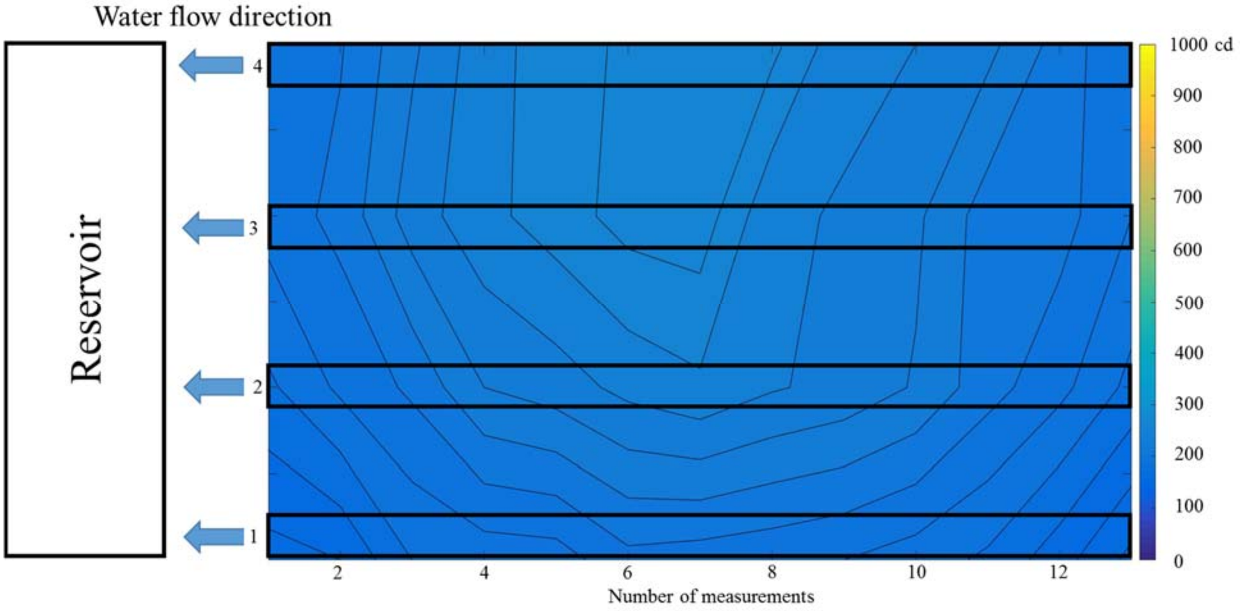

Figure 20 Light illumination map (Photon flux density). The light intensity unit is in candela.

The system was operated in a continuous mode by recirculating 57 L (15 gal) of freshwater nutrient solution to a common rectangular reservoir (Figure 20). Water flow through each lane was controlled using a separate centrifugal submersible pump (Supreme Mag Drive, Model MD 5, Danner Manufacturing, Islandia, New York, USA) submerged in the reservoir to pump water through PVC pipelines into a release water into the lane at a constant flow rate. The flow rates across the 4 flow lanes averaged 8.76 (range 8.59-8.87) L/min. The water velocity in the 4 flow lanes averaged 17.59 (range 15.93-20.07) m/min. The water velocity was calculated by measuring the travel time over the flow lanes. The mean depth was 3.82 cm. The reservoir residence time was 97.28 s. The Reynolds number (Equation 4) in the 4 flow lanes averaged 0.038 which shows linear flow characteristic [81]. The flow lanes' raw data is presented in Appendix I.

$$Re = \frac{\rho V l}{\mu} = \frac{V l}{\nu} \tag{4}$$

Where *Re* is Reynolds number, ρ is the density of the DI water ($1\,\frac{g}{m}\times10^{6}$), V is the velocity of the water in flow lanes ($0.2931\,\frac{m}{s}$), l is the width of the flow lane ($12\ m\times10^{-2}$), μ is the dynamic viscosity of the DI water ($\frac{Ns}{m^2}\times10^{-3}$), and v is the kinematic viscosity of DI water ($0.9248\,\frac{m^2}{s}\times10^{-6}$) at 72°F.

Figure 21 Common rectangular reservoir for all four lanes

The flow-way reactor was inoculated with algal community colonized on rocks that were collected from Chewacla Creek, located in Chewacla State Park (Figure 5), Auburn, Alabama (32°32'51.0"N 85°28'53.7"W). The species were identified following the illustrated key for identifying the genera of the commoner freshwater algae [82]. This yielded 12 conspicuous species (i.e., *Gyrosigma sp,* *Oscillatoria trichomes, Cymbella sp, Stauroneis sp, Caloneis amphisbaena, Microspora willeana, Coleochaete orbicularis, Synedra ulna, Chaetophora sp, Stigeoclonium tenue, Aphanothece clathrate, Aphanocapsa, elachista*) of algae in the stream that were identified and occurred with relatively high frequency [67]. A large number of diatoms (division *Bacillariophyta*) were observed. The most abundant alga identified was *Choleochate orbicularis*. Three species belonging to the division *Chlorophyta* were identified, *Bacillariophyta*, *Mougeotia scalaris,* and *Ulothrix cylindricum*. The dominant species after cultivation in the lab environment and conditions for one month was *Mougeotia scalaris,* with *Ulothrix cylindricum* (Figure 22) also present. Both species, *Mougeotia scalaris* and *Ulothrix cylindricum,* have similar morphology (long and thin like human hair). They do not represent the entire diversity of species that were inoculated from Chewacla Creek.

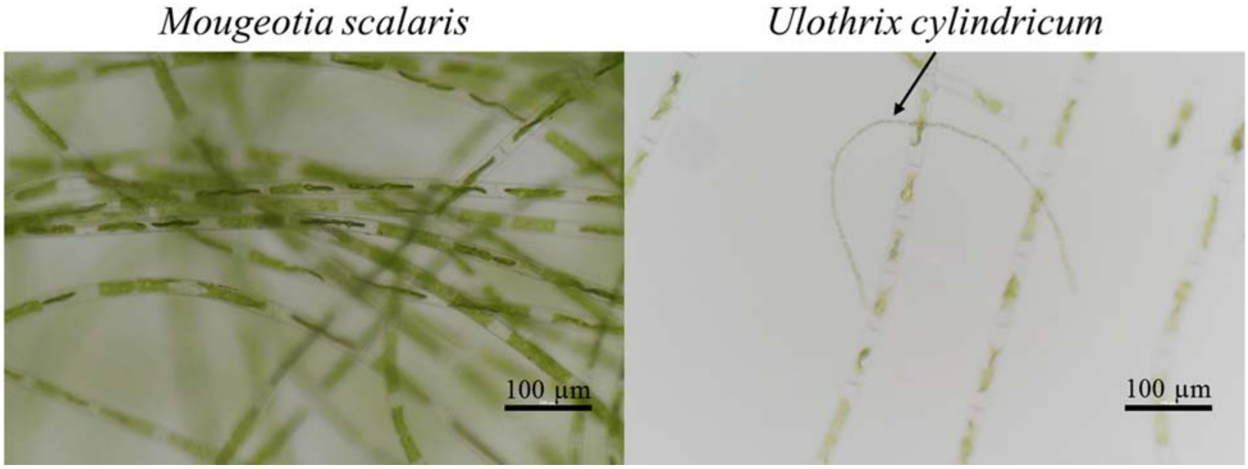

Figure 22 *Mougeotia scalaris* (left) and *Ulothrix cylindricum* (right) that occurred and were observed to be dominant in community used to inoculate reservoir

Three runs of the inoculation process were performed in this experiment. In each run, the fabricated tiles in the bioreactor were inoculated for a period of seven days (168 hours). Run 1 was implemented from 6:00 PM on December 3rd, 2017 to 6:00 PM, December 10th, 2017. Run 2 was implemented from 8:00 PM on December 10th, 2017 to 8:00 PM, December 17th, 2017. Run 3 was implemented from 10:00 PM on December 17th, 2017 to 10:00 PM, December 24th, 2017. In each run, 24 fabricated tiles in the bioreactor were inoculated for a period of seven days (168 hours). For each run, as shown in Figure 12, twelve replicates were considered for each treatment level for a total of twenty-four (2 (levels) × 12 (replicates in each run)) acrylic polymer reversed engineered surfaces (50 mm × 50 mm × 7 mm). In total, seventy-two tiles were fabricated for the three runs (3 (runs) × 2 (levels) × 12 (replicates in each run)). During each run, the reservoir was dosed daily with modified F/2 media (Pentair Co., Apopka, FL). Room temperature, water temperature, pH, and conductivity were measured daily using a handheld combination pH/EC probe (HI 98130, Hanna Instruments, Woonsocket, Rhode Island) and nitrate was measured using a RQflex reflectometer (RQflex plus 10, Sigma-Aldrich Corporation, St. Louis, Missouri). To avoid reservoir concentrations increasing over time, half of the reservoir volume (28.39 L or 7.5 gal) was replaced with distilled water every day. In order to follow the low nutrient environment in a natural stream, a low nutrient level environment was provided by using modified F/2 media (Pentair Co., Apopka, FL) available commercially and mixed according to manufacturer specifications. A dosage of 0.5 mL of F/2 media per gallon of water was replaced to keep the nutrient level constant. More detailed composition of F/2 media is presented in Appendix I. The water temperature averaged 75.1 ± 1.2 (range 70.7 – 76.8, n (number of measurements) = 43)°F for the reservoir. The room temperature averaged 66.9 ± 2.3 (range 61.8 – 70.7, n = 43)°F close to the flow lanes. The conductivity averaged 0.03 ± 0.00 (range 0.03 – 0.03, n = 43), while the pH had an average value of 6.87 ± 0.4 (range 5.42 – 7.63, n = 43) for the reservoir. Dissolved N concentrations were measured as NO3-N: 1.74 ± 0.46 ppm for the reservoir, using RQflex reflectometer (RQflex plus 10, Sigma-Aldrich Corporation, St. Louis, Missouri). These were measured three times a day. Raw data of room temperature, water temperature, pH, conductivity, and nitrate records for the reservoir are provided in the Appendix.

Algal biomass was sacrificially harvested four times every seven days from the entire growing area of each of the flow lanes before placing the tiles. The starting date for colonization was November 3rd, and the main experiment started on December 3rd. On harvesting days, the pumps were turned off to stop the flow of water through the four lanes of the bioreactor system, and the water was allowed to drain out for about 10 minutes. Each of the four lanes was then harvested mechanically [83], [84] using a commercial wet/dry vacuum (Rigid, Model WD1637, Emerson Electric Company, St. Louis, Missouri, USA). Each lane to be harvested was first detached from the flow-way system. Once, the flow lanes were sacrificially harvested, the tiles were placed in flow lanes with the pattern shown in Figure 23. Each flow lane contained six samples (three of each level) that were placed with equal spacing. Between consecutive samples, several smooth, unglazed ceramic tiles (50 mm × 50 mm) were placed to avoid the possibility of elaborate “loading edge effect”. As it is shown in Figure 23, each flow lane was divided into three sections (i.e., up-stream, middle, and downstream) with each section containing a tile of each level of surface condition. In addition, tiles with the same level were never adjacent. The orientations of the tiles before placing in the flow lanes were chosen randomly.

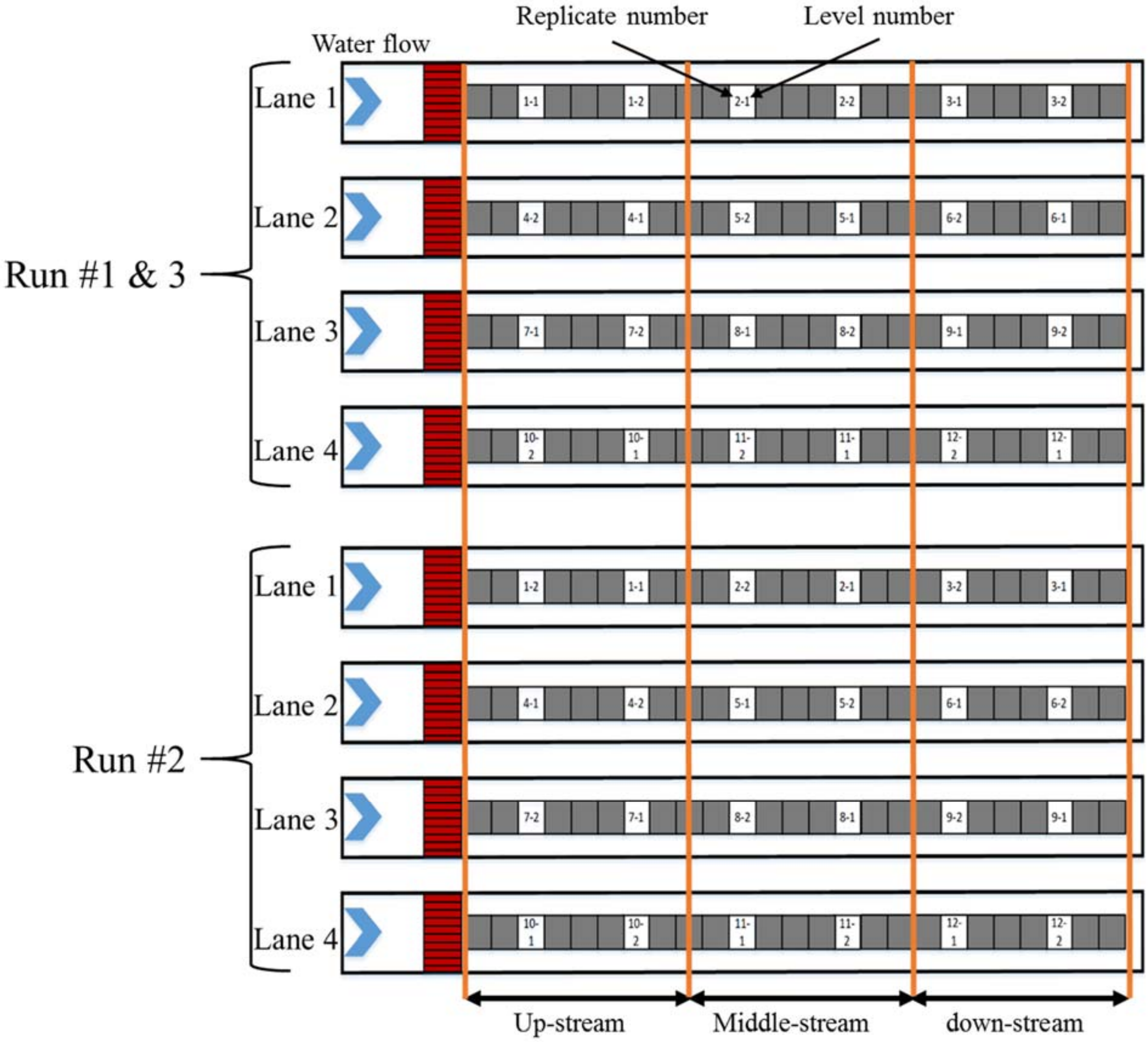

Figure 23 Pattern of the positioning of tiles in flow lanes in a run 1-3

In order to measure the biomass, the system was shut down and allowed to drain for 10 minutes. Then, the samples were gently removed from the system. If there were any algae filaments attached to the underside of the tiles, they were removed with a scraper and disposed of. An overview of the measuring biomass methodology performed in this work is depicted in the general workflow shown in Figure 24.

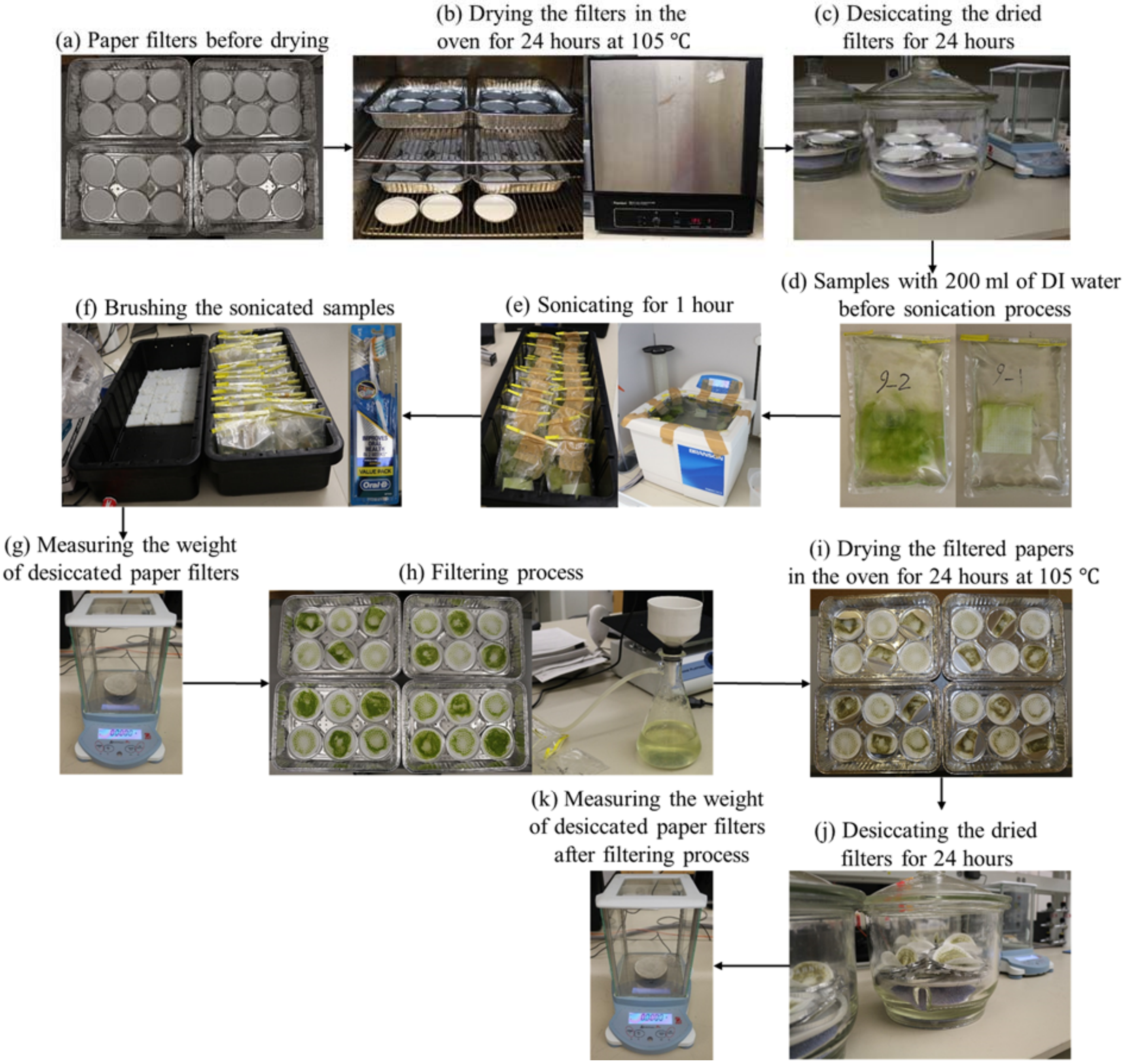

Figure 24 Schematic of biomass measurement process

For the filtration process, 9 cm (diameter) extra thick-glass fiber filter papers (Q8, Fisher Scientific, Pittsburgh, Pennsylvania) were used (Figure 24 (a)). The filter papers employed were first preheated in the oven at 105°C for 24 hours and then placed in a glass desiccator and allowed to cool for 24 hours (Figure 24 (b-c)). The removed samples were put in small size Ziploc bags which were sinked in 200 mL of distilled water (Figure 24 (d)) to submerge the samples entirely in distilled water. In order to harvest the algae from samples, a sonicator bath (Branson 5800, Branson Ultrasonics Corporation, Danbury, Connecticut) with a frequency of 40 kHz was used. The samples were placed in sonicator bath and sonicated for 60 minutes (Figure 24 (e)). To remove the remaining biomass, a soft brush was used. The samples were then brushed gently inside the Ziplocs to detach all remaining biomass. Then, the tiles were rinsed with 50 mL of distilled water to capture all remaining biomass (Figure 24 (f)). The weights of dried filter papers were measured by an Acculab analytical laboratory balance (ALC-80.4, Arvada, Colorado, USA) (Figure 24 (g)). The accuracy of the laboratory balance was 0.0001gr. To measure the biomass harvested from each tile, filtration and drying procedures were processed. Each sample was then filtered by using the glass fiber filter and laboratory vacuum pressure (Figure 24 (h)). The glass fiber filter was then placed in an oven for 24 hours at 105℃ to dry the biomass (Figure 24 (i)). After oven drying, the glass fiber filter was retrieved and placed in the glass desiccator to cool down to room temperature (Figure 24 (j)). The weight of biomass in each sample was then calculated as the difference between the weights of the dry glass fiber filter paper before and after oven drying (Figure 24 (k)).

The growth rate and attachment/settlement observations were performed by taking a photograph with a Canon EOS Rebel T5i DSLR camera with 18-55mm lens each twelve-hour interval for each substratum treatment level. The distance of camera lens and the samples were kept constant at 20 cm distance from the sample. The light intensity during the shooting process was kept constant and similar to the experiment condition (Figure 20).

The species identification was conducted as well through digital microscopy utilizing a Motic optical microscope (Motic Corp., Richmond, BC). The process involved mixing the content of each vial thoroughly, then taking a sample out of the vial using a tweezer and placing it on a glass slide. The glass slide was then placed under the microscope for observation. From each of the 24 vials, three subsamples were drawn. The microscope was set at 400 X magnification to obtain 3 images from random (across the coverslip) biomass each subsample.

4. *Results*

Three runs of inoculation process were considered in this experiment. In each run, 24 fabricated tiles in the bioreactor were inoculated for seven days (168 hours). For each run, as shown in Figure 12, twelve replicates were considered for each treatment level for a total of twenty-four (2 (levels) × 12 (replicates in each run)) acrylic polymer reversed engineered surfaces (50 mm × 50 mm × 7 mm). In total seventy-two tiles were fabricated for the three runs (3 (runs) × 2 (levels) × 12 (replicates in each run)). The raw data obtained for the weekly biomass for the two substratum treatment levels (level 1 and level 2) over the three harvests performed for the experiment are presented in Figure 25. Detailed records of harvested biomass for each substratum treatment level, measured after the drying process, are presented in Appendix II.

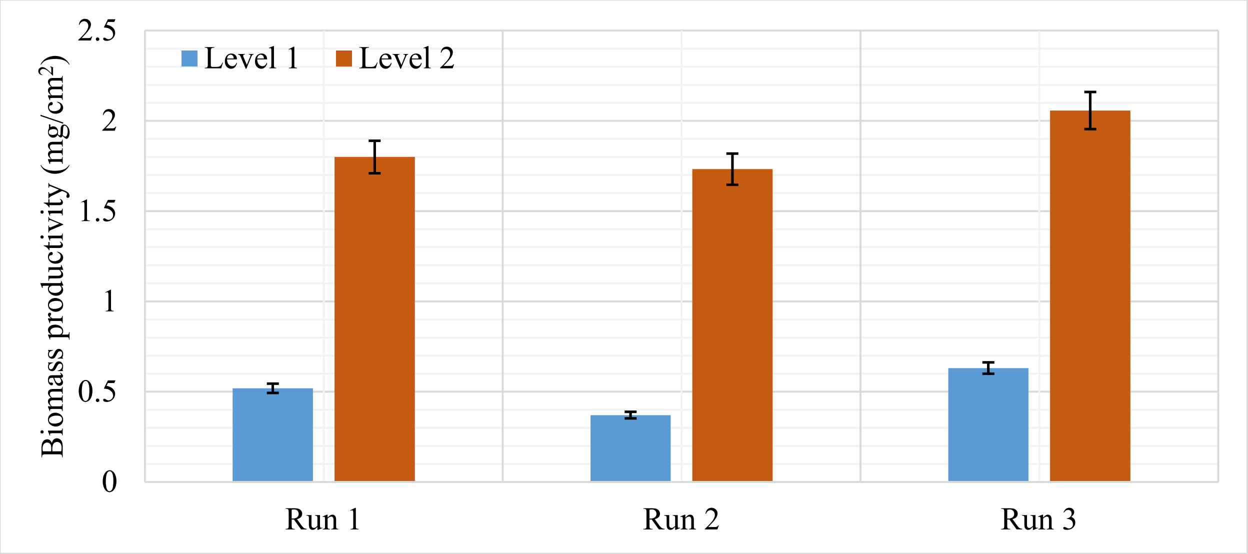

Figure 25 Algal biomass dry weight versus run for two levels of substratum type after 168 hours (7 days) of growth.

Analysis of underlying ANOVA assumptions of homoscedasticity was performed to determine a suitable approach to analyze the data statistically. Tests of normality and analyses of residual plots were conducted. As shown in Figure 26, the biomass data were normally distributed. Parametric statistical tests were employed after checking the conformity of ANOVA assumptions. A one-way ANOVA test was conducted using Minitab 18. All the plots and histograms for residual analyses on harvested algal biomass are presented in Figure 26. The results show that the variance of the residuals was the same for both treatment levels.

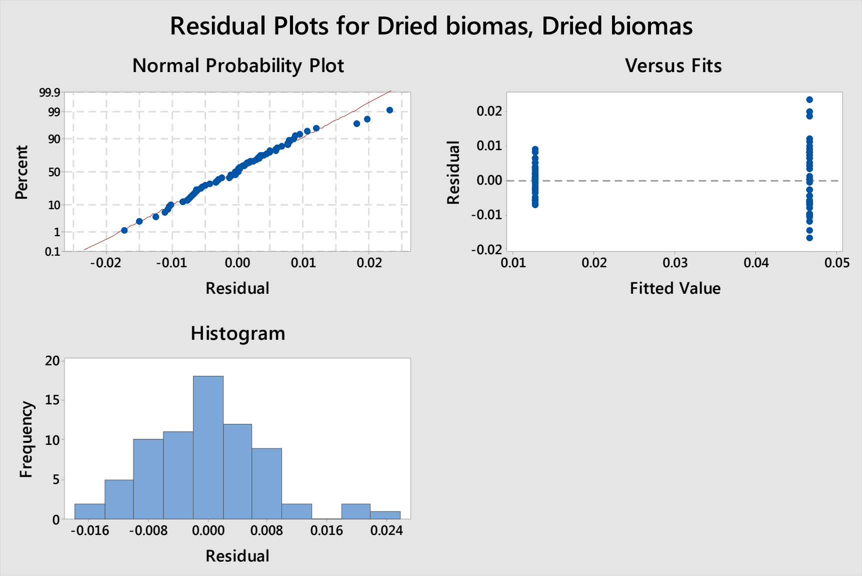

Figure 26 Residual plots for algal biomass (gr)

The total algal biomass for level 2 (46.6±10.0 mg) is significantly higher than level 1 (12.7±4.1 mg) as shown in Figure 27. The result of ANOVA testing showed that the main effect of substratum type was significant (F [1, 70] =352.47, $p < 0.001$).

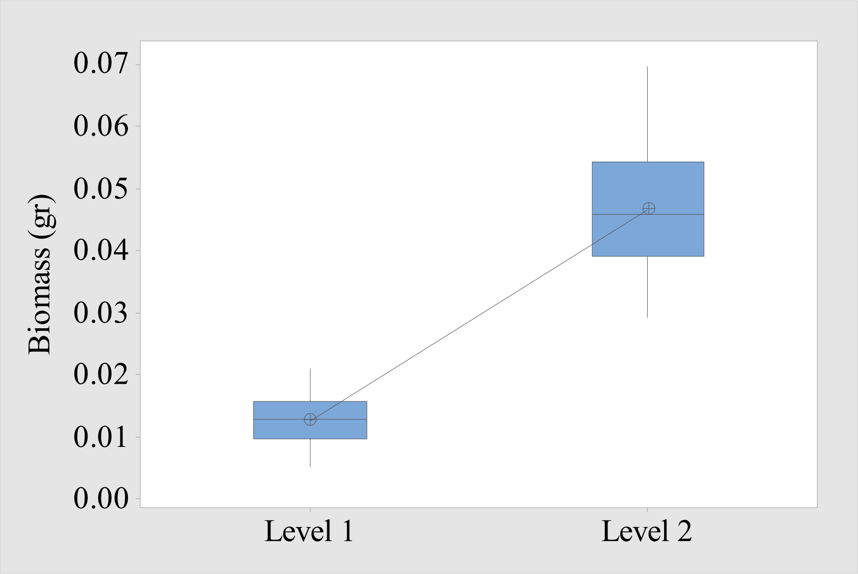

Figure 27 Box plot for total algal biomass for both level 1 and level 2 substratum

The results of biomass measured are matched with the observations through the seven-day inoculation process. Figure 28 shows the trapped and attached algae on the tiles of Run 1 after 168 hours of inoculation. As it is shown in Figure 28, there is a significant difference between colonization of Level 1 and Level 2 in all replicates throughout 1-week inoculation. The first and second number under each tile represents the replicate and the substrate level respectively (e.g., 6-2 is replicate 6 for substrate level 2).

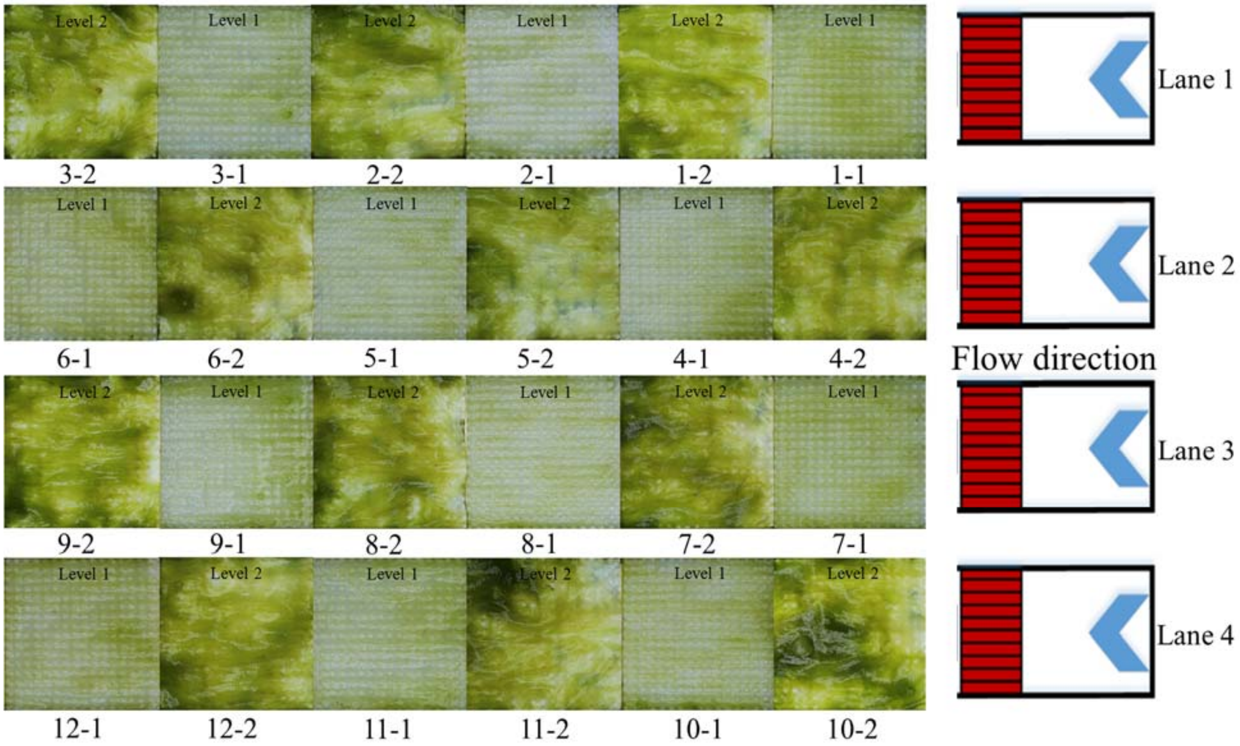

Figure 28 Algal attachment/settlement of run 1 after 168 hours (7 days) of inoculation

Detailed records of attachment/settlement observations at a twelve-hour interval throughout run 1 (168 hours) for each substratum treatment level is presented in Figure 29.

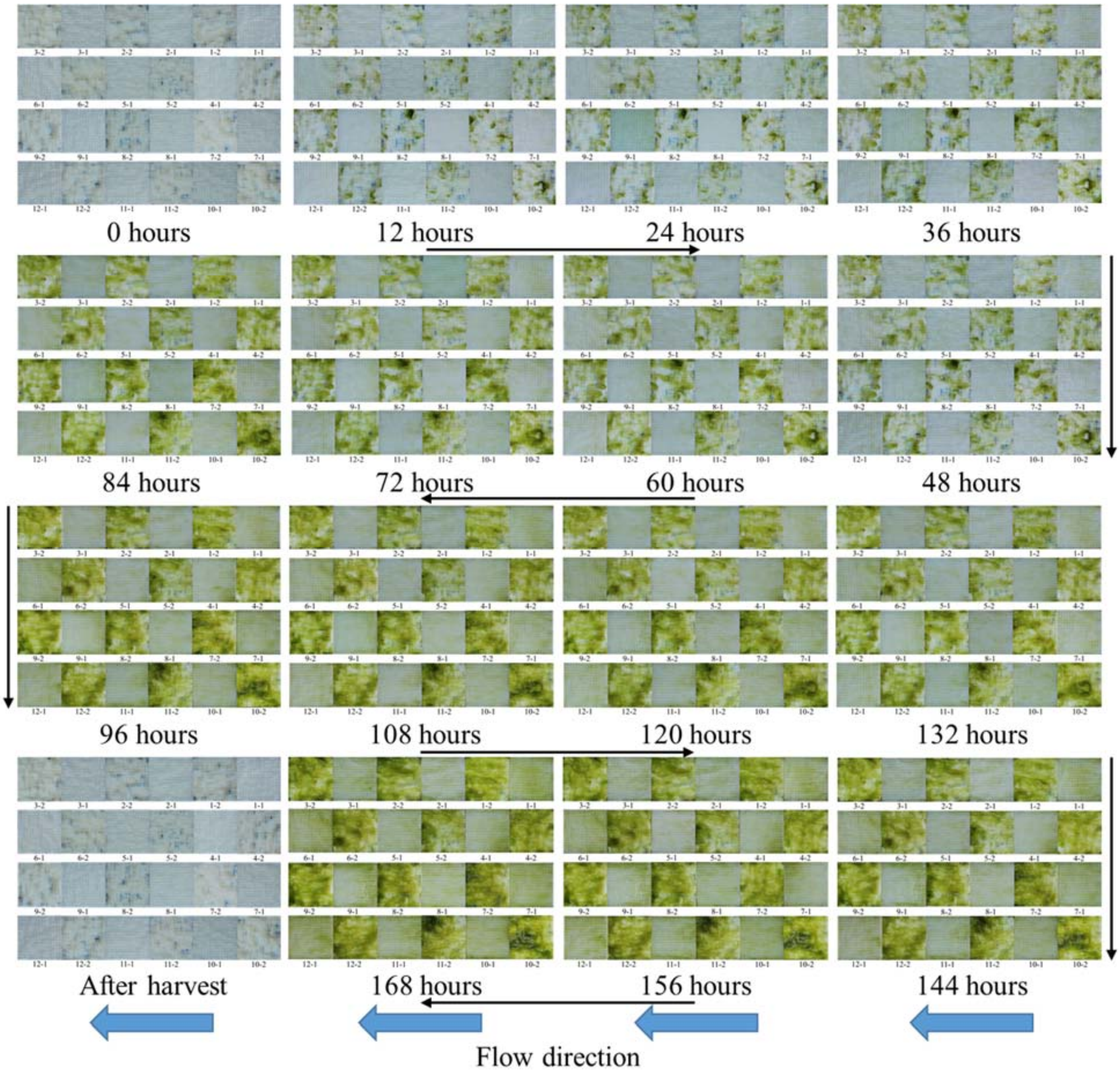

Figure 29 Attachment/settlement observations at twelve hours intervals throughout the run 1 (168 hours)

To test the consistency of conditions on the 4 flow lanes, a Tukey test was conducted to compare the sum of the dried biomass of three samples of each level on flow lanes. The result of the Tukey test showed that there was no significant difference between the 4 flow lanes for both level 1 (Table 7).

Table 7 Summary of Tukey test comparison for dried biomass between the flow lanes

	Level 1 (p-value)			Level 2 (p-value)		
	Lane 2	Lane 3	Lane 4	Lane 2	Lane 3	Lane 4
Lane 1	0.79	0.90	0.24	0.92	0.09	0.11
Lane 2		0.97	0.33		0.12	0.14
Lane 3			0.46			0.89

5. *Discussion*

Based on the statistical analyses of colonized and bare areas of the natural rock surfaces it was hypothesized that certain surface texture parameters (i.e., S_a, S_v, and S_{mr}) show promise in predicting surface adhesion of freshwater algal species. Therefore, this study intended to reverse engineer (develop surface features that are biomimetically inspired from the desired rock specimens) and fabricate pseudo-randomized artificial surfaces with additive manufacturing which are characterized by specific values for the promising surface texture parameters obtained from the rocks' surfaces analyses. For this purpose, a reverse engineering method (Figure 3) has been proposed in this study to test and validate the attained hypothesis. By using the Pearson function, a Matlab® model is coded in this study that is able to generate surface topography and roughness in infinite scale with controlled surface parameters. Since the S_a, S_v, and S_{mr} parameters are mathematically dependent, it is impossible to study the effects of each of them independently on algal attachment. Hence, two treatment levels have been chosen that have specific values (Table 4) for the parameters on each level. Because of manufacturing restriction, a 100 μm resolution (actual resolution of 3D printer) was chosen for the computer models.

After the model was fabricated with the material jetting process, the accuracy of the fabrication was examined by an optical profilometer. For this purpose, eight surface parameters were examined to test the fidelity of the method, (i.e., S_{mr}, S_p, S_{ku}, S_{sk}, S_z, S_q, S_a, and S_v). Figure 14 and

Table 5 present the average errors (the deviation of the actual measured value from the targeted value of computer model) of the eight parameters that are calculated for the computer model and measured from scanned data. It was observed that the S_{mr} had the lowest average percentage error and the S_a, and S_v have the largest errors, among others. In addition, based on the obtained results it is hypothesized that the accuracy of the printer machine is variable depending on features' aspects such as size, geometry, etc. This hypothesis is supported by the minimum feature size analysis of material jetting processes (Chapter III). As Figure 15 indicates, the protrusion features are fabricated with higher fidelity, presenting smaller error than hole features, especially in small sizes (< [700 µm-length and 350 µm-height]). This can be a reason for why the parameter S_p had a higher error percentage than S_v. Based on this analysis it can be concluded that the accuracy of the machine is higher when printing the hills (average error 12.5%) than the dales (average error 33.8%) as shown in Figure 15. The S_{mr} was more robust (average error < 6%) compared to other parameters because it is more dependent on lower frequency signals (waviness) than the higher frequency roughness of the surface (Figure 16). Because of the printers' manufacturing limitations, it should be easier to reproduce the waviness profile than features in the roughness scale.

After the samples were fabricated and their fidelity analyzed a validation experiment was performed to test the hypothesis that certain surface texture parameters (i.e., S_a, S_v, and S_{mr}) show promise in predicting surface adhesion of freshwater algal species. For this purpose, benthic algal channels were used to cultivate attached benthic algae for the purpose of harvesting biomass. Then in three cultivations (each 168 hours-1 run period), a total of 72 samples (two treatment levels with 36 of each) were placed and inoculated to observe and measure the biomass settlement and attachment. The attached/settled biomass was harvested, filtered, dried, and then measured to compare the two treatment levels with different surface characteristics.

The results show that the algal biomass attachment/settlement for the treatment level 2 (46.6±10.0 mg) is significantly higher than level 1 (12.7±4.1 mg) as shown in Figure 27. The results of measured biomass are matched with the observations through the seven-day inoculation progress (Figure 28 and Figure 29). Based on the observations and the statistical results, it can be concluded that the surface topography and physical interactions significantly affect the algal colonization and attachment. Based on the hypothesis obtained from analyzing the specific colonized and bare areas of the natural rocks' surface and validation experiment performed, it was concluded that the surface topography, as described by the parameters S_a, S_v, and S_{mr}, significantly affects the colonization rate of benthic algal species.

Each flow lane can be divided into three sections: up-stream, middle-stream, and downstream (Figure 23). Based on the previous observations, it was hypothesized that growth rate in the middle-stream area is lower than in the up and down-stream areas due to different velocity and turbulence regime on different sections in a flow lane. In the up-stream area, because of existing collimators, water flow is regulated. In the down-stream area, the velocity of the water is higher because it is closer to the end of flow lane. In the middle-stream area, there is a pushing force from the proceeding water that reduces the velocity. Also, the water flow is less regulated compared to in the upstream area. To test the effectiveness of sections on growth rate, a Tukey test was conducted on the measured biomass on each treatment level to compare the three sections (i.e., up-stream, middle-stream, and downstream) on flow lanes. Although Figure 30 shows the middle section for both levels has a lower average algal biomass, the Tukey results show there are no statistical differences between the sections in flow lanes for both treatment levels (Level 1: p-value$_{\text{up-stream, middle-stream}}$=0.36, p-value$_{\text{middle-stream, down-stream}}$=0.12, p-value$_{\text{up-stream, down-stream}}$=0.57, Level 2: p-value$_{\text{up-stream, middle-stream}}$=0.08, p-value$_{\text{middle-stream, down-stream}}$=0.394, p-value$_{\text{up-stream, down-stream}}$=0.152).

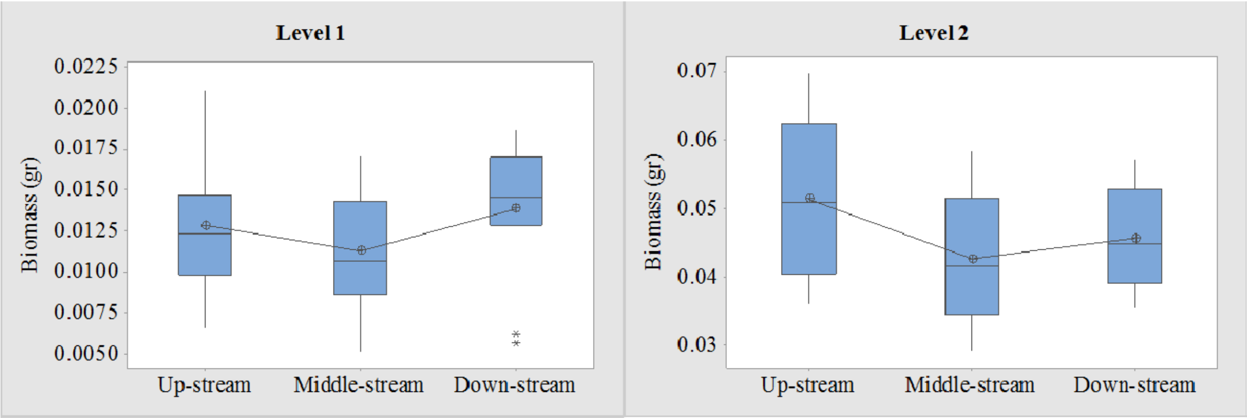

Figure 30 Box plot for algal biomass versus three sections for both level 1 and level 2 substratum

The correlation between the algal biomass and the value of S_a, S_v, S_{mr} has also been analyzed. The results show that there is a statistically significant correlation between the S_a and the algal biomass for the level 2 (Figure 31 (d)) substratum (correlation=0.489, p=0.002) at a significant level of α=0.05. The correlation of S_v and the algal biomass for level 2 is not statistically significant, but close to significant level (correlation=0.317, p=0.060). As it can be seen from Figure 31, the other correlations are not significant. The analysis showed that for the S_a in the range of 1.7 mm to 2.5 mm, there is a positive correlation between the dried biomass and the S_a values. The correlation of S_v and the algal biomass for level 2 is not statistically significant but close to significant level. Other correlations were not significant. Figure 31 shows that the parameters in isolation do not have a significant correlation with dried biomass, but together they show significant.

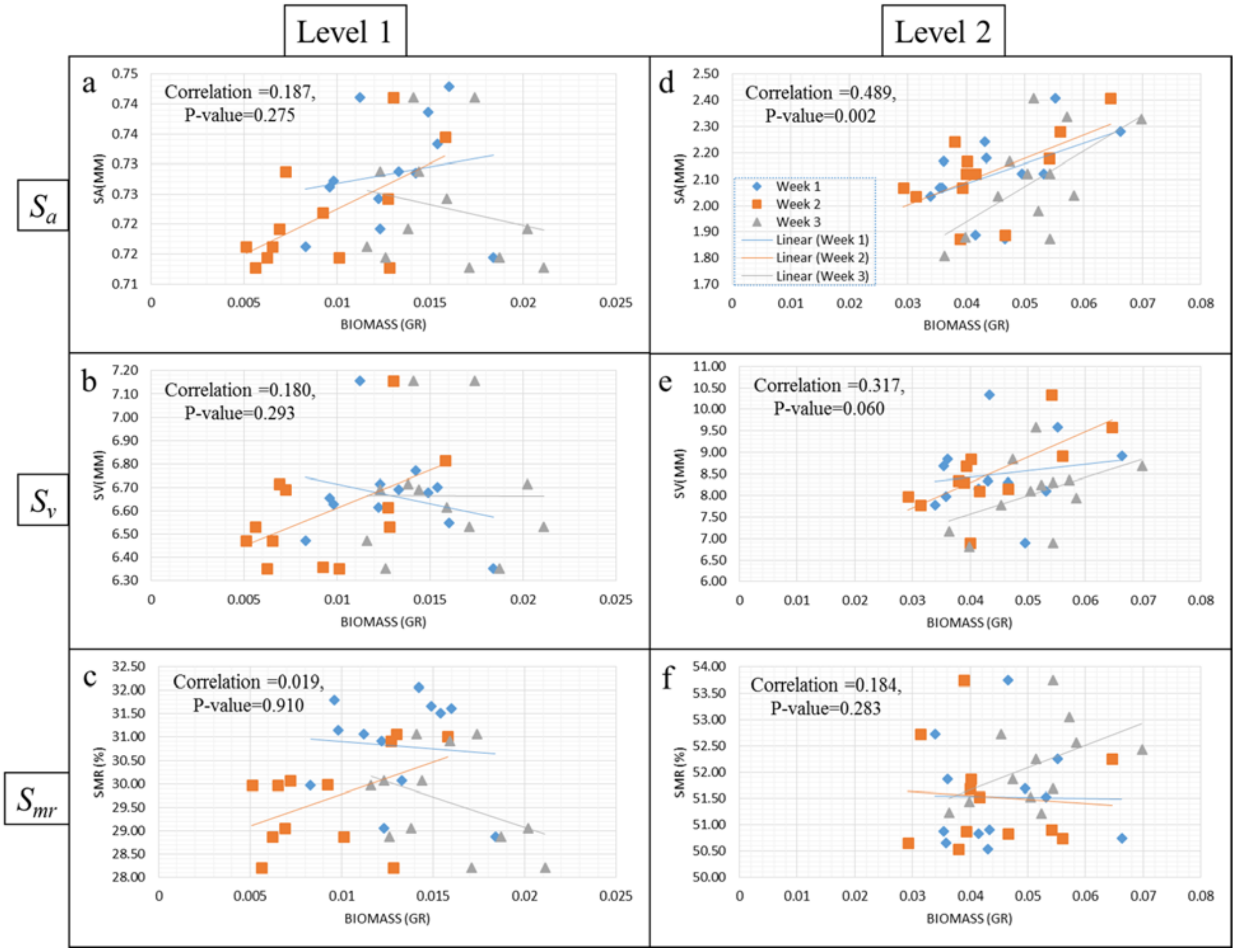

Figure 31 Correlation of algal biomass with targeted surface texture parameters

The colonization process was analyzed based on the treatment level 2 since its growth rate is significantly higher than treatment level 1. A surface with higher average roughness (higher deviation from the mean surface plane) has, on average, taller hills and deeper dales that may help to increase the chance of trapping algal filaments during the colonization process. Figure 32, Figure 33, and Figure 34 show the images of treatment level 2 after 12 hours, 72 hours and 144 hours, respectively, of inoculation and their profilometry heat map. Based on the observations (Figure 32), it was hypothesized that when the flow that carries algal filaments (which are long and thin filaments like human hair) reaches the tall hills, the flow dynamics of the water changes and the chances of being trapped by the topographies are increased. In the first few hours of colonization on Treatment level 2, it was observed (Figure 32) that a number of algal filaments were being trapped by hills: topographies above the mean plane (yellow and red areas in profilometry images in Figure 32). The images were taken with a wide-area 3D measurement system (VR-3000, Keyence, Osaka, Japan). This appearance is clearer when the hills are surrounded by a set of dales such as samples 10-2 and 11-2 in Figure 32. Then, it was hypothesized that the trapped filaments become seed sources to adsorb other algal cells (Figure 33), and it helps to colonize the surface at a higher rate. As the inoculation time passes, the dale sections are becoming habitats for the cells (Figure 34). In general, it was hypothesized that the hills are trapping the species and the dale sections (especially the ones which are adjacent to the hills that trapped filaments) become habitats to adsorb more individual cells. This appearance may be explained as the dale sections become interstitial areas between the hills in the surface topography and help to attract the following cells in the flow that are attracted by the trapped filaments over the hill sections.

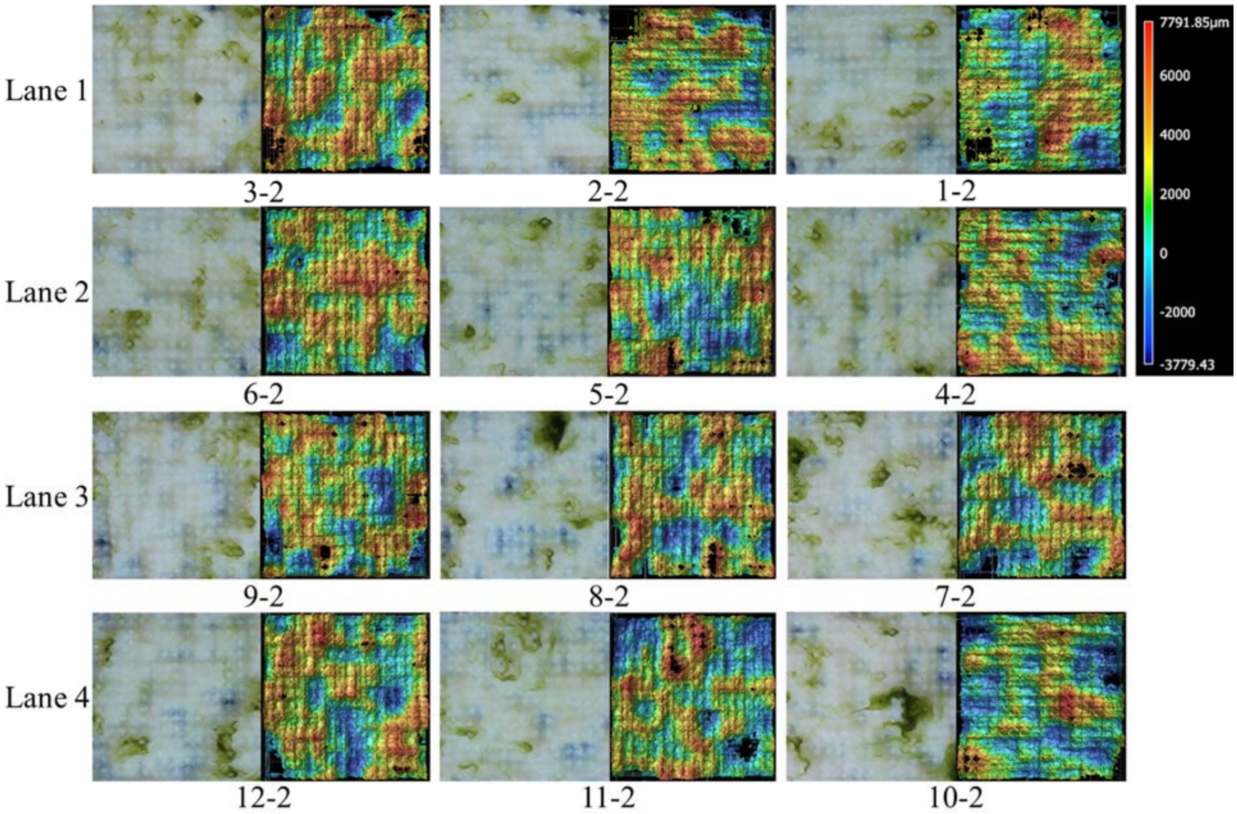

Figure 32 Photographs of treatment level 2 in run 1 after twelve hours of inoculation and their profilometry heat map

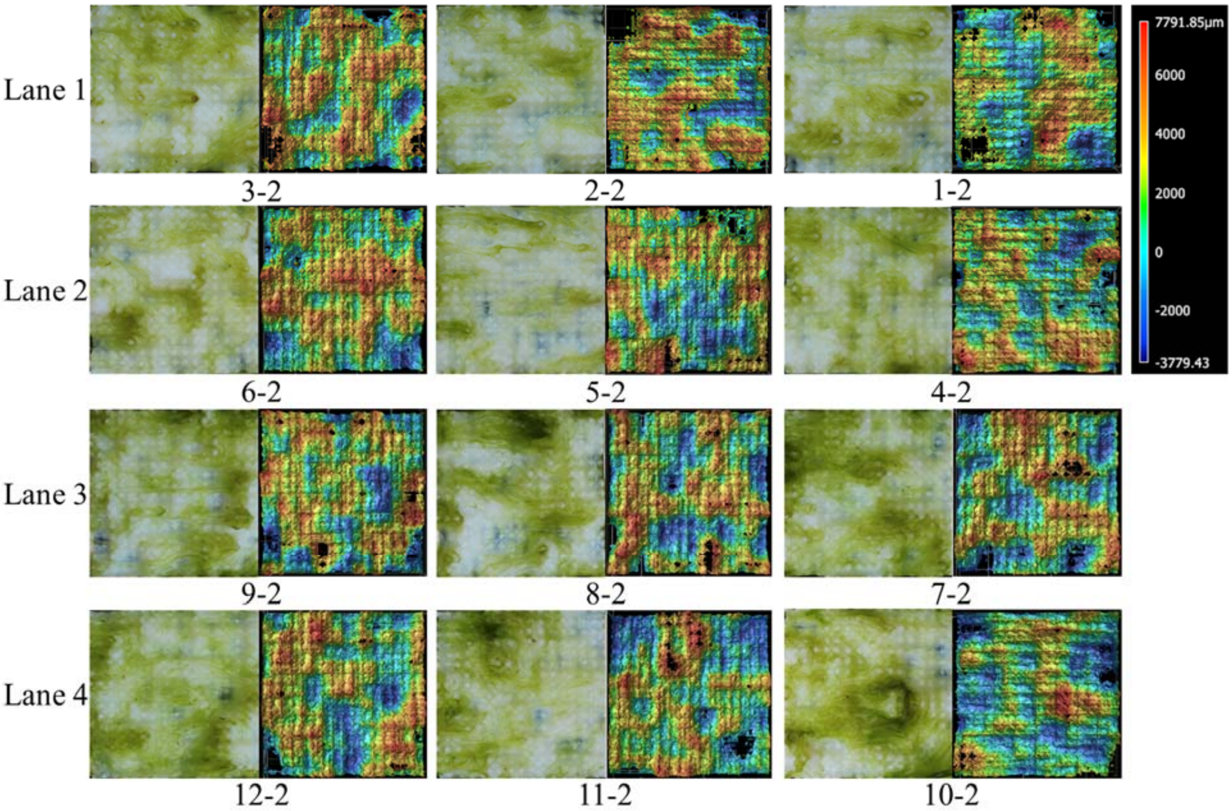

Figure 33 Photographs of treatment level 72 in run 1 after twelve hours of inoculation and their profilometry heat map

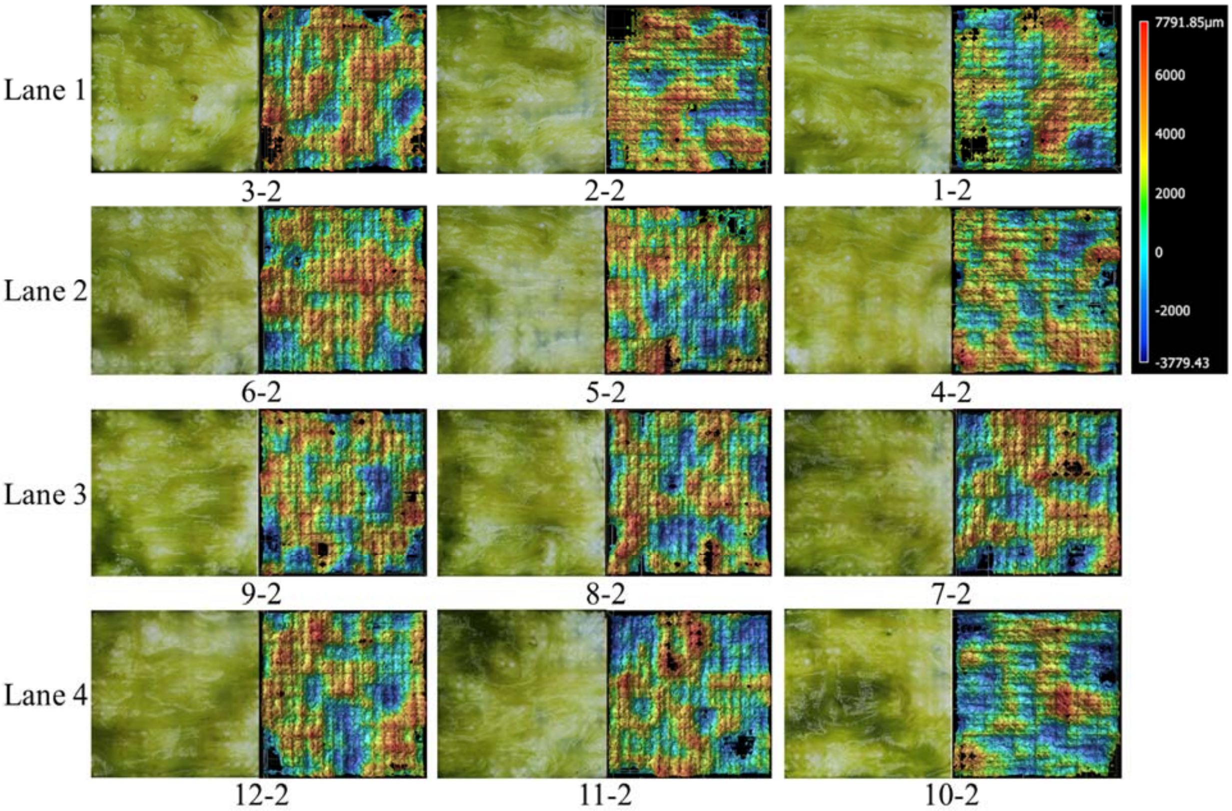

Figure 34 Photographs of treatment level 144 in run 1 after twelve hours of inoculation and their profilometry heat map

6. *Conclusion*

This work sought to reveal the surface topography parameters that were significant for algal attachment by manipulating surface topographies using additive manufacturing. In this study, a method for capturing and developing surface features that are biomimetically inspired from the desired natural substrata has been developed and proven feasible. Natural rocks and surfaces with attached biofilms were retrieved from streams, scanned with optical profilometry, and the surface characteristics were analyzed. The results show that certain texture parameters (e.g., S_{mr}, S_a, and S_v) show promise in predicting surface colonization by algae. The Pearson distribution was utilized to generate pseudo-randomized surfaces with surface characteristics. A material jetting process was used to additively manufacture the surfaces followed by optical profilometry to validate the resultant topography.

Surface metrology parameters (i.e., S_{mr}, S_p, S_{ku}, S_{sk}, S_z, S_q, S_a, and S_v) are utilized to test the fidelity of the proposed method. The results showed that the accuracy of metrology parameters are varied depending on the resolution of the machine in different axes. Among the selected metrology parameters for the validation process, S_{mr} had the lowest average error (5.7 %), while S_v and S_a had the highest average error (33.8 %). The precision of the additive machine was lower than the computer model which causes the error in reverse engineering method.

It was observed that what had been designed as sharp peaks become smooth curves after fabrication, which affects the S_v and S_a parameters the most. The S_{mr} was more robust compared to other parameters since it was dependent on waviness rather than roughness profile.

An experiment was conducted to validate the proposed reverse engineering method. A floway bioreactor has been used to cultivate attached benthic algae for the purpose of harvesting biomass. The results validated that the set of S_a, S_v, and S_{mr} significantly affect and predict the surface adhesion of benthic algal species.

Chapter II

Study the Effects of 3D Printed Microtextured Surfaces on Contact Angle

1. Introduction

Wetting behavior and adhesion properties of solid substrata are important characteristics in many industrial and laboratory studies. Contact angle measurement is a common way to evaluate the wetting behavior of a solid substrate [85]. Once the three phases of liquid, solid, and gas reached a steady state, a static contact angle developed between the three phases (Figure 2). A significant amount of research has investigated how surface energy and contact angle are correlated. Initially, Young (1805) recognized this relationship over an ideal (homogenous and smooth) surface (Equation 4) [85], [86] through the relationship:

$$Cos\theta\gamma_{lv} = \gamma_{sv} - \gamma_{sl} - \pi_e \tag{5}$$

where θ, is the contact angle between liquid and solid, γ_{lv}, is the free energy of the liquid and gas, γ_{sv} is the free energy of solid and gas, γ_{sl} is the free energy of the interface between liquid and solid, and π_e is the equilibrium pressure of adsorbed vapor of the liquid on the solid. Wenzel (1936) extended Young's equation for rough but homogenous surfaces (Equation 6) [87].

$$Cos\theta_w = \frac{\delta(\gamma_{sv} - \gamma_{sl})}{\gamma_{lv}} \tag{7}$$

Where δ is defined as a ratio of the actual surface area to the geometrically projected area, and θ_w is the Wenzel contact angle.

Several physical and chemical factors such as type, shape, and size of the particles of material, surface roughness, and surface geometry influence the contact angle [6]. Surface roughness is one of the well-studied factors that affect contact angle. For the surfaces with an average roughness below $0.1\ \mu\mathrm{m}$ ($\mathrm{R_a} < 0.1\ \mu\mathrm{m}$), the contact angle is independent of the average roughness. However, for surfaces with $\mathrm{R_a} > 0.1\ \mu\mathrm{m}$, the contact angle and average roughness are codependent variables [88], [89]. Chau et al. (2009) studied how surface geometry and roughness influence the wetting behavior of a surface. They concluded that increasing the surface roughness decreases the contact angle of hydrophobic materials and increases the contact angle of hydrophilic materials [6].

One of the ways of approaching hydrophobic/super-hydrophobic surfaces is to create patterned microtextures on the solid surfaces. Several studies investigated how microtexture designs affect the contact angle and surface energy. Jopp et al. (2004) studied the wetting behavior of circular and square protrusions and holes. The effects of pore fraction, roughness factor, and geometric parameters of designed microtextures on the hydrophobicity of PDMS rubber were examined in this study [90]. Kanungo et al. (2014) studied the effect of pitch size (distance between a peak and an adjacent peak) on the contact angle of spherical microtextured surfaces. They observed that for a given pitch, spherical holes and protrusions gave comparable static contact angle [91]. Lee et al. (2009) compared three different types of microtextures (square holes, protrusions, and hexagonal holes). They patterned their tiles using by silicon wafer and processed them using AZ5214E photoresist. With a given pore fraction, the square protrusion had a higher contact angle than those of holes. They perceived that the pore fraction has a positive correlation with contact angle [92]. Lee et al. (2011) studied the hydrophobicity of a nickel micro-mesh surface designed with circular holes and micro-fences. Their results show that mirco-fence microtextures are more hydrophobic than circular holes in this size range. The diameter of circular holes is negatively correlated with the contact angle, while the diameter of the hole of a micro-fence has a positive correlation with the contact angle [93]. The effects of geometric parameters (diameter, height, pitch, and solid area fraction) on the circular protrusion on the wettability of fluorosilane (FOTS) surfaces were analyzed in a study by Zhao et al. (2012). The results show that the influences of diameter, height, pitch, and solid area fraction are negligible on advancing contact angles while receding contact angles reveal a negative correlation with solid area fraction [94]. The advancing and receding contact angle is depicted in Figure 35. Greiner et al. (2007) reveal the effects of aspect ratio (diameter over height) of circular protrusions on wettability. The patterns are fabricated by epoxy-based photoresist material [95]. Kwon et al. (2009) tested the hydrophobicity of square protrusion microtextures. They fabricated the patterns on a silicon surface etched by a gas phase of Si with XeF2 vapor [96]. Lv et al. (2010) tested contact angles on silicon wafer surfaces covered by a photoresist layer. The square protrusion features were patterned by the ICP dry etching method [97]. Li et al. (2016) studied the effects of diameter size and height of circular microtextures on advancing and receding contact angles. The patterned surfaces were prepared by etching silicon and hydrophobized by chemical vapor deposition of self-assembled monolayers of fluorosilane. They concluded that the advancing contact angle is not dependent on diameter and height size of circular protrusions, whereas receding contact angles reveal a negative correlation with the diameter of protrusions [98]. Ng et al. (2016) created groove and square protrusion patterns on aluminum surfaces processed by the micro-rolling-based texturing method to test its wetting properties. They studied the effects of surface area over volume ratio and groove aspect ratio (diameter over height) on the contact angle [99]. Nosonovsky et al. (2007) tracked the changes of static contact angle, and contact angle hysteresis (log or difference between advancing and receding contact angle) by the ratio of the diameter over pitch size (space factor) of circular protrusion PMMA textured surfaces [100]. Additional information on literature regarding the effects of microtextures' parameters such as shape, length, height, pitch, fabrication method, material, and dependent variables on contact angle is summarized in Table 8.

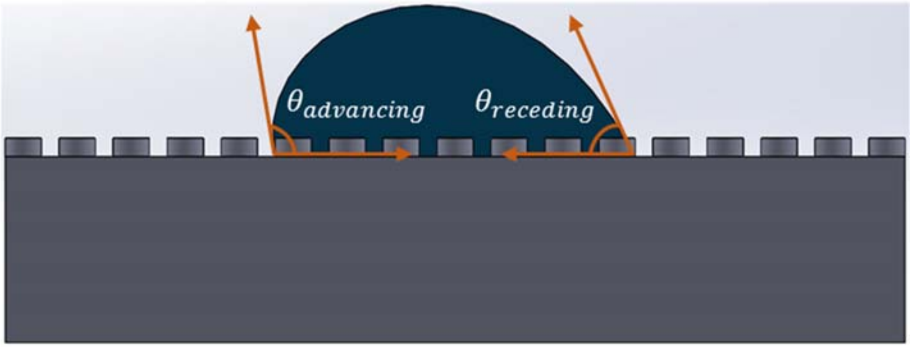

Figure 35 Advancing contact angle, θ_{adv} and receding contact angle θ_{rec}

Table 8 Relative literature which investigated the effects of geometric parameters of microtextures and roughness on contact angle

Literature	Shape	Length/ Diameter (μm)	Height/ Depth (μm)	Pitch (μm)	Texture Fabrication Method	Material	Dependent variable
Kanungo et al., 2014 **[91]**	Spherical protrusion, square protrusion	3	1.5	[4.5, 96]	Photolithographic technique	FOTS coated Polydimethylsiloxane (PDMS)	roughness factor (surface area/projected area), solid area fraction (solid-water interface area)
Long et al., 2005 **[101]**	Square protrusion, trapezoid protrusion, saw tooth protrusion	[2, 100]	[1.5, 100]	40			
Callow et al., 2002 **[102]**	Square protrusion, groove	5	[1.5, 5]	[5, 20]	Patterns are etched in silicon wafers using the Bosch process	Polydimethylsiloxane (PDMS)	aspect ratio (diameter/depth)
Greiner et al., 2007 **[95]**	Circular protrusion	[2.5, 80]	[2.5, 25]	>5	Lithographic technique	Sylgard 184 polymer	aspect ratio (diameter/depth
(Ng et al., 2016) **[99]**	Groove, square protrusion	[15, 60]	[30, 110]	[80, 200]	Microrolling-based Texturing (μRT) and Laser Induced Plasma Micro-Machining (LIPMM)	Aluminum (AA3003)	aspect ratio (diameter/depth)
Jopp et al., 2004 **[90]**	Circular hole and protrusion, square hole and protrusion	[40, 150]	[100, 110]	[100, 160]		Polydimethylsiloxane (PDMS) covered by Photoresist NanoTM SU-8	the roughness factor (surface area/projected area), pore fraction
Lee et al., 2009 **[92]**	Square hole and protrusion,	[5, 502]	[2, 20]	[2.5, 50]	photolithography,	Silicon wafer covered by PPFC	

	hexagonal hole				silicon dry etching by DRIE, removal of photoresist, and PPFC deposition		
Lee et al., 2011 **[93]**	Cylindrical protrusion and circular hole	[10, 50]	24	100	Lithography and DRIE, metal seed layer deposition, electroplating, etching, and PPFC coating	Silicon wafer covered by PPFC	
Zhao et al., 2012 **[94]**	Circular protrusion	3	7	[1.5, 9]	Photolithographic technique followed by surface modification with a conformal nanocoating.	Silicon wafer	the solid area fraction
Kwon et al., 2009 **[96]**	Circular protrusion	~20	~40	~150	Chemical etching, polymeric deposition, electrochemical corrosion, and laser etching	Silicon wafer	space factor (pitch/diameter)
Lv et al., 2010 **[97]**	Square protrusion	[10-45]	35	[10, 30]	Photolithography and etching of inductively coupled plasma (ICP)	Silicon wafer	
Li et al., 2016 **[98]**	Circular protrusion and holes	[10-200]	10	varied	Etching of silicon, hydrophobized via chemical vapor deposition of self-assembled monolayers of fluoro silane	Silicon wafer	the solid area fraction
Nosonovsky et al., 2007 **[100]**	Close to Circular protrusion	~ [0.04, 10]	~ [0.78,13]	~0.2	PMMA HAR is coated with Hydrophobic perfluorodecyltriehoxysilane (PFDTES)	Poly-methyl-methacrylate (PMMA)	space factor (pitch/diameter)
H. J. Busscher et al. 1984 **[89]**					Specimens are polished with 400 and 1200 grit Carborundum paper	Polymers: PTFE, PE, PP, PVC, PS, PMMA, PC, PA 6, PA 6.6, PA 6.10, PA 11, PA 12	average roughness: [0.037, 9] µm

With respect to measurement methods, the contact angle is measured in different ways with instruments such as SEM, goniometer and macro-lensed cameras [6], [7], [103], [104]. A sessile-drop is the most common vehicle to measure contact angle (Figure 36). In this approach, a precisely measured drop of liquid is placed on the surface by a syringe/pipette. Then a low-power microscope or macro-lensed camera is utilized to obtain a digital image of the drop and surface. By determining a tangent to the image at the contact point of the drop, the contact angle is measured.

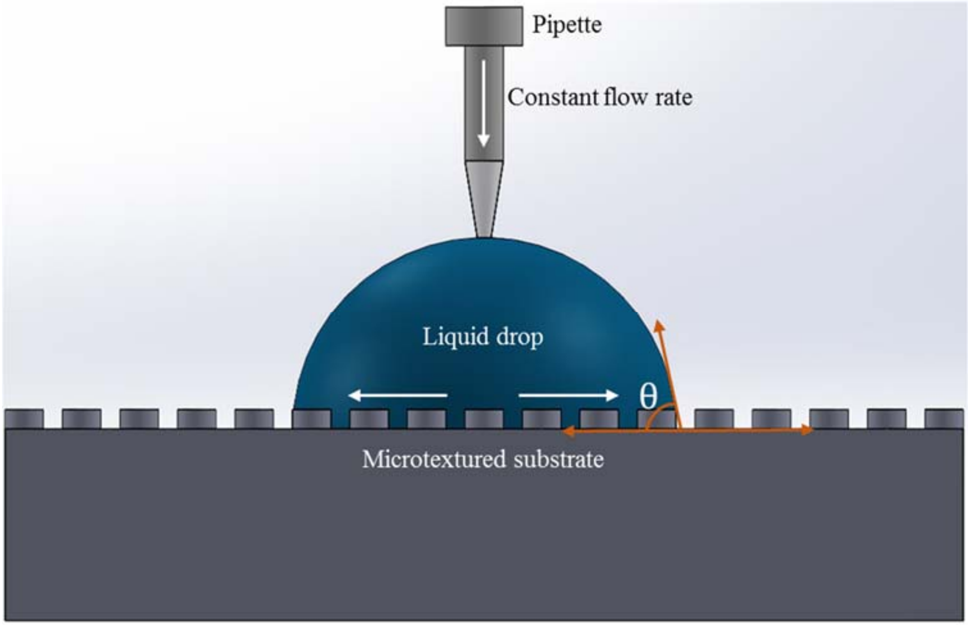

Figure 36 Sessile-drop method

One of the key points in measuring the contact angle is that the size of the drop should be large enough that it does not affect the curvature of the drop surface close to the contact line [105]. Li (1996) explains that the drop size dependency of contact angles on ideal smooth surfaces is a result of the line tension effect. However, on rough surfaces, the contact angles not only depend on line tension, but also on surface roughness, surface heterogeneity, and drop size [106]. Ponter and Yekta-Fard (1985) examined the effects of drop size change on water-PTFE, water-copper, water stainless steel, and water-PMMA. The contact angles were measured at 25℃ in the air and at the boiling point in a vapor environment. At a 25℃ contact angle, the drop size had a positive correlation (same conclusion as Herzberg and Marian (1970) [107]), while at the boiling point they are negatively correlated [103]. Drelich et al. (1997) examined different drop volumes on various solids such as smooth and homogeneous, rough and homogeneous, smooth and heterogeneous, and surfaces covered with unstable organic films. They observed that the drop sizes less than 5 mm significantly affect the receding contact angles [108]. In another study, Drelich et al. (1996)

tested two different techniques, sessile-drop, and captive-bubble, for measuring the advancing and receding contact angles. They found that for each technique used, different advancing and receding contact angles were obtained for rough and heterogeneous surfaces, while for closer ideal surfaces these two techniques had agreement on the measured contact angles [109]. These discrepancies between the two different techniques increased with increasing the roughness of the surface. These imperfections also affected the variation of the contact angles with drop size. Their results showed that the receding contact angles best reveal the contact angle and drop size relationship for drops with 1-7 mm base diameters [108]–[110]. Meiron et al. (2004) imply that if the drop size is about three orders of magnitude larger than the average vertical irregularities of the surface and almost two orders of magnitude greater than its average wavelength, the drop would be considered sufficiently large to hold a Wenzel equation [111]. Based on the reviewed literature, choosing the drop size is critical, and it should be large enough compared to the scale of the microtextures and average roughness to not influence the measurement significantly.

Contact angle and surface energy study is a well-known topic since the 1930s, and many studies have investigated different factors such as chemical and physical interactions, environmental and experimental conditions. Among these, several researchers studied the effects of microtextures on contact angle and surface energy mostly to create super-hydrophobic surfaces. However, there is no study to date that takes advantage of the advances in 3D printing to investigate the effects of geometric parameters of microtextures and their interactions on contact angle. This study aims to reveal how each of these parameters (i.e., shape, length or diameter, height, and pitch size) and their interactions would change the hydrophobicity of the surfaces.

This work aims to study the effects of geometric shape parameters (i.e., shape, length, height, and pitch of features) on custom-3-D printed microtextured surfaces on receding and advancing water contact angles.

2. *Preliminary Experiment*

A preliminary experiment was performed to test the manufacturability of the 3D printer (Objet30 3-D (Stratasys Ltd., Eden Prairie, MN) printer with 28 µm layer thickness). All samples were fabricated in glossy finish (the best surface finish option for the machine). As presented in Table 9, several texture shapes such as groove, triangular groove, cone, pyramid, cylindrical, and spherical protrusion printed in various nominal length (300, 400, and 500 µm), height (150, 200, and 250 µm), and pitch (200, 300, 400, and 500 µm) sizes to evaluate the fidelity of the 3-D printer. Results are shown in Table 9. Among all shapes, the cylindrical protrusion and groove provided the best dimensional accuracy. Also, it was observed that the lowest reliable level for length, height, and pitch size (distance between peak to peak) is 400 µm. Because accuracy in finding the edges is difficult, the peak to peak (S) values are presented in Table 9 instead of pitch size.

Table 9 Preliminary experiment results. *L* is length, *H* is height, *P* is pitch, and *S* is the peak to peak length.

Shape	Nominal (**µm**): L=400, H=150, P=200, S=600			Nominal (**µm**): L=300, H=150, P=300, S=600			Nominal (**µm**): L=400, H=200, P=400, S=800			Nominal (**µm**): L=500, H=250, P=500, S=1000		
	L (µm)	H (µm)	S (µm)	L (µm)	H (µm)	S (µm)	L (µm)	H (µm)	S (µm)	L (µm)	H (µm)	S (µm)
Cone protrusion	500	60	610	360	60	510	375	110	810	550	155	1010
Pyramid protrusion	320	80	608	345	65	508	370	112	800	555	170	1008
Cylindrical protrusion	185	140	612	220	92	506	390	185	818	444	235	1017
Groove	174	146	605	212	92	498	424	175	801	492	208	1009
Spherical protrusion	195	106	614	350	70	794	421	150	812	485	172	1011
Triangular groove	168	75	611	208	71	501	380	110	810	487	162	1015

An experimental apparatus was built to measure contact angles based on the setup proposed by Lamour et al. (2010) [7]. This comprised a digital camera (Canon EOS Rebel T5i DSLR) with 18-55 mm lens, a set of +1, +2, +4, and +10 macro lenses assembled together, a custom-built adjustable tripod table, an adjustable tripod stand for the samples, diffused light, a dark box, a leveling platform with two levels between the table and the sample stand (Figure 37). Figure 37 (a) shows the external elements of such as lighting system, camera, stands, and the external dark box, Figure 37 (b) shows the internal elements of the experimental apparatus, and Figure 37 (c) precisely sketches the configuration and the critical distances between some essential parts such as camera, lens, and sample area.

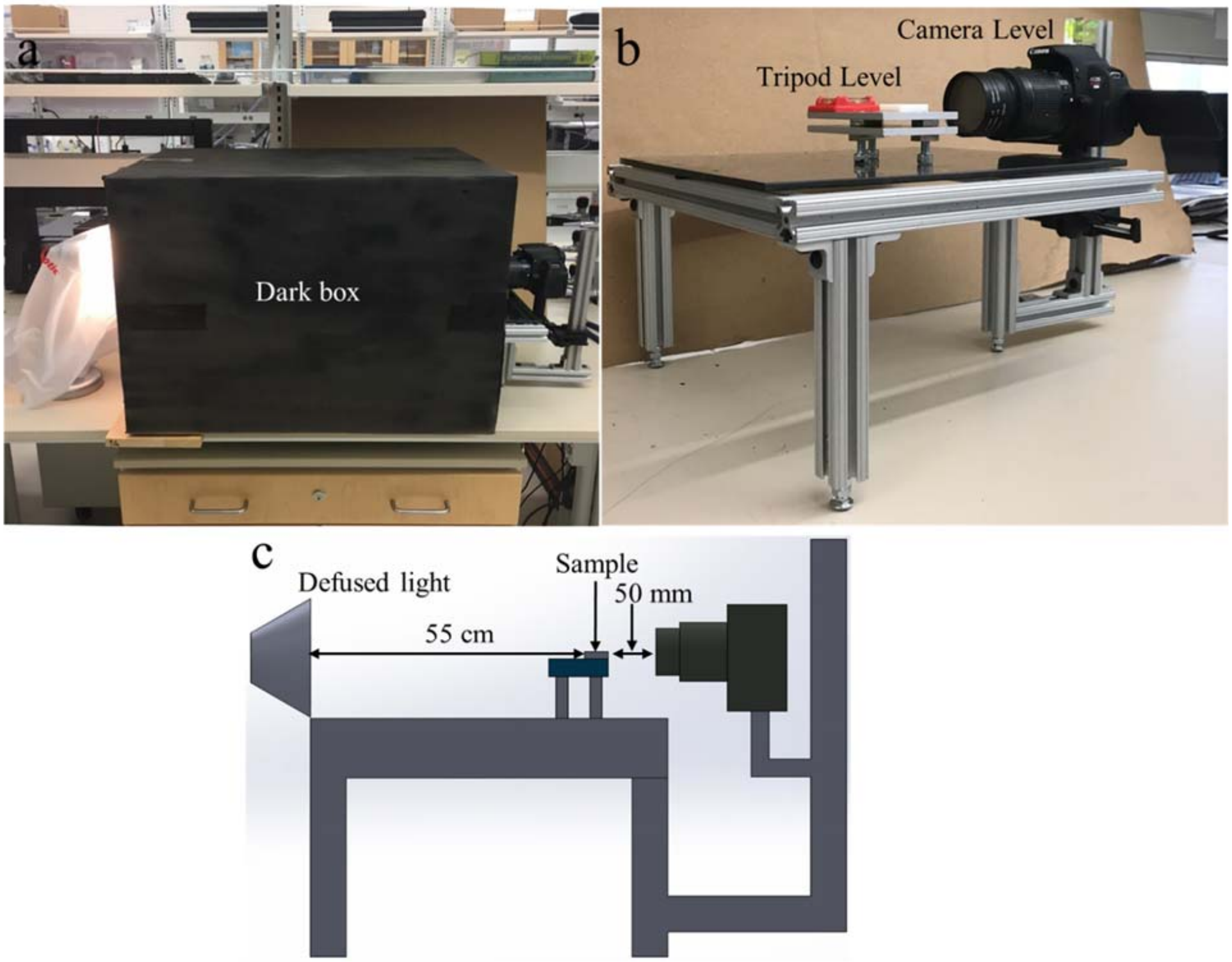

Figure 37 Photographs (a and b) and schematic (c) of the experiment setup

A second preliminary experiment was performed to evaluate the effect of diameter size of spherical holes (from 250 µm to 1500 µm with a 250 µm interval) on receding and advancing contact angle. Three replicates of each size were designed and printed. Three contact angle measurements were performed on each replicate. The method of measuring contact angles is described in detail in the Materials an Methods section (section 3). In this preliminary experiment, all microtextures have the same aspect ratio (length over height). The results show significant differences between the diameter sizes of 1000 µm and 1500 µm diameter for both receding ($p=0.027$) and advancing ($p=0.016$) contact angles of microtextures (Figure 38). The promising results from this preliminary experiment led to the design of the main experiment with more geometric factors such as shape, height or depth, and pitch size.

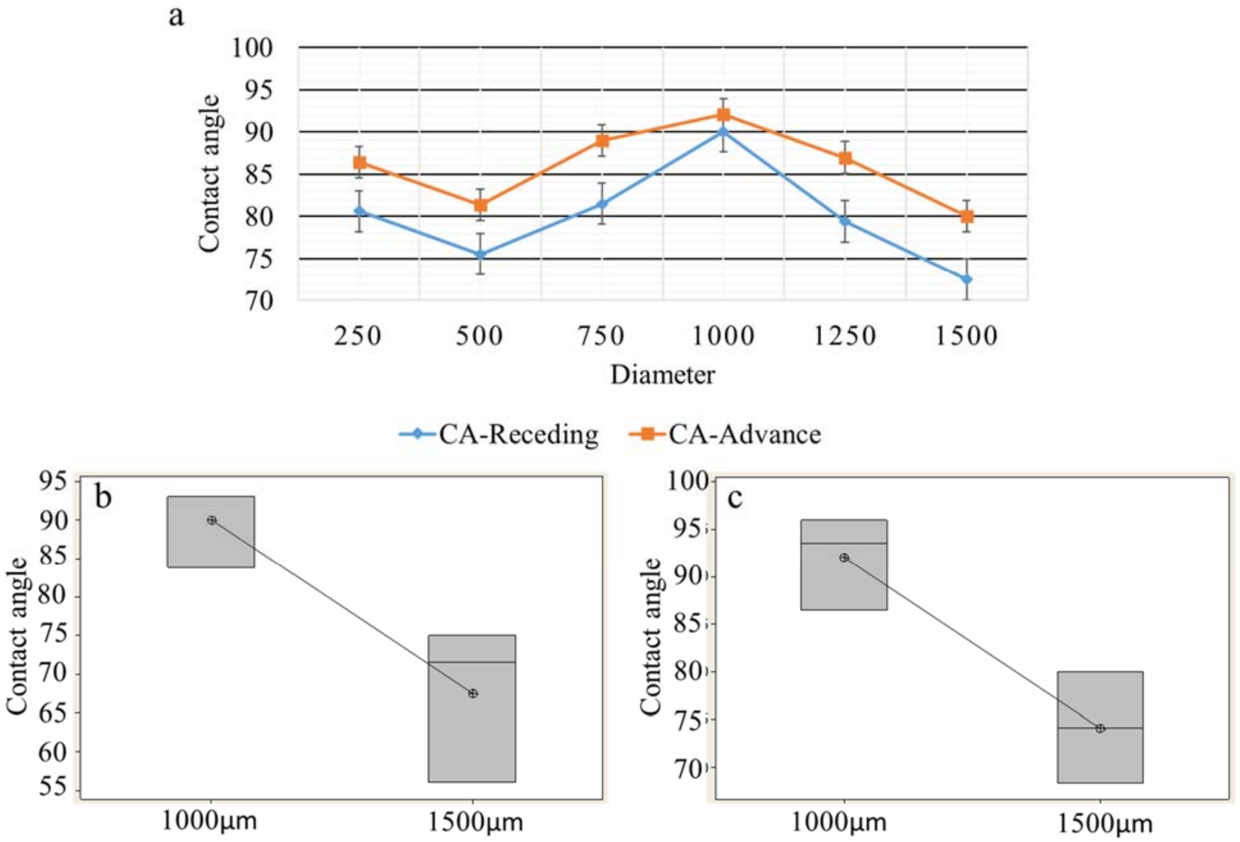

Figure 38 Preliminary experiment contrast between spherical holes with diameter sizes from 250 µm to 1500 µm

3. Materials and Methods

This experiment tries to investigate the impact of geometric parameters of micro textured surfaces on receding and advancing contact angles. A full-factorial design considering four factors (i.e., shape, length, height, and pitch size) with different numbers of levels and three replicates is performed for this purpose. The interactions between the factors are analyzed as well.

Based on the distortion study presented in Chapter III, the distortion in 6 mm thickness tiles is sufficiently small, especially if the dimensions of the tiles (length and width) are homogeneous and small enough. Therefore, 6 mm thickness was chosen for the tiles in this study to minimize the possible distortion effects on contact angle. The tiles are designed with 30 mm × 30 mm × 6 mm dimensions (Figure 39).

The Objet30 3-D (Stratasys Ltd., Eden Prairie, MN) printer with 28 μm layer thickness is used to fabricate the tiles in glossy finish (best surface finish option for the machine). The full factorial design performed in this study is shown in Table 10. For this purpose, three replicates of each design, two levels of shape (circular protrusion and groove), three levels of length or diameter (400 μm, 900 μm, and 1400 μm), three levels of height (200 μm, 450 μm, and 700 μm), and two levels of pitch (400 μm and 900 μm) were considered (Figure 39). During the printing process, the grooved tiles were oriented on the build tray in a way that their grooves were perpendicular to the printing direction because the printing quality is higher in that orientation. The orientation does not affect the circular protrusion patterns due to their homogeneity on printing plane.

Table 10 Factors and levels of full factorial experiment

Factor	Level 1	Level 2	Level 3
Shape	Circular protrusions	Groove	
Length or diameter (μm)	400	900	1400
Height (μm)	200	450	700
Pitch (μm)	400	900	

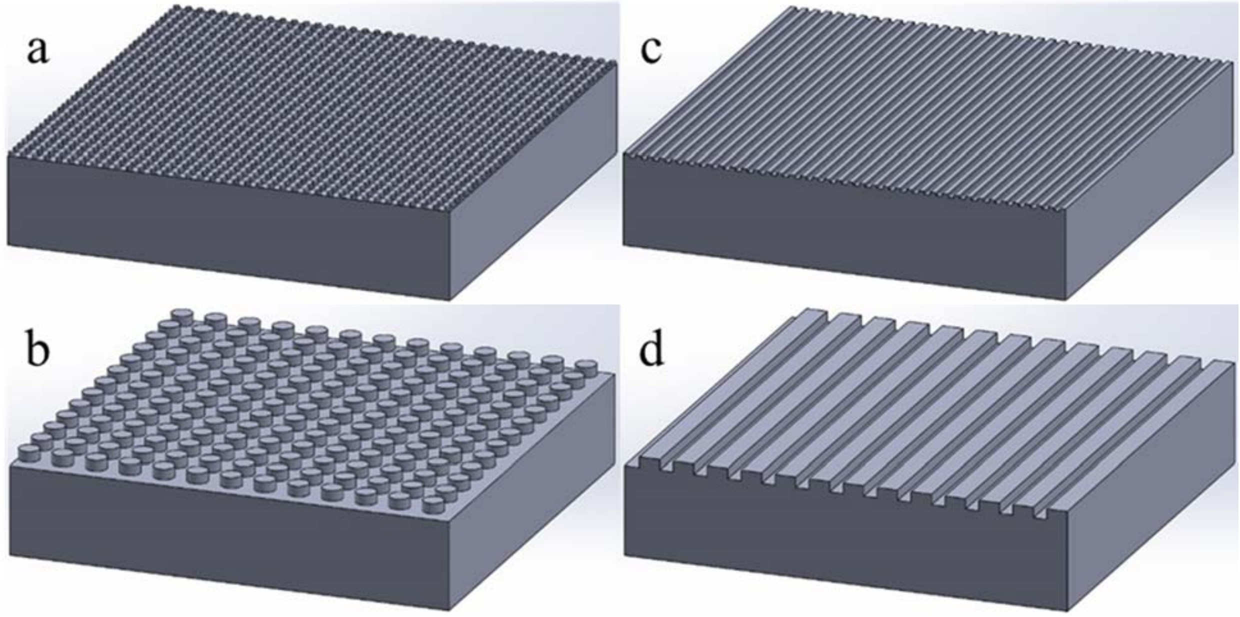

Figure 39 Tile surfaces design. Circular protrusion with 400 µm diameter, 200 µm height, and 400 µm pitch size (a), circular protrusion with 1400 µm diameter, 700 µm height, and 900 pitch size (b), groove with 400 µm diameter, 200 µm height, and 400 pitch size (c), and groove with 1400 µm diameter, 700 µm height, and 900 pitch size (d)

One of the key points in measuring the contact angle is that the size of the drop should be large enough that it does not affect the curvature of the drop surface close to the contact line [105]. Li (1996) explains that the drop size dependency of contact angles on ideal smooth surfaces is only because of the line tension effect. However, on rough surfaces, the contact angles not only depend on line tension (“line tension is the excess free energy per unit length of a contact line where three distinct phases coexist” [112]), but also on surface roughness and surface heterogeneity which can cause different patterns of drop size dependency of contact angle [106]. Drelich et al. (1997) examined different drop volumes on various solids such as smooth and homogeneous, rough and homogeneous, smooth and heterogeneous, and surfaces covered with unstable organic films. They observed that the drop sizes less than 5 mm significantly affect the receding contact angles [108].

Other studies have shown that the receding contact angles better reveal the contact angle and drop size relationship for drops with 1-7 mm base diameters [108]–[110]. Based on the reviewed literature [111], choosing the drop size is critical, and it should be large enough compared to the scale of the microtextures and the average roughness so as not to affect the measurements significantly. Therefore, a 40 µl volume of the drop was chosen for this experiment. A 40 µl drop size has 4-6 mm diameter over the microtextured surfaces, depending on the level of hydrophobicity of the surface. It is recognized that one of the causes of error and uncertainty in measuring the contact angle is in the manual process of pipetting. In this study, a 20-200 µl pipette (20-200 µl Eppendorf, Hamburg, Germany) with the precision of 0.0002 gr (0.2 µl) was used. To estimate the magnitude of this operator error, the weight of 50 drops of ultrapure water (with 18.2 MΩ·cm in resistivity) calibrated on 0.04 gr (40 µl volume) were measured with a scale with a precision of 0.0001 gr. The results are shown in Figure 40 and indicate that 48 drops out of 50 deviated less than 0.002 gr from the targeted 0.04 gr. The mean and standard deviation of the drop weights are 0.039218 gr and 0.000524 gr respectively. Ultrapure water was used in this experiment using a water purification system (Barnstead Model 7148 Nanopure® ultrapure water system of the Thermo Scientific, Asheville, North Carolina, USA) to reduce the contamination and water impurity as much as possible. The detailed information of the used ultrapure water is presented in Table 11.

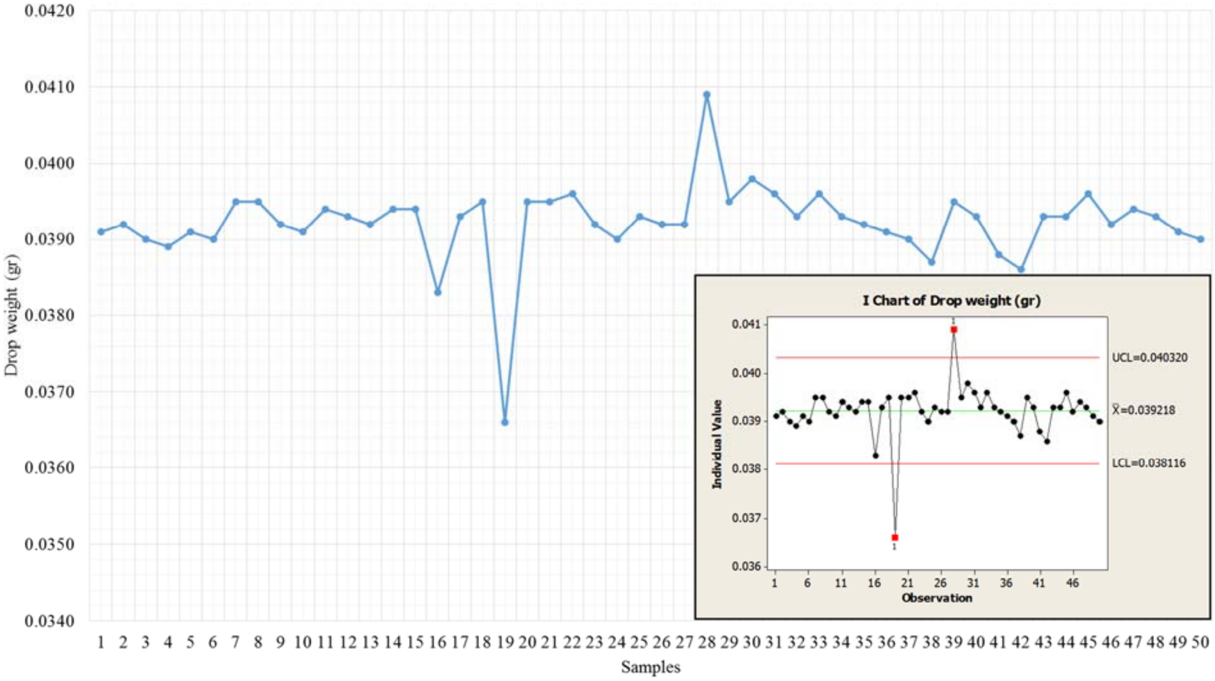

Figure 40 Estimation of operator variability in the manual pipetting process (target drop volume: 40 μm)

Table 11 Ultrapure water quality standards [124]

Test Parameter	Measurement values
Resistivity (25 °C)	>18.18 MΩ·cm
Total Organic Carbon (on-line for <10 ppb)	<1 µg/L
On-line dissolved oxygen	10 µg/L
On-line particles (>0.05 µm)	<200 particles/L
Non-Volatile Residue	0.1 µg/L
Silica (total and dissolved)	0.5 µg/L
Metals/Boron (by ICP/MS)	
22 Most common elements (see F63-0213 **[113]** for details)	<0.001-0.01 µg/L
Ions (by IC)	
7 Major Anions and ammonium (see F63-0213 **[113]** for details)	0.05 µg/L
Microbiological	
Bacteria	<1 CFU/100 mL

The repeatability of the contact angles are evaluated on a smooth surface at a constant condition (i.e., constant drop volume and a constant time of capturing photographs after pipetting). The time for capturing the drops' photograph after pipetting is critical as well due to the evaporation and movements of the drop in different periods of the time [114]. Woodward studied the effects of time on receding and advancing contact angles. It was observed that the advancing contact angles have a negative correlation with time. Receding contact angle increases with time before 25 seconds and then decrease after 25 seconds. Hence, a constant range of time 45 ± 10 s is considered to take the photographs after pipetting [114].

The material used to print the tiles is Objet Vero/white/plus Rgd835, which is a commercial resin provided by Stratasys. The general information of the resin composition ingredients is shown in Table 12 [115].

Table 12 Formulation of Objet Vero/white/plus Rgd835 [39]

Component	Percent
Acrylic monomer	<30
Isobornyl acrylate	<25
Phenol, 4,4'-(1-methylethylidene) bis-, polymer with (chloromethyl)oxirane, 2-propenoate	<15
Diphenyl-2,4,6-trimethylbenzoyl phosphine oxide	<2
Titanium dioxide	<0.8
Acrylic acid ester	<0.3
Propylene glycol monomethyl ether acetate	[0.1, 0.125]
Phosphoric acid	[0.002, 0.015]

An X-ray photoelectron spectroscopy (XPS) spectrum analysis was performed for the material after printing (solidified material) to find out the detailed elemental composition and the contamination at the surface. XPS spectra are attained by X-raying a material with a beam of X-rays while instantaneously measuring the kinetic energy and number of electrons that emit from the top 0 to 10 nm of the material being analyzed [116]. The results of the XPS survey spectrum is presented in Table 13 and shows all elements on the smooth printed specimens. As shown in Table 13, 72.8% of the mole fraction is carbon, 19.3% is oxygen, 5.2% is sodium, 2.4% is sulfur, and 0.3% is calcium. The XPS results depicted in Figure 41 (a) shows that all of the elements exist at their orbital level except for hydrogen.

As shown in Figure 41 (a), an XPS spectrum is a plot of the number of electrons detected per unit time in Y-axis, versus the binding energy of the electrons detected in X-axis. Each element provides a unique characteristic set of XPS peaks at specific binding energy values which detect each item that exists in/on the surface of the material being analyzed. These spectral peaks correspond to the electron configuration of the atoms (e.g., 1s, 2s, 2p, 3s, etc.). The higher the number of the detected electrons in each of the characteristic peaks, the higher mole fraction of an element within the XPS sampling volume. Hydrogen is not detected in the XPS survey, and it is excluded in these atomic percentages [117]. The XPS survey provides the chemical state identification and local bonding of carbon in the cured materials (Figure 41 (b)). As shown in Figure 41 (b), 100% of local bonding for carbon at the binding energy of 285 eV is either $C-C$ or $C-H_x$ which x is the unknown number of hydrogen bonded to carbon. The results (Table 13) show that 92.1% of the tiles are Carbon (72.8%) and Oxygen (19.3) which reveals that less than 8% are impurities or contaminations. The impurities can be somewhat due to the support material attached to the tile and the other contaminations which exist in the environment.

Table 13 XPS survey spectrum for Objet Vero/white/plus Rgd835

XPS Surface Elemental Composition (at mole fraction %)				
C	O	Na	S	Ca
72.8	19.3	5.2	2.4	0.3

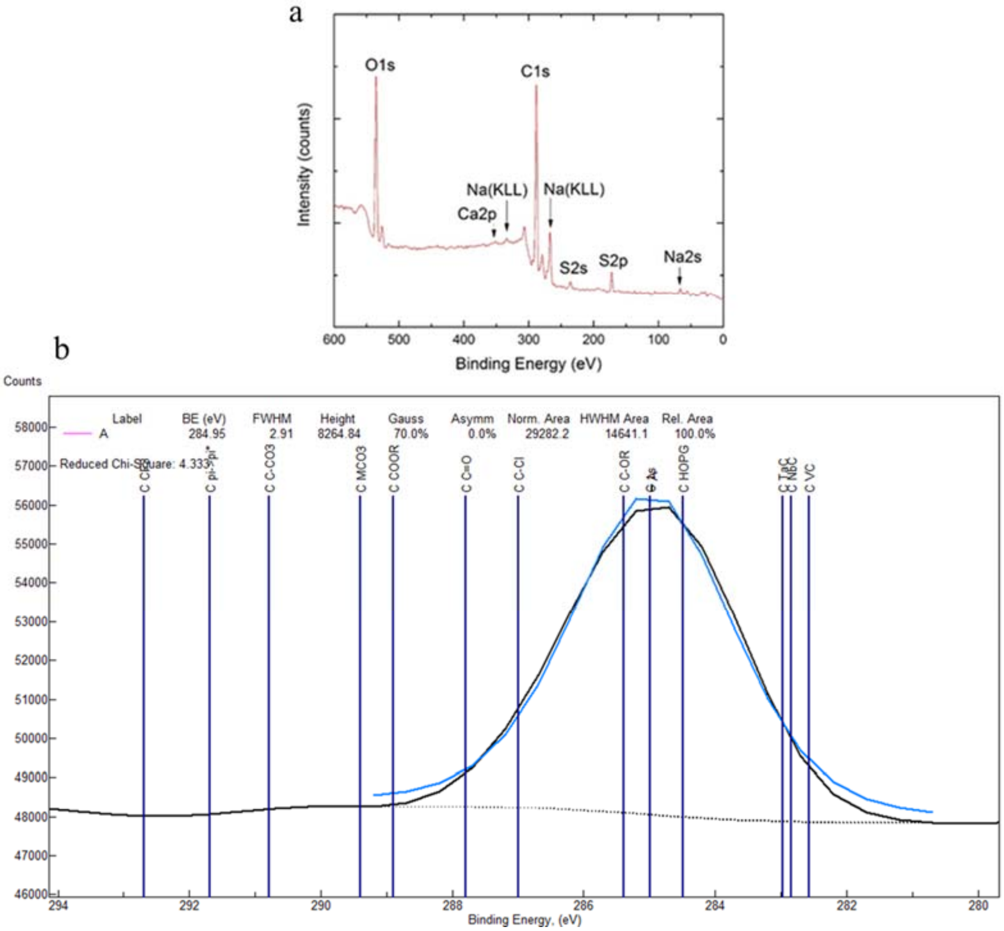

Figure 41 XPS High-Resolution Spectrum, C1s Region (C-C Bonding: 100%)

For each drop, four photographs were taken by the Canon EOS Rebel T5i DSLR camera in the manual mode with shuttle speed of 2 seconds and aperture of F25. Some samples of the photographs with contact angle measurement are shown in Figure 42.

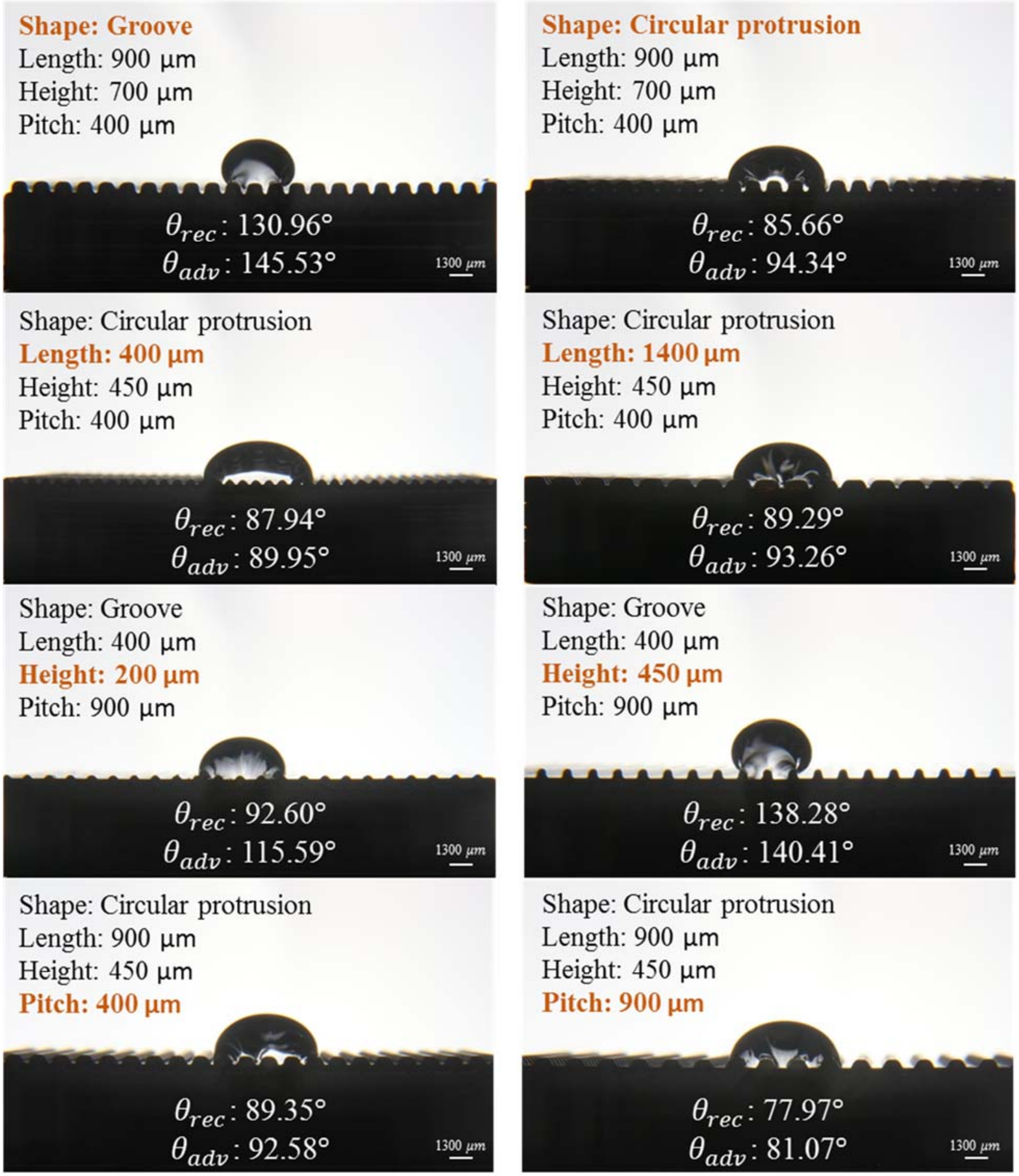

Figure 42 Photographs of selected contact angles measurements

After the photographs were captured by the camera, they were processed with a custom image processing algorithm tool developed in Matlab® for this specific application (Figure 43). This algorithm employs a binary image conversion of the original photo is captured by the camera to a black and white image. Then, a polynomial function with a degree of 6 (Equation 8) is fitted to the boundaries of the drop to calculate the tangent angle on of the drop. Polynomial functions with various degrees (i.e., 2, 3, 4, 5, 6, 7, 8, 9, and 10) have been tested to best fit the drop boundaries; it was found that the degree of 6 has the lowest error among other degrees.

$$\sum_{k=0}^{6} a_k x^k \tag{8}$$

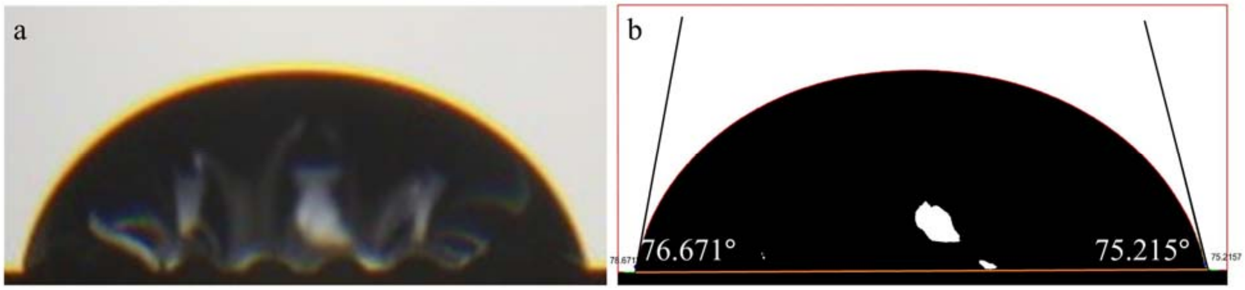

Figure 43 Image processing algorithm (a) photograph and (b) binary processed image

Once the data was obtained from contact angle measurements, a full factorial analysis was performed to study the effects of the geometric parameters and their interactions on receding and advancing contact angles. The results of the full factorial analysis reveal the importance and significance level(s) of each parameter (shape, length or diameter, height, and pitch size) and their interactions. Also, two regression models for receding and advancing contact angle was modeled. These two models would be able to mathematically demonstrate the relationships of the geometric factors of the microtextures and contact angle. Also, the correlations of some other dependent variables such as aspect ratio (length over height), space factor (length over pitch size), roughness factor (surface area over the projected area), and solid area fraction (solid-water interface) were analyzed.

4. Results

Homogeneity tests were performed on both receding and advancing contact angle to examine the normality of measured data. The results show that both receding and advancing contact angles are statistically normal at the $p<0.05$ level.

Two full factorial analyses were performed on both receding and advancing contact angles to analyze the effects of studied geometrical factors at all levels on contact angle.

The results (Table 14) of full factorial analysis on receding and advancing contact angles indicate that all considered factors: (shape, length, height, and pitch size) are significant at the $p<0.05$ level for a total of nine replicates (three replicates of tiles and three contact angle measurements). The effects of each factor on receding and advancing contact angles can be seen in Figure 44 and Figure 45 respectively. As Figure 44 and Figure 45 show, the effects of factor shape are much more significant compared to other factors.

Table 14 Full factorial results on contact angles

Factor	Receding contact angles			Advancing contact angles		
	Degree of freedom	F-value	P-value	Degree of freedom	F-value	P-value
Shape	1	894.27	<0.001	1	890.13	<0.001
Length	1	10.92	<0.001	1	11.91	<0.001
Height	1	19.79	<0.001	1	18.89	<0.001

Pitch	1	12.69	<0.001	1	13.79	<0.001

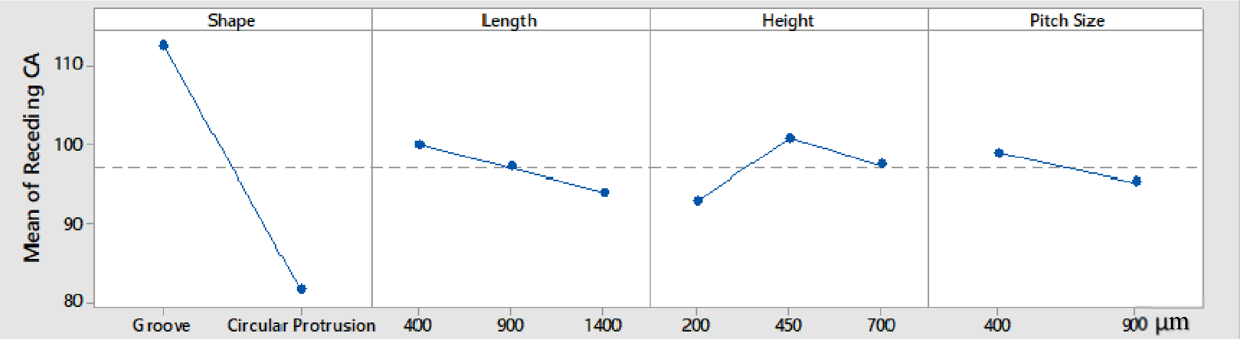

Figure 44 Effects plot on the receding contact angles

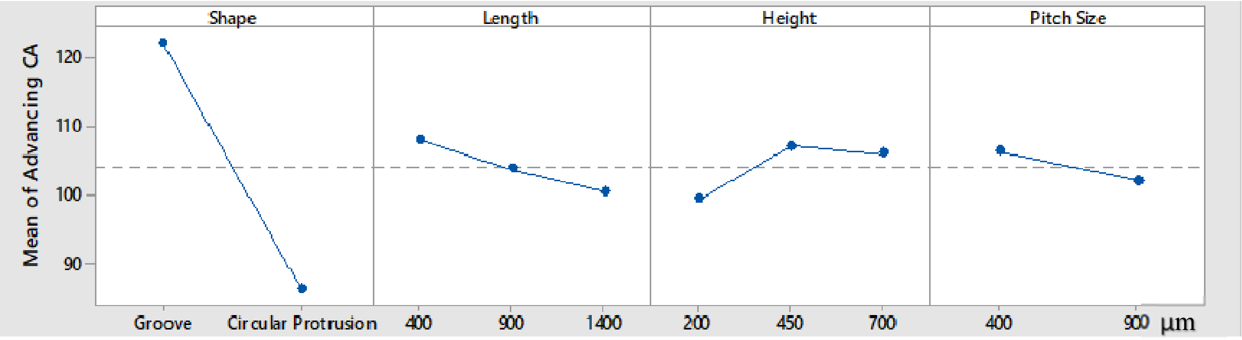

Figure 45 Effects plot on the advancing contact angles

To compare the effectiveness of factors, a set of levels (i.e., shape: circular protrusion, length: 900 µm, height: 450 µm, and pitch size: 900 µm) have been considered as a reference. Six alterations were performed (Figure 46) to watch the changes in receding and advancing contact angles. At each time just one factor changes and the other factors kept constant. Figure 47 shows that the changing the level of shape factor from circular protrusion to groove has the greatest effect (~47%) on receding and advancing contact angles. The values are the average of nine replicates. After shape factor, changing the level of height factor from 450 µm to 700 µm results in the most changes (~17%) on receding and advancing contact angles.

Figure 46 Effects of changing from the reference level

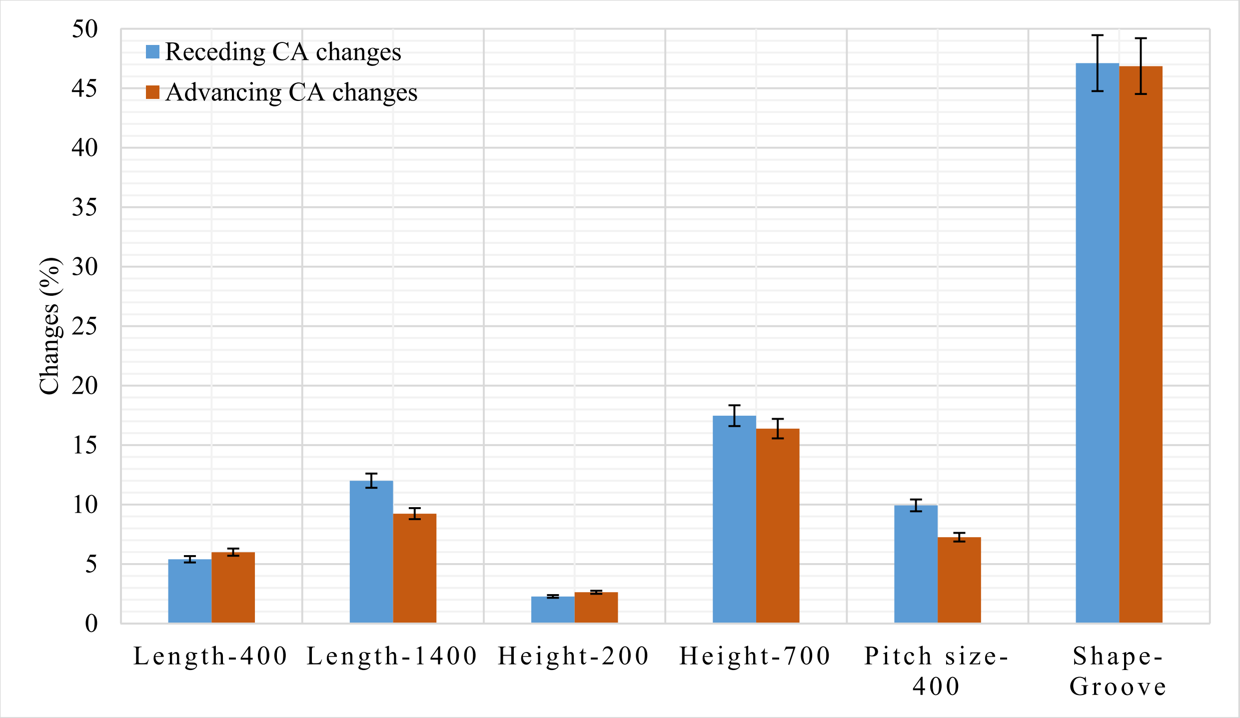

Figure 47 Effects of changing from reference level in all factors

The interactions of factors are found statistically significant on receding contact angle at all levels of two-way (F (13, 288) =14.28, $p<0.001$), three-way (F (12, 288) =8.83, $p<0.001$), and four-way (F (4, 288) =2.99, $p=0.019$) interactions at the $p<0.05$ level. Figure 48 shows the plots of two-way interactions between the factors on the receding contact angles.

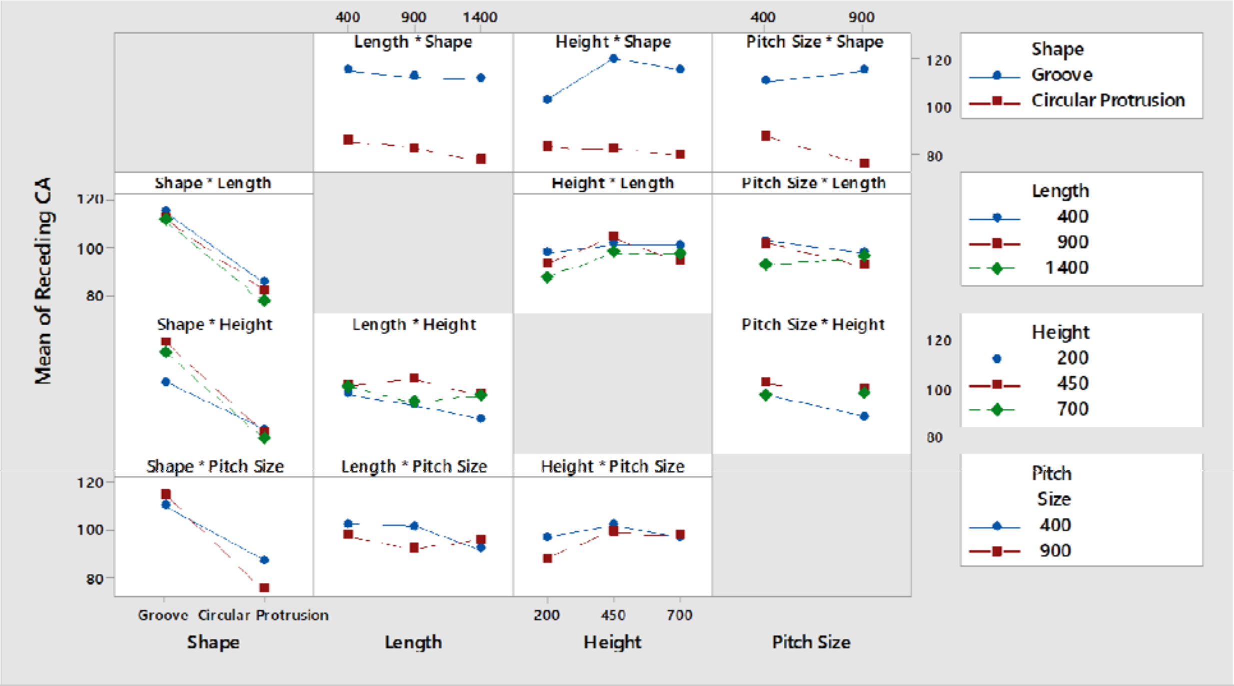

Figure 48 Two-way interaction plots on the receding contact angles

The interactions of factors are found statistically significant on advancing contact angle at levels of two-way (F (13, 288) =10.83, $p<0.001$) and three-way (F (12, 288) =7.89, $p<0.001$) interactions at the $p<0.05$ level. The four-way interaction is not significant (F (4, 288) =1.75, $p=0.139$). Figure 49 shows the plots of two-way interactions between the factors on the advancing contact angles.

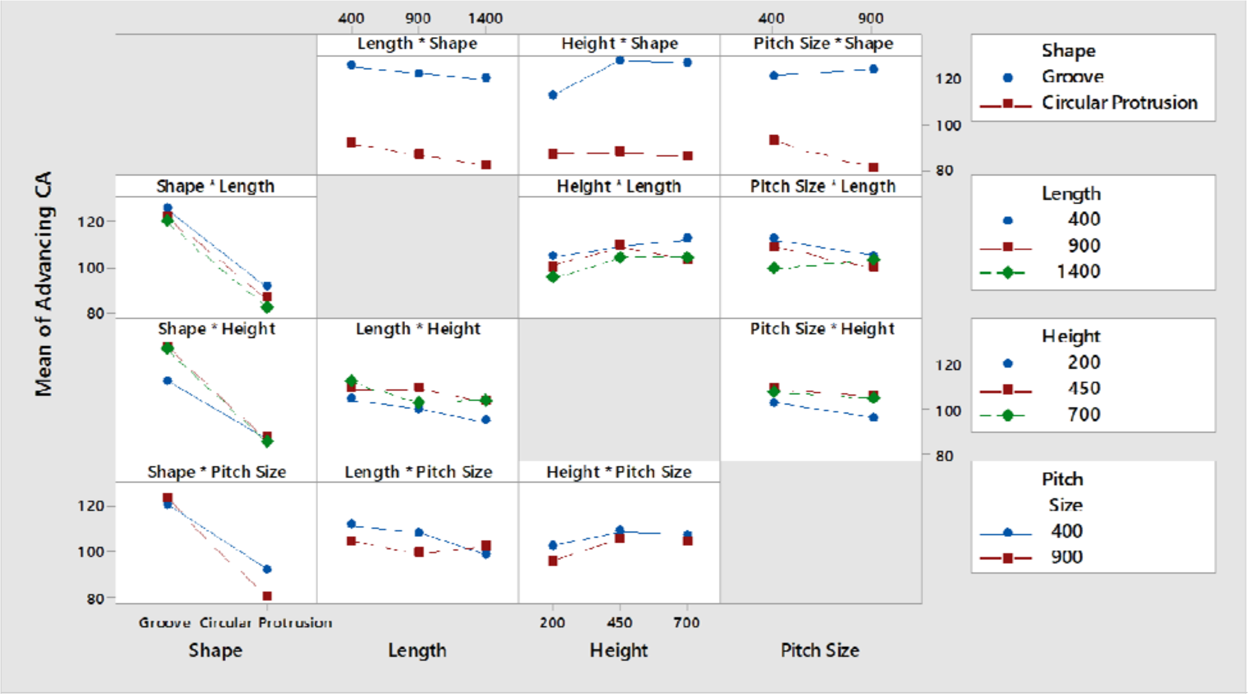

Figure 49 Two-way interaction plots on the advancing contact angles

The main effects and interactions of the factor shape with other factors reveals that regardless of the levels of length, height, and pitch size, the groove patterned surfaces have higher receding and advancing contact angles comparing to the circular protrusion patterned surfaces. Both groove and circular protrusions followed a decreasing trend as the length of the shapes increased. The interaction of shape with height on both receding and advancing contact angles shows that circular protrusions have a slightly decreasing trend, while for the groove pattern the height 450 µm has higher contact angles than heights of 700 and 200 µm. The interaction of shape with pitch size shows opposite trends. The groove patterns have higher contact angles of 900 µm pitch size, while the circular protrusions have higher contact angles on 400 µm pitch size.

The interaction of length with height shows that for the length 400 µm, the heights of 700 µm, 450 µm, and 200 µm have the highest to lowest contact angles, respectively. For the length 900 µm, the heights of 900 µm, 1400 µm, and 400 µm have the highest to lowest contact angles respectively. The interaction of length and pitch size indicate that for the lengths 400 µm and 900 µm, the pitch size 400 µm has higher contact angles, while for the length 1400 µm, the pitch size 900 µm has higher contact angles.

The interaction of height and pitch size indicate that for all heights of 200 µm, 450 µm, and 700 µm, the pitch size of 400 µm has higher contact angles.

Two two-sample t-tests were performed on both receding and advancing contact angles to compare the levels of the shape factor (i.e., groove and the circular protrusions). The results indicate that shape groove has higher contact angles than the circular protrusion at $p<0.05$ level for both receding (p-value=0.000) and advancing (p-value=0.000) contact angles (Figure 50). Figure 50 shows that receding and advancing contact angles have the same trend and there are apparent differences between receding and advancing contact angles of groove shape and circular protrusion regardless of the levels of other impacting factors (i.e., length, height, pitch).

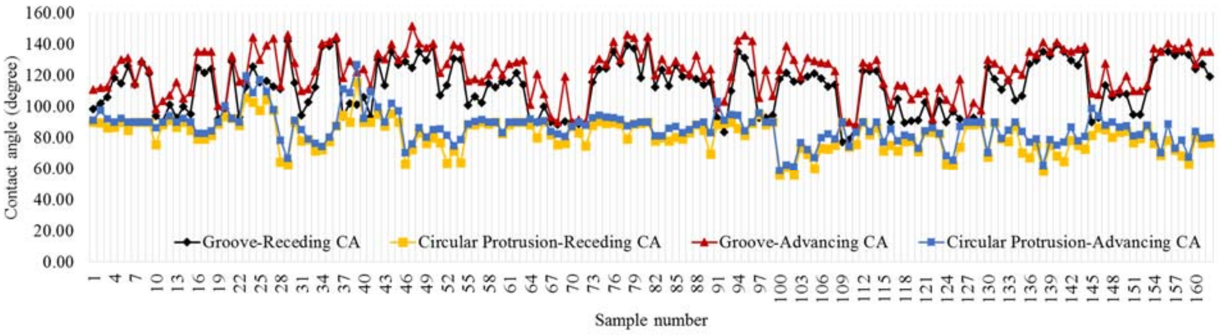

Figure 50 Receding and advancing contact angles data for both groove and circular protrusion for totally 162 samples

Tukey and Fisher tests were performed to compare the three levels (i.e., 400 µm, 900 µm, and 1400 µm) of the length factor on both receding and advancing contact angles. The results of the Tukey test indicate that there are no significant differences between the means of the levels at the $p<0.05$ for receding contact angles. For advancing contact angles, the level 400 µm is significantly more hydrophobic than the level 1400 µm. No differences were found between the pairs of [400 µm, 900 µm] and [900 µm, 1400 µm] for advancing contact angles.

On the other hand, the results of Fisher test show that the level 400 µm has a significantly higher contact angle than the level 1400 µm for both receding and advancing contact angles (Figure 51). No differences were found between the pairs of [400 µm, 900 µm] and [900 µm, 1400 µm].

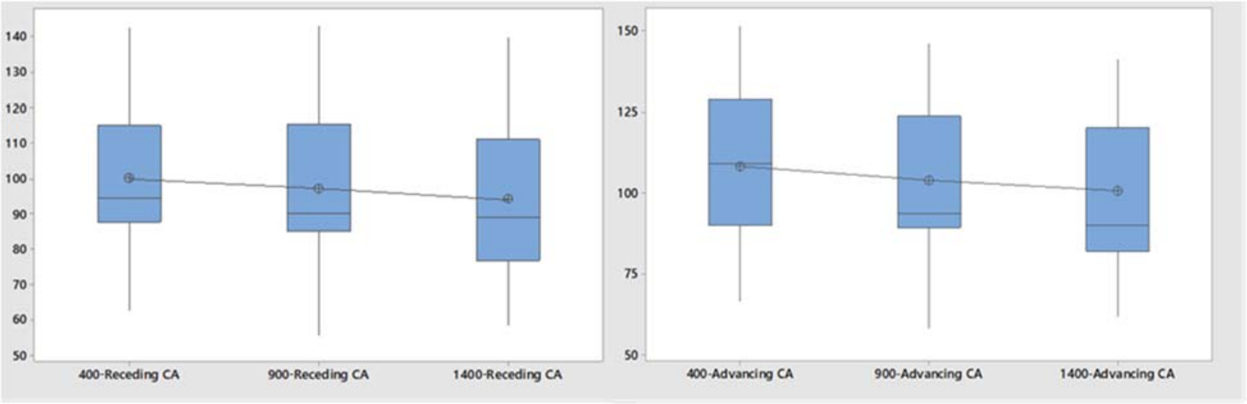

Figure 51 Box plot for levels of the factor length on both receding (left) and advancing (right) contact angles

Tukey and Fisher tests were performed to compare the three levels (i.e., 200 µm, 450 µm, and 700 µm) of the height factor on both receding and advancing contact angles. The results of both Tukey and Fisher tests show that there are significant differences between the means of levels 200 µm and 450 µm at the level of $p<0.05$ on both receding and advancing contact angles. No differences were found between the pairs of [200 µm, 700 µm] and [450 µm, 700 µm] (Figure 52) on both receding and advancing contact angles.

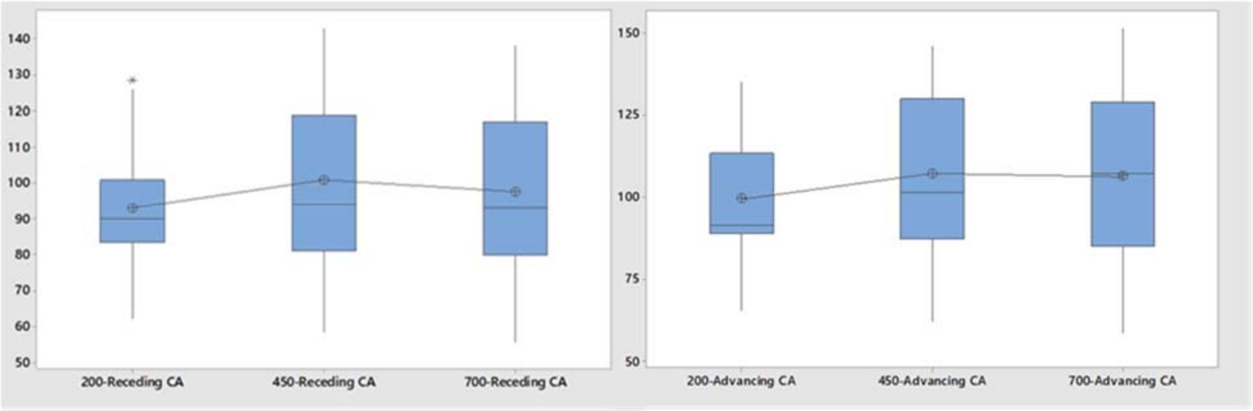

Figure 52 Box plot for levels of the factor height on both receding (left) and advancing (right) contact angles

Two sample t-tests were performed on both receding and advancing contact angles to compare the levels of the pitch size factor (i.e., 400 µm and 900 µm). The results show that there are no significant differences between the levels of the pitch size for both receding (p-value=0.105) and advancing (p-value=0.08) contact angles at the $p<0.05$ level (Figure 53).

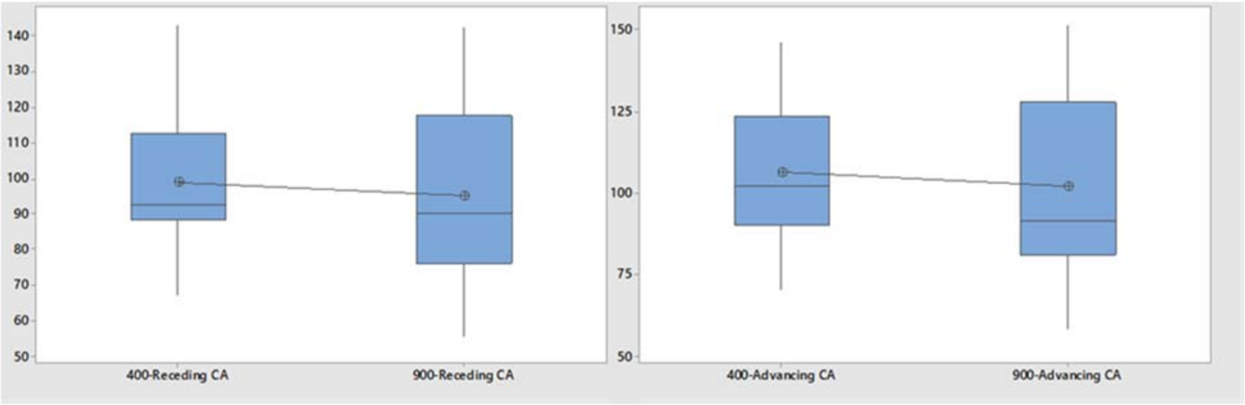

Figure 53 Box plot for levels of the factor pitch size on both receding (left) and advancing (right) contact angles

The correlation between the receding and advancing contact angles, with the value of roughness factor (*r,* surface area over the projected area), solid area fraction (solid-water interface area), aspect ratio (length over height), and space factor (length/pitch size) have been analyzed. Figure 54 shows the plots of receding and advancing contact angles versus roughness factor, *r,* and solid area fraction. The results show that there are statistically significant correlations between the receding (R=0.574, p<0.001) and advancing (R=0.598, p<0.001) contact angles with solid area fraction at a significant level of α=0.05. As it can be seen from Figure 54, as solid area fraction is increasing, both receding and advancing contact angles are increasing. The correlation of advancing contact angle with roughness factor is not statistically significant but close to significant level (R=0.324, p=0.054). Also, the correlation of receding contact angle with roughness factor is not statistically significant (R=0.269, p=0.113). The correlation of receding (R=-0.203, p=0.235) and advancing (R=-0.216, p=0.206) contact angles with aspect ratio are not statistically significant. Also, the correlation of receding (R=-0.023, p=0.892) and advancing (R=-0.035, p=0.841) contact angles with space factor are not statistically significant.

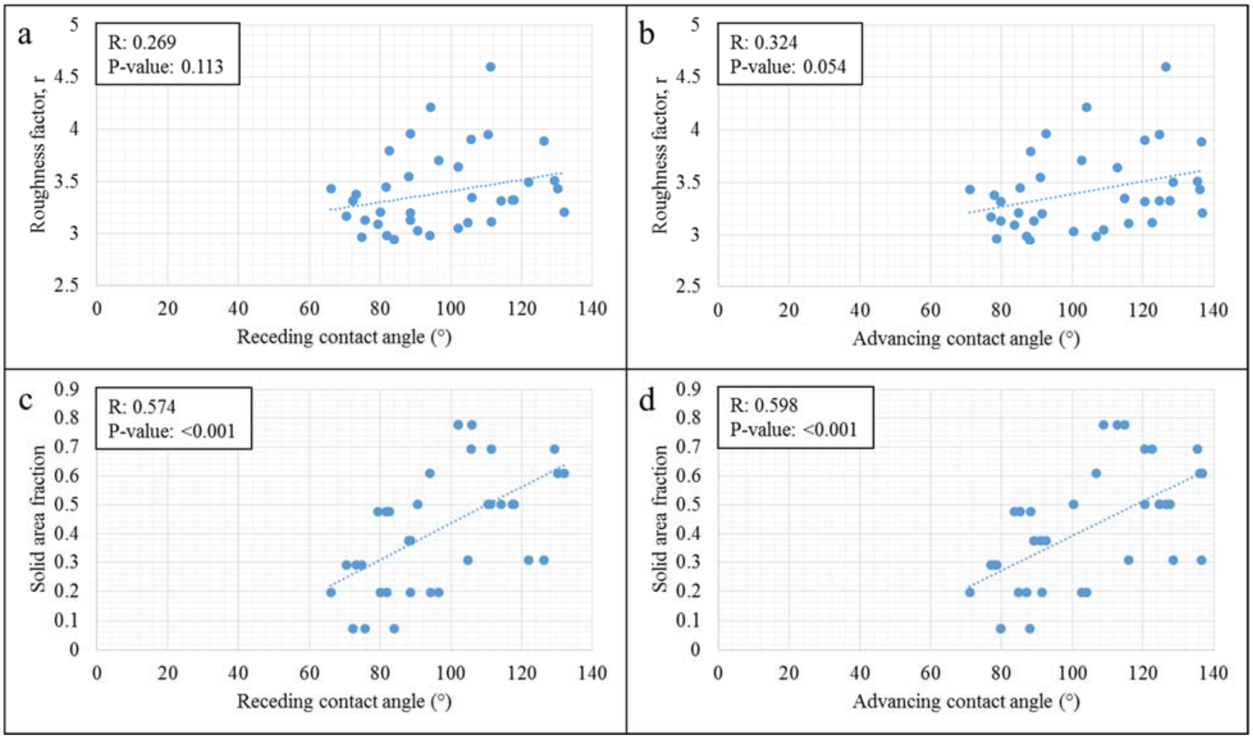

Figure 54 Plot of receding and advancing contact angles versus roughness factor, *r,* and solid area fraction

Figure 55 shows the solid area fraction trend based on shape (Figure 55 (a)), length (Figure 55 (b)), and pitch size (Figure 55 (c)). As Figure 55 shows for the same level of pitch size, length, and height grooves have higher solid area fraction. Length and pitch size have a positive and negative correlation with solid area fraction respectively.

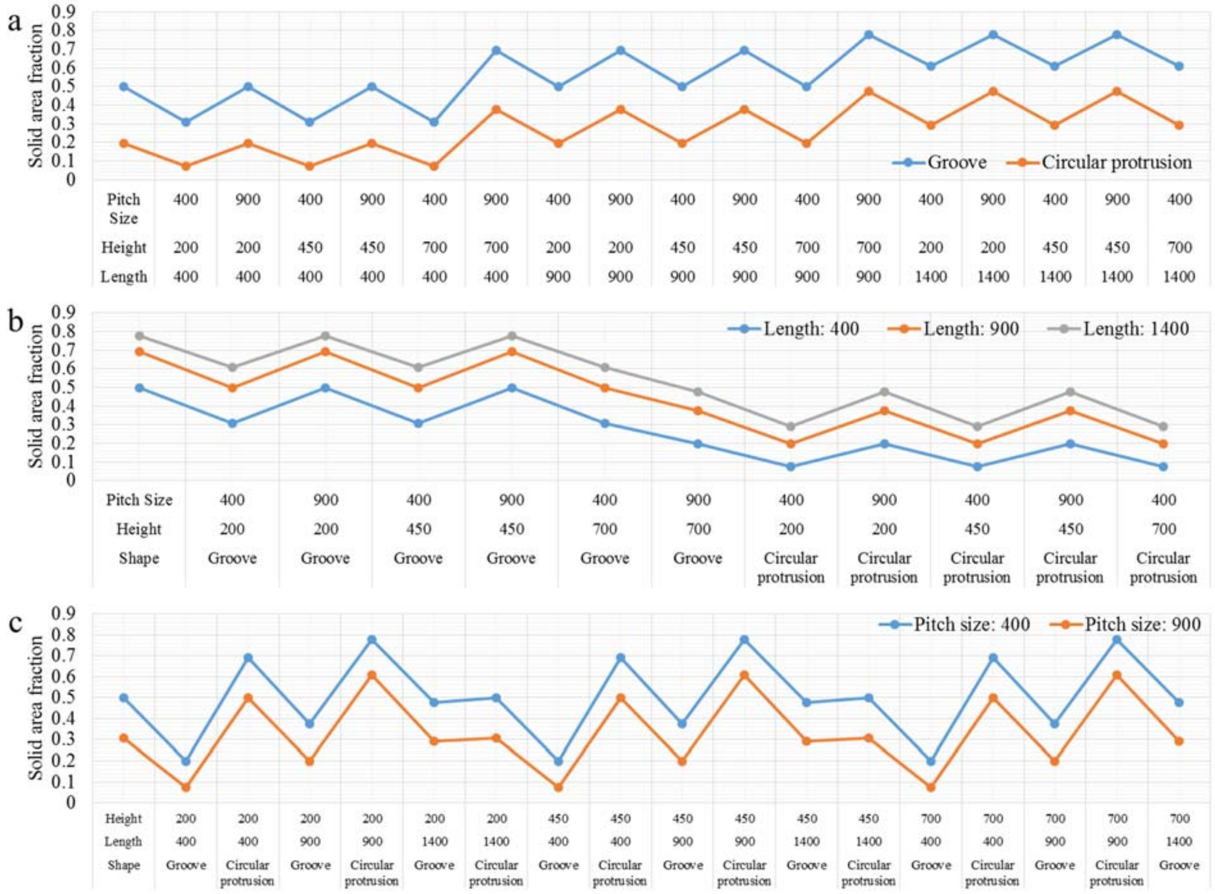

Figure 55 Plots of solid area fraction versus geometrical factors: shape (a), length (b), and pitch size (c)

5. *Discussion*

Contact angle hysteresis occurs when the strength of the defect is beyond a certain threshold due to irregularities (i.e., surface roughness and non-homogeneous contamination of the surface) of the solid surface [118]. In macroscopic scale, contact angles are key in determining the wettability and then estimating the wetting behavior of the same material structure in another geometry or technological process. While on a microscopic scale, contact angles are extensively employed to characterize the surface chemistry [119]. The microscopic contact angle is characterized by the intermolecular forces close to the contact line between the molecules of the liquid and the solid surface [120]. Based on the Young equation, the microscopic contact angle on homogeneous surfaces is independent of the macroscopic size and shape of the fluid body. For a system in static equilibrium, this is not true due to the existing differences in the system that changes both the volume of the liquid phase as well as the interfacial energies entering the Young equation and controlling the contact angles. In reality, equilibrium may be very difficult to attain: curved liquid-vapor interfaces must be in equilibrium with any flat liquid-vapor interfaces in the experimental system, precursory layers can grow gradually and may never reach equilibrium [119].

In heterogeneous surfaces (surfaces with variant chemistry and/or roughness), the microscopic contact angle differs across the surfaces. The spatial variations of the contact angle distort the liquid-vapor interface [119]. Figure 39 compares images of distorted and undistorted liquid-vapor interfaces near the contact line.

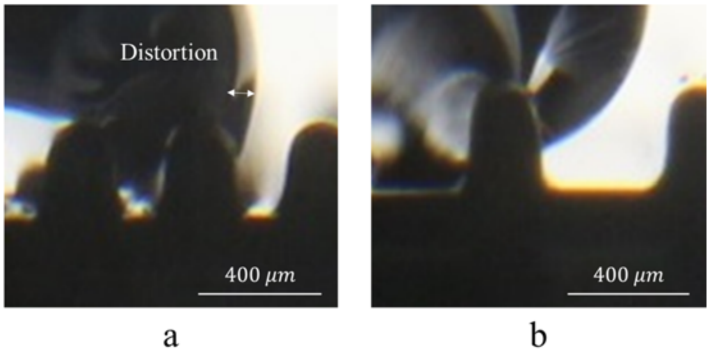

Figure 56 Liquid meniscus (water). (a) Distorted contact line and liquid-vapor interface. (b) Smooth contact line and liquid-vapor interface

The results of full factorial analysis on receding and advancing contact angles indicate that all factors including, shape, length, height, and pitch size are statistically significant. The results show that the factor shape is the most effective factor on both receding and advancing contact angles. In

Figure 58, the liquid/vapor interfaces are drawn straight, due to the constant radius of curvature of the drop, which is much larger than the size of the texture. The existence of such interfaces below the drop is due to possible pinning on the corners of the features (i.e., groove and circular protrusion). In general, such pinning is possible on textured surfaces, providing that it is sufficiently rough. The contact angle discontinuously moves to a value close to π (but smaller) as soon as air trapping is possible, and then fluctuates very slowly. A complete drying cannot be achieved by texturing a surface [121]. In the hydrophilic case ($\theta < \frac{\pi}{2}$), the solid can be assumed as a kind of porous material, in/on which the liquid can be absorbed (Figure 57 (a)) [122]. This is a rather particular imbibition, since this porous material is close to be 2D (unlike usual 3D porous media). In other words, the surface is experiencing porous condition and the body of the specimens is experiencing solid condition [121]. Thus, a liquid-air interface develops during the imbibition which is called hemi-wicking, since it is intermediate between spreading and imbibition. Therefore, the condition is between the spreading (θ=0) and imbibition ($\frac{\pi}{2}$) criteria. If a small amount of liquid is sucked into the texture (Figure 57 (b)), the remaining drop sets on a patchwork of solid and liquid. This case has similarities to the super-hydrophobic condition, except that here the vapor phase below the drop is replaced by the liquid phase. Therefore, it can be concluded that the value of the contact angle is highly dependent on texture design and this is the capability of a textured surface that can drive a liquid and tune its shape [121].

Figure 57 Texture design tuned the surface into hydrophilic (a) and hydrophobic (b) cases

For a given surface composition and liquid (i.e., fixing θ), the nature of the texture (which determines r (roughness factor) and solid area fraction decides the wettability conditions of the surface. In general, both roughness factor and solid area fraction deeply intricate, and solid area fraction may depend on contact angle. In the hydrophobic case (Figure 57 (b)), if the contact line can pin on the texture, a super-hydrophobic behavior can be generated, of obvious practical interest: a drop does not stick on such a surface and can be easily removed [121]. This phenomenon was observed in grooves (Figure 56). Grooves also due to existing walls on both sides of the drop traps the air and the water more compared to the circular protrusion and generate a hydrophobic behavior.

In the hydrophilic case (Figure 57 (a)), the drop either follows the topography, which significantly decreases the contact angle, or it spreads inside the solid texture. Then it coexists with the solid filled with liquid. There again, the contact angle is decreased, but remains strictly larger than zero in a situation of partial wetting, because of the presence of emerged islands [121].

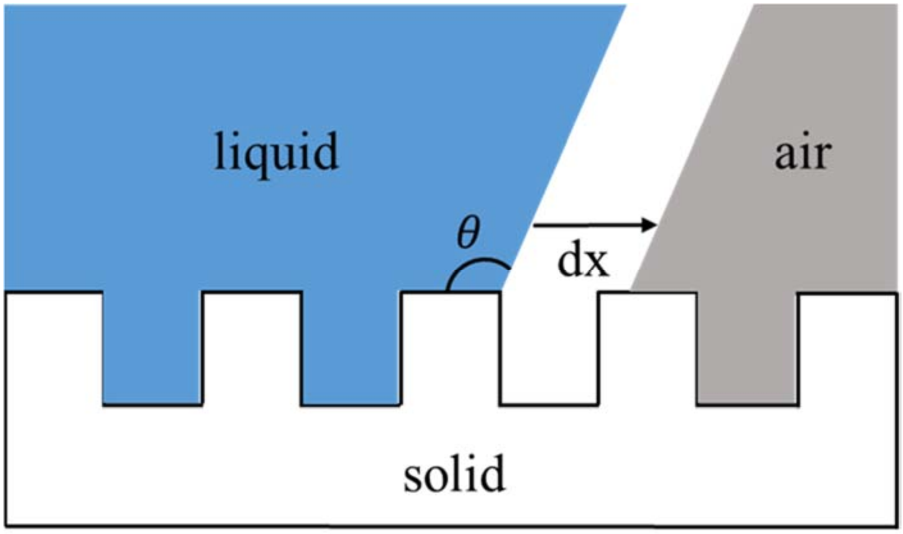

Figure 58 Liquid deposited on a model surface with texture: for contact angles larger than $\frac{\pi}{2}$, air is trapped below the liquid including a composite interface between the solid and the drop

Results (Figure 54) indicated that there are positive correlations between receding and advancing contact angles with solid area fraction. This effect can be attributable to the increase in pinning as the solid area fraction increases [94]. As Figure 55 shows, with the same level of pitch size, length, and height, grooves textures have higher solid area fraction. Length and pitch size have positive and negative correlations with solid area fraction respectively.

The interactions of factors are found statistically significant on both receding and advancing contact angles at levels of two-way and three-way interactions. The interaction of the factor shape with other factors reveals that regardless of the levels of length, height, and pitch size the groove patterned surfaces have higher receding and advancing contact angles compared to the circular protrusion patterned surfaces. This means that even the interactions between the geometrical parameters significantly affect the wetting behavior of the textured surfaces and up to three-way interactions show significant effects on contact angles.

Both groove and circular protrusion following decreasing trend as the length of the shapes are increased. The results show that the level 400 µm is significantly more hydrophobic than the level 1400 µm for both receding and advancing contact angles. No differences found between the pairs of [400 µm, 900 µm] and [900 µm, 1400 µm]. The main reason for this phenomena is that in textures with lower length the air is being trapped more under the drop causing more hydrophobic behaviors.

The results show that there are significant differences between the means of levels 200 µm and 450 µm for the height factor at the level of $p<0.05$ for both receding and advancing contact angles. The observations and the statistical results indicate that the textures with a height of 450 µm generate more hydrophobic behavior than 200 µm.

6. Conclusion

This study reveals that the wetting behavior is highly dependent on the texture design. In addition, the geometrical parameters of the design such as shape, length, height, and pitch size significantly affect the contact angle. The shape was the highest impact factor among the geometrical parameters on contact angle the results indicated that groove design is strongly more hydrophobic than circular protrusion textures. In grooves, the contact line pins on the texture which causes a hydrophobic behavior generates. Also due to existing walls on both sides of a drop in grooves, the air and water are trapped more compared to the circular protrusion and increase the contact angles.

Chapter III

Characterizing Material Jetting Processes

1. Introduction

Numerous studies have analyzed the surface finish of AM technologies such as Fused Deposition Modelling (FDM) [123], Laminated Object Manufacturing (LOM) [124], stereolithography (SL) [125], [126], Selective Laser Sintering (SLS) [127], Selective Laser Melting (SLM) [128], Electron Beam Melting (EBM) [128], and High Speed Sintering (HSS) [129].

To date, there are very few efforts that have aimed at the surface finish and dimensional accuracy in material jetting processes [12], [130]. Khoshkhoo et al. [14] proposed a method to generate pseudo-randomized surfaces with certain surface characteristics with specific S_{mr}, S_a, and S_v values). Surface metrology parameters (i.e., S_{mr}, S_p, S_{ku}, S_{sk}, S_z, S_q, S_a, and S_v) are used to test the fidelity of the proposed method. Their results showed that the accuracy of metrology parameters are varied depending on the resolution of the machine in different axes. Among selected metrology parameters for validation process, S_{mr} had the lowest average error (5.7 %), while S_v and S_a had the highest average error (33.8 %). Carrano et al. [13] studied natural surfaces (rocks) to understand and engineer desired surface topography with material jetting processes for biofilms in biological applications.

There are many design guidelines available that address surface finish and dimensional accuracy in AM processes. These studies (Campbell [131]) suggest minimum wall thicknesses, clearances, and angles for features such as pins, holes, bosses, threads, and overhangs for powder bed fusion and fused deposition processes, or for better surface roughness, mechanical properties or lower fabrication cost or time [131], [132]. Phan and Masood [133] tested spherical and prismatic protrusions to evaluate the accuracy level and surface roughness of the FDM process. Different nozzle tip sizes were used in this study, which concluded that both tip size and build orientation affect the dimensional accuracy and surface finish.

Other efforts have targeted the effects of size, build orientation, and build location on the dimensional accuracy of flat surfaces of material jetting processes. It was found that the surface finish is affected by build orientation and size of the specimen, whereas part location has a smaller influence. It is recommended that XY orientation (parts' longest dimension along the printing head direction) has the best dimensional accuracy [3, 18]. Udroiu et al. [134] studied the effects of build type (glossy and matte), and Kumar et al. [135] investigated the effects of surface slope on the average roughness of fabricated specimens in a Polyjet process, respectively. It is shown that both build type and surface slope significantly affect the average roughness of fabricated specimens.

However, there are very few studies available to provide design guidelines for material jetting processes. Meisel and Williams [136] studied minimum resolvable feature size and the self-supporting angle in the absence of support material to establish a set of design for additive manufacturing (DfAM) guidelines for material jetting [136]. This study suggests some design guidelines, including channels and holes, should be larger than 50 mm^2 and minimum resolvable feature sizes should be larger than 0.897 mm in diameter. It was also found that orientation was a statistically significant factor and that to achieve the minimum self-supporting angle, critical angled faces should be oriented in the YX direction in the build tray. Several other studies [12]–[14], [130] have pushed the fabrication limits on resolvable feature sizes but have stopped short of proposing quantitative guidelines.

Stair-stepping is one of the major artifacts on the printed surfaces due to sloping part features. The stair-stepping effect happens when a surface orientation is not orthogonal to the axis of the source of energy. This study aims at uncovering the effects of stair-stepping on surface parameters. Also, there currently is a need for understanding and quantifying the conditions that affect surface finish and dimensional accuracy produced with material jetting technologies. This work aims at understanding the impact of surface angle and build orientation parameters in material jetting additive manufacturing on surface finish and dimensional accuracy. The contributions of this effort include laying the foundation for design guidelines for material jetting technology that will benefit the user community and industry.

This study is also intended to investigate the capability of the material jetting machine to find out how small and well it can print. This study also tried to present a method to quantify the quality of the final specimens of the material jetting processes and show how quality changes in a wide range of sizes for different designed features. The goal and the evaluation method presented in this work can be applied in other additive manufacturing processes as well to assess the minimum feature size and the quality of the printed features under different conditions.

Dimensional distortion is defined as an alteration of the nominal part geometry and can be the consequence of various factors, including shrinkage of the resin during the solidification process, uneven heat dissipation, and others. In some instances, the solidification of newer layers may cause curl or warpage in previously cured layers that lie directly underneath [137]. Dimensional distortion is especially pervasive among photopolymerization processes, including those supporting additive manufacturing. Thus it is critical that an understanding of the conditions that cause (or minimize) such distortion be developed and disseminated. The objectives of this work are to understand which factors affect the distortion on parts fabricated with material jetting and to quantify the type and amount of distortion under various conditions.

Several previous efforts have investigated the mechanical properties and surface quality of specimens manufactured with material jetting processes. These addressed mechanical properties such as fatigue behavior, fracture toughness, surface roughness, tensile and compressive strength, and general anisotropy derived from build orientation [138]–[143]. Also, other available works investigated the effects of aging on mechanical properties in specimens fabricated by material jetting processes [144]. However, none of these efforts have specifically aimed at understanding distortion in material jetting processes.

The available scientific literature on the causes of distortion in the broader additive manufacturing domain is also very limited. Vatani et al. (2012) modeled distortion on stereolithography (SL) parts using classical lamination theory [145]. In this study, it was found that distortion has negative correlations with both specimen and layer thickness, with the magnitude of distortion increasing exponentially as the layer thickness decreased. Huang and Jian (2003) proposed a model of curl distortion on SL parts using finite element methods, finding that when the build orientation is performed with shorter rasters (print direction along the shorter dimension of the specimen in the build tray), there is less curl distortion than when performed with longer rasters [146]. Tröger et al. (2008) analyzed the effect of thermal and humidity aging of acrylate-based resins on distortion for parts manufactured with SL [147]. The studies of both Huang and Jian (2003) and Tröger et al. (2008) agree that distortion increases with higher exposure energy and lower layer thickness. El-

Sherif (2015) characterized process factors (i.e., scan speed, exposure energy, hatching space, curing depth, critical exposure, and depth penetration) on dimensional errors such as distortion, creep and warpage in the curing process of photopolymerization in SL process. The exposure energy and scan speed were found to assist in moderating distortion: lower scan speed increased the exposure time and resulted in less severe distortion [148]. Huang and Lan (2006) studied the effects of scanning properties such as pattern, length, and width on curl distortion, showing that curl distortion varies directly with scanning length (raster) [132]. There has also been research on reducing distortion through hatching patterns in stereolithography. These include variations of hatching methods [149] and their parameters [115], [150], [151]. These findings, however, are not directly applicable to the material jetting processes because their curing process is unidirectional and follows the UV light path.

Despite the paucity of research on specimen distortion in material jetting processes, other efforts on fundamental stress formation on thermoplastics offer valuable insights. When studying layered thermoplastic composites, Parlevliet et al. (2006) found that the main residual stress direction was orthogonal to the primary orientation of the deposited layers and suggested this was a consequence of unequal thermal dissipation gradients along different orientations. Monzon et al. (2017), while investigating the anisotropy of tensile and flexural properties in several acrylate-based photopolymers using digital light processing (DLP), found that the build orientation was significant only when the resin had not been fully cured and that this difference disappeared after the post-curing process had taken place [152].

The material jetting processes and technologies have achieved relative maturity and technological readiness for a number of applications, including dental, biomedical, and aerospace among others. The interlayer bonding and densification from these processes are excellent, and with layer thicknesses under 30 µm for most commercial embodiments, the feature resolution of this technology is conducive to applications that require a high level of detail. However, there are no general design guidelines available that address flatness and distortion. Other efforts (Campbell, 2015) have disseminated AM process guidelines that suggest minimum wall thicknesses, clearances, and angles for features such as pins, holes, bosses, threads, and overhangs for powder bed fusion and fused deposition processes, or for better surface roughness, mechanical properties or lower fabrication cost or time [132]. Other design guidelines and decision support tools have been developed specifically for SL [131], [152], [153] and selective laser sintering [131] but none to date on material jetting processes.

There are very few design guidelines available for material jetting processes [136]. Meisel and Williams (2015) investigated minimum resolvable feature size, and the self-supporting angle in the absence of support material to establish a set of design for additive manufacturing (DfAM) guidelines for material jetting [136]. This study offers some preliminary design guidelines. They include channels and holes, which should be larger than 50 mm^2 and minimum resolvable feature sizes should be larger than 0.897 mm in diameter. It was also found that orientation was a statistically significant factor and that to obtain the minimum and most consistent self-supporting angle, critical angled faces should be oriented in the y-direction in the build tray. Several other studies [12]–[14] have pushed the fabrication limits on resolvable feature sizes but have stopped short of proposing quantitative guidelines.

There currently is a need for understanding and quantifying the conditions that cause distortion on specimens produced with material jetting technologies as well as to quantify the severity of distortion. This work aims at understanding the impact of part thickness and build orientation parameters in material jetting additive manufacturing on specimen distortion. The contributions of this effort include laying the foundation for design guidelines for material jetting technology that will benefit the user community and industry.

Many studies have investigated the effects of different printing setups on surface finish and mechanical properties (e.g., such as tensile strength, hardness, fatigue, etc.) of final specimens, but there has been no published work on printing setup factors (i.e., specimen thickness and build orientation) on distortion. This work attempts to fill this gap in additive manufacturing studies. Since the considered factors are common and controllable in all additive manufacturing processes, the outcome of this study can be applied to printing setups of other polymeric additive manufacturing processes as well to reduce the distortion and warpage of the final specimens.

2. *Minimum Feature Size Analysis of Material Jetting Processes*

2.1. *Materials and Methods*

Finding the smallest feature size achievable has always been a concern of different AM technologies. The factors that affect the minimum achievable size of various AM machines depend on different methods and operation principles. The size of the nozzle, types of materials, layer thickness, and resolution of motion motors in all three axes are a few of the main factors that define the accuracy of the machine [154]. The Material jetting machine from Stratasys has a resolution of 42 µm in X and Y direction, while the specified layer thickness is 28 µm. This study aims to explore the limits of the Material jetting's dimensional accuracy when printing different texture types. For this purpose, four different designs (spherical and square protrusions and holes) have been modeled in Solidworks® to be fabricated by Material jetting machine.

Figure 59 shows the specimen designed for this experiment. Three replicates of each specimen have been fabricated by the best possible surface finish option ("Glossy"). The "Glossy" surface finish is the option that the printer fabricates the specimens with no supports on top of the surface (if possible, based upon the design). This can be performed with the printer's setting before the printing process. The height and depth of designed features vary from 12.5 µm to 800 µm. The length and diameter of 72 designed features are varying from 25 µm to 1600 µm at 5 mm intervals. All replicates are fabricated in same position and orientation (specimen's longest dimension along the X-axis) in the build tray.

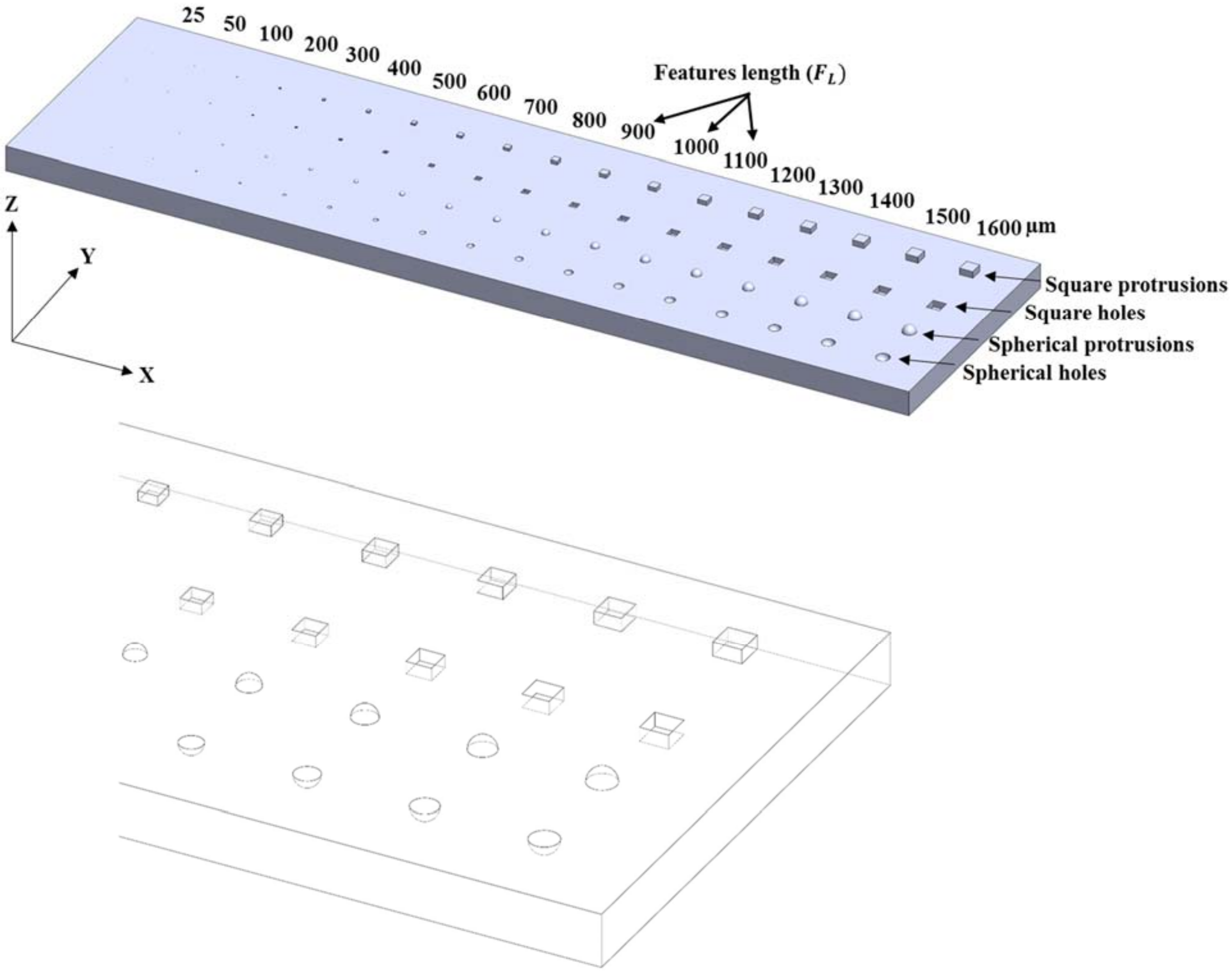

Figure 59 Solidworks model of the test specimen for the minimum feature

For this experiment, both dimensional accuracy measurements and shape analysis have been performed in all three axes where X and Y lie on the printing plane, and Z is the build axis normal to the plane (Figure 59). For assessing the dimensional accuracy, the deviations of printed features from the designed model were measured in each of the axes. The feature parameters included: length or diameter, height or depth, the edge lengths, and the projected area in XY, XZ, and YZ. For this purpose, surface profiles of the features were taken by a confocal white-light profilometer (ST-400 Nanovea, Irving, California) with 20 nm resolution in the vertical direction. A step size of 7 µm in each x and y-direction is chosen. The missing points area accounted for less than 5% of the total raw data. The cut-off length of profilometer was 0.8mm. The acquisition rate of scanning was 100 Hz. The features of each replicate were scanned once, and two surface profiles in X and Y direction were taken. For each feature, twenty-five measurements were made to measure length or diameters' (four measures), height or depth (four measures), edge lengths (four measures), projected areas in XY (one measure) (Figure 60), XZ (two measures), and YZ (two measures) planes, and side angles (eight measures) in both X and Y direction.

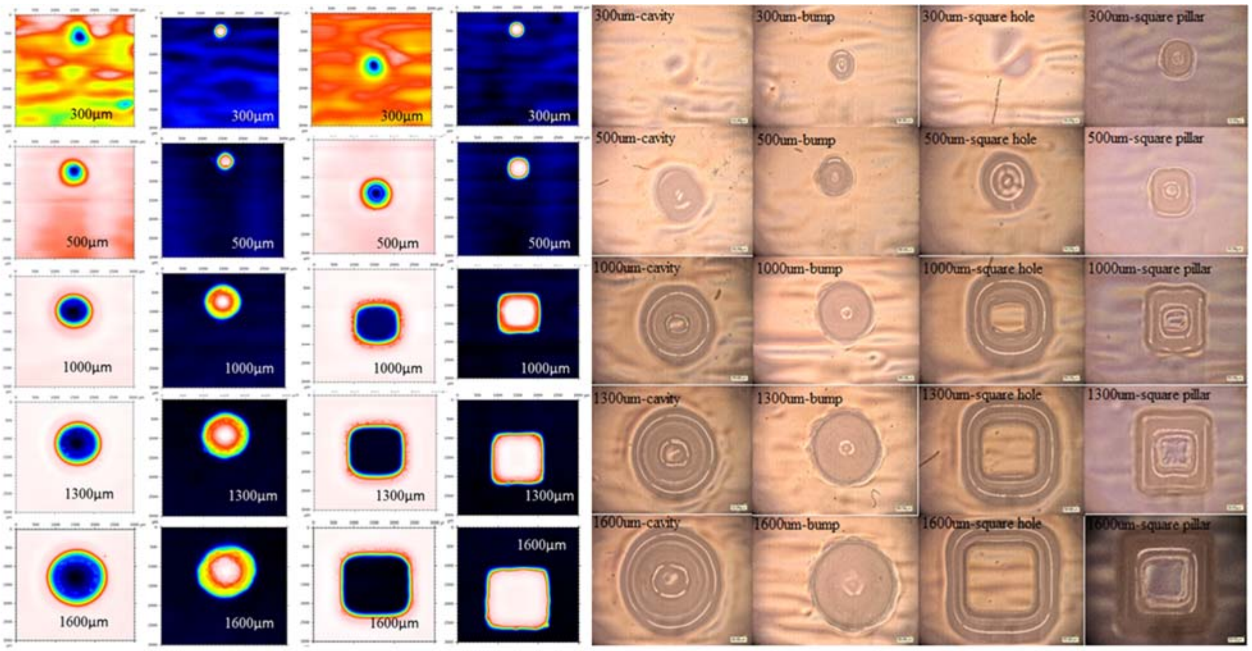

spherical hole Spherical protrusion Square hole square protrusion spherical hole Spherical protrusion Square hole square protrusion

Figure 60 Shape analysis by use of surface profilometry (left) and Micro images (right) of the printed features in XY direction

The measurements were performed by the Professional 3-D7.0 version of MountainsMap® software and a digital microscope (VHX-5000, Keyence, Osaka, Japan). MountainsMap is a surface imaging and metrology software published by the company Digital Surf [155]. Figure 60 shows the profilometry and micro images of the features and ranged from 300 µm to 1600 µm. The observations reveal that the material jetting machine is not accurately printing the features with sizes less than 500 µm. Further analyses are performed to mathematically present the dimensional accuracy and printing quality of the considered features in different sizes in material jetting processes.

2.2.Results

The actual diameter/length (F_L) of features were measured by profilometer. The edges of the features are identified and excluded. The edges are apparent in 3-D surface profiles attained from the optical profilometer (Figure 61). To measure the actual size, 2-D profiles of features are utilized. The profiles in Figure 62 (a) are for XZ plane and show the full-scale screenshot of the features. The profiles in Figure 62 (b) and (c) are zoomed in 50 μm scale in Z-axis around the edges of features. The breakpoints of the 2-D profiles help to distinguish the edges. The holed features (spherical and square hole) have rounded shape edges on the top surface, and the protrusion features (spherical and square) have ogee shaped edges at the bottom of the surface. Figure 62 (b) shows the measurements for actual length/diameter plus edges for both square and spherical features, and Figure 62 (c) shows the measurements for length/diameter (F_L) for square and spherical features.

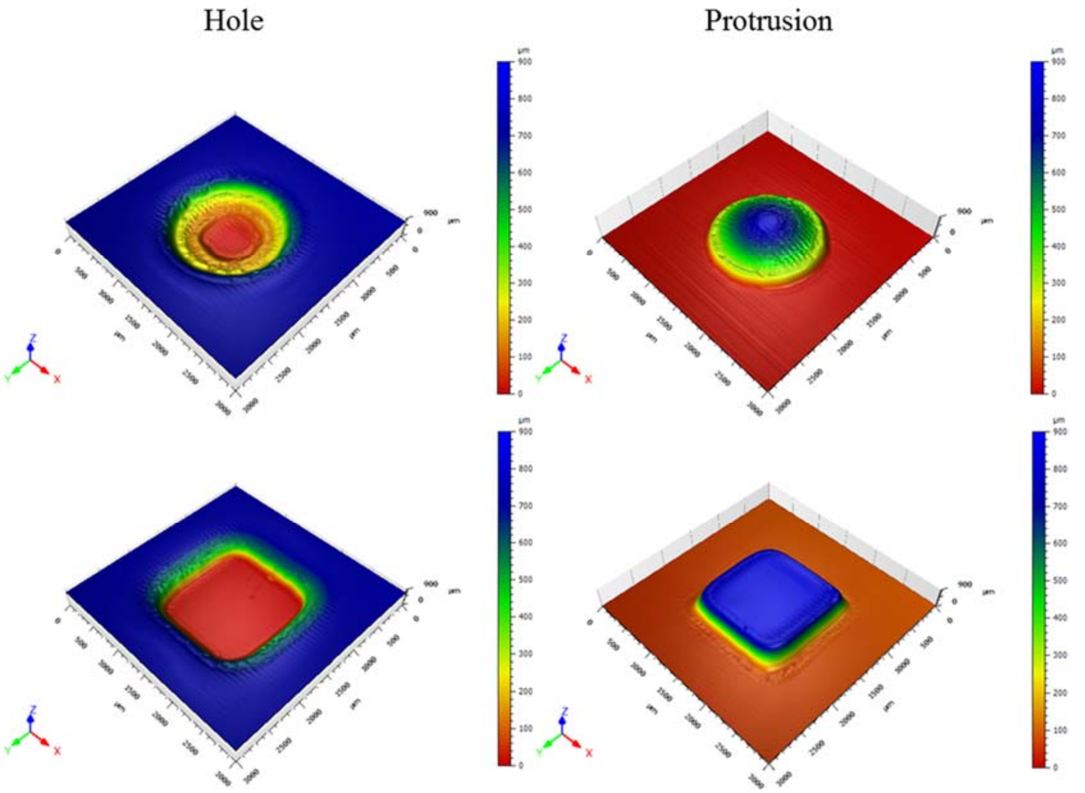

Figure 61 3-D Surface profiles attained from optical profilometer

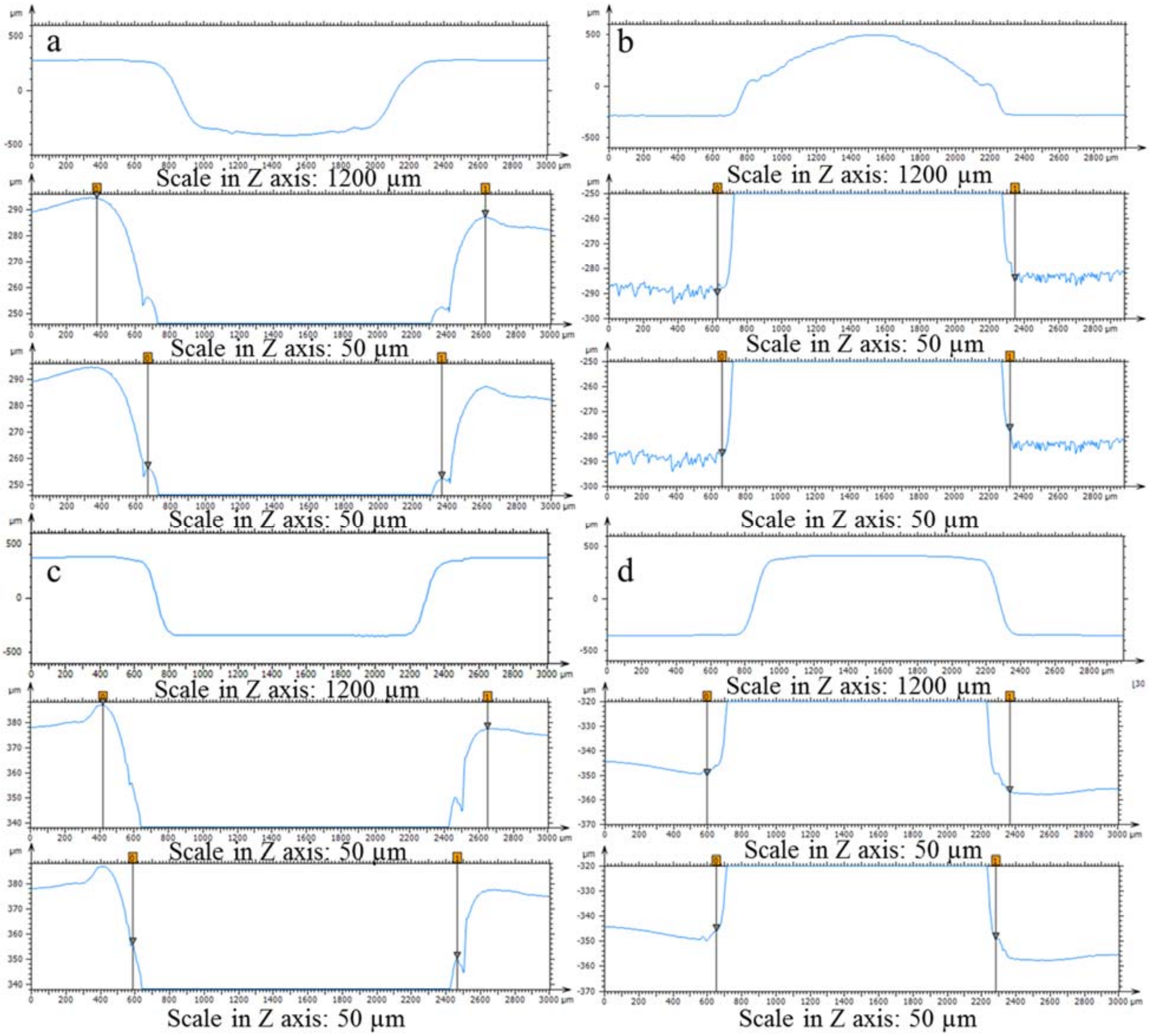

Figure 62 2-D profiles of features in XZ plane with the nominal lengths of 1500 µm. (a) Spherical hole, (b) spherical protrusion, (c) square hole, and (d) square protrusion

The length of edges of features roughly is constant in different sizes. The length of edges for holed features are significantly higher than protrusion features. For estimating the dimensional accuracy, the deviation of dimensions of the printed features from the designed model is calculated.

Figure 63 demonstrates the results of calculated dimensional errors for lengths of features. The results show that protrusion features have fewer errors (F_L) than holed features, especially for the sizes less than 700 µm.

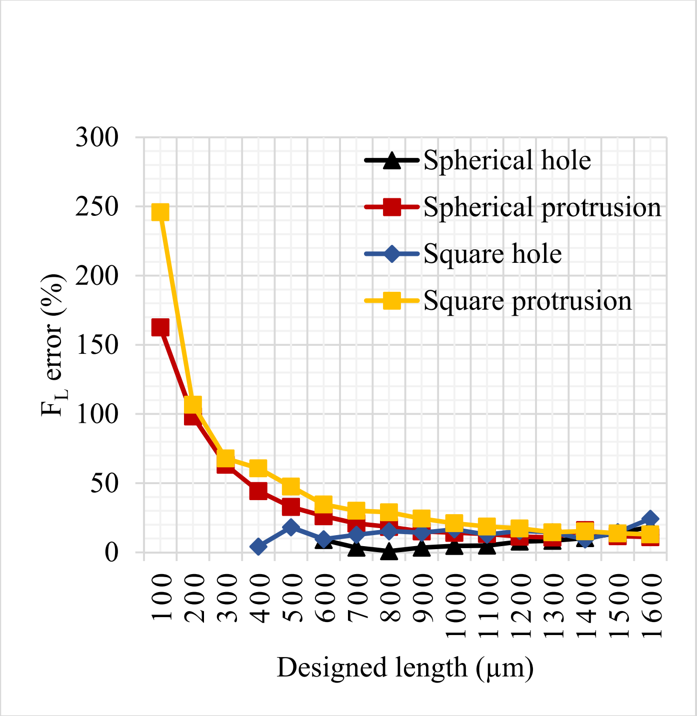

Figure 63 Feature lengths' (*F_L*) errors for designed features

Areal fidelity in XY plane

The areal fidelity of the features has been analyzed in this study as well. Figure 64 shows the surface profiles and micro images of printed features in XY plane (top view). The size of features ranged from 300 µm to 1600 µm. Figure 60 shows that in sizes less than 500 µm the design of features is indistinguishable and all printed features appear spherical.

Figure 64 shows the results of the actual projected area (A_L) of the printed features in XY plane. It can be concluded that the fidelity of actual projected area of protrusion features are significantly greater than holed features. Protrusion features (spherical and square) have less deviation from the nominal projected area due to their smaller edges.

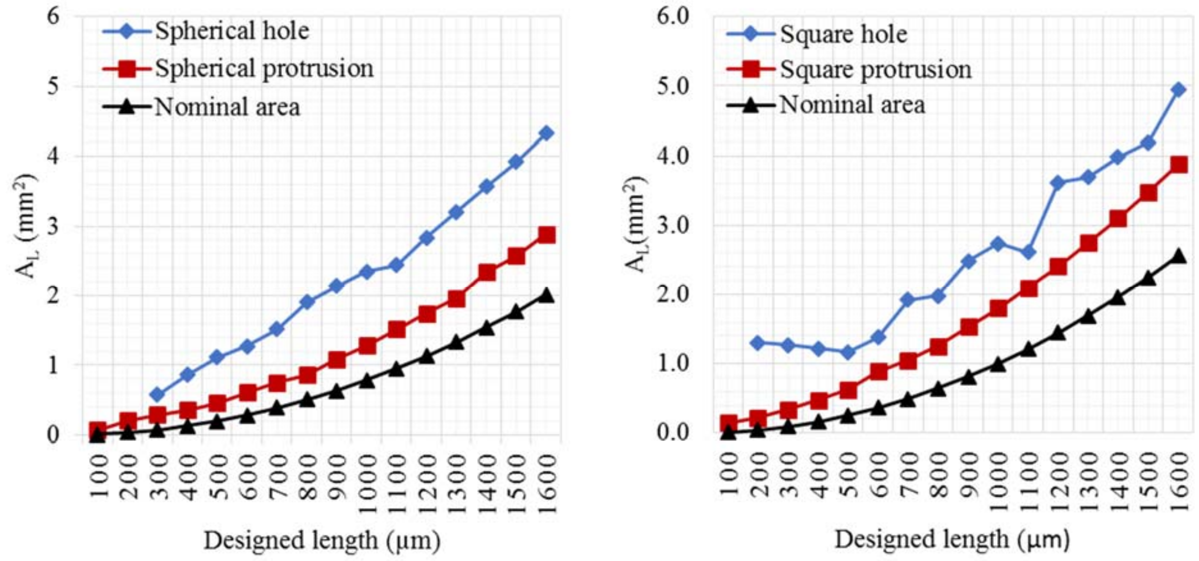

Figure 64 Actual projected area (A_L) of the printed features in XY plane with considering the edges. Spherical features (left) and square features (right)

Dimensional accuracy measurements along the Z direction

For assessing the dimensional accuracy in the Z direction, the error of depth/height ($F_{D/H}$) of the printed features from the designed model is measured by 2-D profiles. The measurements and dimensional error in Z direction are shown in Figure 65. Each point in Figure 65 is the average of six profiles along X and Y direction. The protrusion features (spherical protrusion and square protrusion) for the lengths less than 600 μm have less dimensional error along Z axis than holed features. Moreover, the protrusion features have taller heights/depths comparing to the holed features in all ranges of sizes. The fidelity of height/depth is higher than the length/diameter which reveals that the accuracy of the material jetting process in the Z direction is higher than X and Y directions.

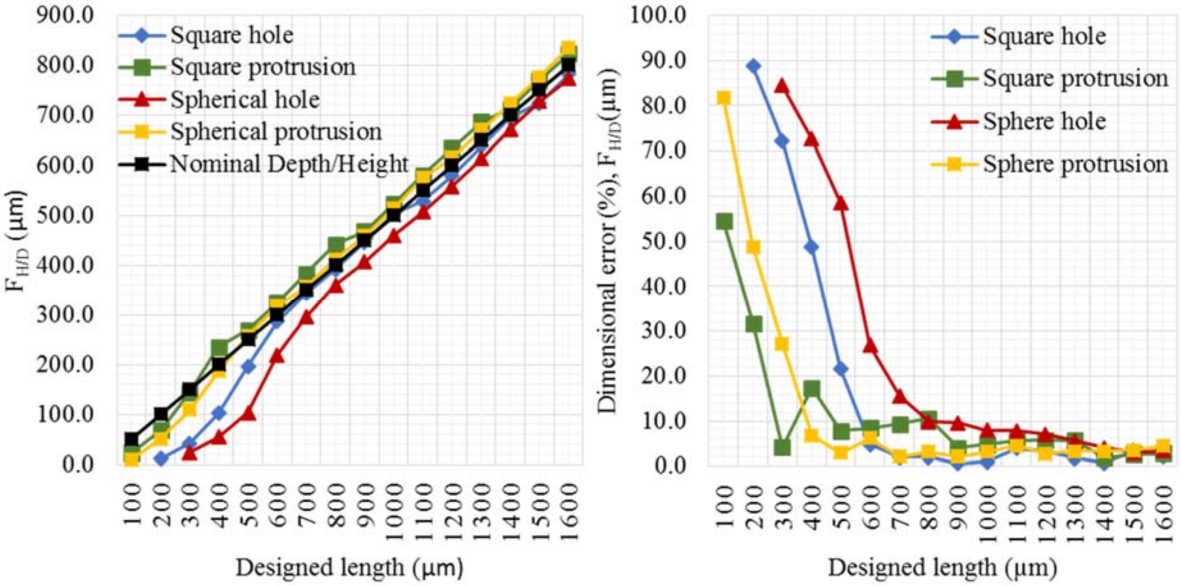

Figure 65 Height/Depth (*$F_{H/D}$*) measurements (left). Dimensional error in the Z direction (right)

Figure 66 shows the results of measured side angles for square features. The results show that the side angles are noticeably less than 90° (printed side angles are less than 82°) in all sizes. The deviation is much higher for the lengths less than 700 µm and the features are closer to isosceles trapezoid than square. Figure 66 shows the deviation of side angles of the square protrusion is much less than the square hole features. Each point in Figure 66 is the average of twelve profiles for XZ and YZ planes.

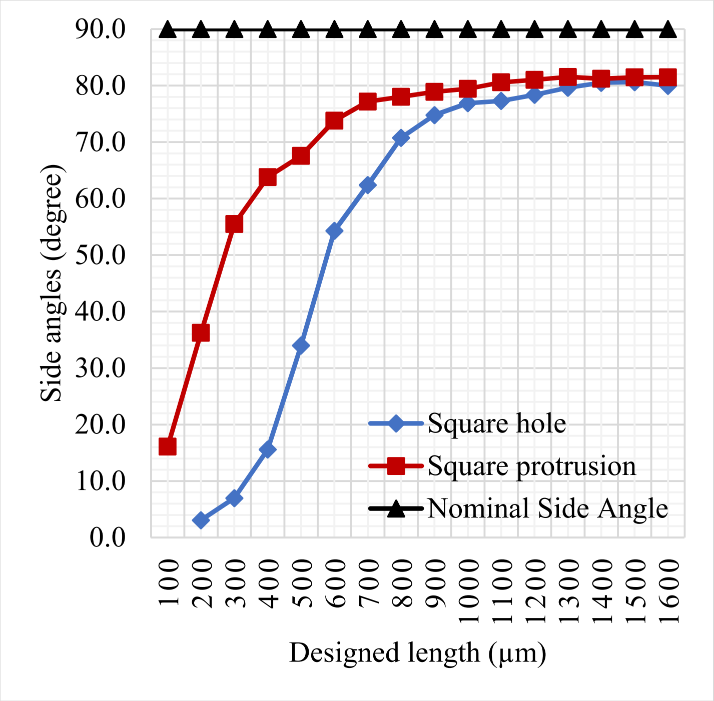

Figure 66 Side angles measurements for square features (square hole and square protrusion)

Areal fidelity in XZ and YZ planes

The shapes of the features are similar in XZ and YZ planes (Figure 67). As it can be seen from Figure 67, in small sizes (diameter≤500 µm) both square and spherical features have a similar shape which shows that the accuracy of the machine in sizes less than 500 µm are very low.

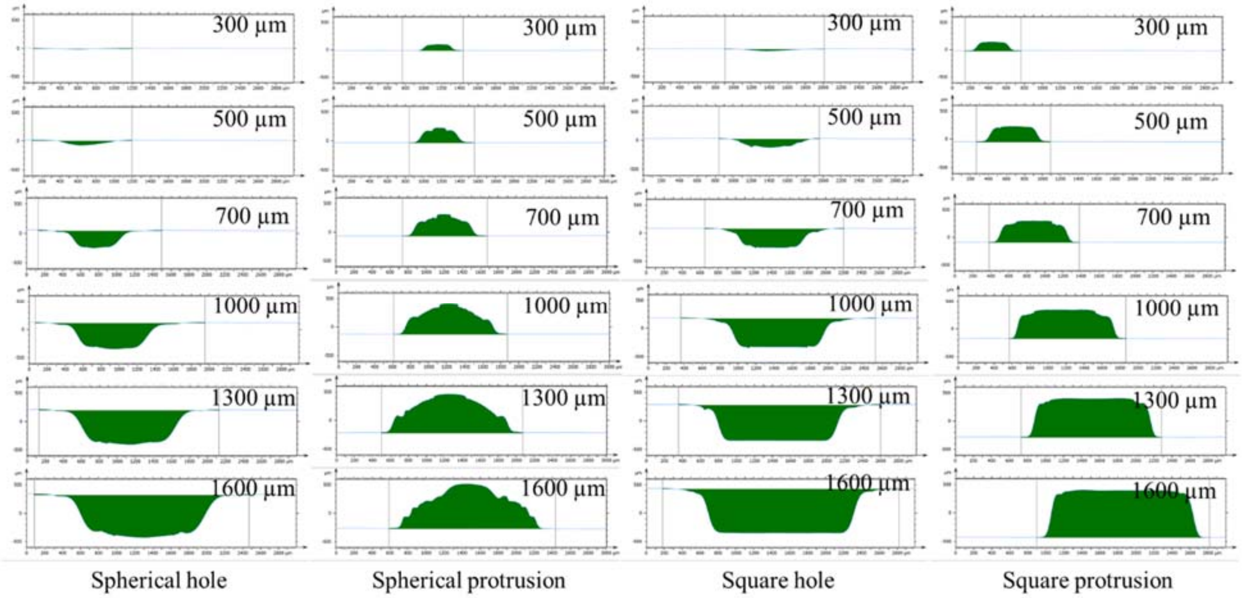

Figure 67 Projected area in YZ plane in different sizes (i.e., 300 µm, 500 µm, 700 µm, 1000 µm, 1300 µm, and 1600 µm)

To analyze the area of the features in XZ and YZ planes, the projected area of the printed features are measured with MountainsMap® software and compared with the nominal model. The average values of the projected area for XZ and YZ and the results of measured projected area errors for features are presented in Figure 68. The results show that the protrusion features have much less area error than holed features, especially for the sizes less than 700 µm.

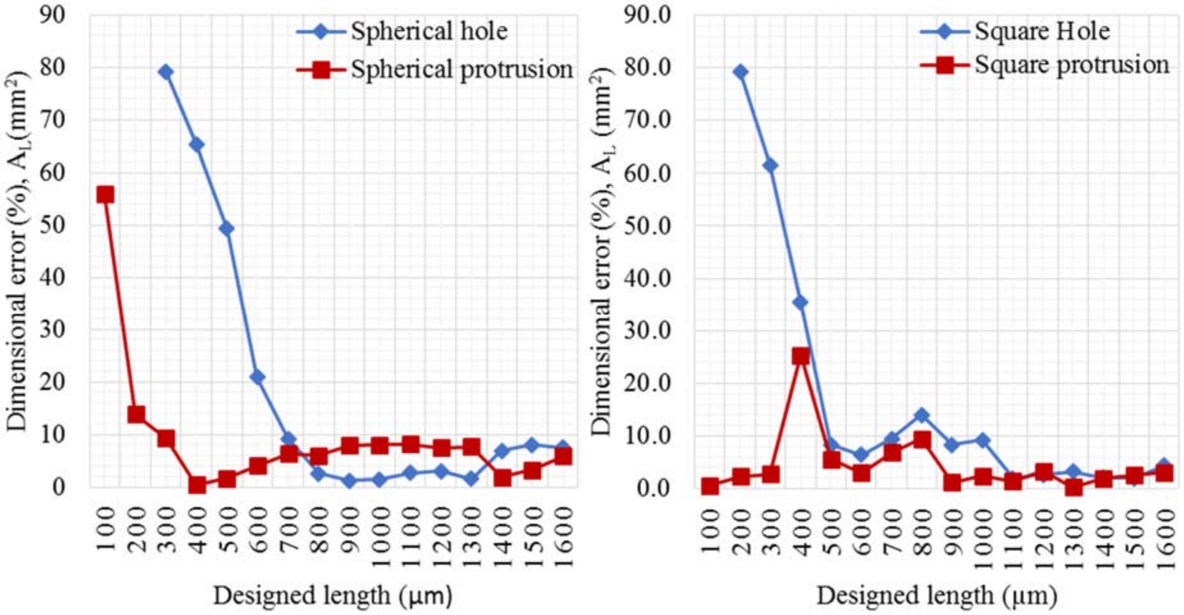

Figure 68 Area error along XZ/YZ of spherical features (left) and square features (right)

2.3.Discussion and Conclusions

The results show that protrusion features have less dimensional errors (F_L, $F_{H/D}$, and A_L) than holed features, especially for the sizes less than 500 µm. The designs of features in sizes less than 500 µm are indistinguishable, and all printed features appear spherical. Slipping of partially cured (solidified) materials deposited right at the edge of features results in rounded shape edges and dimensional errors in fabricated designs. This occurrence is more extreme for holed features due to the slipping of materials occurring inside the depressions and partially accumulating at the bottom of the holes. For protrusion features, the partially cured materials deposited at the edges slips outside the features which results in lower dimensional error compared to holed features. In small sizes, the features are forming with few drops of materials and due to slipping of partially cured materials, the fidelity of fabricated features are extremely low. This phenomenon is more extreme for holed features because slip of material occurring inside the features. Moreover, the protrusion features have taller heights/depths comparing to the holed features in all ranges of sizes due to the accumulation of slipped materials inside the depressions. The fidelity of height/depth is higher than the length/diameter which reveals that the accuracy of the material jetting process in the *Z* direction is higher than *X* and *Y* directions. The fidelity of actual projected area of protrusion features is significantly higher than holed features. Protrusion features (spherical and square) have less deviation from the nominal projected area due to their smaller edges. In small sizes, the features are forming with few drops of materials and due to slipping of partially cured materials, the fidelity of fabricated features are extremely low. This phenomenon is more extreme for holed features because slipping of material is occurring inside the features.

Also, the results show that the side angles are noticeably less than 90° (printed side angles are less than 82°) in all sizes. The deviation is much higher for the lengths less than 700 μm and the features are closer to isosceles trapezoid than square. The deviation of side angles of the square protrusion is much less than the square hole features. When the new layer is applied, the weight force of the layer presses the previously deposited partially cured layers to the sides of the features and causes the material to slip, creating side angles less than 90°. The more layers deposited, the more force is applied to the previously deposited materials due to the weight. This phenomenon is similar to when you press a biscuit on the cream which pushes the cream to the sides of the biscuit. The side angles deviation can be reduced if the sides of the features can be dominated with support materials around their sides. Support material partially prevents the slipping of material from the edges of the printed layers over the targeted features.

3. *Effects of Surface Slope and Build Orientation on Surface Finish and Dimensional Accuracy in Material Jetting Processes* [156]

3.1.Materials and Methods

Four features (spherical and prismatic protrusions and holes), as well as a flat area, were modeled in Solidworks® (Dassault Systemes, SolidWorks Corp., Waltham, MA) (Figure 69). Three replicates of each specimen were fabricated to the best possible surface finish option (i.e., glossy) from the machine. The specimens were fabricated with an Objet30 (Stratasys Ltd., Eden Prairie, MN) printer with a 28 µm target layer thickness. The height and length of designed features are 800 µm and 1600 µm respectively. These feature sizes were chosen with two considerations: the limitation of the optical profilometer (ST-400 Nanovea, Irving, California) in the Z-axis (approximately 900 µm); and dimensional accuracy of printed features with sizes greater than 700 µm is higher than 90%. The specimens were printed one at a time in the middle of the build tray to minimize the distorting effect of a possible cooling gradient caused by the edge of the tray. All features were designed and arranged in a matrix layout on each specimen and each row, with each column containing all representative feature types in a pseudo-randomized position order (Figure 69).

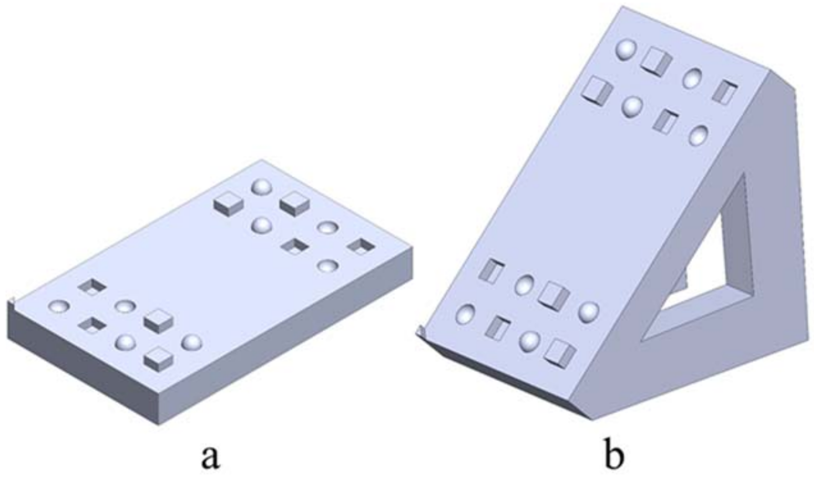

Figure 69 Computer models of (a) horizontal (0°) and (b) tilted (45°)

Prior this experiment, a preliminary trial was conducted to determine the levels of each factor. The preliminary experiment examined two factors: surface slope with three levels (0° (horizontal), 45°, and 90° (upright)) and build orientation with two levels, longest dimension along (XY), and across (YX) the printing head direction (Figure 70) to examine the feasibility and repeatability of the conditions. Those specimens with a 90° surface slope required significant coverage of the features with support material due to their location in the cantilever. The removal of this amount of support material required a combination of mechanical scraping and the use of chemical solvents and resulted in undesired alteration of the original surface. Consequently, the experimental orientation level of 90° was discarded. The specimens with a 45° surface slope required minimal support material below the protruded features and inside the depressions so its removal was possible with a waterjet system which did not affect the features or surface. The flat area was printed without any support material, so no post-processing was required. Therefore, two levels of surface slope (0° and 45°) and two levels of build orientation (XY and YX) were considered in this study.

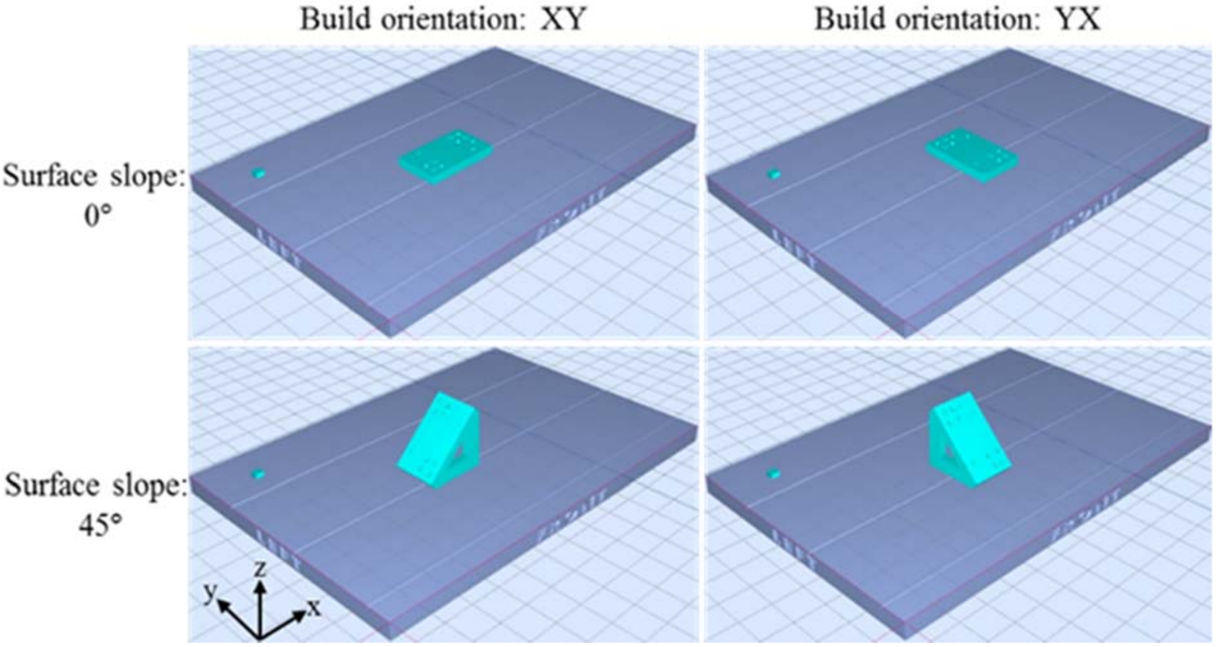

Figure 70 Specimen orientation and surface slope

The flat area was characterized by twenty-three surface texture parameters established by the ISO 25178-2 standard [71], and the features were analyzed by estimating dimensional and areal fidelity. For this purpose, surface profiles were taken with an axio-chromatic white-light profilometer (ST-400 Nanovea, Irving, California). Selected flat areas of 10 mm × 10 mm were scanned by a step size of 10 μm in *X* and *Y* directions and acquisition with a rate of 1000 Hz and a cut-off length of 0.8 mm. In all reading setups, the missing points accounted for less than 5% of the total raw data. The Abbott Curve (Figure 71) represents the cumulative probability density function of the surface profile's height and extrapolates numbers of functional surface and volumetric parameters including the distance between the highest and lowest level of the core surface (S_k), the average height of the protruded peaks above the core surface (S_{pk}), and the average height of the protruded dales below the core surface (S_{vk}), peak material volume (V_{mp}), core material volume (V_{mc}), core void volume (V_{vc}), and valley void volume (V_{vv}) [157, p. 13656], [158], [159]. Based on the ISO 25178 standard, the bearing ratio thresholds, 20% (S_{mr1}) and 80% (S_{mr2}) are considered for the

Abbott Curve to measure the functional parameters. The S_{mr1} and S_{mr2} represent the percentage limits of the core roughness profile [159]. Figure 71 (a) and (b) show the functional (i.e., stratified and volumetric) parameters in Abbott Curve. In addition to the Abbot Curve parameters, height parameters and spatial parameters were considered to analyze the effect of stair-stepping on surface quality. The list of all studied parameters with their definitions is presented in Appendix III.

Dimensional and areal fidelity have been studied in all three axes. For assessing the dimensional accuracy, the geometrical features, the deviations from the design targets (i.e., length (F_L), height (F_H), and the projected area in XY plane (A_L)) have been analyzed through white-light profilometry. The actual diameter and length have been measured for spherical and prismatic features after excluding the edges created by the creep-like flow of uncured material immediately after deposition. The profiles are analyzed by the Mountain® software (Digital Surf, Professional 3-D7.0, Besancon, France). The features of each replicate were scanned once, and two surface profiles in X and Y directions were taken. For each feature, ten measurements were made to measure length, diameters, height, depth, projected areas in XZ and YZ planes as well as side angles in X and Y direction.

Several statistical analyses were performed to examine the dimensional and areal fidelity of the printed features. Several 2^2 factorial analyses were conducted to study the effects of surface slope, build orientation, and their interactions on the dimensional accuracy of printed features. These included one-way ANOVA and Tukey's pairwise comparisons. Then, t-tests were performed to compare the length of features fabricated on 45° sloped surfaces along the width (F_{LW}) and the slope (F_{LS}) of the specimens.

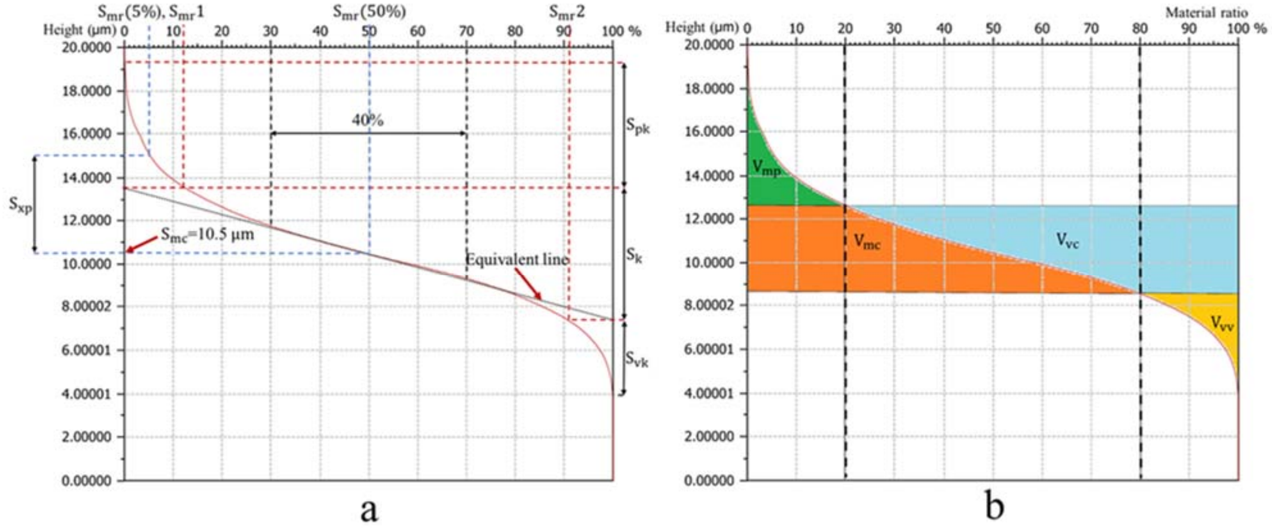

Figure 71 (a) 2D and (b) volumetric parameters of Abbot Curve

3.2.Results

3.2.1. Flat surface characterization

Twenty-three 2^2-factorial analyses performed to observe the effects of surface slope (0° and 45°) and build orientation (XY and YX) on each of the surface parameters. The results are summarized in Table 15. Broadly, the height, functional material ratio, and functional volume groups stood out with the most statistically significant parameters.

In height parameters, the surface slope is significant at $p<0.05$, for S_a (F (1, 8) =5.97, p=0.040). Build orientation is not significant for any of the height parameters.

Table 15 Summary of twenty-five 22-factorial analyses at the significant level of 0.05 for the build orientation, surface slope, and their interactions. The significant parameters are bolded.

Type of parameter	Parameter	Surface slope	Build orientation	Two-way interaction
Height Parameters	S_q(μm)	0.062	0.682	0.580
	S_{sk}	0.915	0.729	0.551
	S_{ku}	0.378	0.854	0.284
	S_p (μm)	0.648	0.392	0.460
	S_v (μm)	0.463	0.819	0.600
	S_z (μm)	0.487	0.696	0.499
	S_a (μm)	**0.040**	0.099	0.470
Functional Parameters (material ratio)	S_{mr} (%)	0.872	0.106	0.344
	S_{mc} (μm)	**0.047**	0.102	0.501
	S_{xp} (μm)	**0.020**	0.083	0.215
Spatial Parameters	**S_{al} (mm)**	0.147	**0.033**	0.476
	S_{tr}	0.249	0.455	0.205
Functional Parameters (Volume)	**V_m (mm³/mm²)**	**0.019**	0.380	0.856
	V_v (mm³/mm²)	**0.045**	0.106	0.512
	V_{mp} (mm³/mm²)	**0.019**	0.380	0.856
	V_{mc} (mm³/mm²)	0.052	0.074	0.392
	V_{vc} (mm³/mm²)	0.052	0.102	0.539
	V_{vv} (mm³/mm²)	**0.007**	0.433	0.253
Functional Parameters (Stratified surfaces)	S_k (μm)	0.344	0.461	0.376
	S_{pk} (μm)	0.555	0.392	0.495
	S_{vk} (μm)	0.607	0.354	0.275
	S_{mr1} (%) (peaks)	0.845	0.511	0.403
	S_{mr2} (%) (dales)	0.233	0.977	0.700

In the functional material ratio parameters, surface slope is a significant factor for S_{mc} (F (1, 8) =5.48, p=0.047) and S_{xp} (F (1, 8) =8.45, p=0.020). Build orientation is not significant for any of the functional material ratio parameters. Neither surface slope nor build orientation is significant for the functional stratified parameters.

In volumetric functional parameters, surface slope is a significant factor for V_m (material volume) (F (1, 8) =8.57, p=0.019), V_v (void volume) (F (1, 8) =5.62, p=0.045), V_{mp} (peak material volume)

(F (1, 8) =8.57, p=0.019), and V_{vv} (dale void volume) (F (1, 8) =12.75, p=0.007). Build orientation is not a significant factor for any of the functional volumetric parameters. These parameters are calculated based on the suggested material ratio values (by the ISO 25178 standard) of 20 % (S_{mr1}) and 80% (S_{mr2}) [71]. Also, the results show that the interactions of the surface slope and build orientation are insignificant for the selected parameters.

In spatial parameters, build orientation is significant at $p< 0.05$, for S_{al} (F (1, 8) = 6.57, p=0.040). Surface slope is not significant for any of the spatial parameters.

3.2.2. Dimensional and areal fidelity of features

Twelve 2^2-factorial analyses were performed on a surface slope, build orientation, and on their interactions on features' dimensional and areal fidelity. Actual length (F_L), features' height (F_H), and the projected area in XY plane (A_L) have been considered to analyze the dimensional and areal fidelity. The results (Table 16) show that both factors and their interactions have a significant impact on different geometrical aspects of features. Surface slope and build orientation appear to have a greater influence on the recessed features compared to the protruded features.

Tukey tests were used to compare the means of the features' length, height, and area. The summary of Tukey results at the level of $p<0.05$ denotes that: (a) the mean values of feature' length, F_L for spherical protrusion are significantly lower than prismatic hole (F (1, 30) =18.37, p<0.001), (b) there is no significant difference between the mean values of height, F_H for spherical and prismatic holes and protrusions (F (3, 60) =0.73, p=0.538) (c) spherical hole has significantly higher projected area than the spherical protrusion (F(1, 30) = 47.04, p<0.001) and prismatic hole has significantly higher area than the prismatic protrusion (F(1, 30) = 34.10, p<0.001).

Eight paired t-tests were performed on 45° sloped specimens to determine if the geometrical dimensions of features along width and slope of the tile are significantly different. For this purpose, the histograms for the ratio of lengths of the features along the width of the tiles (F_{LW}) over lengths of the features along the slope of the surface (F_{LS}) have been analyzed (Figure 72). This ratio ($k = F_{LW}/F_{LS}$) explains how the dimensions of the features along width and slope of printed surfaces are different. The results of Tukey tests reveal that the lengths of prismatic protrusions along the slope of the tiles are longer than the lengths along width of the tiles in both build orientations, XY (F (1, 6) = 8.79, p=0.025) and YX (F (1, 6) = 6.59, p=0.043). In contrast, the lengths of prismatic holes along the slope of the tiles are shorter than the ones along width of the tiles in build orientations YX (F (1, 6) = 404.34, p<0.001). No significant differences were found in spherical features.

Table 16 Results of factorial analyses at p<0.05. The significant parameters are bolded

Factor	Feature	Parameter	F-value	P-value
Surface slope	Spherical hole	**F_L**	**1626.84**	**0.000**
		F_H	**19.39**	**0.001**
		A_L	**1192.87**	**0.000**
	Square hole	**F_L**	**1538.60**	**0.000**
		F_H	**22.07**	**0.001**
		A_L	**529.92**	**0.000**
	Spherical protrusion	**F_L**	**25.92**	**0.000**
		F_H	**142.69**	**0.000**
		A_L	1.64	0.225
	Square protrusion	**F_L**	**9.26**	**0.010**
		F_H	2.99	0.109
		A_L	3.30	0.094
Build orientation	Spherical hole	**F_L**	**12.22**	**0.004**
		F_H	**8.36**	**0.014**
		A_L	4.69	0.051
	Square hole	**F_L**	**49.31**	**0.000**
		F_H	**35.73**	**0.000**
		A_L	**5.69**	**0.034**
	Spherical protrusion	**F_L**	**6.00**	**0.031**
		F_H	0.33	0.575
		A_L	0.02	0.881
	Square protrusion	F_L	1.13	0.308
		F_H	**5.06**	**0.044**
		A_L	**27.79**	**0.000**

Two-way interactions	Spherical hole	**F_L**	**15.59**	**0.002**
		F_H	**9.13**	**0.011**
		A_L	**11.63**	**0.005**
	Square hole	**F_L**	**52.11**	**0.000**
		F_H	**37.42**	**0.000**
		A_L	**16.84**	**0.001**
	Spherical protrusion	F_L	2.81	0.119
		F_H	2.32	0.154
		A_L	1.46	0.251
	Square protrusion	F_L	1.56	0.236
		F_H	1.21	0.293
		A_L	**27.20**	**0.000**

Eight Tukey tests were performed to assess the effect of surface slope on dimensional accuracy. The results indicate that for several designs surface slope increases dimensional accuracy compared to when they are fabricated on the horizontal plate. The results show that when the build orientation is XY, the 45° surface slope increases the areal (A_L) dimensional accuracy for spherical hole (F (1, 6) =124.16, p<0.001), prismatic protrusion (F (1, 6) = 6.18, p=0.047), and prismatic hole (F (1, 6) = 257.26, p<0.001). When the build orientation is YX, the 45° surface slope increases the areal (A_L) dimensional accuracy for spherical hole (F (1, 6) = 1346.52, p<0.001) and prismatic hole (F (1, 6) = 313.80, p<0.001). The horizontal plate has a higher dimensional accuracy (F (1, 6) = 23.21, p=0.003) in the projected area (A_L) for prismatic features when fabricated on YX build orientation. In other cases, no significant differences have been found.

The effect of build orientation on dimensional accuracy were evaluated by eight Tukey tests. . The results show that when the surface slope is 45°, the build orientation XY lowers the areal (A_L) dimensional error for prismatic protrusion (F (1, 6) =47.27, p<0.001) and prismatic hole (F (1, 6) =20.70, p=0.002), while the build orientation YX lowers the areal (A_L) dimensional error for spherical hole (F (1, 6) =26.48, p=0.002). In other cases, the no significant difference has been found.

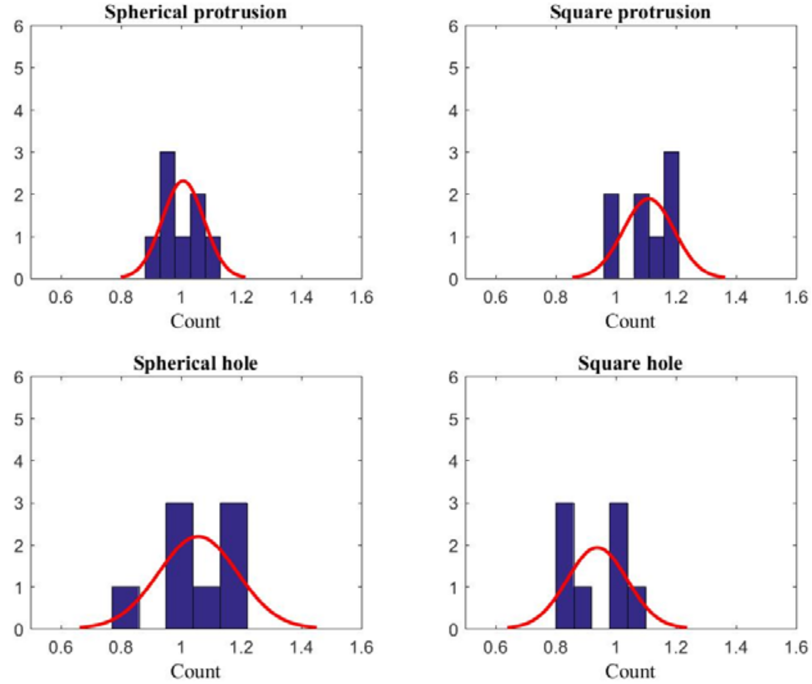

Figure 72 Histograms for the ratio (*k*) of lengths of the features along the width of the tiles (F_{LW}) over lengths of the features along the slope of the surface (F_{LS})

3.3.Discussion

The results showed that the stair-stepping significantly influences the height (i.e., S_a) and functional parameters (i.e., S_{mc}, S_{xp}, V_m, V_v, V_{mp}, and V_{vv}) since they are highly dependent on deviations from the average height. There are positive correlations between the height and functional parameters with deviations from the average height (Figure 73).

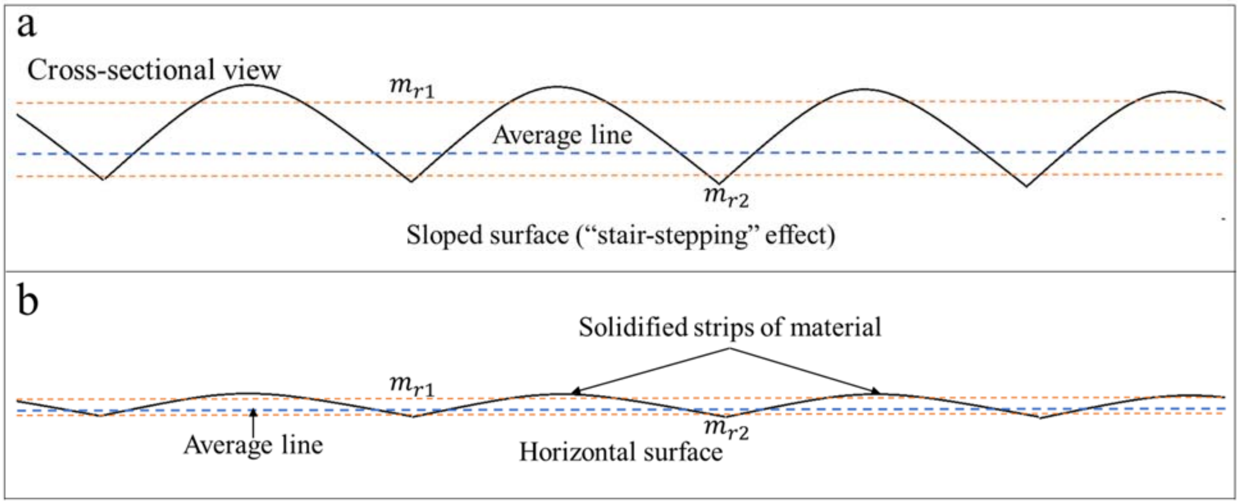

Figure 73 Sketch of cross-sectional views of the flat surface after the fabrication on (a) 45° sloped and (b) horizontal angles

The 0° surface slope has a better surface finish compared to the 45° one due to the positioning of deposited material which results in minimal displacement and a reduced layer effect (stair-stepping) in horizontal surfaces. One of the factors that might play a role in this uncured material flow is the delay between the material deposition and the cure lamp travel over the recently deposited layer. Although only fractions of a second, the effects of such delay are likely accentuated as the slope increases. Also, stair-stepping effects appear more prominently when the surface orientation is not orthogonal (in the Z-direction) to the axes (XY and YX) of the source of energy when the part is printing on sloped surfaces which causes the photopolymerization process to take place with a different light incidence angle and curing delay.

On the surface printed on a 45° sloped surface, the build orientation changes the direction of the stair-stepping on sloped surfaces. This effect can be analyzed by studying the autocorrelation length (S_{al}) which determines the general texture specification of the surface. The specimens printed in the YX build orientation showed lower autocorrelation length than the specimens with orientation XY. The lower the value of the autocorrelation length results in faster and sharper decay in created texture [160].

When the parts are printed on sloped surfaces, the effect of build orientation on shape and direction of stair-steps increases. In YX orientation (printing head moves along the shorter dimension of the specimen), the interval time between the two consequent passes of exposure is shorter, which results in a higher degree of photopolymerization. This causes the time for displacement of uncured or partially cured material to be shorter and creates sharper and faster decay on the existing stair-steps. Likely, this may have the opposite effect on horizontal surfaces, where flow and creep of uncured materials might alleviate layer effects.

The statistical results reveal that surface slope, build orientation, and their interactions are significant on different geometrical and fidelity aspects of surface features. Both surface slope and build orientation impact recessed features more than protruded ones. Also, significant differences between the mean values of features' lengths, F_L of the spherical protrusion and prismatic hole have been found in all orientations and slopes. The results showed that there is no significant difference between the mean values of height F_H for spherical and prismatic holes and protrusions which can be evidence of higher resolution in Z-direction in material jetting technologies. Also, it was observed that spherical holes have significantly higher cross section areas than spherical protrusions. Similarly, it was found that prismatic holes have significantly higher cross section areas than prismatic protrusions.

When parts are printing on a 0° surface slope, flow and creep of uncured or partially cured materials deposited right at the edge of features result in rounded shape edges and dimensional errors in fabricated designs. This occurrence is more extreme for debossed features due to the slipping of materials is occurring inside the depressions and partially accumulating at the bottom of the holes. For protrusion features, the partially cured materials deposited at the edges slipping outside the features which results in lower dimensional error compared to debossed features. When parts are printing on a 45° surface slope, the cavities in the debossed features are filled with support material which prevents the gravity-induced flow of uncured material and helps maintain the targeted geometry. Protrusion features do not benefit from this support.

The results (Figure 72) show that the surface slope significantly changes the dimensions of prismatic features along and across the slope direction. The partially cured material somewhat descends towards the slope of the surface and creates trace lines across the slope direction. This causes the perpendicular sides of the prismatic features to become unequal. The features printed on horizontal surfaces appear to be more repeatable than those printed in the 45° surfaces, and their surfaces have a better finish. The top edges of the prismatic features printed on 45° sloped surfaces are rounded shape, and the bottom edges are sharp due to slipping the material toward the slope direction. The trace lines of slipped material are visible in images of features printed with 45° surface slopes in Figure 74.

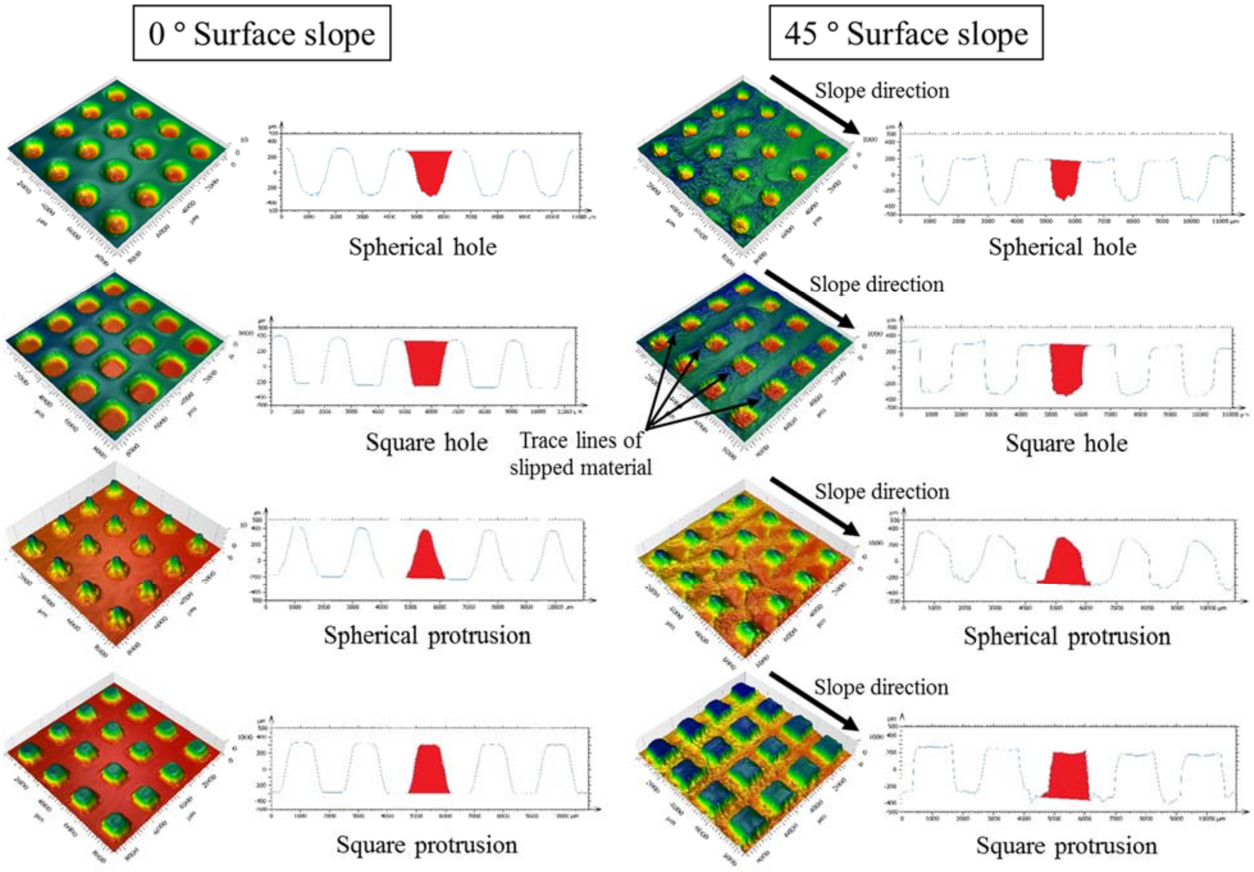

Figure 74 Surface profile and roughness profile of features fabricated in horizontal (left) and 45 ° (right) surface slope

The statistical results showed the 45° surface slope presents higher areal (A_L) fidelity compared to the horizontal surface for many features (i.e., spherical holes (in XY and YX orientations), prismatic protrusions (in XY orientation), and prismatic holes (in XY orientation)) while the horizontal surface only presents higher areal fidelity for prismatic protrusions fabricated in YX orientation. These observations suggest that for several designs (i.e., prismatic and recessed features) an inclined surface might provide better dimensional accuracy and fidelity of the build due to the accompanying support material.

3.4. Conclusion

Improving the surface finish and dimensional accuracy in material jetting processes requires considerations of both part design and process conditions. This work investigated the effects of surface slope and build orientation on surface finish and dimensional accuracy in material jetting processes. The introduction of a surface slope creates stair-stepping which affects different aspects of surface characteristics. The height and volumetric functional parameters are significant and show better surface finish for the 0° surface slope compared to the 45°. Build orientation affects the shape and direction of stair-steps. The orientation that is across the printing head direction (YX) has faster decay (sharper), and the surface is dominated by high spatial frequency components of texture patterns.

This study showed that if the build tray is orientable through the printing process, the build tray can be tilted to variable degrees to increase the dimensional accuracy and creates sharper edges for some designs such as polygons (not curved features) and features with recess designs. As is discussed in this study, surface slope also brings disadvantages such as stair-stepping effects, rough surface, asymmetry, and traces of flowed material along the slope. Build orientation affects the autocorrelation length which shows that the orientation that is across the printing head direction (YX) has faster decay (sharper) and the surface is dominated by high spatial frequency components of texture patterns.

If manufacturers were to provide more advanced machines with tiltable print trays and the printing parameters such as localized build orientation, surface slope, and selective support structures, it would be possible to achieve higher levels of dimensional accuracy, design fidelity, and surface finish. Immediate future work includes developing design guidelines for material jetting technology.

4. *Effect of Build Orientation and Part Thickness on Dimensional Distortion in Material Jetting Processes* [130]

4.1.Materials and Methods

In this research, three levels of thickness (1mm, 3mm, and 6mm) and two levels of build orientation along (XY) and across (YX), the print head main axes of motion, were selected for the study, for a total of $2^1 \times 3^1 = 6$ distinct treatment level combinations. These thickness levels were developed through preliminary experiments and encompass the range of values found in the previous literature [131], [137], [145], [152], [153]. The specimens were designed using Solidworks (Dassault Systemes, SolidWorks Corp., Waltham, MA) and fabricated with an Objet30 (Stratasys Ltd., Eden Prairie, MN) printer with a 28 μm target layer thickness. The specimens were designed with a high (10:1) aspect ratio (Figure 75 (a)) between length and width to magnify distortion effects [149], [150].

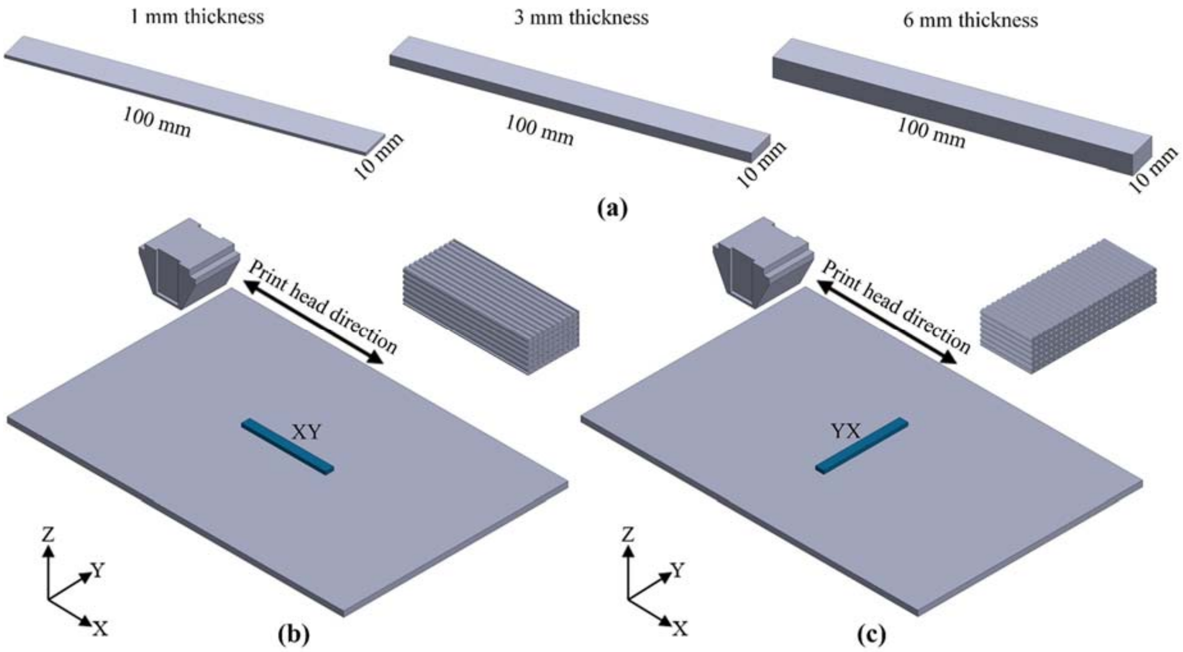

Figure 75 (a) Computer model of specimens, (b) build tray with print orientations along the main axis of motion (XY), and (c) across the main axis of motion (YX)

The overall specimen dimension was 100 mm ×10 mm. The material used to build the test specimens was a commercially available resin, Vero/white/plus Rgd835 (Stratasys Ltd., Eden Prairie, MN), which is a formulation that contains over 55% of acrylic/acrylate [115]. Even though previous efforts have reported that the location of the specimens on the build platform under UV light photopolymerization processes does not impact the mechanical properties [152], the specimens were printed one at a time in the middle of the build tray. This was aimed at minimizing the potential effects of cooling gradients or light reflection caused by proximity to the edge of the tray. Figure 75 (b) and (c) shows the orientations and positions of the specimens with respect to the build tray through the printing process. The ASTM A1030/A1030M-16 Standard names different geometry discrepancies as distortion types. These are wavy edge, ridge buckle, full center, coil set, reverse coil set, crossbow, and reverse crossbow [151]. Depending on the type of distortion, the quantification approach varies.

A preliminary experiment was conducted to understand which types of distortion occur under various thicknesses and build orientations. The preliminary results show that the specimens with 1 mm thickness distorted in a unique manner (wavy edge) that was different from the reverse coil set distortion that predominated in the thicker specimens (3 and 6 mm). Figure 76 depicts the two types of distortion later found as frequently occurring in this study: reverse coil set and wavy edge.

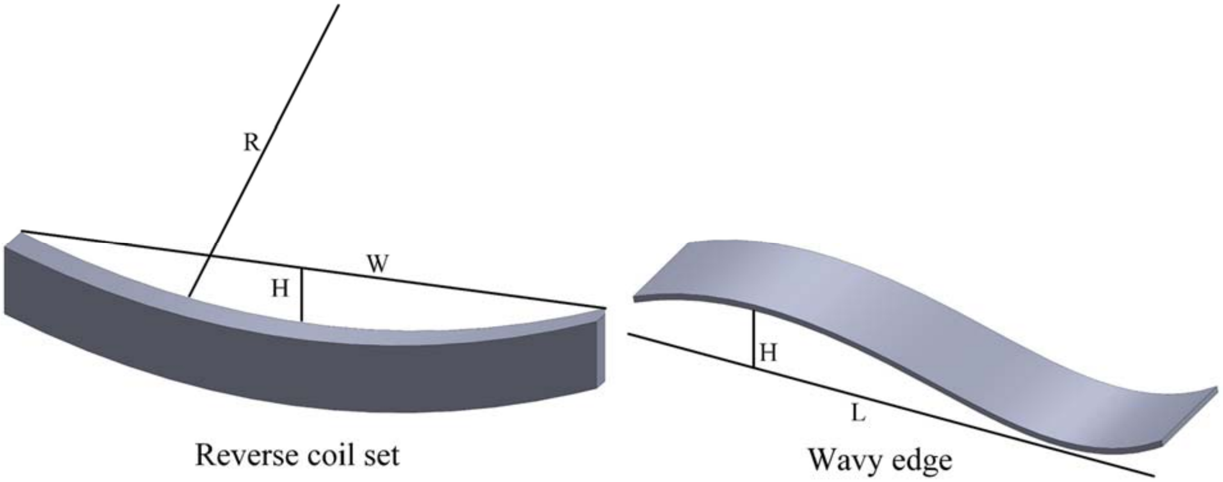

Figure 76 Computer models of reverse coil set (left), and wavy edge (right) distortion characterized by a peak (H) a cycle (L), the length of the specimen (W), and a radius (R) [21]

In order to measure the corresponding parameters, each specimen was scanned along its longer dimension by a white-light profilometer (ST-400, Nanovea, Irving, California). The linear scans were calibrated with a step size of 20 μm in each X and Y-direction, with an acquisition rate of 1000 Hz and a cut-off length of 0.8 mm.

In adherence to the ASTM A1030/A1030M-16 Standard, and depending on the type of distortion, up to four flatness parameters (height of the highest peak (H), steepness index (S), flatness index or I-unit (I), and profiles radius (R)) were measured and analyzed based on the method to mathematically characterize distortion [151].

The height of the highest peak (H) is the maximum deviation of the top surface from the nominal flat surface in the Z-direction, such that for the same part thickness, more distorted tiles have higher H values. The radius of surface profiles (R), another flatness parameter, is used to quantify reverse coil set distortion. Distortion has an inverse correlation with the profile radius, with the specimens presenting higher profile radii being closer to a nominally flat surface (i.e., an ideally flat surface has an infinite profile radius). Data measured by the profilometer were visualized and analyzed with Matlab® (MathWorks, Natick, MA) to calculate the average profile radius of the tiles as presented in Equation 1. Based on the step size of 20 μm along X and Y axis, each specimen is approximated by 426 scanned profiles traversing the length of the specimen, and each with 4925 scanned points. An individual profile radius was calculated by measuring the length and height of the highest peak (H) point in each surface profile following Equation 7 in Matlab®. Then, the average profiles radius for each specimen were obtained from the arithmetic average of 426 surface profile radii along the length of the specimen. The calculations for these parameters are presented in Equations 7, 8 and 9.

$$R = \frac{H}{2} + \frac{W^2}{8H} \tag{9}$$

The steepness and flatness indices are presented in the equations 11 and 12. The I-unit index expresses the relationship between the elongation of a deposited layer strip with respect to a reference plane. The I-unit index is used to show the distribution of the relative elongation of the layers deposited [161], effectively capturing the deviation from the reference plane in XY plane. The steepness represents edge waves with the height of H and interval of L. In calculating the I-unit, a series of lengthwise cuts to the sample is created which alleviates stresses that exist in the surfaces and results in narrow strips of various lengths. By defining the length of the shortest strip as a reference (L_{ref}), the I-unit value for a single strip is calculated by equation 3 [151].

$$S\% = \left(\frac{H}{L}\right) \times 100 \tag{10}$$

$$I = \left(\frac{\Delta L}{L_{ref}}\right) \times 10^5 \tag{11}$$

Also, the relationship between steepness index and I-unit is presented in Equation 9 [151].

$$I = 2.5\ (\pi S)^2 \tag{12}$$

where L is the wave interval, ΔL is the difference between the length of a given strip, the reference strip, L_{ref}, is the length of the shortest possible strip, and R is the profile radius [162].

In order to analyze the effects of part thickness (3- and 6- mm) and build orientation (XY and YX), three replicates for each treatment level combination were used. In total, $3 \times 2^2 = 12$ specimens were fabricated and analyzed for reverse coil set distortion. In addition, with regards to wavy edge distortion, five replicates were used to understand the effect of build orientation on inter 1 mm thickness for a total of $5 \times 2^1 = 10$ specimens. Once the flatness parameters for each type of distortion were measured and calculated, an ANOVA was performed to determine the effects of part thickness, build orientation, and their interaction effects on each of the flatness parameters as distortion indicators. The significant levels of the factors and their interaction effects on distortion were identified, and a Tukey test was performed on each flatness parameter to statistically examine if there is a significant difference between the levels of each factor.

4.2.Results

The images depicted in Figure 77 show isometric imaging from the profilometry scans of six of the printed specimens with thicknesses 1mm, 3mm, and 6mm. This shows the wavy edge distortion that appeared exclusively in the 1-mm specimens as well as the reverse coil set distortion that appeared both in the 3- and 6-mm specimens. In these scans and throughout the study, missing data points accounted for less than 5% of the total raw data. The images were produced from raw profilometry data using MountainsMap® (Digital Surf, Professional 3-D7.0, Besancon, France).

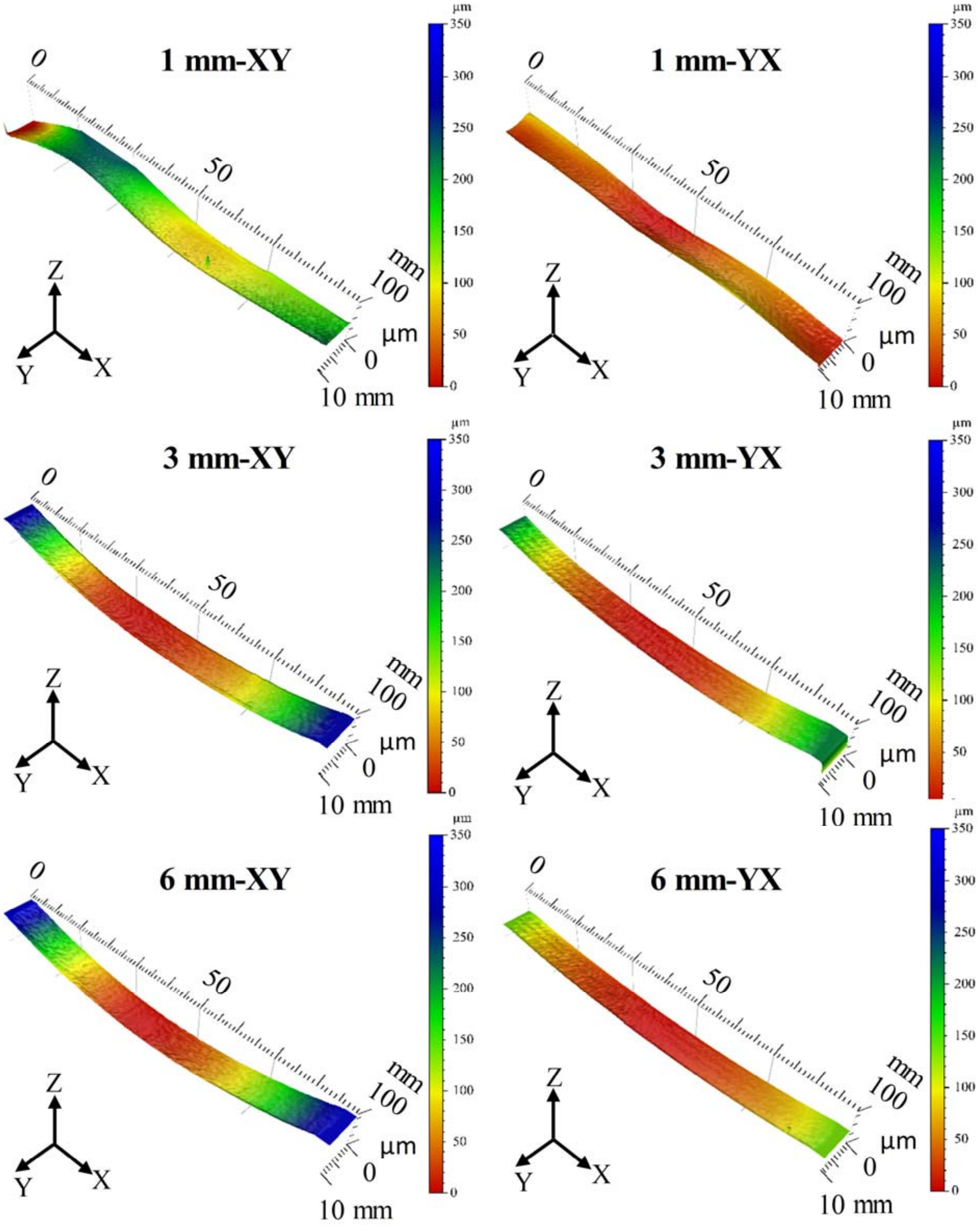

Figure 77 Isometric imaging from profilometry scans for six specimens of varying thicknesses and build orientations

Reverse coil set distortion

Reverse coil distortion occurred exclusively in the 3- and 6- mm thick specimens. Two parameters were employed in quantifying and analyzing the reverse coil set distortion type: height of the highest peak (H) and profiles radii (R). An F-test analysis was performed to examine the homoscedasticity of the data, confirming equal variance and normal distribution of the residuals.

With respect to the response height of the highest peak (H), the results from the ANOVA show that the difference of means for different levels of the factor part thickness is statistically significant (F (1, 10) = 6.82, p =0.031) while the factor build orientation is not (F (1, 10) = 0.09, p =0.777). Figure 4 (a) and (b) depict the main effects of the factors. It can be seen that the average distortion (as depicted by H) for specimens with 3 mm thickness is 57% more pronounced than the distortion found in 6 mm specimens. There is no interaction effects (F (1, 10) = 0.99, p=0.35) effect between the part thickness and build orientation for the 3 mm and 6 mm thicknesses.

Figure 4 (c) and (d) compare the main effect for the average radius (R) of the specimen profiles that were printed in two orientations (XY and YX) and two thicknesses (3 mm and 6 mm). With respect to the response height of the profiles' radius (R), the results from the ANOVA show that the effect of thickness on the profiles radius was significant (F (1, 10) = 8.08, p =0.022) while the factor build orientation was not (F (1, 10) = 0.44, p=0.527). It's revealed that the average distortion (as depicted by R) for specimens with 3 mm thickness is 51% less pronounced than the distortion found in 6 mm specimens. There are no interaction effects (F (1, 10) =2.46, p=0.156) between the part thickness and build orientation for the 3 mm and 6 mm thicknesses.

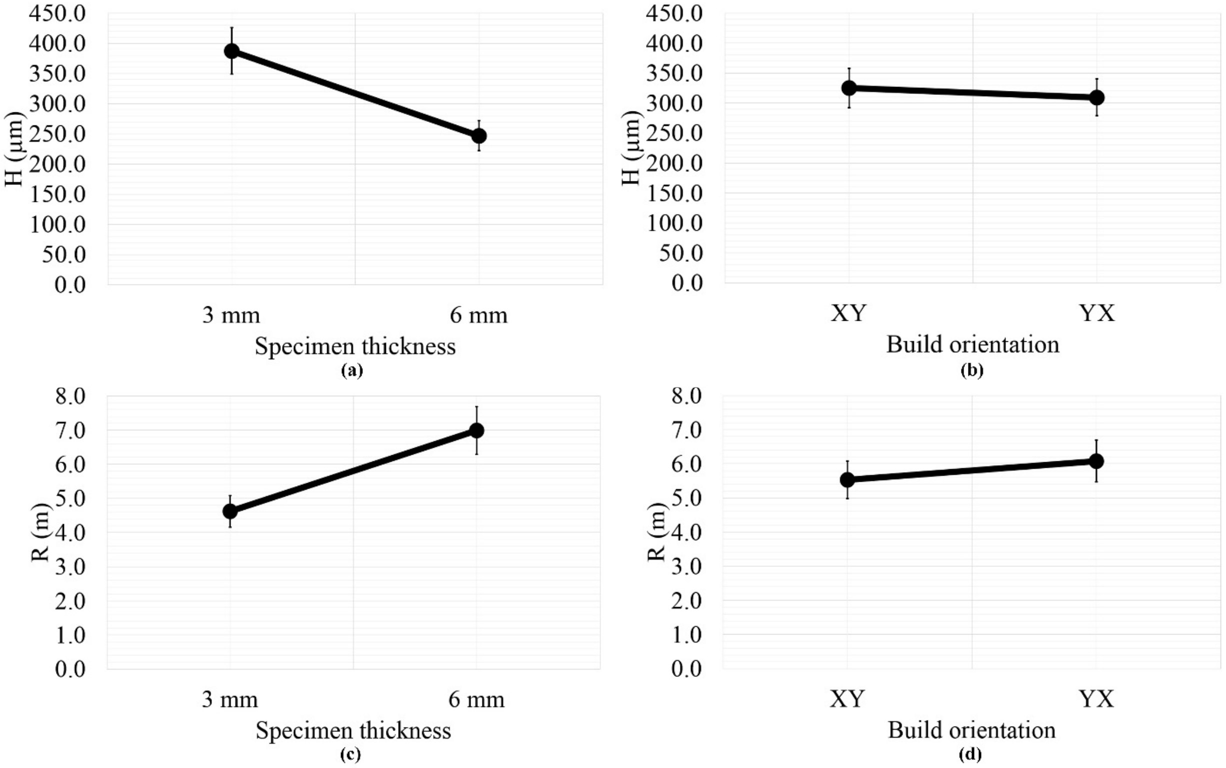

Figure 78 Main effect of thickness and build orientation on the height of the highest peak (a, b) and profiles radius (c, d)

Wavy edge distortion

Figure 79 shows the results of the three indices (steepness index, I-unit, and height of the highest peak) for the 1 mm specimens. Lower values of I-unit, steepness, and height of the highest peak indicate lower deviation and distortion [161]. For all indices, Tukey tests were performed to compare the results for orientations in XY and YX axis.

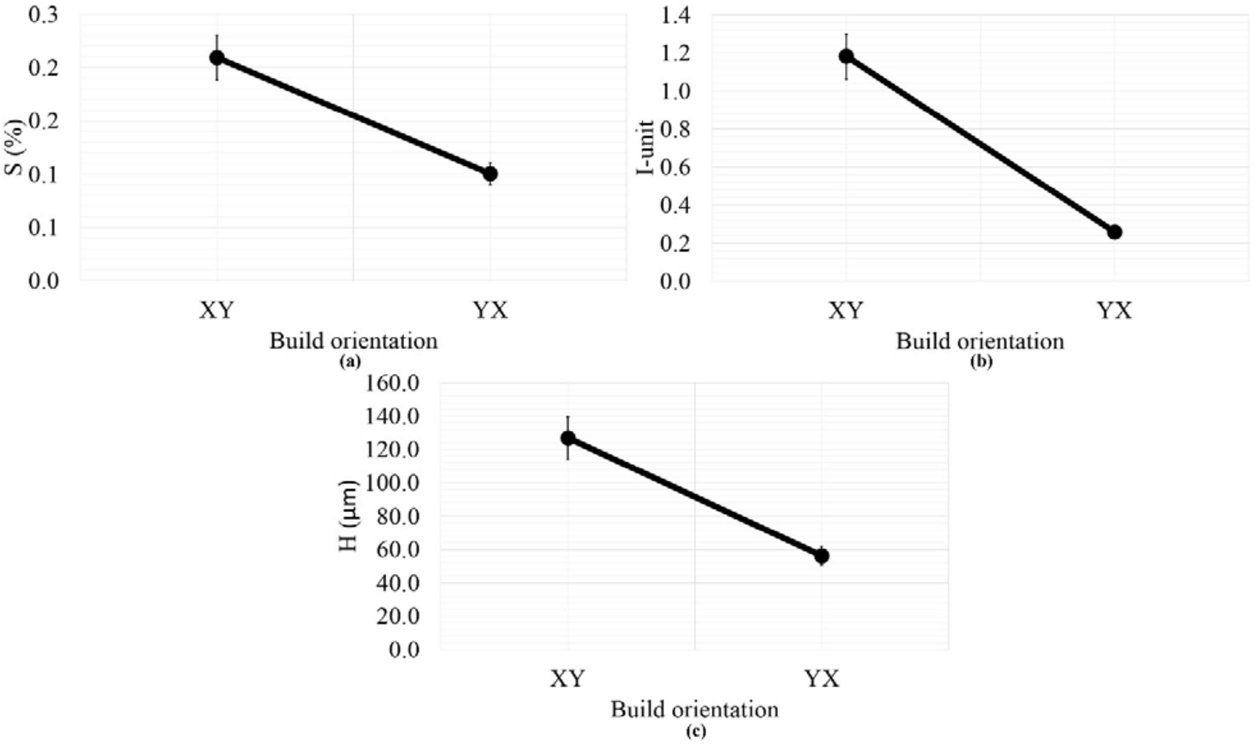

Figure 79 Main effect plots for Steepness index (a), I-unit index (b), and height of the highest peak (c) for 1 mm specimens

With respect to the response height of the highest peak (H), the statistical tests show that the factor build orientation is significant (F (1, 8) = 9.07, p =0.017) but this was not the case for the I-unit (F (1, 8) = 4.33, p =0.071) and the steepness index (F (1, 8) = 3.29, p =0.107). However, it should be noted that the build orientation factor is close to significance level for both I-unit and steepness indices.

4.3.Discussion

One of the main observations is that the thinner specimens (1 mm thick) always manifested a wavy edge type of distortion, while the thicker specimens (3- and 6-mm) displayed a reverse coil set type of distortion. During the printing process, welding of freshly deposited layers onto cured layers underneath are bound to form internal stresses on the specimen. These stresses form from a variety of reasons, including the existence of partially cured center raster or plies surrounded and stacked between already cured ones. The magnitude of these stresses is dependent on the contact area between consecutive raster or plies. This causes a parabolic distribution of compressive residual stresses in the surface plies and tensile stresses in the center plies [125], [149], [153], [163]. For the thinner specimens, the force is strong enough to twist the specimens' edges and form wavy edge distortion type. However, for the thicker specimens, the interlayer bond created by the higher number of welded layers prevent relief of internal stresses in a manner that causes the twisting that is characteristic of wavy edge distortion.

For the thicker (3- and 6-mm) specimens, the factor thickness was significant for both H and R responses. The 3-mm thick specimen experienced a more pronounced distortion measurement (57% higher H and 51% lower R, respectively) than the distortion found in the 6-mm specimens. The magnitudes of the distortion, as measured by H, on the 3-mm specimens were 422 μm (XY) and 353 μm (YX). For the 6-mm specimens, the magnitudes of the distortion were 266 μm (XY) and 228 μm (YX). It has been shown in the literature that thinner parts have lower shear moduli and higher stresses that may result in higher distortion [149]. This can be due to lower exposure since thinner specimens are exposed to fewer UV light passes, which would lead to a lower curing percentage; a factor found in the literature to impact distortion [146], [147].

Under the same resin characteristics, curing head speed, and irradiance, the lower exposure can be the consequence of the lower number of passes needed by the UV light onto the specimen to manufacture a thinner specimen. For the conditions, type, and color of resin employed in this study, the cure depth is estimated between 10-14 layers deep. Since the 1 mm thickness specimen is composed of approximately 36 layers of 28 μm each, then only 61-72% of the layers receive the maximum exposure and achieve the highest curing percentage. This is contrasted with the 3- and 6 mm specimens which boast 87-91% and 93-95% of layers receiving maximum exposure, respectively. These findings are consistent with those from Bushko and Stokes (1995) who studied the effects of part thickness on shrinkage and residual stresses of amorphous thermoplastics. They concluded that part thickness has a reverse correlation with residual stresses; the thicker the parts, the more thermal stress relaxation can occur due to lower cooling gradients [164]. The resin employed in this study contains over 55% amorphous crystalline in structure. Finally, the fact that the responses of both H and R provided identical insights to be expected since they are geometrically correlated.

With respect to the thinner 1 mm specimens, the factor orientation was found statistically significant for H (and close to significance for the I-unit index). As measured by H, the magnitudes of the distortion on the 1-mm specimens were 222 µm (XY) and 104 µm (YX). Distortion was found to be 114% and 185% less severe in the YX orientation when measured by the H and I-unit indices, respectively. This is likely due to the lay of the machine deposition of material and the ensuing gradient generated during curing. Huang and Jian (2003) found that, when the build orientation is performed with longer raster (print direction XY along the longer specimen axis), the distortion was more severe. This was likely due to the steeper cooling gradient which causes residual stresses between adjacent strips. Huang and Lan (2006) also found that that the degree of distortion is a function of the length of the scanning (raster) [132], also in agreement with the findings of this study.

Finally, an important aspect to consider is whether the magnitude of the distortion is large enough to cause functional issues during part use or subsequent processing (e.g., assembly, etc.). While this is dependent on the application, straightness and flatness tolerances on the sheet and molding products using similar acrylic polymers are around +/- 0.100 mm for precision parts. Since the distortion (when measuring the height of the highest peak [H]) for all levels of the two factors ranged between [104-422 µm], then it appears that the magnitudes of such distortion effects are severe enough to cause issues with the part functionality or subsequent processing.

4.4.Preliminary Design Recommendations

With respect to a preliminary set of quantitative design recommendations, when trying to minimize dimensional distortion in flat walls, it is recommended to ensure that no wall is thinner than 6 mm regardless of the build orientation. If thinner wall thicknesses are required, it should be noted that a different type of distortion (wavy edge, which can be more difficult to post-process or relieve), appears to predominate in thicknesses below 3 mm. Finally, for precision applications and any wall thicknesses below 6 mm, it is recommended that the part positioning in the tray (build orientation) is such that it is printed across the main head axis of motion (YX).

4.5.Conclusion

Minimizing the dimensional distortion in material jetting processes requires considerations of both part design and process conditions. The type of distortion generated by high aspect ratio specimen is dependent on the thickness of the specimen while the build orientation only becomes a significant process parameter when in very thin sections. The development of design guidelines should incorporate the knowledge that most geometries will experience distortion along the longest axis and that increasing wall thicknesses will help minimize potential deformations. Also, whenever thin part sections (~1 mm) are designed and fabricated; the YX build orientation appears to decrease the amplitude of the deformation wave, as expressed by the height of the highest peak. Future work will explore a wider array of aspect ratios as well as a continuum of thickness values in order to produce a more prescriptive design guideline. Higher aspect ratios are expected to magnify the distortion effects and trends found in this study as they grow more pronounced. However, it is unclear if the magnitude and rate of distortion will be proportional to the change in the ratio.

References

[1] ASTM, “Standard terminology for additive manufacturing technologies,” ASTM International, 2012.

[2] A. Cazón, P. Morer, and L. Matey, “PolyJet technology for product prototyping: Tensile strength and surface roughness properties,” *Proc. Inst. Mech. Eng. Part B J. Eng. Manuf.*, vol. 228, no. 12, pp. 1664–1675, Dec. 2014.

[3] N. Beltrán, F. Carriles, B. J. Álvarez, D. Blanco, and J. C. Rico, “Characterization of factors influencing dimensional and geometric errors in polyjet manufacturing of cylindrical features,” *Procedia Eng.*, vol. 132, pp. 62–69, 2015.

[4] J. Kechagias, P. Stavropoulos, A. Koutsomichalis, I. Ntintakis, and N. Vaxevanidis, “Dimensional accuracy optimization of prototypes produced by polyjet direct 3d printing technology,” in *Advances in Engineering Mechanics and Materials*, 2014, pp. 61–65.

[5] “Material Jetting: How Does It Work? - Make Parts Fast.” [Online]. Available: https://www.makepartsfast.com/material-jetting/. [Accessed: 12-Apr-2018].

[6] T. T. Chau, W. J. Bruckard, P. T. L. Koh, and A. V. Nguyen, “A review of factors that affect contact angle and implications for flotation practice,” *Adv. Colloid Interface Sci.*, vol. 150, no. 2, pp. 106–115, Sep. 2009.

[7] G. Lamour *et al.*, “Contact Angle Measurements Using a Simplified Experimental Setup,” *J. Chem. Educ.*, vol. 87, no. 12, pp. 1403–1407, Dec. 2010.

[8] E. Sachs *et al.*, “Three-Dimensional Printing: The Physics and Implications of Additive Manufacturing,” *CIRP Ann. - Manuf. Technol.*, vol. 42, no. 1, pp. 257–260, Jan. 1993.

[9] D. M. Blersch, K. Kardel, A. L. Carrano, and M. Kaur, “Customized 3D-printed surface topography governs species attachment preferences in a fresh water periphyton community,” *Algal Res.*, vol. 21, pp. 52–57, Jan. 2017.

[10] K. Kardel, A. L. Carrano, D. M. Blersch, and M. Kaur, “Preliminary Development of 3D-Printed Custom Substrata for Benthic Algal Biofilms,” *3D Print. Addit. Manuf.*, vol. 2, no. 1, pp. 12–19, 2015.

[11] R. J. Stevenson, M. L. Bothwell, R. L. Lowe, and J. H. Thorp, *Freshwater Benthic Ecosystem*. Algal ecology, 1996.

[12] Olivia Elliott *et al.*, “Design and Manufacturing of High Surface Area 3D-Printed Media for Moving Bed Bioreactors for Wastewater Treatment,” *J. Contemp. Water Res. Educ.*, vol. 160, no. 1, pp. 144–156, 2017.

[13] Carrano A. L, Blersch D. M, Kardel K, and Khoshkhoo A, “Understanding attachment preferences of benthic algae through controlled surface topographies on 3D printed substrata,” in *International Conference of Surface Metrology*, Poznań, Poland, 2016.

[14] Khoshkhoo A, Carrano A. L, Blersch D. M, Ghaednia H, and Kardel K, “Understanding and engineering of natural surfaces with additive manufacturing,” in *Proceedings of the 28th*, Austin, Texas, 2017.

[15] W. H. Adey, P. C. Kangas, and W. Mulbry, “Algal Turf Scrubbing: Cleaning Surface Waters with Solar Energy while Producing a Biofuel,” *BioScience*, vol. 61, no. 6, pp. 434–441, Jun. 2011.

[16] H. N. Sandefur, R. Z. Johnston, M. D. Matlock, T. A. Costello, W. H. Adey, and H. D. Laughinghouse IV, “Hydrodynamic regime considerations for the cultivation of periphytic

biofilms in two tertiary wastewater treatment systems," *Ecol. Eng.*, vol. 71, pp. 527–532, Oct. 2014.

[17] P. Kangas and W. Mulbry, "Nutrient removal from agricultural drainage water using algal turf scrubbers and solar power," *Bioresour. Technol.*, vol. 152, pp. 484–489, Jan. 2014.

[18] W. Mulbry, P. Kangas, and S. Kondrad, "Toward scrubbing the bay: Nutrient removal using small algal turf scrubbers on Chesapeake Bay tributaries," *Ecol. Eng.*, vol. 36, no. 4, pp. 536–541, Apr. 2010.

[19] W. Mulbry, S. Kondrad, C. Pizarro, and E. Kebede-Westhead, "Treatment of dairy manure effluent using freshwater algae: Algal productivity and recovery of manure nutrients using pilot-scale algal turf scrubbers," *Bioresour. Technol.*, vol. 99, no. 17, pp. 8137–8142, Nov. 2008.

[20] N. T. W. Ellwood, F. Di Pippo, and P. Albertano, "Phosphatase activities of cultured phototrophic biofilms," *Water Res.*, vol. 46, no. 2, pp. 378–386, Feb. 2012.

[21] W. Mulbry, S. Kondrad, and J. Buyer, "Treatment of dairy and swine manure effluents using freshwater algae: fatty acid content and composition of algal biomass at different manure loading rates," *J. Appl. Phycol.*, vol. 20, no. 6, pp. 1079–1085, Dec. 2008.

[22] W. H. Adey *et al.*, "Algal turf scrubber (ATS) floways on the Great Wicomico River, Chesapeake Bay: productivity, algal community structure, substrate and chemistry1," *J. Phycol.*, vol. 49, no. 3, pp. 489–501, Jun. 2013.

[23] *Algal Ecology: Freshwater Benthic Ecosystem*. Academic Press, 1996.

[24] J. M. Burkholder and R. G. Wetzel, "Microbial Colonization on Natural and Artificial Macrophytes in a Phosphorus-Limited, Hardwater Lake1," *J. Phycol.*, vol. 25, no. 1, pp. 55–65, Mar. 1989.

[25] A. R. Miller, R. L. Lowe, and J. T. Rotenberry, “Succession of Diatom Communities on Sand Grains,” *J. Ecol.*, vol. 75, no. 3, pp. 693–709, 1987.

[26] Y. Vadeboncoeur, J. Kalff, K. Christoffersen, and E. Jeppesen, “Substratum as a driver of variation in periphyton chlorophyll and productivity in lakes,” *J. North Am. Benthol. Soc.*, vol. 25, no. 2, pp. 379–392, Jun. 2006.

[27] J. Cao, W. Yuan, Z. J. Pei, T. Davis, Y. Cui, and M. Beltran, “A Preliminary Study of the Effect of Surface Texture on Algae Cell Attachment for a Mechanical-Biological Energy Manufacturing System,” *J. Manuf. Sci. Eng.*, vol. 131, no. 6, pp. 064505-064505–4, Dec. 2009.

[28] Burkholder, JoAnn M, “Interactions of Benthic Algae with Their Substrata-9,” in *Freshwater Benthic Ecosystems. Academic Press*, 1996, pp. 253–297.

[29] R. J. Stevenson, “Effects of Current and Conditions Simulating Autogenically Changing Microhabitats on Benthic Diatom Immigration,” *Ecology*, vol. 64, no. 6, pp. 1514–1524, Dec. 1983.

[30] R. J. Stevenson, “Scale-Dependent Determinants and Consequences of Benthic Algal Heterogeneity,” *J. North Am. Benthol. Soc.*, vol. 16, no. 1, pp. 248–262, Mar. 1997.

[31] Y. Liu and J.-H. Tay, “Detachment forces and their influence on the structure and metabolic behaviour of biofilms,” *World J. Microbiol. Biotechnol.*, vol. 17, no. 2, pp. 111–117, Mar. 2001.

[32] B. J. Cardinale, “Biodiversity improves water quality through niche partitioning,” *Nature*, vol. 472, no. 7341, pp. 86–89, Apr. 2011.

[33] B. J. Cardinale, M. A. Palmer, C. M. Swan, S. Brooks, and N. L. Poff, “The Influence of Substrate Heterogeneity on Biofilm Metabolism in a Stream Ecosystem,” *Ecology*, vol. 83, no. 2, pp. 412–422, Feb. 2002.

[34] Y. Cui, W. Yuan, and J. Cao, “Effects of surface texturing on microalgal cell attachment to solid carriers,” *Int. J. Agric. Biol. Eng.*, vol. 6, no. 4, pp. 44–54, Dec. 2013.

[35] M. F. Hassan, H. P. Lee, and S. P. Lim, “Effects of Shear and Surface Roughness on Reducing the Attachment of Oscillatoria sp. Filaments on Substrates,” *Water Environ. Res.*, vol. 84, no. 9, pp. 744–752, Sep. 2012.

[36] R. Sekar, V. P. Venugopalan, K. K. Satpathy, K. V. K. Nair, and V. N. R. Rao, “Laboratory studies on adhesion of microalgae to hard substrates,” in *Asian Pacific Phycology in the 21st Century: Prospects and Challenges*, P. O. A. Jr, Ed. Springer Netherlands, 2004, pp. 109–116.

[37] A. V. Bers and M. Wahl, “The Influence of Natural Surface Microtopographies on Fouling,” *Biofouling*, vol. 20, no. 1, pp. 43–51, Feb. 2004.

[38] J. Guenther and R. D. Nys, “Surface microtopographies of tropical sea stars: lack of an efficient physical defence mechanism against fouling,” *Biofouling*, vol. 23, no. 6, pp. 419–429, Nov. 2007.

[39] T. L. Dudley and C. M. D’Antonio, “The Effects of Substrate Texture, Grazing, and Disturbance on Macroalgal Establishment in Streams,” *Ecology*, vol. 72, no. 1, pp. 297–309, Feb. 1991.

[40] A. V. Bers, G. S. Prendergast, C. M. Zürn, L. Hansson, R. M. Head, and J. C. Thomason, “A comparative study of the anti-settlement properties of mytilid shells,” *Biol. Lett.*, vol. 2, no. 1, pp. 88–91, Mar. 2006.

[41] S. R. Brown, “A note on the description of surface roughness using fractal dimension,” *Geophys. Res. Lett.*, vol. 14, no. 11, pp. 1095–1098, Nov. 1987.

[42] F. Lanaro, “A random field model for surface roughness and aperture of rock fractures,” *Int. J. Rock Mech. Min. Sci.*, vol. 37, no. 8, pp. 1195–1210, Dec. 2000.

[43] S. L. Huang, S. M. Oelfke, and R. C. Speck, “Applicability of fractal characterization and modelling to rock joint profiles,” *Int. J. Rock Mech. Min. Sci. Geomech. Abstr.*, vol. 29, no. 2, pp. 89–98, Mar. 1992.

[44] Y. Jiang, B. Li, and Y. Tanabashi, “Estimating the relation between surface roughness and mechanical properties of rock joints,” *Int. J. Rock Mech. Min. Sci.*, vol. 43, no. 6, pp. 837–846, Sep. 2006.

[45] W. L. Power and T. E. Tullis, “Euclidean and fractal models for the description of rock surface roughness,” *J. Geophys. Res. Solid Earth*, vol. 96, no. B1, pp. 415–424, Jan. 1991.

[46] A. P. Oron and B. Berkowitz, “Flow in rock fractures: The local cubic law assumption reexamined,” *Water Resour. Res.*, vol. 34, no. 11, pp. 2811–2825, Nov. 1998.

[47] R. W. Zimmerman, S. Kumar, and G. S. Bodvarsson, “Lubrication theory analysis of the permeability of rough-walled fractures,” *Int. J. Rock Mech. Min. Sci. Geomech. Abstr.*, vol. 28, no. 4, pp. 325–331, Jul. 1991.

[48] N. Fardin, O. Stephansson, and L. Jing, “The scale dependence of rock joint surface roughness,” *Int. J. Rock Mech. Min. Sci.*, vol. 38, no. 5, pp. 659–669, Jul. 2001.

[49] J. B. Taylor, A. L. Carrano, and S. G. Kandlikar, “Characterization of the effect of surface roughness and texture on fluid flow—past, present, and future,” *Int. J. Therm. Sci.*, vol. 45, no. 10, pp. 962–968, 2006.

[50] S. G. Kandlikar, D. Schmitt, A. L. Carrano, and J. B. Taylor, “Characterization of surface roughness effects on pressure drop in single-phase flow in minichannels,” *Phys. Fluids*, vol. 17, no. 10, Oct. 2005.

[51] Taylor J.B., Carrano A. L, and Kandlikar, S. G., “Characterization of the Effect of Surface Roughness and Texture on Fluid,” presented at the ICNMM2005-75075, 2005.

[52] Taylor J.B., Carrano A. L, and Kandlikar, S. G., “Characterization of the effect of surface roughness and texture on fluid flow: past, present, and future (keynote),” in *American Society of Mechanical Engineers*, 2005, pp. 11–18.

[53] Kandlikar, S. G., Schmitt, D., Carrano A. L, and Taylor J.B., “Characterization of surface roughness effects and pressure drop in single-phase flow in mini/micro channels,” in *Proceedings of the ECI-conference*, Kona, Hawaii, 2004, vol. 8.

[54] M. J. Reeves, “Rock surface roughness and frictional strength,” *Int. J. Rock Mech. Min. Sci. Geomech. Abstr.*, vol. 22, no. 6, pp. 429–442, Dec. 1985.

[55] Brown, Stephen R and Christopher H. Scholz, “Broad bandwidth study of the topography of natural rock surfaces,” *J Geophys*, vol. 90, no. B14, pp. 12575–12582, 1985.

[56] C. Fischer and A. Lüttge, “Converged surface roughness parameters—A new tool to quantify rock surface morphology and reactivity alteration,” *Am. J. Sci.*, vol. 307, no. 7, pp. 955–973, Sep. 2007.

[57] E. Eilam, *Reversing: Secrets of Reverse Engineering*. John Wiley & Sons, 2011.

[58] M. L. Nelson, “A Survey of Reverse Engineering and Program Comprehension,” *arXiv:cs/0503068*, Mar. 2005.

[59] E. J. Chikofsky and J. H. Cross, “Reverse engineering and design recovery: a taxonomy,” *IEEE Softw.*, vol. 7, no. 1, pp. 13–17, Jan. 1990.

[60] A. L. Carrano, J. B. Taylor, and R. L. Lemaster, “Machining-induced subsurface damage of wood,” *For. Prod. J.*, vol. 54, no. 1, pp. 85–91, 2004.

[61] S. Motavalli, “Review of reverse engineering approaches,” *Comput. Ind. Eng.*, vol. 35, no. 1, pp. 25–28, Oct. 1998.

[62] P. N. Chivate and A. G. Jablokow, “Review of surface representations and fitting for reverse engineering,” *Comput. Integr. Manuf. Syst.*, vol. 8, no. 3, pp. 193–204, Aug. 1995.

[63] J. B. Taylor, A. L. Carrano, and R. L. Lemaster, “Quantification of process parameters in a wood sanding operation,” *For. Prod. J.*, vol. 49, no. 5, pp. 41–46, May 1999.

[64] A. L. Carrano and H. Kataria, “Effect of Abrasive Tooling Geometry on Surface Roughness Descriptors,” *IIE Annu. Conf. Proc. Norcross*, pp. 1–6, 2003.

[65] R. D. Lewis, J. Kennedy, M. Andruskiewicz, C. A. Brown, and S. Condoor, “Surface Characterization of Replicate Wood Surfaces for Cleaning Studies,” *J. ASTM Int.*, vol. 8, no. 10, pp. 1–15, Aug. 2011.

[66] A. L. Carrano, J. B. Taylor, and R. Lemaster, “Parametric characterization of peripheral sanding,” *For. Prod. J. Madison*, vol. 52, no. 9, pp. 44–50, 2002.

[67] K. Kardel, “An analytical and experimental study on 3D-printed custom surfaces for benthic algal biofilms,” Jul. 2016.

[68] R. L. Lowe and W. F. Gale, “Monitoring river periphyton with artificial benthic substrates,” *Hydrobiologia*, vol. 69, no. 3, pp. 235–244, Mar. 1980.

[69] USGS Chewacla Creek, “USGS Chewacla Creek at Chewacla State Park Auburn,” Auburn, Alabama.

[70] Sluiter A., Hames B., Ruiz R., Scarlata C., Sluiter J., and Templeton D., “Determination of Ash in Biomass, Laboratory Analytical Procedure (LAP),” National Renewable Energy Laboratory, Midwest Research Institute, Technical Report NREL/TP-510-42622, 2008.

[71] 25178-2 ISO, “Geometrical product specifications (GPS) — surface texture: areal — part 2: terms, definitions and surface texture parameters,” Standard, Apr. 2012.

[72] Stout, K. J., “The Pearson system of distributions: its application to non-gaussian surface metrology and a simple wear model,” *J. Lubr. Technol.*, p. 495, Oct. 1980.

[73] C. A. Kotwal and B. Bhushan, “Contact Analysis of Non-Gaussian Surfaces for Minimum Static and Kinetic Friction and Wear,” *Tribol. Trans.*, vol. 39, no. 4, pp. 890–898, Jan. 1996.

[74] N. Tayebi and A. A. Polycarpou, “Modeling the effect of skewness and kurtosis on the static friction coefficient of rough surfaces,” *Tribol. Int.*, vol. 37, no. 6, pp. 491–505, Jun. 2004.

[75] A. L. Carrano, B. K. Thorn, and G. Lopez, “An integer programming approach to the construction of trend-free experimental plans on split-plot designs,” *J. Manuf. Syst.*, vol. 25, no. 1, pp. 39–44, 2006.

[76] A. L. Carrano and B. K. Thorn, “The Construction of Trend-Free Experimental Plans on Two-Level Split-Plot Designs,” *IIE Annu. Conf. Proc. Norcross*, pp. 1–6, 2004.

[77] W. P. Elderton and N. L. Johnson, “Systems of frequency curves,” *CERN Document Server*, 1969. [Online]. Available: http://cds.cern.ch/record/109766. [Accessed: 01-Mar-2017].

[78] S. Boulêtreau, F. Garabétian, S. Sauvage, and J.-M. Sánchez-Pérez, “Assessing the importance of a self-generated detachment process in river biofilm models,” *Freshw. Biol.*, vol. 51, no. 5, pp. 901–912, May 2006.

[79] V. Gosselain, C. Hudon, A. Cattaneo, P. Gagnon, D. Planas, and D. Rochefort, “Physical variables driving epiphytic algal biomass in a dense macrophyte bed of the St. Lawrence River (Quebec, Canada),” *Hydrobiologia*, vol. 534, no. 1–3, pp. 11–22, Feb. 2005.

[80] Hondzo M and Wang H, “Effects of turbulence on growth and metabolism of periphyton in a laboratory flume,” *Water Resour. Res.*, vol. 38, Dec. 2002.

[81] J. M. Piau, N. El Kissi, and B. Tremblay, “Low Reynolds number flow visualization of linear and branched silicones upstream of orifice dies,” *J. Non-Newton. Fluid Mech.*, vol. 30, no. 2, pp. 197–232, Jan. 1988.

[82] G. W. Prescott, “How to know the freshwater algae.,” *Know Freshw. Algae*, 1964.

[83] K. R. Jensen, “Method and system for water purification by culturing and harvesting attached algal communities,” US5573669 A, 12-Nov-1996.

[84] L. Christenson and R. Sims, “Production and harvesting of microalgae for wastewater treatment, biofuels, and bioproducts,” *Biotechnol. Adv.*, vol. 29, no. 6, pp. 686–702, Nov. 2011.

[85] T. Young, “An Essay on the Cohesion of Fluids,” *Philos. Trans. R. Soc. Lond.*, vol. 95, pp. 65–87, 1805.

[86] D. K. Owens and R. C. Wendt, “Estimation of the surface free energy of polymers,” *J. Appl. Polym. Sci.*, vol. 13, no. 8, pp. 1741–1747, Aug. 1969.

[87] R. N. Wenzel, “RESISTANCE OF SOLID SURFACES TO WETTING BY WATER,” *Ind. Eng. Chem.*, vol. 28, no. 8, pp. 988–994, Aug. 1936.

[88] W. Teughels, N. Van Assche, I. Sliepen, and M. Quirynen, “Effect of material characteristics and/or surface topography on biofilm development,” *Clin. Oral Implants Res.*, vol. 17, no. S2, pp. 68–81, Oct. 2006.

[89] H. J. Busscher, A. W. J. van Pelt, P. de Boer, H. P. de Jong, and J. Arends, “The effect of surface roughening of polymers on measured contact angles of liquids,” *Colloids Surf.*, vol. 9, no. 4, pp. 319–331, May 1984.

[90] J. Jopp, H. Grüll, and R. Yerushalmi-Rozen, “Wetting Behavior of Water Droplets on Hydrophobic Microtextures of Comparable Size,” *Langmuir*, vol. 20, no. 23, pp. 10015–10019, Nov. 2004.

[91] M. Kanungo, S. Mettu, K.-Y. Law, and S. Daniel, “Effect of Roughness Geometry on Wetting and Dewetting of Rough PDMS Surfaces,” *Langmuir*, vol. 30, no. 25, pp. 7358–7368, Jul. 2014.

[92] S. M. Lee, C. Y. Park, S. I. Bae, J. S. Go, B. Shin, and J. S. Ko, “Surface Wettability in Terms of the Height and Depression of Diverse Microstructures and Their Sizes,” *Jpn. J. Appl. Phys.*, vol. 48, no. 9, p. 095504, Sep. 2009.

[93] J. M. Lee, S. M. Lee, P. G. Jung, and J. S. Ko, “Superhydrophobic nickel micromesh with microfences,” *J. Micromechanics Microengineering*, vol. 21, no. 10, p. 105003, 2011.

[94] H. Zhao, K.-C. Park, and K.-Y. Law, “Effect of Surface Texturing on Superoleophobicity, Contact Angle Hysteresis, and ‘Robustness,’” *Langmuir*, vol. 28, no. 42, pp. 14925–14934, Oct. 2012.

[95] C. Greiner, A. del Campo, and E. Arzt, “Adhesion of Bioinspired Micropatterned Surfaces: Effects of Pillar Radius, Aspect Ratio, and Preload,” *Langmuir*, vol. 23, no. 7, pp. 3495–3502, Mar. 2007.

[96] Y. Kwon, N. Patankar, J. Choi, and J. Lee, “Design of Surface Hierarchy for Extreme Hydrophobicity,” *Langmuir*, vol. 25, no. 11, pp. 6129–6136, Jun. 2009.

[97] C. Lv, C. Yang, P. Hao, F. He, and Q. Zheng, “Sliding of Water Droplets on Microstructured Hydrophobic Surfaces,” *Langmuir*, vol. 26, no. 11, pp. 8704–8708, Jun. 2010.

[98] D. Li, Y. Xue, P. Lv, S. Huang, H. Lin, and H. Duan, “Receding dynamics of contact lines and size-dependent adhesion on microstructured hydrophobic surfaces,” *Soft Matter*, vol. 12, no. 18, pp. 4257–4265, May 2016.

[99] M.-K. Ng, I. Saxena, K. F. Ehmann, and J. Cao, “Improving Surface Hydrophobicity by Microrolling-based Texturing,” *J. Micro Nano-Manuf.*, May 2016.

[100] M. Nosonovsky and B. Bhushan, “Hierarchical roughness optimization for biomimetic superhydrophobic surfaces,” *Ultramicroscopy*, vol. 107, no. 10–11, pp. 969–979, Oct. 2007.

[101] J. Long, M. N. Hyder, R. Y. M. Huang, and P. Chen, “Thermodynamic modeling of contact angles on rough, heterogeneous surfaces,” *Adv. Colloid Interface Sci.*, vol. 118, no. 1–3, pp. 173–190, Dec. 2005.

[102] M. E. Callow *et al.*, “Microtopographic Cues for Settlement of Zoospores of the Green Fouling Alga Enteromorpha,” *Biofouling*, vol. 18, no. 3, pp. 229–236, Jan. 2002.

[103] A. B. Ponter and M. Yekta-Fard, “The influence of environment on the drop size — contact angle relationship,” *Colloid Polym. Sci.*, vol. 263, no. 8, pp. 673–681, Aug. 1985.

[104] C. W. Extrand and A. N. Gent, “Contact Angle and Spectroscopic Studies of Chlorinated and Unchlorinated Natural Rubber Surfaces,” *Rubber Chem. Technol.*, vol. 61, no. 4, pp. 688–697, Sep. 1988.

[105] J. Goodwin, *Colloids and Interfaces with Surfactants and Polymers*. John Wiley & Sons, 2009.

[106] D. Li, “Drop size dependence of contact angles and line tensions of solid-liquid systems,” *Colloids Surf. Physicochem. Eng. Asp.*, vol. 116, no. 1, pp. 1–23, Sep. 1996.

[107] W. J. Herzberg and J. E. Marian, “Relationship between contact angle and drop size,” *J. Colloid Interface Sci.*, vol. 33, no. 1, pp. 161–163, May 1970.

[108] J. Drelich, “The Effect of Drop (Bubble) Size on Contact Angle at Solid Surfaces,” *J. Adhes.*, vol. 63, no. 1–3, pp. 31–51, Jun. 1997.

[109] J. Drelich, J. D. Miller, and R. J. Good, “The Effect of Drop (Bubble) Size on Advancing and Receding Contact Angles for Heterogeneous and Rough Solid Surfaces as Observed with Sessile-Drop and Captive-Bubble Techniques,” *J. Colloid Interface Sci.*, vol. 179, no. 1, pp. 37–50, Apr. 1996.

[110] J. Drelich and J. D. Miller, “The Effect of Solid Surface Heterogeneity and Roughness on the Contact Angle/Drop (Bubble) Size Relationship,” *J. Colloid Interface Sci.*, vol. 164, no. 1, pp. 252–259, Apr. 1994.

[111] T. S. Meiron, A. Marmur, and I. S. Saguy, “Contact angle measurement on rough surfaces,” *J. Colloid Interface Sci.*, vol. 274, no. 2, pp. 637–644, Jun. 2004.

[112] J. H. Weijs, A. Marchand, B. Andreotti, D. Lohse, and J. H. Snoeijer, “Origin of line tension for a Lennard-Jones nanodroplet,” *Phys. Fluids*, vol. 23, no. 2, p. 022001, Feb. 2011.

[113] “SEMI F63-0213 - Guide for Ultrapure Water Used in Semiconductor Processing.” [Online]. Available: http://ams.semi.org/ebusiness/standards/SEMIStandardDetail.aspx?ProductID=211&DownloadID=2950. [Accessed: 03-Apr-2017].

[114] Woodward R. P, “Contact angle measurements using the drop shape method,” First Ten Angstroms Inc., Portsmouth, Virginia, Technical Report, 1999.

[115] Stratasys, Ltd., “Safety data sheet for Objet VeroWhiteplus RGD835 material,” Jul. 2014.

[116] K. Siegbahn and K. Edvarson, “β-Ray spectroscopy in the precision range of 1 : 105,” *Nucl. Phys.*, vol. 1, no. 8, pp. 137–159, Jan. 1956.

[117] “X-ray photoelectron spectroscopy,” *Wikipedia*. 21-Feb-2017.

[118] J. F. Joanny and P. G. de Gennes, “A model for contact angle hysteresis,” *J. Chem. Phys.*, vol. 81, no. 1, pp. 552–562, Jul. 1984.

[119] E. L. Decker, B. Frank, Y. Suo, and S. Garoff, “Physics of contact angle measurement,” *Colloids Surf. Physicochem. Eng. Asp.*, vol. 156, no. 1–3, pp. 177–189, Oct. 1999.

[120] R. G. Cox, “Inertial and viscous effects on dynamic contact angles,” *J. Fluid Mech.*, vol. 357, pp. 249–278, Feb. 1998.

[121] J. Bico, U. Thiele, and D. Quéré, “Wetting of textured surfaces,” *Colloids Surf. Physicochem. Eng. Asp.*, vol. 206, no. 1, pp. 41–46, Jul. 2002.

[122] J. Bico, C. Tordeux, and D. Quéré, “Rough wetting,” *EPL Europhys. Lett.*, vol. 55, no. 2, p. 214, Jul. 2001.

[123] Boschetto, A., Giordano, V., and Veniali, F., “3D roughness profile model in fused deposition modelling,” *Rapid Prototyp. J.*, vol. 19, no. 4, pp. 240–252, Jun. 2013.

[124] D. Ahn, J. H. Kweon, J. Choi, and S. Lee, “Quantification of surface roughness of parts processed by laminated object manufacturing,” *J. Mater. Process. Technol.*, vol. 212, no. 2, pp. 339–346, Feb. 2012.

[125] S. L. Campanelli, G. Cardano, R. Giannoccaro, A. D. Ludovico, and E. L. J. Bohez, “Statistical analysis of the stereolithographic process to improve the accuracy,” *Comput.-Aided Des.*, vol. 39, no. 1, pp. 80–86, Jan. 2007.

[126] J. G. Zhou, D. Herscovici, and C. C. Chen, “Parametric process optimization to improve the accuracy of rapid prototyped stereolithography parts,” *Int. J. Mach. Tools Manuf.*, vol. 40, no. 3, pp. 363–379, Feb. 2000.

[127] P. B. Bacchewar, S. K. Singhal, and P. M. Pandey, “Statistical modelling and optimization of surface roughness in the selective laser sintering process,” *Proc. Inst. Mech. Eng. Part B J. Eng. Manuf.*, vol. 221, no. 1, pp. 35–52, Jan. 2007.

[128] A. Triantaphyllou *et al.*, “Surface texture measurement for additive manufacturing,” *Surf. Topogr. Metrol. Prop.*, vol. 3, no. 2, p. 024002, 2015.

[129] A. Ellis, R. Brown, and N. Hopkinson, “The effect of build orientation and surface modification on mechanical properties of high speed sintered parts,” *Surf. Topogr. Metrol. Prop.*, vol. 3, no. 3, p. 034005, 2015.

[130] Khoshkhoo A, Carrano A. L, and Blersch D. M, “Effect of build orientation and part thickness on dimensional distortion in material jetting processes,” *Rapid Prototyp. J.*, 2018.

[131] Campbell L, “Design for additive manufacturing guidelines,” Wohlers Associates, Inc., NASA Marshall Space Flight Center, Huntsville, Alabama, Aug. 2015.

[132] Y.-M. Huang and H.-Y. Lan, “Compensation of distortion in the bottom exposure of stereolithography process,” *Int. J. Adv. Manuf. Technol.*, vol. 27, no. 11–12, pp. 1101–1112, Feb. 2006.

[133] Phan T. D. and S. H. Masood, “An analysis of textured features fabricated by FDM rapid prototyping process,” *Int. J. IE Theory Appl.*, vol. 6, no. 1, pp. 13–22, 2010.

[134] R. Udroiu and L. Mihail, “Experimental determination of surface roughness of parts obtained by rapid prototyping,” in *8th WSEAS International Conference on Circuits, Systems, Electronics, Control and Signal Processing*, Puerto De La Cruz, Tenerife, Canary Islands, Spain, 2009, pp. 283–286.

[135] K. Kumar and G. S. Kumar, “An experimental and theoretical investigation of surface roughness of poly-jet printed parts,” *Virtual Phys. Prototyp.*, vol. 10, no. 1, pp. 23–34, 2015.

[136] N. Meisel and C. Williams, “An Investigation of Key Design for Additive Manufacturing Constraints in Multimaterial Three-Dimensional Printing,” *J. Mech. Des.*, vol. 137, no. 11, pp. 111406-111406–9, Oct. 2015.

[137] Bugeda G, Cervera M, Lombera G, and Onate E, “Numerical analysis of stereolithography processes using the finite element method,” *Rapid Prototyp. J.*, vol. 1, no. 2, pp. 13–23, Jun. 1995.

[138] Vu I, Bass L, Meisel N, and Orler B, “Characterization of multi-material interfaces in polyjet additive manufacturing,” presented at the Solid Freeform Fabrication Symposium, 2014, pp. 959–982.

[139] N. A. Fleck, J. W. Hutchinson, and S. Zhigang, “Crack path selection in a brittle adhesive layer,” *Int. J. Solids Struct.*, vol. 27, no. 13, pp. 1683–1703, Jan. 1991.

[140] A. Pilipović, P. Raos, and M. Šercer, “Experimental analysis of properties of materials for rapid prototyping,” *Int. J. Adv. Manuf. Technol.*, vol. 40, no. 1–2, pp. 105–115, Jan. 2009.

[141] Mueller J, Kim S, Shea K, and Daraio C, “Tensile properties of inkjet 3d printed parts: critical process parameters and their efficient analysis,” presented at the ASME Computers and Information in Engineering Conference, Boston, MA, 2015, pp. 1–10.

[142] Mueller J and Shea K, “The effect of build orientation on the mechanical properties in inkjet 3d printing,” presented at the International Solid Freeform Fabrication Symposium, Austin, TX, 2015, pp. 983–992.

[143] Moore J and Williams C, “Fatigue properties of parts printed by polyjet material jetting,” *Rapid Prototyp. J.*, vol. 21, no. 6, pp. 675–685, Oct. 2015.

[144] L. Bass, N. A. Meisel, and C. B. Williams, “Exploring variability of orientation and aging effects in material properties of multi-material jetting parts,” *Rapid Prototyp. J.*, vol. 22, no. 5, pp. 826–834, Aug. 2016.

[145] Vatani M, Barazandeh F, Rahimi A, and Nezhad A, “Distortion modeling of SL parts by classical lamination theory,” *Rapid Prototyp. J.*, vol. 18, no. 3, pp. 188–193, Apr. 2012.

[146] Y. M. Huang and C. P. Jiang, “Curl distortion analysis during photopolymerisation of stereolithography using dynamic finite element method,” *Int. J. Adv. Manuf. Technol.*, vol. 21, no. 8, pp. 586–595, Jun. 2003.

[147] Tröger C, Arthur B, Bermes G, Klemmer R, Lenz J, and Irsen S, “Ageing of acrylate-based resins for stereolithography: thermal and humidity ageing behaviour studies,” *Rapid Prototyp. J.*, vol. 14, no. 5, pp. 305–317, Sep. 2008.

[148] El-Sherif L, “Modeling stereolithography process parameters using system dynamics,” Arab Academy for Science, Technology & Maritime Transport, Alexandria, Egypt, 2015.

[149] Parlevliet P. P, Bersee H. E. N, and Beukers A, “Residual stresses in thermoplastic composites—a study of the literature—part I: formation of residual stresses,” *Compos. Part Appl. Sci. Manuf.*, vol. 37, no. 11, pp. 1847–1857, Nov. 2006.

[150] J. A. Nairn and P. Zoller, “The development of residual thermal stresses in amorphous and semicrystalline thermoplastic matrix composites,” in *Toughened Composites*, ASTM International, 1987, pp. 328–341.

[151] ASTM, “Standard practice for measuring flatness characteristics of steel sheet products,” Standard, Spring 2016.

[152] M. Monzón, Z. Ortega, A. Hernández, R. Paz, and F. Ortega, “Anisotropy of photopolymer parts made by digital light processing,” *Materials*, vol. 10, no. 1, p. 64, Jan. 2017.

[153] J. Mueller, K. Shea, and C. Daraio, “Mechanical properties of parts fabricated with inkjet 3d printing through efficient experimental design,” *Mater. Des.*, vol. 86, pp. 902–912, Dec. 2015.

[154] N. Meisel and C. Williams, “Design for additive manufacturing: an investigation of key manufacturing considerations in multi-material polyjet 3d printing,” in *The solid freeform fabrication symposium*, Austin, TX, 2014, pp. 746–763.

[155] “Surface Imaging, Analysis and Metrology Software.” [Online]. Available: http://www.digitalsurf.com/en/index.html. [Accessed: 22-Mar-2017].

[156] Khoshkhoo A, Carrano A. L, and Blersch D. M, “Effect of surface slope and build orientation on surface finish and dimensional accuracy in material jetting processes,” in *NAMRC 46*, College station, Texas, 2018.

[157] ISO 13565-2, “Geometrical product specifications (GPS) — surface texture: profile method; surfaces having stratified functional properties — part 2: height characterization using the linear material ratio curve,” Standard, 1996.

[158] ISO 13565-3, “Geometrical Product Specifications (GPS) — Surface texture: Profile method; Surfaces having stratified functional properties — Part 3: Height characterization using the material probability curve,” Standard, 1998.

[159] G. Bitelli, A. Simone, F. Girardi, and C. Lantieri, “Laser scanning on road pavements: a new approach for characterizing surface texture,” *Sensors*, vol. 12, no. 7, pp. 9110–9128, Jul. 2012.

[160] F. Blateyron, “The areal field parameters,” in *Characterisation of Areal Surface Texture*, Springer, Berlin, Heidelberg, 2013, pp. 15–43.

[161] J. Molleda, R. Usamentiaga, D. F. García, and F. G. Bulnes, “Real-time flatness inspection of rolled products based on optical laser triangulation and three-dimensional surface reconstruction,” *J. Electron. Imaging*, vol. 19, no. 3, pp. 35–47, 2010.

[162] D. Zwillinger, *Standard mathematical tables and formulae*, 31st ed. in CRC press, 2002.

[163] J.Y.H. Fuh, L. Lu, C.C. Tan, Z.X. Shen, and S. Chew, “Curing characteristics of acrylic photopolymer used in stereolithography process,” *Rapid Prototyp. J.*, vol. 5, no. 1, pp. 27–34, Mar. 1999.

[164] W. C. Bushko and V. K. Stokes, “Solidification of thermoviscoelastic melts. Part II: Effects of processing conditions on shrinkage and residual stresses,” *Polym. Eng. Sci.*, vol. 35, no. 4, pp. 365–383, Feb. 1995.

Appendix I (Surface Texture Parameters)

1. *Terms, definitions, and Surface Texture Parameters*

In the following terminological parameters, each term is followed by its parameter and symbol.

1.1. *Height Parameters*

All height parameters are defined over the definition area.

1.1.1. *Root mean square height of the scale-limited surface*

S_q, is the root mean square value of the ordinate values within a definition area (A).

$$S_q = \sqrt{\frac{1}{A}\iint_A z^2(x,y)dxdy}$$

1.1.2. *Skewness of the scale-limited surface*

Ssk is the quotient of the mean cube value of the ordinate values and the cube of S_q within a definition area (A).

$$Ssk = \frac{1}{S_q^3}\left[\frac{1}{A}\iint_A z^3(x,y)dxdy\right]$$

1.1.3. *Kurtosis of the scale-limited surface*

Sku is the quotient of the mean quartic value of the ordinate values and the fourth power of S_q within a definition area (A).

$$Sku = \frac{1}{S_q^4}\left[\frac{1}{A}\iint_A z^4(x,y)dxdy\right]$$

1.1.4. *The maximum peak height of the scale-limited surface*

S_p is the largest peak height value within a definition area.

1.1.5. *Maximum pit height of the scale-limited surface*

S_v is the smallest pit height value within a definition area.

1.1.6. The maximum height of the scale-limited surface

S_z is the sum of the maximum peak height value and the maximum pit height value within a definition area.

1.1.7. The arithmetical mean height of the scale-limited surface

S_a is the arithmetical mean of the absolute of the ordinate values within a definition area (A).

$$S_a = \frac{1}{A}\iint_A |z(x,y)|dxdy$$

1.2. Spatial Parameters

All spatial parameters are defined over the definition area.

1.2.1. Autocorrelation length

S_{al} is the horizontal distance of the $f_{ACF}(t_x,t_y)$ which has the fastest decay to a specified value s, with $0 \leq s < 1$.

$$S_{al} = \min_{t_x,t_y \epsilon R}\sqrt{t_x^2+t_y^2} \text{ where } R = \{(t_x,t_y): f_{ACF}(t_x,t_y) \leq s\}.$$

1.2.2. Texture aspect ratio

S_{tr} is the ratio of the horizontal distance of the $f_{ACF}(t_x,t_y)$ which has the fastest decay to a specified value s, to the horizontal distance of the $f_{ACF}(t_x,t_y)$ which has the lowest decay to s, with $0 \leq s < 1$.

$$S_{tr} = \frac{\min_{t_x,t_y \epsilon R}\sqrt{t_x^2+t_y^2}}{\max_{t_x,t_y \epsilon Q}\sqrt{t_x^2+t_y^2}} \text{ where } \begin{matrix} R=\{(t_x,t_y):f_{ACF}(t_x,t_y)\leq s\} \\ Q=\{(t_x,t_y):f_{ACF}(t_x,t_y)\geq s \text{ and} **\} \end{matrix} .$$

Where ** is the property that the $f_{ACF} \geq s$ on the straight line connecting the point (t_x,t_y) to the origin.

1.3. Hybrid parameters

1.3.1. Root mean square gradient of the scale-limited surface

S_{dq} is the root mean square of the surface gradient within the definition area (A) of a scale-limited surface.

$$S_{dq} = \sqrt{\frac{1}{A}\iint_A \left[\frac{\partial_z(x,y)}{\partial_x}\right]^2 + \left[\frac{\partial_z(x,y)}{\partial_y}\right]^2 dxdy}$$

1.3.2. The developed interfacial area ratio of the scale-limited surface

S_{dr} is the ratio of the increment of the interfacial area of the scale-limited surface within the definition area (A) over the definition area.

$$S_{dr} = \frac{1}{A}\left[\iint_A \left(\sqrt{1 + \left[\frac{\partial_z(x,y)}{\partial_x}\right]^2 + \left[\frac{\partial_z(x,y)}{\partial_y}\right]^2} - 1\right)dxdy\right]$$

1.4. Functions and Related Parameters

1.4.1. Areal material ratio function of the scale-limited surface

The function is representing the areal material ratio of the scale-limited surface as a function of height.

1.4.2. The areal material ratio of the scale-limited surface

$S_{mr}(c)$ is the ratio of the material at a specified height c to the evaluation area.

1.4.3. The inverse areal material ratio of the scale-limited surface

$S_{mc}(mr)$, is height c at which a given material ratio (mr) is satisfied.

1.4.4. The areal parameter for scale-limited stratified functional surfaces

A parameter representing the areal material ratio of the scale-limited stratified functional surfaces as a function of height.

1.4.5. Core surface

Scale-limited surface excluding core-protruding hills and dales.

1.4.6. Core height

S_k is the distance between the highest and lowest level of the core surface.

1.4.7. Reduced peak height

S_{pk} is the average height of the protruding peaks above the core surface.

1.4.8. Reduced dale height

S_{vk} is the average height of the protruding dales below the core surface.

1.4.9. Material ratio

S_{mr1} is the (peaks) ratio of the area of the material at the intersection line which separates the protruding hills from the core surface to the evaluation area.

1.4.10. Material ratio

S_{mr2} is the (dales) ratio of the area of the material at the intersection line which separates the protruding dales from the core surface to the evaluation area.

1.4.11. The areal material probability curve

Representation of the areal material ratio curve in which the areal material ratio is expressed as a Gaussian probability in standard deviation values plotted linearly on the horizontal axis.

1.4.12. Dale root mean square deviation

S_{vq} is the angle of a linear regression performed through the dale region.

1.4.13. Plateau root mean square deviation

S_{pq}, is the angle of a linear regression performed through the plateau region

1.4.14. Material ratio

S_{mq}, (plateau-to-dale) areal material ratio at the plateau-to-dale intersection.

1.4.15. Void volume

$V_v(p)$, is the volume of the voids per unit area at a given material ratio calculated from the areal material ratio curve.

$$V_v(p) = \frac{K}{100\%}\int_p^{100\%}[S_{mc}(p) - S_{mc}(q)]dq$$

Where K is a constant to convert to milliliters per meters squared.

1.4.16. Dale void volume of the scale-limited surface

V_{vv}, is dale volume at p material ratio.

$$V_{vv} = V_v(p)$$

1.4.17. Core void volume of the scale-limited surface

V_{vc} is the difference in void volume between p and q material ratio.

$$V_{vc} = V_v(p) - V_v(q)$$

1.4.18. Material volume

$V_m(p)$ is the volume of the material per unit area at a given material ratio calculated from the areal material ratio curve.

$$V_m(p) = \frac{K}{100\%}\int_p^{100\%}[S_{mc}(q) - S_{dc}(p)]dq$$

Where K is a constant to convert to milliliters per meters squared.

1.4.19. Peak material volume of the scale-limited surface

V_{mp} is material volume at p.

1.4.20. Core material volume of the scale-limited surface

V_{mc} the difference in material volume between the p and q material ratio.

$V_{mc} = V_m(q) - V_m(p)$

1.4.21. Peak extreme height

S_{xp} is the difference in height between the p and q material ratio.

$S_{xp} = S_{mc}(p) - S_{mc}(q)$

1.5. Named Feature Parameters

1.5.1. Density of peaks

S_{xp} is the number of peaks per unit area.

1.5.2. Arithmetic mean peak curvature

S_{pc} is the arithmetic mean of the principle curvatures of peaks within a definition area

1.5.3. The ten-point height of the surface

S_{10z} is the average value of the heights of five peaks with largest global peak height added to the average value of the heights of the five pits with largest global pit height, within the definition area.

$S_{10z} = S_{5p} + S_{5v}$

1.5.4. Five-point peak height

S_{5p} is the average value of the heights of the five peaks with largest global peak height, within the definition area.

1.5.5. Five-point pit height

S_{5v} is the average value of the heights of the five pits with largest global pit height, within the definition area.

1.5.6. Mean dale area

$S_{da}(c)$

1.5.7. Mean hill area

$S_{ha}(c)$

1.5.8. Mean dale volume

$S_{dv}(c)$

1.5.9. Mean hill volume

$S_{hv}(c)$

Appendix II (Chapter I: Reverse Engineering of Natural Surfaces with Additive Manufacturing)

Log Data from Bioreactor

Date	Time	Room temperature (F)	Water Temperature (F)	pH	Conductivity	Nitrate (mg/l NO3^-)	Nitrate (mg/l NO3-N)	Comments
12/3/2017	6:17 PM	70.70	73.00	5.42	0.03	10.00	2.26	Colonization 1
12/4/2017	8:32 AM	70.70	76.40	7.57	0.03	12.00	2.71	
	8:17 PM	69.70	76.40	7.42	0.03	12.00	2.71	
12/5/2017	8:37 AM	70.00	74.60	7.63	0.02	8.00	1.81	
	8:17 PM	70.20	76.60	7.55	0.03	9.00	2.03	
12/6/2017	8:31 AM	68.90	75.70	7.26	0.03	8.00	1.81	
	8:25 PM	67.00	75.30	7.57	0.03	8.00	1.81	
12/7/2017	8:33 AM	64.80	75.20	6.89	0.03	6.00	1.36	
	8:03 PM	69.20	75.30	6.60	0.03	6.00	1.36	
12/8/2017	8:44 AM	67.50	75.20	7.24	0.03	6.00	1.36	
	8:59 PM	68.00	75.20	6.85	0.03	7.00	1.58	
12/9/2017	8:43 AM	67.70	75.00	6.40	0.03	7.00	1.58	
	8:29 PM	61.80	74.40	6.86	0.03	5.00	1.13	
12/10/2017	8:39 AM	64.80	74.60	7.24	0.03	6.00	1.36	
	7:00 PM	66.10	74.00	7.16	0.03	4.00	0.90	Colonization 2
12/11/2017	8:44 AM	66.80	74.80	6.80	0.03	5.00	1.13	
	8:35 PM	66.40	75.00	7.05	0.03	4.00	0.90	
12/12/2017	8:29 AM	65.70	75.20	6.42	0.03	5.00	1.13	
	9:00 PM	66.00	75.00	6.73	0.03	8.00	1.81	
12/13/2017	10:06 AM	62.70	74.30	6.20	0.03	8.00	1.81	
	9:25 PM	67.70	74.00	6.80	0.03	7.00	1.58	

12/14/2017	8:37 AM	63.00	74.60	6.72	0.03	8.00	1.81	
	8:31 PM	63.00	74.70	6.82	0.03	8.00	1.81	
12/15/2017	8:41 AM	65.80	70.70	6.86	0.03	9.00	2.03	
	8:18 PM	65.50	74.40	6.67	0.03	8.00	1.81	
12/16/2017	7:30 AM	63.80	74.60	6.69	0.03	10.00	2.26	
	8:25 PM	66.50	74.60	6.84	0.03	7.00	1.58	
12/17/2017	8:12 AM	66.10	74.70	6.87	0.03	9.00	2.03	
	5:15 PM	66.80	76.10	6.41	0.03	8.00	1.81	Colonization 3
12/18/2017	8:25 AM	68.90	76.50	6.90	0.03	10.00	2.26	
	8:21 PM	68.10	76.00	6.96	0.03	8.00	1.81	
12/19/2017	8:21 AM	67.30	76.80	6.86	0.03	10.00	2.26	
	8:34 PM	68.00	76.70	6.87	0.03	9.00	2.03	
12/20/2017	8:47 AM	68.10	76.80	6.55	0.03	8.00	1.81	
	8:31 PM	67.90	77.00	6.58	0.03	8.00	1.81	
12/21/2017	8:31 AM	67.90	76.80	6.94	0.03	8.00	1.81	
	8:19 PM	68.20	76.60	6.81	0.03	7.00	1.58	
12/22/2017	8:25 AM	67.90	77.00	6.30	0.03	8.00	1.81	
	8:26 PM	68.10	76.90	6.30	0.03	5.00	1.13	
12/23/2017	8:23 AM	68.40	77.30	6.94	0.03	8.00	1.81	
	7:42 PM	68.50	77.00	6.38	0.03	7.00	1.58	
12/24/2017	8:19 AM	67.50	76.10	6.62	0.03	7.00	1.58	
	5:52 PM	67.00	75.80	6.93	0.03	10.00	2.26	

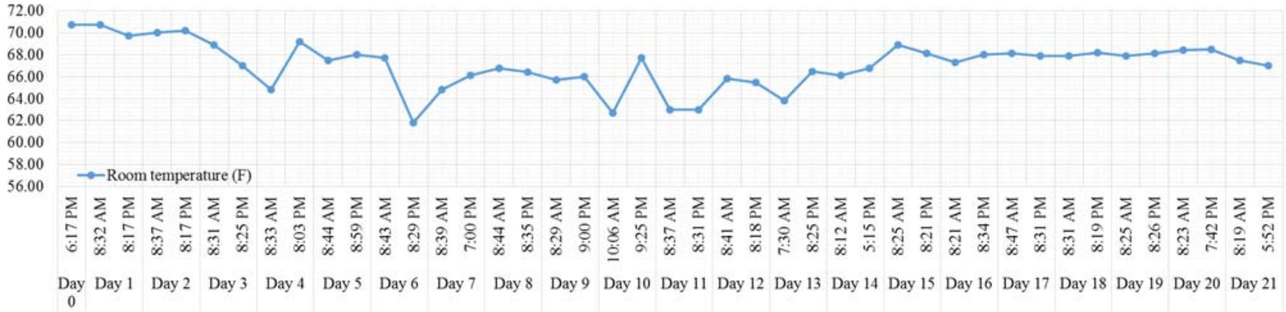

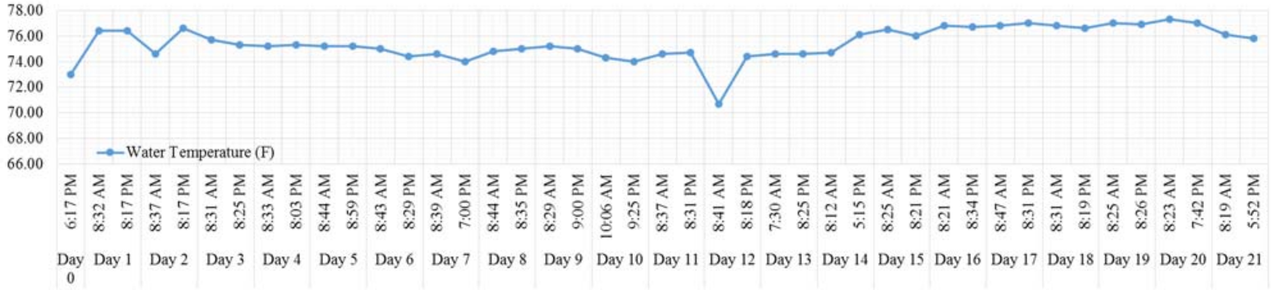

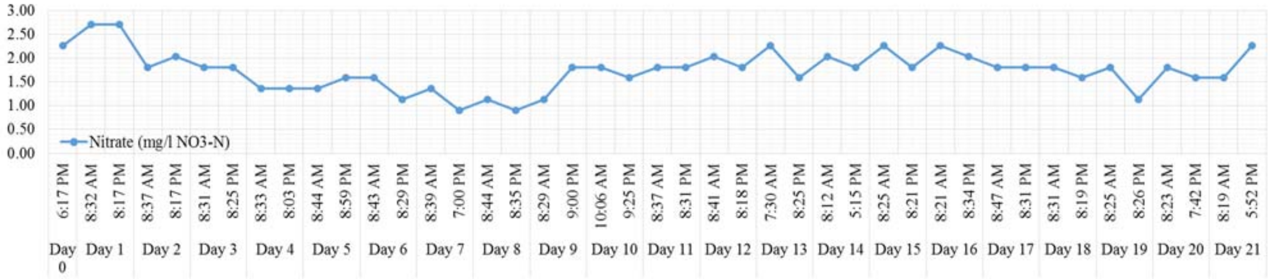

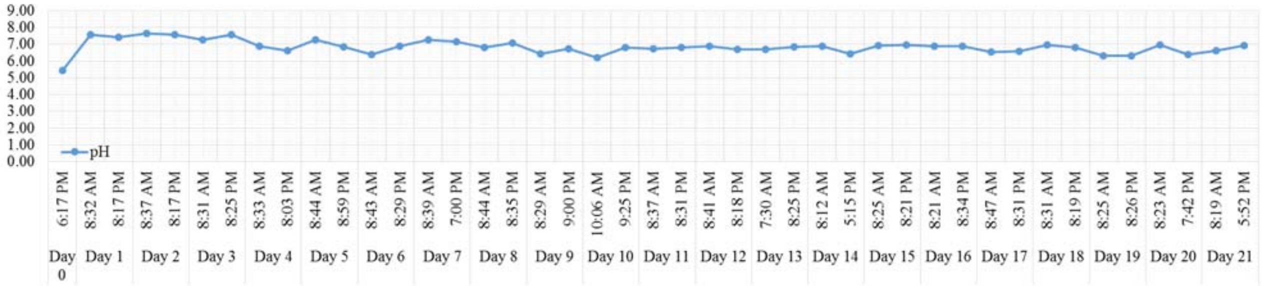

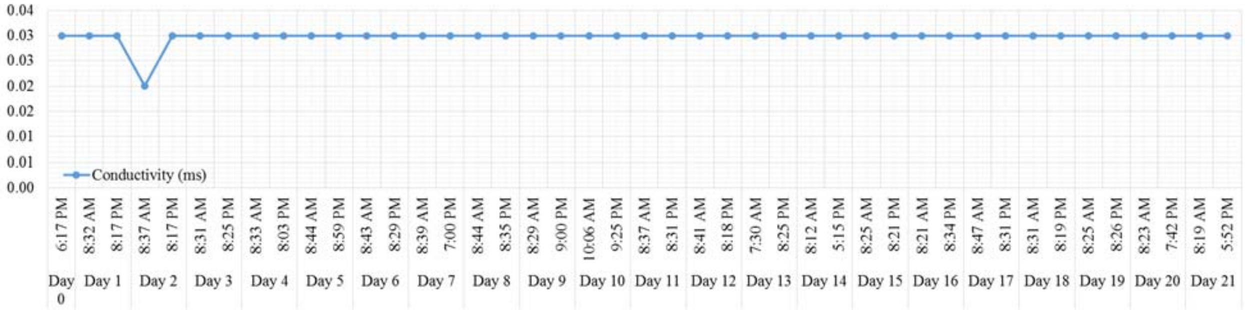

Time to fill 2 litters (s)				
	Lane 1	Lane 2	Lane 3	Lane 4
Rep 1	13.980	13.560	13.510	13.500
Rep 2	13.860	13.830	13.570	13.780
Rep 3	14.130	13.680	13.730	13.400
Rep 4	13.960	13.660	13.730	13.520
Rep 5	13.880	13.530	13.910	13.450
Average	13.962	13.652	13.690	13.530
STD	0.107	0.118	0.157	0.147

Flow rate (m^3/s)				
	Lane 1	Lane 2	Lane 3	Lane 4
Rep 1	0.0001431	0.0001475	0.0001480	0.0001481
Rep 2	0.0001443	0.0001446	0.0001474	0.0001451
Rep 3	0.0001415	0.0001462	0.0001457	0.0001493

Rep 4	0.0001433	0.0001464	0.0001457	0.0001479
Rep 5	0.0001441	0.0001478	0.0001438	0.0001487
Average	0.0001433	0.0001465	0.0001461	0.0001478
STD	0.0000011	0.0000013	0.0000017	0.0000016

	Travel time (s)			
	Lane 1	Lane 2	Lane 3	Lane 4
Rep 1	3.620	4.340	4.050	4.640
Rep 2	3.610	4.250	4.280	4.470
Rep 3	3.620	4.360	4.190	4.140
Rep 4	3.630	4.130	4.140	4.920
Rep 5	3.610	4.220	4.490	4.900
Average	3.618	4.260	4.230	4.614
STD	0.008	0.094	0.167	0.325

	Velocity (m/s)			
	Lane 1	Lane 2	Lane 3	Lane 4
Rep 1	0.334	0.281	0.299	0.263
Rep 2	0.335	0.287	0.283	0.273
Rep 3	0.334	0.280	0.289	0.295
Rep 4	0.333	0.295	0.292	0.248
Rep 5	0.335	0.289	0.269	0.249
Length (m)	1.210	1.220	1.210	1.220
Average	0.334	0.286	0.286	0.265
STD	0.001	0.006	0.011	0.019

Log Data from Computer Model

Reps	Level 1								
	Zavg	Sa	Sq	Ssk	Sku	Sv	Sp	Sz	Smr
Rep 1	-1.62	0.74	0.92	0.98	2.81	6.68	2.83	9.51	31.67
Rep 2	-1.43	0.73	0.92	0.96	2.81	6.63	2.52	9.14	31.16
Rep 3	-1.65	0.73	0.91	0.98	2.76	6.69	2.54	9.24	30.07
Rep 4	-1.52	0.73	0.92	0.95	2.82	6.77	2.52	9.29	32.07
Rep 5	-1.66	0.74	0.93	0.93	2.85	7.16	2.75	9.91	31.06
Rep 6	-1.53	0.74	0.92	1.01	2.82	6.55	2.74	9.28	31.62

Rep 7	-1.47	0.72	0.91	0.98	2.79	6.71	2.51	9.22	29.05
Rep 8	-1.42	0.72	0.90	1.00	2.79	6.47	2.43	8.90	29.96
Rep 9	-1.56	0.71	0.89	1.05	2.77	6.35	2.56	8.91	28.88
Rep 10	-1.53	0.72	0.91	0.98	2.81	6.61	2.80	9.42	30.92
Rep 11	-1.62	0.73	0.92	0.95	2.82	6.65	2.68	9.33	31.80
Rep 12	-1.70	0.73	0.91	0.99	2.79	6.70	2.60	9.30	31.52
Rep 13	-1.42	0.72	0.90	1.00	2.79	6.47	2.43	8.90	29.96
Rep 14	-1.56	0.71	0.89	1.05	2.77	6.35	2.56	8.91	28.88
Rep 15	-1.51	0.71	0.90	1.04	2.81	6.53	2.43	8.96	28.21
Rep 16	-1.60	0.72	0.90	1.05	2.79	6.36	2.58	8.94	29.98
Rep 17	-1.65	0.73	0.91	0.98	2.76	6.69	2.54	9.24	30.07
Rep 18	-1.66	0.74	0.93	0.93	2.85	7.16	2.75	9.91	31.06
Rep 19	-1.47	0.72	0.91	0.98	2.79	6.71	2.51	9.22	29.05
Rep 20	-1.42	0.72	0.90	1.00	2.79	6.47	2.43	8.90	29.96
Rep 21	-1.56	0.71	0.89	1.05	2.77	6.35	2.56	8.91	28.88
Rep 22	-1.53	0.72	0.91	0.98	2.81	6.61	2.80	9.42	30.92
Rep 23	-1.53	0.73	0.92	0.97	2.79	6.81	2.59	9.40	31.02
Rep 24	-1.51	0.71	0.90	1.04	2.81	6.53	2.43	8.96	28.21
Rep 25	-1.65	0.73	0.91	0.98	2.76	6.69	2.54	9.24	30.07
Rep 26	-1.66	0.74	0.93	0.93	2.85	7.16	2.75	9.91	31.06
Rep 27	-1.47	0.72	0.91	0.98	2.79	6.71	2.51	9.22	29.05
Rep 28	-1.42	0.72	0.90	1.00	2.79	6.47	2.43	8.90	29.96
Rep 29	-1.56	0.71	0.89	1.05	2.77	6.35	2.56	8.91	28.88
Rep 30	-1.53	0.72	0.91	0.98	2.81	6.61	2.80	9.42	30.92
Rep 31	-1.51	0.71	0.90	1.04	2.81	6.53	2.43	8.96	28.21
Rep 32	-1.65	0.73	0.91	0.98	2.76	6.69	2.54	9.24	30.07
Rep 33	-1.66	0.74	0.93	0.93	2.85	7.16	2.75	9.91	31.06
Rep 34	-1.47	0.72	0.91	0.98	2.79	6.71	2.51	9.22	29.05
Rep 35	-1.51	0.71	0.90	1.04	2.81	6.53	2.43	8.96	28.21
Rep 36	-1.56	0.71	0.89	1.05	2.77	6.35	2.56	8.91	28.88
Average	-1.55	0.72	0.91	0.99	2.80	6.64	2.58	9.22	30.04
STD	0.083563	0.01	0.011313	0.037362	0.025987	0.23	0.128491	0.31066	1.16
CV (%)	5.40	1.35	1.24	3.76	0.93	3.44	4.98	3.37	3.87
Min	-1.70	0.71	0.89	0.93	2.76	6.35	2.43	8.90	28.21
Max	-1.42	0.74	0.93	1.05	2.85	7.16	2.83	9.91	32.07

Reps	Level 2								
	Zavg	Sa	Sq	Ssk	Sku	Sv	Sp	Sz	Smr

Rep 1	-1.92	2.17	2.74	-0.09	3.00	8.84	9.71	18.56	51.86
Rep 2	-0.84	2.03	2.52	-0.23	2.78	7.78	7.62	15.40	52.72
Rep 3	-1.10	2.18	2.73	-0.25	3.20	10.34	8.44	18.78	50.90
Rep 4	-2.19	1.89	2.38	-0.13	2.91	8.17	7.81	15.97	50.84
Rep 5	-0.72	2.07	2.54	0.00	2.60	7.97	8.03	16.01	50.65
Rep 6	-1.39	2.07	2.57	-0.13	2.84	8.67	7.66	16.33	50.88
Rep 7	-1.67	2.41	2.96	-0.20	2.68	9.58	8.45	18.03	52.25
Rep 8	-0.95	2.12	2.62	-0.06	2.57	6.90	8.21	15.10	51.68
Rep 9	-1.08	1.87	2.35	-0.26	2.93	8.31	7.56	15.87	53.75
Rep 10	-1.35	2.28	2.87	-0.02	3.07	8.91	9.62	18.53	50.74
Rep 11	-1.89	2.24	2.78	0.06	2.76	8.33	9.00	17.34	50.54
Rep 12	-1.41	2.12	2.63	-0.13	2.72	8.10	7.77	15.87	51.52
Rep 13	-1.92	2.17	2.74	-0.09	3.00	8.84	9.71	18.56	51.86
Rep 14	-0.84	2.03	2.52	-0.23	2.78	7.78	7.62	15.40	52.72
Rep 15	-1.10	2.18	2.73	-0.25	3.20	10.34	8.44	18.78	50.90
Rep 16	-2.19	1.89	2.38	-0.13	2.91	8.17	7.81	15.97	50.84
Rep 17	-0.72	2.07	2.54	0.00	2.60	7.97	8.03	16.01	50.65
Rep 18	-1.39	2.07	2.57	-0.13	2.84	8.67	7.66	16.33	50.88
Rep 19	-1.67	2.41	2.96	-0.20	2.68	9.58	8.45	18.03	52.25
Rep 20	-0.95	2.12	2.62	-0.06	2.57	6.90	8.21	15.10	51.68
Rep 21	-1.08	1.87	2.35	-0.26	2.93	8.31	7.56	15.87	53.75
Rep 22	-1.35	2.28	2.87	-0.02	3.07	8.91	9.62	18.53	50.74
Rep 23	-1.89	2.24	2.78	0.06	2.76	8.33	9.00	17.34	50.54
Rep 24	-1.41	2.12	2.63	-0.13	2.72	8.10	7.77	15.87	51.52
Rep 25	-1.92	2.17	2.74	-0.09	3.00	8.84	9.71	18.56	51.86
Rep 26	-0.84	2.03	2.52	-0.23	2.78	7.78	7.62	15.40	52.72
Rep 27	-1.67	2.41	2.96	-0.20	2.68	9.58	8.45	18.03	52.25
Rep 28	-0.95	2.12	2.62	-0.06	2.57	6.90	8.21	15.10	51.68
Rep 29	-1.08	1.87	2.35	-0.26	2.93	8.31	7.56	15.87	53.75
Rep 30	-1.41	2.12	2.63	-0.13	2.72	8.10	7.77	15.87	51.52
Rep 31	-0.77	1.88	2.32	-0.16	2.69	6.81	7.10	13.90	51.44
Rep 32	-2.02	2.04	2.55	-0.19	2.78	7.94	8.65	16.59	52.57
Rep 33	-1.61	2.34	2.89	-0.31	2.71	8.36	8.18	16.54	53.05
Rep 34	-0.98	2.33	2.91	-0.15	2.86	8.67	10.06	18.73	52.43
Rep 35	-1.65	1.98	2.52	-0.15	3.16	8.24	8.28	16.52	51.21
Rep 36	-1.31	1.81	2.23	-0.14	2.73	7.17	7.10	14.26	51.23
Average	-1.37	2.11	2.63	-0.14	2.82	8.35	8.29	16.64	51.73
STD	0.439486	0.16	0.199729	0.093453	0.17743	0.86	0.793722	1.402544	0.94
CV (%)	32.12	7.74	7.60	67.55	6.28	10.33	9.57	8.43	1.82
Min	-2.19	1.81	2.23	-0.31	2.57	6.81	7.10	13.90	50.54

Max	-0.72	2.41	2.96	0.06	3.20	10.34	10.06	18.78	53.75

Log Data from Biomass Measurement (Reverse Engineering of Natural Surfaces with Additive Manufacturing)

	Level 1	
	Sample	Dried biomass-level 1
Run 1	1_1	0.0149
	2_1	0.0098
	3_1	0.0133
	4_1	0.0142
	5_1	0.0112
	6_1	0.016
	7_1	0.0123
	8_1	0.0083
	9_1	0.0184
	10_1	0.0122
	11_1	0.0096
	12_1	0.0154
Run 2	1_1	0.0065
	2_1	0.0101
	3_1	0.0128
	4_1	0.0092
	5_1	0.0072
	6_1	0.013
	7_1	0.0069
	8_1	0.0051
	9_1	0.0062
	10_1	0.0127
	11_1	0.0158
	12_1	0.0056
Run 3	1_1	0.0123
	2_1	0.0141
	3_1	0.0138
	4_1	0.0116
	5_1	0.0126
	6_1	0.0159
	7_1	0.0211
	8_1	0.0144
	9_1	0.0174

	10_1	0.0202
	11_1	0.0171
	12_1	0.0187
Average		0.0127
STD		0.0041
Max		0.0211
Min		0.0051
Median		0.01275

Recipe of F/2 algae food (Guillard and Ryther 1962, Guillard 1975)

Chemical Component	Mass ($gmol^{-1}$)	Final concentration (M)	Final concentration (gL^{-1})
$NaNO_3$	84.98	8.82×10^{-4}	0.075
$NaH_2PO_4.H_2O$	137.97	3.62×10^{-5}	0.005
$F2Cl_3.6H_2O$	270.30	1.17×10^{-5}	0.0032
$MnCl_2.4H_2O$	197.01	9.10×10^{-7}	1.79×10^{-4}
$ZnSO_4.7H_2O$	186.00	7.65×10^{-8}	2.19×10^{-5}
$CoCl_2.6H_2O$	237.00	4.20×10^{-8}	9.95×10^{-6}
$CuSO_4.5H_2O$	249.00	3.93×10^{-8}	9.79×10^{-6}
$Na_2MoO_4.2H_2O$	237.88	2.60×10^{-8}	6.18×10^{-6}
Thiamine. HCl (Vitamin B1)	333.27	2.96×10^{-7}	1.00×10^{-4}
Biotin (Vitamin H)	242.45	2.05×10^{-9}	5.00×10^{-7}
Cyanocobalamin (Vitamin B12)	1355.4	3.69×10^{-10}	5.00×10^{-7}
$Na_2SiO_3.9H_2O$	284.04	1.06×10^{-4}	0.030
$Na_2EDTA.2H_2O$	374.24	1.17×10^{-5}	0.0044

Appendix III (Chapter II: The Study of 3D Printed Microtextured Surfaces on Contact Angle)

Log Data from Contact Angle Measurements

Shape	Length	Height	Pitch Size	Receding CA	Advancing CA	Apparent CA	Hysteresis CA
Groove	400	200	400	98.44	110.58	104.51	12.14
Groove	400	200	400	101.88	111.86	106.87	9.98
Groove	400	200	400	106.04	112.35	109.20	6.31
Groove	400	200	400	118.28	123.25	120.77	4.97
Groove	400	200	400	114.79	129.77	122.28	14.98
Groove	400	200	400	125.76	131.10	128.43	5.34
Groove	400	200	400	113.82	114.55	114.19	0.73
Groove	400	200	400	128.24	128.86	128.55	0.62
Groove	400	200	400	121.14	123.25	122.20	2.11
Groove	400	200	900	93.99	98.28	96.14	4.29
Groove	400	200	900	90.00	103.43	96.72	13.43

Groove	400	200	900	101.11	106.88	104.00	5.77
Groove	400	200	900	92.60	115.59	104.10	22.99
Groove	400	200	900	99.80	105.02	102.41	5.22
Groove	400	200	900	95.10	109.02	102.06	13.92
Groove	400	200	900	124.76	135.00	129.88	10.24
Groove	400	200	900	121.56	135.00	128.28	13.44
Groove	400	200	900	123.98	135.00	129.49	11.02
Groove	400	450	400	91.97	100.23	96.10	8.26
Groove	400	450	400	98.60	99.60	99.10	1.00
Groove	400	450	400	128.68	132.36	130.52	3.68
Groove	400	450	400	92.88	116.01	104.45	23.13
Groove	400	450	400	112.56	116.93	114.75	4.37
Groove	400	450	400	125.61	144.39	135.00	18.78
Groove	400	450	400	115.63	129.94	122.79	14.31
Groove	400	450	400	116.14	139.13	127.64	22.99
Groove	400	450	400	112.81	143.37	128.09	30.56
Groove	400	450	900	110.90	113.06	111.98	2.16
Groove	400	450	900	141.97	145.64	143.81	3.67
Groove	400	450	900	115.15	127.80	121.48	12.65
Groove	400	450	900	94.33	109.65	101.99	15.32
Groove	400	450	900	102.55	111.20	106.88	8.65
Groove	400	450	900	112.17	122.52	117.35	10.35
Groove	400	450	900	138.28	140.41	139.35	2.13
Groove	400	450	900	138.76	141.60	140.18	2.84
Groove	400	450	900	142.40	144.65	143.53	2.25
Groove	400	700	400	93.40	118.25	105.83	24.85
Groove	400	700	400	101.68	129.16	115.42	27.48
Groove	400	700	400	101.07	121.77	111.42	20.70
Groove	400	700	400	105.98	123.84	114.91	17.86
Groove	400	700	400	93.18	112.36	102.77	19.18
Groove	400	700	400	129.74	133.71	131.73	3.97
Groove	400	700	400	113.28	130.16	121.72	16.88
Groove	400	700	400	135.00	139.82	137.41	4.82
Groove	400	700	400	126.78	129.65	128.22	2.87
Groove	400	700	900	128.61	134.02	131.32	5.41
Groove	400	700	900	124.49	151.36	137.93	26.87
Groove	400	700	900	135.00	140.14	137.57	5.14
Groove	400	700	900	129.52	137.49	133.51	7.97
Groove	400	700	900	138.28	140.43	139.36	2.15
Groove	400	700	900	106.86	121.26	114.06	14.40
Groove	400	700	900	113.63	126.91	120.27	13.28

Groove	400	700	900	130.74	139.26	135.00	8.52
Groove	400	700	900	129.89	138.15	134.02	8.26
Groove	900	200	400	100.65	116.25	108.45	15.60
Groove	900	200	400	106.31	117.63	111.97	11.32
Groove	900	200	400	102.15	115.69	108.92	13.54
Groove	900	200	400	114.58	120.18	117.38	5.60
Groove	900	200	400	112.13	128.18	120.16	16.05
Groove	900	200	400	116.03	120.28	118.16	4.25
Groove	900	200	400	115.24	127.00	121.12	11.76
Groove	900	200	400	121.34	128.11	124.73	6.77
Groove	900	200	400	113.84	129.53	121.69	15.69
Groove	900	200	900	90.00	101.18	95.59	11.18
Groove	900	200	900	90.00	120.56	105.28	30.56
Groove	900	200	900	99.93	107.73	103.83	7.80
Groove	900	200	900	90.00	93.10	91.55	3.10
Groove	900	200	900	88.35	89.95	89.15	1.60
Groove	900	200	900	90.31	119.20	104.76	28.89
Groove	900	200	900	90.00	90.00	90.00	0.00
Groove	900	200	900	88.69	91.31	90.00	2.62
Groove	900	200	900	88.79	90.00	89.40	1.21
Groove	900	450	400	115.42	123.87	119.65	8.45
Groove	900	450	400	123.88	130.43	127.16	6.55
Groove	900	450	400	124.24	127.23	125.74	2.99
Groove	900	450	400	135.00	141.54	138.27	6.54
Groove	900	450	400	127.48	130.02	128.75	2.54
Groove	900	450	400	138.88	146.03	142.46	7.15
Groove	900	450	400	137.11	143.77	140.44	6.66
Groove	900	450	400	118.23	130.58	124.41	12.35
Groove	900	450	400	142.94	144.46	143.70	1.52
Groove	900	450	900	112.32	119.65	115.99	7.33
Groove	900	450	900	123.30	130.31	126.81	7.01
Groove	900	450	900	113.23	123.22	118.23	9.99
Groove	900	450	900	126.46	129.04	127.75	2.58
Groove	900	450	900	119.13	124.61	121.87	5.48
Groove	900	450	900	119.40	120.62	120.01	1.22
Groove	900	450	900	117.26	132.46	124.86	15.20
Groove	900	450	900	113.79	119.09	116.44	5.30
Groove	900	450	900	115.53	123.69	119.61	8.16
Groove	900	700	400	92.81	98.86	95.84	6.05
Groove	900	700	400	83.26	102.98	93.12	19.72
Groove	900	700	400	109.87	118.98	114.43	9.11

Groove	900	700	400	135.00	142.26	138.63	7.26
Groove	900	700	400	130.96	145.53	138.25	14.57
Groove	900	700	400	120.56	141.93	131.25	21.37
Groove	900	700	400	92.52	105.32	98.92	12.80
Groove	900	700	400	92.56	123.27	107.92	30.71
Groove	900	700	400	94.27	106.45	100.36	12.18
Groove	900	700	900	117.47	123.36	120.42	5.89
Groove	900	700	900	121.27	138.51	129.89	17.24
Groove	900	700	900	116.00	129.81	122.91	13.81
Groove	900	700	900	116.07	119.17	117.62	3.10
Groove	900	700	900	119.22	130.95	125.09	11.73
Groove	900	700	900	121.10	129.01	125.06	7.91
Groove	900	700	900	117.93	127.95	122.94	10.02
Groove	900	700	900	112.75	127.61	120.18	14.86
Groove	900	700	900	113.93	122.77	118.35	8.84
Groove	1400	200	400	77.24	90.00	83.62	12.76
Groove	1400	200	400	78.46	89.71	84.09	11.25
Groove	1400	200	400	86.70	88.07	87.39	1.37
Groove	1400	200	400	122.64	127.76	125.20	5.12
Groove	1400	200	400	122.83	125.74	124.29	2.91
Groove	1400	200	400	122.44	129.77	126.11	7.33
Groove	1400	200	400	112.47	114.63	113.55	2.16
Groove	1400	200	400	90.00	100.71	95.36	10.71
Groove	1400	200	400	104.74	113.54	109.14	8.80
Groove	1400	200	900	89.64	112.95	101.30	23.31
Groove	1400	200	900	90.49	104.79	97.64	14.30
Groove	1400	200	900	91.13	108.20	99.67	17.07
Groove	1400	200	900	102.56	109.98	106.27	7.42
Groove	1400	200	900	90.00	92.02	91.01	2.02
Groove	1400	200	900	103.57	111.80	107.69	8.23
Groove	1400	200	900	90.00	104.19	97.10	14.19
Groove	1400	200	900	96.83	99.55	98.19	2.72
Groove	1400	200	900	92.00	117.38	104.69	25.38
Groove	1400	450	400	90.41	91.22	90.82	0.81
Groove	1400	450	400	92.69	102.26	97.48	9.57
Groove	1400	450	400	90.00	97.36	93.68	7.36
Groove	1400	450	400	125.07	130.03	127.55	4.96
Groove	1400	450	400	117.26	127.51	122.39	10.25
Groove	1400	450	400	110.65	123.28	116.97	12.63
Groove	1400	450	400	116.78	117.21	117.00	0.43
Groove	1400	450	400	103.87	124.33	114.10	20.46

Groove	1400	450	400	106.50	120.17	113.34	13.67
Groove	1400	450	900	126.96	135.00	130.98	8.04
Groove	1400	450	900	129.41	132.92	131.17	3.51
Groove	1400	450	900	135.00	141.13	138.07	6.13
Groove	1400	450	900	132.35	135.00	133.68	2.65
Groove	1400	450	900	139.64	141.11	140.38	1.47
Groove	1400	450	900	135.00	136.81	135.91	1.81
Groove	1400	450	900	129.31	135.00	132.16	5.69
Groove	1400	450	900	126.40	136.68	131.54	10.28
Groove	1400	450	900	135.00	138.31	136.66	3.31
Groove	1400	700	400	90.00	108.15	99.08	18.15
Groove	1400	700	400	92.79	107.62	100.21	14.83
Groove	1400	700	400	113.58	127.49	120.54	13.91
Groove	1400	700	400	106.03	108.76	107.40	2.73
Groove	1400	700	400	107.85	110.83	109.34	2.98
Groove	1400	700	400	107.98	119.60	113.79	11.62
Groove	1400	700	400	94.51	109.68	102.10	15.17
Groove	1400	700	400	94.51	109.68	102.10	15.17
Groove	1400	700	400	111.40	113.61	112.51	2.21
Groove	1400	700	900	129.71	136.97	133.34	7.26
Groove	1400	700	900	135.00	135.00	135.00	0.00
Groove	1400	700	900	135.00	140.33	137.67	5.33
Groove	1400	700	900	132.80	137.20	135.00	4.40
Groove	1400	700	900	135.00	136.96	135.98	1.96
Groove	1400	700	900	133.22	141.01	137.12	7.79
Groove	1400	700	900	123.91	127.02	125.47	3.11
Groove	1400	700	900	127.19	135.00	131.10	7.81
Groove	1400	700	900	118.93	135.00	126.97	16.07
Circular Protrusion	400	200	400	90.00	91.15	90.58	1.15
Circular Protrusion	400	200	400	89.46	97.40	93.43	7.94
Circular Protrusion	400	200	400	86.17	91.90	89.04	5.73
Circular Protrusion	400	200	400	86.73	90.00	88.37	3.27
Circular Protrusion	400	200	400	90.00	92.42	91.21	2.42
Circular Protrusion	400	200	400	84.64	90.00	87.32	5.36
Circular Protrusion	400	200	400	90.00	90.00	90.00	0.00
Circular Protrusion	400	200	400	90.00	90.00	90.00	0.00
Circular Protrusion	400	200	400	90.00	90.00	90.00	0.00
Circular Protrusion	400	200	900	75.45	86.15	80.80	10.70
Circular Protrusion	400	200	900	88.12	89.72	88.92	1.60
Circular Protrusion	400	200	900	91.03	93.67	93.67	2.64
Circular Protrusion	400	200	900	86.73	90.00	88.37	3.27

Circular Protrusion	400	200	900	90.00	92.42	91.21	2.42
Circular Protrusion	400	200	900	84.64	90.00	87.32	5.36
Circular Protrusion	400	200	900	79.24	82.70	80.97	3.46
Circular Protrusion	400	200	900	78.94	82.71	80.83	3.77
Circular Protrusion	400	200	900	81.57	84.08	82.83	2.51
Circular Protrusion	400	450	400	88.59	90.00	89.30	1.41
Circular Protrusion	400	450	400	93.46	100.43	96.95	6.97
Circular Protrusion	400	450	400	92.13	92.22	92.18	0.09
Circular Protrusion	400	450	400	87.94	90.00	88.97	2.06
Circular Protrusion	400	450	400	105.34	119.25	112.30	13.91
Circular Protrusion	400	450	400	102.48	108.77	105.63	6.29
Circular Protrusion	400	450	400	97.46	116.93	107.20	19.47
Circular Protrusion	400	450	400	104.14	109.58	106.86	5.44
Circular Protrusion	400	450	400	97.45	97.75	97.60	0.30
Circular Protrusion	400	450	900	64.27	78.42	71.35	14.15
Circular Protrusion	400	450	900	62.65	66.53	64.59	3.88
Circular Protrusion	400	450	900	90.00	91.15	90.58	1.15
Circular Protrusion	400	450	900	77.77	85.08	81.43	7.31
Circular Protrusion	400	450	900	78.80	79.19	79.00	0.39
Circular Protrusion	400	450	900	71.46	76.24	73.85	4.78
Circular Protrusion	400	450	900	72.09	74.23	73.16	2.14
Circular Protrusion	400	450	900	77.51	80.41	78.96	2.90
Circular Protrusion	400	450	900	87.30	87.35	87.33	0.05
Circular Protrusion	400	700	400	94.34	111.12	102.73	16.78
Circular Protrusion	400	700	400	90.00	108.52	99.26	18.52
Circular Protrusion	400	700	400	115.37	126.57	120.97	11.20
Circular Protrusion	400	700	400	90.00	92.20	91.10	2.20
Circular Protrusion	400	700	400	90.00	109.47	99.74	19.47
Circular Protrusion	400	700	400	95.02	99.63	97.33	4.61
Circular Protrusion	400	700	400	87.62	90.00	88.81	2.38
Circular Protrusion	400	700	400	95.33	101.88	98.61	6.55
Circular Protrusion	400	700	400	90.00	97.08	93.54	7.08
Circular Protrusion	400	700	900	63.10	70.09	63.10	6.99
Circular Protrusion	400	700	900	72.24	75.96	74.10	3.72
Circular Protrusion	400	700	900	82.93	86.14	84.54	3.21
Circular Protrusion	400	700	900	76.10	80.37	78.24	4.27
Circular Protrusion	400	700	900	79.73	85.06	82.40	5.33
Circular Protrusion	400	700	900	76.72	85.27	81.00	8.55
Circular Protrusion	400	700	900	63.55	81.51	72.53	17.96
Circular Protrusion	400	700	900	71.57	74.85	73.21	3.28
Circular Protrusion	400	700	900	63.86	78.54	71.20	14.68

Circular Protrusion	900	200	400	88.45	88.76	88.76	0.31
Circular Protrusion	900	200	400	88.43	90.39	89.41	1.96
Circular Protrusion	900	200	400	90.00	91.28	90.64	1.28
Circular Protrusion	900	200	400	88.84	90.00	89.42	1.16
Circular Protrusion	900	200	400	90.00	90.00	90.00	0.00
Circular Protrusion	900	200	400	82.79	83.16	82.98	0.37
Circular Protrusion	900	200	400	88.23	90.00	89.12	1.77
Circular Protrusion	900	200	400	90.00	90.00	90.00	0.00
Circular Protrusion	900	200	400	90.00	90.00	90.00	0.00
Circular Protrusion	900	200	900	88.24	91.76	90.00	3.52
Circular Protrusion	900	200	900	79.88	90.00	84.94	10.12
Circular Protrusion	900	200	900	90.34	90.74	90.54	0.40
Circular Protrusion	900	200	900	81.93	83.68	82.81	1.75
Circular Protrusion	900	200	900	75.62	82.44	79.03	6.82
Circular Protrusion	900	200	900	76.40	80.69	78.55	4.29
Circular Protrusion	900	200	900	87.14	87.20	87.17	0.06
Circular Protrusion	900	200	900	82.95	90.00	86.48	7.05
Circular Protrusion	900	200	900	74.67	87.99	81.33	13.32
Circular Protrusion	900	450	400	88.04	92.70	90.37	4.66
Circular Protrusion	900	450	400	90.43	94.08	92.26	3.65
Circular Protrusion	900	450	400	89.16	93.05	91.11	3.89
Circular Protrusion	900	450	400	89.35	92.58	90.97	3.23
Circular Protrusion	900	450	400	88.64	91.36	90.00	2.72
Circular Protrusion	900	450	400	79.03	87.36	83.20	8.33
Circular Protrusion	900	450	400	88.69	88.78	88.74	0.09
Circular Protrusion	900	450	400	89.02	90.00	89.51	0.98
Circular Protrusion	900	450	400	90.00	90.00	90.00	0.00
Circular Protrusion	900	450	900	77.97	81.07	79.52	3.10
Circular Protrusion	900	450	900	79.97	80.88	80.43	0.91
Circular Protrusion	900	450	900	77.69	86.03	81.86	8.34
Circular Protrusion	900	450	900	80.29	87.19	83.74	6.90
Circular Protrusion	900	450	900	79.08	83.00	81.04	3.92
Circular Protrusion	900	450	900	83.23	84.89	84.06	1.66
Circular Protrusion	900	450	900	88.42	88.43	88.43	0.01
Circular Protrusion	900	450	900	84.81	90.00	87.41	5.19
Circular Protrusion	900	450	900	69.34	82.95	76.15	13.61
Circular Protrusion	900	700	400	88.41	103.02	95.72	14.61
Circular Protrusion	900	700	400	89.01	90.99	90.00	1.98
Circular Protrusion	900	700	400	90.00	94.76	92.38	4.76
Circular Protrusion	900	700	400	85.66	94.34	90.00	8.68
Circular Protrusion	900	700	400	81.53	84.25	82.89	2.72

Circular Protrusion	900	700	400	89.11	90.00	89.56	0.89
Circular Protrusion	900	700	400	94.58	95.73	95.16	1.15
Circular Protrusion	900	700	400	88.25	90.00	89.13	1.75
Circular Protrusion	900	700	400	90.00	90.00	90.00	0.00
Circular Protrusion	900	700	900	55.79	58.48	57.14	2.69
Circular Protrusion	900	700	900	60.70	62.08	61.39	1.38
Circular Protrusion	900	700	900	55.70	61.05	58.38	5.35
Circular Protrusion	900	700	900	72.96	76.73	74.85	3.77
Circular Protrusion	900	700	900	69.32	72.43	70.88	3.11
Circular Protrusion	900	700	900	59.88	67.17	63.53	7.29
Circular Protrusion	900	700	900	72.86	80.01	76.44	7.15
Circular Protrusion	900	700	900	72.55	82.11	77.33	9.56
Circular Protrusion	900	700	900	75.13	79.15	77.14	4.02
Circular Protrusion	1400	200	400	90.00	90.00	90.00	0.00
Circular Protrusion	1400	200	400	73.88	74.37	74.13	0.49
Circular Protrusion	1400	200	400	75.43	83.61	79.52	8.18
Circular Protrusion	1400	200	400	90.00	90.00	90.00	0.00
Circular Protrusion	1400	200	400	81.67	83.87	82.77	2.20
Circular Protrusion	1400	200	400	86.17	90.00	88.09	3.83
Circular Protrusion	1400	200	400	71.26	77.04	74.15	5.78
Circular Protrusion	1400	200	400	74.86	85.60	80.23	10.74
Circular Protrusion	1400	200	400	71.30	77.98	74.64	6.68
Circular Protrusion	1400	200	900	77.32	81.37	79.35	4.05
Circular Protrusion	1400	200	900	77.79	80.15	78.97	2.36
Circular Protrusion	1400	200	900	70.91	72.99	71.95	2.08
Circular Protrusion	1400	200	900	83.36	84.33	83.85	0.97
Circular Protrusion	1400	200	900	83.58	86.28	84.93	2.70
Circular Protrusion	1400	200	900	82.08	82.46	82.27	0.38
Circular Protrusion	1400	200	900	62.67	68.32	65.50	5.65
Circular Protrusion	1400	200	900	62.13	65.42	63.78	3.29
Circular Protrusion	1400	200	900	73.99	86.96	80.48	12.97
Circular Protrusion	1400	450	400	88.15	90.00	89.08	1.85
Circular Protrusion	1400	450	400	88.15	90.00	89.08	1.85
Circular Protrusion	1400	450	400	88.79	90.00	89.40	1.21
Circular Protrusion	1400	450	400	67.36	70.29	68.83	2.93
Circular Protrusion	1400	450	400	89.29	89.68	89.49	0.39
Circular Protrusion	1400	450	400	79.15	79.39	79.27	0.24
Circular Protrusion	1400	450	400	77.34	84.51	80.93	7.17
Circular Protrusion	1400	450	400	87.43	90.00	88.72	2.57
Circular Protrusion	1400	450	400	70.09	83.66	76.88	13.57
Circular Protrusion	1400	450	900	66.89	77.21	72.05	10.32

Circular Protrusion	1400	450	900	74.84	79.07	76.96	4.23
Circular Protrusion	1400	450	900	58.43	61.98	60.21	3.55
Circular Protrusion	1400	450	900	74.97	78.48	76.73	3.51
Circular Protrusion	1400	450	900	68.24	75.10	71.67	6.86
Circular Protrusion	1400	450	900	64.81	77.01	70.91	12.20
Circular Protrusion	1400	450	900	78.23	86.49	82.36	8.26
Circular Protrusion	1400	450	900	75.21	77.95	76.58	2.74
Circular Protrusion	1400	450	900	72.65	80.54	76.60	7.89
Circular Protrusion	1400	700	400	81.32	98.68	90.00	17.36
Circular Protrusion	1400	700	400	86.15	93.85	90.00	7.70
Circular Protrusion	1400	700	400	85.25	87.93	86.59	2.68
Circular Protrusion	1400	700	400	80.12	90.00	85.06	9.88
Circular Protrusion	1400	700	400	83.55	86.77	85.16	3.22
Circular Protrusion	1400	700	400	84.40	87.40	85.90	3.00
Circular Protrusion	1400	700	400	76.81	81.04	78.93	4.23
Circular Protrusion	1400	700	400	79.39	81.87	80.63	2.48
Circular Protrusion	1400	700	400	86.87	87.84	87.36	0.97
Circular Protrusion	1400	700	900	76.27	80.46	78.37	4.19
Circular Protrusion	1400	700	900	68.85	70.29	69.57	1.44
Circular Protrusion	1400	700	900	78.29	88.67	83.48	10.38
Circular Protrusion	1400	700	900	71.84	73.11	72.48	1.27
Circular Protrusion	1400	700	900	68.40	78.40	73.40	10.00
Circular Protrusion	1400	700	900	63.03	67.57	65.30	4.54
Circular Protrusion	1400	700	900	80.15	83.77	81.96	3.62
Circular Protrusion	1400	700	900	76.18	79.65	77.92	3.47
Circular Protrusion	1400	700	900	76.68	79.84	78.26	3.16

Log Data for computer models

Shape	Length	Height	Pitch Size	Roughness factor, *r*	Aspect ratio	Space factor	Solid area fraction
Groove	400	200	400	3.31	2.00	1.00	0.50
Groove	400	200	900	3.11	2.00	2.25	0.31
Groove	400	450	400	3.96	0.89	1.00	0.50
Groove	400	450	900	3.50	0.89	2.25	0.31
Groove	400	700	400	4.60	0.57	1.00	0.50
Groove	400	700	900	3.89	0.57	2.25	0.31
Groove	900	200	400	3.12	4.50	0.44	0.69
Groove	900	200	900	3.03	4.50	1.00	0.50
Groove	900	450	400	3.51	2.00	0.44	0.69
Groove	900	450	900	3.33	2.00	1.00	0.50
Groove	900	700	400	3.91	1.29	0.44	0.69

Groove	900	700	900	3.33	1.29	1.00	0.50
Groove	1400	200	400	3.05	7.00	0.29	0.78
Groove	1400	200	900	2.98	7.00	0.64	0.61
Groove	1400	450	400	3.35	3.11	0.29	0.78
Groove	1400	450	900	3.21	3.11	0.64	0.61
Groove	1400	700	400	3.64	2.00	0.29	0.78
Groove	1400	700	900	3.43	2.00	0.64	0.61
Circular protrusion	400	200	400	3.20	2.00	1.00	0.20
Circular protrusion	400	200	900	2.95	2.00	2.25	0.07
Circular protrusion	400	450	400	3.71	0.89	1.00	0.20
Circular protrusion	400	450	900	3.13	0.89	2.25	0.07
Circular protrusion	400	700	400	4.21	0.57	1.00	0.20
Circular protrusion	400	700	900	3.32	0.57	2.25	0.07
Circular protrusion	900	200	400	3.13	4.50	0.44	0.38
Circular protrusion	900	200	900	2.98	4.50	1.00	0.20
Circular protrusion	900	450	400	3.55	2.00	0.44	0.38
Circular protrusion	900	450	900	3.21	2.00	1.00	0.20
Circular protrusion	900	700	400	3.96	1.29	0.44	0.38
Circular protrusion	900	700	900	3.44	1.29	1.00	0.20
Circular protrusion	1400	200	400	3.09	7.00	0.29	0.48
Circular protrusion	1400	200	900	2.97	7.00	0.64	0.29
Circular protrusion	1400	450	400	3.45	3.11	0.29	0.48
Circular protrusion	1400	450	900	3.17	3.11	0.64	0.29
Circular protrusion	1400	700	400	3.80	2.00	0.29	0.48
Circular protrusion	1400	700	900	3.38	2.00	0.64	0.29

Appendix IV (Chapter III: Characterizing Material Jetting Processes)

Minimum Feature Size Analysis of Material Jetting Processes

F_L (features' length)				
Nominal length (µm)	Spherical hole	Spherical protrusion	Square hole	Square protrusion
100	*	265.33	*	337.50
200	*	396.63	*	401.21
300	*	490.04	*	503.69
400	*	577.31	416.99	642.93
500	*	664.11	590.92	737.75
600	546.17	757.16	657.31	807.82
700	675.90	846.63	789.13	910.43
800	793.09	947.62	922.57	1031.90
900	930.75	1036.39	1028.23	1119.69
1000	1046.10	1141.90	1166.72	1210.65

1100	1153.74	1246.34	1241.34	1305.74
1200	1293.16	1337.08	1386.80	1407.21
1300	1408.82	1439.84	1488.63	1488.51
1400	1528.92	1517.77	1594.33	1589.44
1500	1666.46	1600.92	1764.39	1680.67
1600	1826.05	1663.92	1852.43	1780.90

A_L (features' area in XZ and YZ planes)

Nominal length (μm)	Spherical hole	Spherical protrusion	Square hole	Square protrusion
100	*	0.001729	*	0.00501
200	*	0.013532	0.00414	0.01954
300	0.00737	0.032064	0.01728	0.04627
400	0.02181	0.062601	0.05169	0.10027
500	0.04975	0.096509	0.11452	0.13201
600	0.11192	0.135605	0.19164	0.18553
700	0.17480	0.180314	0.26812	0.26195
800	0.24497	0.236299	0.36484	0.35046
900	0.31412	0.292860	0.43893	0.40987
1000	0.38710	0.360992	0.54635	0.51258
1100	0.46242	0.436426	0.61741	0.61347
1200	0.54822	0.523276	0.73967	0.74447
1300	0.65380	0.612442	0.87212	0.84738
1400	0.75360	0.697423	1.02362	0.94200
1500	0.86952	0.779338	1.14216	1.07909
1600	1.01782	0.829891	1.32014	1.23597

$F_{H/D}$ (features' height/depth)

Nominal length (μm)	Spherical hole	Spherical protrusion	Square hole	Square protrusion
100	*	9.186	*	22.725
200	*	51.154	11.321	68.255
300	23.278	109.189	41.632	143.742
400	54.745	186.288	102.496	234.797
500	103.312	257.386	195.985	269.360
600	219.660	318.390	285.809	325.419
700	295.322	357.279	342.897	382.497
800	360.793	412.835	391.850	442.047
900	406.950	459.647	446.915	468.190
1000	460.645	515.431	505.152	523.682
1100	507.321	574.806	528.639	581.188
1200	557.789	616.434	580.323	634.795
1300	614.363	670.964	638.942	686.979
1400	656.700	713.268	694.284	717.035
1500	715.266	767.096	724.766	768.661
1600	768.681	800.074	781.718	817.782

Square features' side angles

Nominal length	Square hole	Square protrusion
100	*	16.0922

200	3.0796	36.2288
300	6.9773	55.4899
400	15.5976	63.7988
500	33.9853	67.5529
600	54.2846	73.7827
700	62.3891	77.1623
800	70.7635	78.0108
900	74.7738	78.8910
1000	76.8847	79.4271
1100	77.2820	80.5739
1200	78.3622	81.0050
1300	79.6244	81.5161
1400	80.2935	81.2288
1500	80.0278	81.6481
1600	80.8833	82.2399

Effects of Surface Slope and Build Orientation on Surface Finish and Dimensional Accuracy in Material Jetting Processes

	0 degree-Flat surface						45 degree-Flat surface					
	XY			YX			XY			YX		
	Rep1	Rep2	Rep3	Rep1	Rep2	Rep3	Rep1	Rep2	Rep3	Rep1	Rep2	Rep3
a	98.79	5.86	736.17	5.83	829.26	2135.69	3.39	1580.61	177.53	831.63	381.03	4.40
b	31.38	81.45	14.11	150.89	141.18	35.84	8.44	128.05	9.79	29.98	76.94	7.36
St	199.20	112.64	791.78	286.91	770.47	952.58	101.44	1080.63	1091.12	972.10	1016.01	38.30
Sp	48.02	105.08	14.89	276.24	112.09	15.72	72.36	80.99	57.02	33.82	170.69	23.97
Sv	151.19	7.56	776.89	10.68	658.38	936.86	29.08	999.65	1034.11	938.28	845.32	14.33
Sq	7.44	3.00	3.92	4.32	8.72	2.60	12.81	6.88	17.70	6.07	17.73	5.19
Sa	6.23	2.38	2.67	2.03	2.51	1.89	10.25	3.26	11.83	4.74	4.95	4.13
Ssk	0.49	1.28	-51.66	35.12	-53.66	-48.18	0.14	-79.77	-17.19	-3.25	-31.40	0.68
Sku	2.97	21.69	9100.75	1898.92	3475.01	16915.20	2.59	10334.90	910.18	578.25	1245.35	3.30
SWt	28.83	13.03	19.01	12.20	53.14	11.55	58.16	20.60	69.43	28.40	73.90	24.56
Smr	0.00	0.00	0.00	0.00	0.00	0.00	0.00	0.00	0.00	0.00	0.00	0.00
Smc	11.29	4.03	4.88	3.37	4.60	3.78	16.76	5.78	20.17	8.29	8.10	7.46
Sxp	9.44	4.49	4.55	4.52	4.68	4.42	23.12	7.58	20.26	9.65	8.44	7.43
Smean	-3.79	-31.64	27.96	-39.83	26.47	29.55	3.71	54.53	35.03	10.32	8.90	8.17
Sal	1.66	2.25	2.47	0.76	0.07	1.84	1.65	0.47	1.62	1.03	0.04	0.63
Str	0.32	0.60	0.65	0.15	0.38	0.37	0.33	0.11	0.32	0.21	0.60	0.13
Std	0.34	92.30	3.75	0.36	0.35	0.33	0.63	179.00	0.35	179.00	6.00	0.35
Vm	0.00	0.00	0.00	0.00	0.00	0.00	0.00	0.00	0.00	0.00	0.00	0.00
Vv	0.01	0.00	0.01	0.00	0.00	0.00	0.02	0.01	0.02	0.01	0.01	0.01
Vmp	0.00	0.00	0.00	0.00	0.00	0.00	0.00	0.00	0.00	0.00	0.00	0.00
Vmc	0.01	0.00	0.00	0.00	0.00	0.00	0.01	0.00	0.01	0.00	0.00	0.00
Vvc	0.01	0.00	0.00	0.00	0.00	0.00	0.02	0.01	0.02	0.01	0.01	0.01
Vvv	0.00	0.00	0.00	0.00	0.00	0.00	0.00	0.00	0.00	0.00	0.00	0.00

Sk	2.02	1.70	0.00	1.38	0.00	1.79	3.94	0.00	0.00	4.89	0.00	4.81
Spk	1.00	0.75	1.69	0.83	2.21	0.68	1.46	0.00	0.00	2.12	0.01	1.74
Svk	2.87	0.67	2.32	0.77	2.74	1.00	1.28	0.02	0.01	14.80	0.01	1.88
Smr1	10.20	7.58	11.60	9.15	37.00	9.93	9.85	17.50	13.60	5.87	24.90	6.88
Smr2	84.50	86.10	11.60	78.40	37.00	86.10	91.00	86.50	80.50	85.80	66.50	89.10
FLTt	28.90	13.00	18.90	12.20	52.80	11.50	58.10	0.02	0.07	28.30	0.07	24.50
FLTp	17.00	8.09	10.30	7.02	7.41	6.73	33.40	0.01	0.05	19.20	0.01	17.30
FLTv	11.90	4.91	8.66	5.15	45.40	4.81	24.70	0.01	0.02	9.13	0.06	7.21
FLTq	6.65	2.38	2.79	1.95	2.69	1.91	11.50	0.00	0.01	4.68	0.00	3.93
Sbi	0.22	0.03	0.46	0.02	0.08	0.24	0.25	0.09	0.56	0.27	0.11	0.36
Sci	1.74	1.72	1.57	1.02	0.63	1.72	1.62	1.01	1.38	1.77	0.59	1.81
Svi	0.29	0.08	0.07	0.07	0.05	0.14	0.10	0.09	0.06	0.11	0.06	0.08

F_L (Length of features)		spherical-protrusion	square-protrusion	spherical-hole	square-hole
Flat-XY	Feature 1	1864.89	1932.70	2292.21	2495.28
	Feature 2	1836.88	1850.68	2275.42	2471.42
	Feature 3	1868.64	1935.65	2220.62	2443.39
	Feature 4	1834.56	1886.03	2235.35	2420.99
45-XY	Feature 1	1957.13	1934.11	1614.75	1670.78
	Feature 2	1873.49	1875.595	1706.07167	1688.228
	Feature 3	2019.85667	1927.137	1671.42667	1671.237
	Feature 4	1900.72333	1975.897	1555.48333	1745.33
Flat-YX	Feature 1	1850.24	1913.65	2286.81	2464.07
	Feature 2	1863.93	1890.94	2260.65	2527.16
	Feature 3	1868.12	1889.74	2264.60	2493.44
	Feature 4	1845.24	1911.24	2253.04	2502.53
45-YX	Feature 1	2103.255	2333.882	1639.72667	2218.57
	Feature 2	1996.48167	2297.062	1619.77833	2176.277
	Feature 3	1934.94833	2282.08	1704.515	2115.473
	Feature 4	2116.105	2196.815	1672.44167	1966.71

A_L (Features' area in XZ and YZ planes)				
	Spherical			
	Flat		45	
	Protrusion	Hole	Protrusion	Hole
XY	0.91	1.48	0.90	0.84
	0.91	1.47	0.87	0.91
	0.94	1.39	0.91	0.89
	0.92	1.40	0.90	0.87
YX	0.90	1.41	0.89	0.95
	0.92	1.41	0.93	0.95

	0.91	1.41	0.88	0.97
	0.91	1.44	0.94	0.98
Square				
	Flat		45	
	Protrusion	Hole	Protrusion	Hole
XY	1.30	1.72	1.22	1.15
	1.25	1.70	1.20	1.10
	1.31	1.63	1.23	1.09
	1.24	1.62	1.24	1.19
YX	1.29	1.61	1.38	1.29
	1.27	1.62	1.41	1.27
	1.27	1.64	1.32	1.27
	1.26	1.67	1.40	1.21

$F_{H/D}$ (Features' height/depth)					
		Spherical protrusion	Square protrusion	Spherical hole	Square hole
Flat-H(avg)-XY	Feature 1	819.87	818.41	778.92	787.61
	Feature 2	823.22	820.52	771.40	790.75
	Feature 3	822.58	742.30	779.20	780.12
	Feature 4	824.29	754.86	765.51	779.58
45-H(avg)-XY	Feature 1	776.17	790.70	798.20	783.67
	Feature 2	759.11	787.99	760.91	781.66
	Feature 3	762.60	645.97	791.47	781.56
	Feature 4	755.51	638.68	775.57	778.21
Flat-H(avg)-YX	Feature 1	815.39	810.65	775.30	783.15
	Feature 2	825.09	813.24	783.87	784.89
	Feature 3	818.04	813.40	761.69	783.25
	Feature 4	814.83	809.43	771.20	785.49
45-H(avg)-YX	Feature 1	778.13	806.65	801.24	805.37
	Feature 2	751.88	767.85	814.60	802.64
	Feature 3	784.05	806.77	824.98	818.21
	Feature 4	776.21	804.83	818.58	809.31

Side Angle for square features			
		Square protrusion	Square hole
Flat-Angle(avg)-XY	Feature 1	84.63	88.57
	Feature 2	84.88	88.81
	Feature 3	82.33	88.60
	Feature 4	82.46	88.34
	Feature 1	84.96	88.24

45-Angle(avg)-XY	Feature 2	85.04	87.77
	Feature 3	85.65	87.79
	Feature 4	85.33	87.69
Flat-Angle(avg)-YX	Feature 1	84.38	86.73
	Feature 2	83.33	86.87
	Feature 3	83.19	87.70
	Feature 4	85.36	88.09
45-Angle(avg)-YX	Feature 1	83.69	84.65
	Feature 2	85.24	85.58
	Feature 3	85.78	84.45
	Feature 4	83.92	85.38

Effect of build orientation and part thickness on dimensional distortion in material jetting processes

Factorial Result for Height of the highest peak (H)

StdOrder	RunOrder	CenterPt	Blocks	Thickness	Orientation	H (µm)
9	3	1	1	3 mm	XY	519.8
10	4	1	1	6 mm	XY	160.4
1	5	1	1	3 mm	XY	354.1
2	6	1	1	6 mm	XY	378.1
5	10	1	1	3 mm	XY	392.0
6	9	1	1	6 mm	XY	146.0
11	12	1	1	3 mm	YX	300.1
8	11	1	1	6 mm	YX	329.8
7	1	1	1	3 mm	YX	437.1
4	2	1	1	6 mm	YX	275.6
3	8	1	1	3 mm	YX	321.3
12	7	1	1	6 mm	YX	192.1

Factorial Result for profiles’ radius (R)

StdOrder	RunOrder	CenterPt	Blocks	Thickness	Orientation	R (µm)
5	1	1	1	3 mm	XY	3389500
9	9	1	1	3 mm	XY	3651686
1	11	1	1	3 mm	XY	4049321
10	4	1	1	6 mm	XY	7985265
2	7	1	1	6 mm	XY	5690397
6	8	1	1	6 mm	XY	8413087
7	5	1	1	3 mm	YX	7536277
11	6	1	1	3 mm	YX	4195526
3	10	1	1	3 mm	YX	4919653
8	2	1	1	6 mm	YX	4628277

4	3	1	1	6 mm	YX	7656429
12	12	1	1	6 mm	YX	7545097

		Flatness parameters					
		H	L	I-Unit	I-Unit-avg	S %	S_avg
XY	Rep 1	108.81	142771.60	0.14		0.08	
	Rep 2	232.77	66719.40	3.00		0.35	
	Rep 3	195.74	66035.80	2.17		0.30	
	Rep ex1	302.10	84262.40	3.17		0.36	
	Rep ex2	270.39	109921.60	1.49	2.00	0.25	0.27
YX	Rep 1	97.39	95601.60	0.26		0.10	
	Rep 2	50.99	44449.50	0.32		0.11	
	Rep 3	83.34	57490.40	0.52		0.14	
	Rep ex1	110.36	72338.20	0.57		0.15	
	Rep ex2	175.98	64757.80	1.82	0.70	0.27	0.16